DGK Ausschuss Geodäsie (DGK)
der Bayerischen Akademie der Wissenschaften

Reihe C | Dissertationen | Heft Nr. 968

Mohammad J. Tourian

Hydrogeodesy: A Bayesian perspective

München 2025

Verlag der Bayerischen Akademie der Wissenschaften, München

ISSN 0065-5325 ISBN 978 3 7696 5380 9

DGK Ausschuss Geodäsie (DGK)
der Bayerischen Akademie der Wissenschaften

Reihe C Dissertationen Heft Nr. 968

Hydrogeodesy: A Bayesian perspective

University of Stuttgart
Faculty of Aerospace Engineering and Geodesy
Institute of Geodesy

Habilitation thesis

by

Dr.-Ing. Mohammad J. Tourian

München 2025

Verlag der Bayerischen Akademie der Wissenschaften, München

ISSN 0065-5325 ISBN 978 3 7696 5380 9

Adresse des Ausschusses Geodäsie (DGK)
der Bayerischen Akademie der Wissenschaften:

Ausschuss Geodäsie (DGK) der Bayerischen Akademie der Wissenschaften
Alfons-Goppel-Straße 11 ● D – 80 539 München
Telefon +49 – 89 – 23 031 1113 ● Telefax +49 – 89 – 23 031 - 1283 / - 1100
e-mail post@dgk.badw.de ● http://www.dgk.badw.de

Gutachter: Prof. Nico Sneeuw
Prof. Jürgen Kusche
Prof. Tamlin Pavelsky
Prof. Uwe Sörgel

Tag der Einreichung: 11.11.2024

Tag des Vortrags und des wissenschaftlichen Gesprächs: 17.07.2025

Diese Habilitation ist auf dem Server des Ausschusses Geodäsie (DGK)
der Bayerischen Akademie der Wissenschaften, München unter <http://dgk.badw.de/>
sowie unter Universität Stuttgart,
<https://doi.org/10.18419/opus-16962>, Stuttgart 2025, elektronisch publiziert

ISSN 0065-5325 ISBN 978 3 7696 5380 9

Acknowledgement

This habilitation is the end of a long journey full of challenges, learning, and personal growth. I'm very thankful to everyone who supported, encouraged, and stood by me along the way.

I would first like to thank Prof. Nico Sneeuw, whose unwavering support and sharp insights were invaluable throughout this process. His critical feedback, collegial spirit, and steady confidence in my research left a lasting impact on both the content and direction of this thesis. As one of the reviewers, his comments and thoughtful suggestions further enhanced the quality and clarity of the work.

I am also deeply grateful to the other members of the habilitation review committee: Prof. Jürgen Kusche, Prof. Uwe Sörgel, and Prof. Tamlin Pavelsky, who generously dedicated their time to read this work and attended the final presentation in person. Each brought a distinct perspective from satellite geodesy, remote sensing, and hydrology, which I was genuinely pleased to see represented. Knowing that my work would be examined from such diverse and expert viewpoints motivated me to revise and refine nearly every sentence of this habilitation with great care. I am especially thankful for their insightful questions and constructive feedback, which helped strengthen the final version of this work.

To my colleagues at the Institute of Geodesy, University of Stuttgart, thank you for fostering an environment where ideas could grow and collaborations could thrive. I am especially grateful to Omid Elmi, a friend and collaborator whose scientific input, thoughtful questions, and shared curiosity, often exchanged over countless coffee breaks, hallway discussions, and focused meetings, enriched many aspects of this work with fresh perspectives and deeper understanding. I also want to thank Johannes Engels, whose sharp thinking and wealth of ideas brought clarity and inspiration to several parts of this thesis. I would also like to thank Peyman Saemian, who supported this journey through ongoing scientific exchange and detailed data analysis. His dedication, reliability, and collaborative spirit contributed to the quality and consistency of the work. I would like to sincerely thank all other colleagues at the institute, including Prof. James Foster, for their engagement and for the many insightful formal and informal conversations that helped create a stimulating and supportive research environment

I would also like to extend my heartfelt thanks to all members of the HydroGeoCoPE research group: Omid Elmi, Benjamin Kitambo, Shahin Khalili, Siqi Ke, Peyman Saemian, Shuhua Yu, and Chistrong Wen. I have learned a great deal from our regular meetings, as well as from spontaneous conversations, quick questions, and thoughtful exchanges along the way. Your dedication, curiosity, and collaborative spirit have contributed to this research in more ways than you may realize.

Most of all, I thank my wife, Parisa. Her love, patience, and quiet strength were with me through every step. There were times when I felt stuck or tired, but her calm presence helped me find my way forward. She believed in me wholeheartedly, and her constant support gave me the strength to stay focused and keep going.

Finally, I dedicate this work to my son, Liam. Watching him grow has reminded me to see the world with wonder. He has taught me the value of slowing down, staying curious, and finding balance between work and life. His laughter and hugs often brought me back to what matters most.

Abstract

While historically focused on local scales, modern hydrologic studies have increasingly adopted a global perspective, recognizing water as a finite resource and the interconnection between regions. This global perspective puts hydrology within the water cycle framework, offering a comprehensive view of water dynamics across regions and scales. Despite this framework's conceptual clarity, accurately quantifying the global water cycle remains challenging due to the complexity of capturing localized and large-scale patterns, variations in topography, climate, and land use, as well as temporal variability. These complexities hinder comprehensive measurements, resulting in knowledge gaps around key water cycle components, including river discharge, surface water storage, soil moisture dynamics, and subsurface water storage and flow.

Inspired by the existing knowledge gaps in the water cycle, an emerging field known as ***Hydrogeodesy*** comes to the forefront. Hydrogeodesy is the discipline that uses terrestrial and primarily spaceborne geodetic data, both geometric and gravimetric, to support global water cycle quantification. Utilizing technologies such as satellite altimetry, gravimetry, imaging, InSAR, GNSS, and GNSS-Reflectometry, hydrogeodesy offers direct or indirect measurements of key water cycle components, including terrestrial water storage, and river discharge, significantly advancing our understanding of water dynamics. Despite advancements in spaceborne geodetic sensors, hydrogeodesy faces challenges such as limitations in the spatiotemporal resolution of satellite measurements, measurement uncertainties, unobserved variables, inconsistencies in background models, and the difficulty of separating aggregated measurements. Possible solutions to these challenges involve combining different data types, including satellite, ground-based observations, and model outputs, to benefit from their complementary strengths. However, this presents its own challenges, as it requires reconciling datasets with varying resolutions, accuracies, and temporal scales.

To address some of the challenges listed above, Bayesian approaches offer viable solutions by providing probabilistic interpretations and uncertainty quantification. Bayesian approaches offer a robust framework for updating prior knowledge with new data to yield a posterior distribution, enabling a probabilistic interpretation and explicit uncertainty estimation of parameters. This is especially valuable in hydrogeodesy, where parameters like river discharge, soil moisture, and groundwater storage are often estimated indirectly and carry substantial uncertainties. This habilitation thesis provides a foundational discussion on Bayesian modeling and statistics and demonstrates the versatility and power of Bayesian methods in enhancing our understanding of water cycle components by presenting three distinct Bayesian applications in hydrogeodesy.

The first study applies a Bayesian approach, specifically the Kalman filter, to estimate river discharge using spaceborne geodetic measurements. In hydrogeodetic studies, the Kalman filter and dynamic systems are especially valuable, as they enable the integration of multiple data sources and the continuous updating of estimates with incoming measurements. This is particularly beneficial for river systems, which inherently function as a dynamic system. To assess this potential, a method is introduced that uses the cyclostationary properties of discharge as prior information, while observed altimetric discharge data provide the likelihood. Together, these yield a posterior providing an unbiased daily discharge estimate. The method is applied to the Niger River basin and its main tributaries and validated against *in situ* data from 18 gauges. Results show a high average Correlation Coefficient (CC) of 0.9 and an average relative Root Mean Squared Error (RMSE) and bias of 15%. This method effectively estimates daily river discharge across entire basins and shows promise for global application, especially in data-scarce regions. With satellite altimetry data from multiple virtual stations and historical discharge data, daily discharge estimates with an error under 20%

could be attainable in many river basins worldwide. The growing availability of spaceborne geodetic data, such as that provided by SWOT, further enhances this potential by delivering comprehensive measurements of river height and width, along with global discharge estimates.

In most real-world applications, including hydrogeodesy, the Gaussianity assumption required by the Kalman filter does not hold, limiting its applicability. Inspired by this challenge, and motivated by the need to overcome the limitations of the poor spatial resolution of the GRACE and GRACE-FO missions, the second study proposes a Bayesian method to downscale GRACE data, proposing a nonparametric method to infer the posterior distribution directly, without any assumption for the likelihood or posterior. The prior distribution is obtained based on GRACE data values using the monthly variation of GRACE data. To model the likelihood functions, copulas are employed to capture dependencies among multivariate distributions. Monthly empirical copulas are constructed and fitted to analytical copulas, conditioned on specific quantile values, reflecting the dependency between GRACE and fine-scale data. A key advantage of this copula-supported Bayesian approach is its capacity to represent uncertainties in both data and models, even with variable input quality.

The proposed downscaling approach is applied to the Amazon Basin, utilizing four different fine-scale datasets: WGHM, PCR-GLOBWB, SURFEX-TRIP, and the ensemble of flux data and soil moisture data from GLEAM and ASCAT. Validation is conducted against two independent datasets: space-based Surface Water Storage Change (SWSC) and GPS-observed Vertical Crustal Displacement Change (VCDR). In SWSC validation, downscaled results capture spatial variations in river storage with high CC and a relative RMSE of 26%. VCDR validation involves two analyses: comparing GPS-VCDR with TWSF-based VCDR using Green's function convolution, where downscaled products yield RMSE values between 2.27 and 5.65 mm/month, outperforming input fine-scale data with 14 mm/month RMSE. In terms of CC, downscaled results achieve an average value of -0.81 versus -0.73 for the input. The proposed Bayesian framework effectively downscales GRACE data, with performance highly dependent on input data quality. The copula-supported Bayesian approach offers valuable uncertainty quantification even with inconsistent input data. This method aids in understanding water storage variations in small catchments, supporting local hydrological studies, and can be applied to other water cycle parameters as an alternative to traditional methods.

Although a direct posterior is obtained for each grid cell in the downscaling study, spatial dependencies among neighboring grid cells are not considered. Graphical models are particularly well-suited for capturing such spatial dependencies. To address this limitation—and inspired by the challenge of noisy water level estimates from satellite altimetry over inland water bodies—the third study presents a Bayesian approach that formulates a probabilistic graphical model known as a Markov Random Field (MRF), with a Maximum A Posteriori estimation of the MRF (MRF-MAP) as the objective. There to improve inland altimetry, a retracking method is proposed. Unlike conventional retracking methods that target a single waveform point, a holistic approach by identifying retracking lines within 2D radargrams, treating the radargram as a segmented image. This segmentation divides the radargram into *Front* and *Back* segments, resembling a binary image segmentation task. The proposed MRF-MAP framework uses spatial dependencies as prior information, with the likelihood based on the temporal evolution of pixel labels across groundtrack cycles. Two temporal energy functions are applied: 1D, based solely on pixel intensity, and 2D, which includes both intensity and bin values, with the posterior probability maximized using the maxflow algorithm. The maxflow algorithm is the applied to obtain MAP solution, yielding a segmented radargram where the retracking line is defined as the boundary between segments.

The proposed retracker method is applied to both pulse-limited and SAR altimetry datasets across nine U.S. lakes and reservoirs with varying altimetry characteristics. Validated against in situ data, the proposed method improves RMSE by approximately 0.25 m with the 1D temporal energy function and 0.51 m with the 2D function. The main advantage of the proposed method is its robustness against unexpected waveform variations, making it especially valuable for complex radargrams where conventional retrackers often deliver

outliers. By integrating both spatial and temporal information, this method offers a more comprehensive understanding of the data and has broad applicability, such as improving the classification of SWOT pixel cloud points by incorporating spatiotemporal detail.

Through these case studies, the thesis illustrates the advantages of Bayesian approaches in improving the accuracy and reliability of hydrological estimates—such as river discharge, terrestrial water storage, and water level measurements—derived from spaceborne geodetic sensors. By integrating theoretical insights with practical applications, the thesis demonstrates how Bayesian methods can effectively improve spatiotemporal resolution, obtain uncertainties, enhance data fusion, and accommodate the complexities inherent in hydrological systems. This combination of foundational knowledge and real-world examples shall establish a base for advancing the use of Bayesian approaches in hydrogeodetic research and beyond. Moreover, by highlighting the challenges in hydrogeodesy, this thesis provides a clear direction for future research and development in the field. It emphasizes critical areas requiring attention, such as improving the spatial and temporal resolution of hydrological estimates, addressing inherent uncertainties in geodetic observations, and developing more effective methods for assimilating diverse data sources. The thesis encourages the refinement of geodetic data processing techniques and the adoption of probabilistic frameworks, such as Bayesian modeling, in future work. Building upon the work presented here, future studies can ultimately achieve more accurate and reliable insights into the Earth's systems.

Contents

Preface

After completing my PhD in 2013 on the application of spaceborne geodetic sensors in hydrology, I became increasingly drawn to the principles and applications of Bayesian statistics and modeling. This interest was inspired and amplified by the challenges encountered in satellite geodesy, particularly in hydrogeodesy—the use of spaceborne geodetic sensors for quantifying water cycle components. Addressing some of these challenges required new perspectives, and Bayesian approaches provided a powerful framework to tackle them in this evolving field. As I started lecturing courses like *satellite geodesy*, *hydrogeodesy*, *adjustment theory*, *selected chapters in parameter estimation*, and *remote sensing for hydrology and water resource management*, in the study programs of *Geodesy and Geoinformatics*, *GEOENGINE* and *Environmental Engineering*, the opportunity to incorporate Bayesian approaches into my teaching proved invaluable. Developing materials and designing exercises for students allowed me to delve deeply into these concepts and reflect on their practical significance in geodesy and hydrology.
Moreover, over the years, my involvement in various research projects has provided consistent opportunities to explore Bayesian methods as a versatile and insightful approach. Each project offered a unique context for experimentation, deepening my understanding of hydrogeodesy and the applicability of Bayesian statistics and modeling. These combined experiences in teaching and research have culminated in a series of publications, some of which (listed below) form the basis for the material presented in this thesis.

- Tourian, M. J., Tarpanelli, A., Elmi, O., Qin, T., Brocca, L., Moramarco, T., & Sneeuw, N. (2016). Spatiotemporal densification of river water level time series by multimission satellite altimetry. Water Resources Research, 52(2), 1140-1159.
- Tourian, M. J., Schwatke, C., & Sneeuw, N. (2017). River discharge estimation at daily resolution from satellite altimetry over an entire river basin. Journal of Hydrology, 546, 230-247.
- Tourian, M. J., Saemian, P., Ferreira, V. G., Sneeuw, N., Frappart, F., & Papa, F. (2023). A copula-supported Bayesian framework for spatial downscaling of GRACE-derived terrestrial water storage flux. Remote Sensing of Environment, 295, 113685.
- Tourian, M. J., Elmi, O., Khalili, S., & Engels, J. (2025). Improving inland water altimetry through Bin-Space-Time (BiST) retracking: A Bayesian approach to incorporate spatio-temporal information. IEEE Transactions on Geoscience and Remote Sensing.

The following habilitation thesis, therefore, represents not only a synthesis of my explorations within hydrogeodesy from a Bayesian perspective but also a testament to the part of my knowledge growth achieved in my academic pursuits since completing my PhD. It is my hope that this thesis will contribute to furthering the understanding of Bayesian methods within the fields of hydrogeodesy and geodesy.

Dr.-Ing. Mohammad J. Tourian

July 2025, Stuttgart

1 Hydrogeodesy

As a pure science, hydrology deals with the natural occurrence, distribution, and circulation of water on, in, and over the surface of the Earth. This is how the father of modern hydrology, Dr. Robert E. Horton, opened his speech before the 12th meeting of the American Geophysical Union on May 1, 1931 (Jones et al., 1963). This is a rather modern definition of a science with roots tracing back to ancient civilizations, which devised methods to manage water for irrigation and drinking. While historically focused on local scales, modern hydrologic studies have increasingly adopted a global perspective. This shift is driven by the recognition of water as a finite resource and by the understanding that changes in one region can significantly affect water availability elsewhere (Lettenmaier, 2006; Vörösmarty et al., 2000). With such a global perspective, the water cycle is the framework for studying hydrology, enabling a comprehensive understanding of water dynamics across diverse regions and scales. Although individual water droplets seldom complete the entire water cycle, the concept itself remains vital in understanding how water is continuously recycled and distributed across the planet (Oki et al., 1999). Essentially, exploring the global water cycle yields insights into how climate change, land use, and other factors influence water availability at both local and global scales (Allan et al., 2020).

While the water cycle can be conceptually defined, and we all probably learned about it in school, gaining insight into the global water cycle requires numbers to quantify storages and fluxes and their variations. To obtain such quantities, we need measurements across spatiotemporal scales ranging from local to continental and from daily to decadal (Maidment, 1993). One might assume that with the advancement of technology, achieving such measurements should be trivial, but in fact, it is not. This is challenging for several reasons: 1) due to the complexity of the global water cycle, sophisticated measurement techniques are required to capture both localized phenomena and large-scale patterns (Vargas Godoy et al., 2021). 2) Topography, climate, and land use variations introduce considerable spatial heterogeneity, necessitating a comprehensive network of observation points to adequately represent different scales (Fernández-Prieto et al., 2012). 3) Temporal variability, ranging from diurnal fluctuations to decadal trends and the occurrence of extreme events, demands continuous monitoring over extended periods to discern extremes, long-term patterns, and seasonal variations accurately (Huntington, 2006). 4) Factors such as data accuracy, consistency, and compatibility across different sensors must be carefully addressed to ensure the reliability and comparability of the collected data (Yang et al., 2021). 5) Logistical constraints, including financial resources, infrastructure, and accessibility to remote or inhospitable regions, further complicate the implementation of comprehensive measurement campaigns (Pecora and Lins, 2020). Finally, 6) the interdisciplinary nature of water cycle research necessitates collaboration across various scientific disciplines and stakeholders to address the multifaceted challenges associated with measuring and understanding the global water cycle comprehensively (Horne et al., 2017).

The challenges outlined above contribute to the inadequate quantification of water cycle storages, fluxes, and their temporal variations, establishing some of them as our *known unknowns*, in a nod to the famous quote (Famiglietti, 2012). Precipitation, as a key flux within the hydrological cycle, is perhaps better monitored than other components (Huffman et al., 2009). Although the number of in situ precipitation gauges has decreased recently (Lorenz and Kunstmann, 2012), satellite-based observation systems have increased, providing broader coverage and a preliminary understanding of the water cycle. Nevertheless, the aforementioned challenges give rise to knowledge gaps in other critical hydrological processes and storage components, some of which are outlined below:

- **Limited understanding of river discharge and its variation**: River discharge gauges, essential for monitoring freshwater transport, are becoming less available, resulting in a decline in the number of gauges with updated measurements (Vörösmarty et al., 2000; Tourian et al., 2013; Elmi et al., 2024; Saemian et al., 2025). This decline is compounded by changes in river discharge driven by factors such as water management practices, climate variability (Xu and Luo, 2015), land-use transformations, and modifications to river morphology (Gerten et al., 2008), further complicating the quantification of freshwater transport and its dynamics within the hydrological cycle.
- **Gaps in understanding surface water storage and its variation**: The temporal and spatial variability of surface water storage within lakes, reservoirs, wetlands, and rivers is not fully characterized, indicating significant gaps in understanding the dynamics of water storage on landmasses (Crétaux et al., 2011; Biancamaria et al., 2016). The quantification of surface water storage and its variability is further complicated by anthropogenic activities, such as dam construction and water abstractions, alongside the impacts of climate change (Zhou et al., 2016).
- **Insufficient insights into soil moisture and its dynamics**: Soil moisture serves as a crucial component of the hydrological cycle, playing a significant role in terrestrial water storage and directly influencing processes such as evapotranspiration, vegetation dynamics, and surface runoff (SU et al., 2014). However, soil moisture's spatial and temporal variability remains poorly understood, particularly across diverse land use types and ecological systems (Wilson et al., 2004).
- **Uncertainties in subsurface water storage and flow**: The evaluation of subsurface water storage and its dynamic behavior predominantly relies on monitoring fluctuations in groundwater levels and variations in soil water saturation. This leads to a considerably uncertain estimate, primarily due to the insufficiently known storage coefficients essential for converting groundwater level measurements into accurate storage quantities (Scanlon et al., 2002; Alley et al., 2002; Strassberg et al., 2007; Rodell et al., 2006; Riegger et al., 2012). Moreover, subsurface water's flow paths and timescales are often poorly understood, leading to gaps in understanding groundwater recharge and depletion (Huyakorn, 2012).
- **Complexities in assessing human impacts on the water cycle**: Anthropogenic activities, including irrigation, land-use changes, urbanization, and dam construction, significantly alter natural hydrological fluxes and storages (Vörösmarty and Sahagian, 2000). Quantifying these impacts at global or regional scales presents considerable challenges due to data limitations and the intricate interactions between natural processes and human-induced modifications (Chiang et al., 2021). As argued by Gleason and Brown (2025), a foundational step toward addressing these complexities is to explicitly recognize humans not as external drivers but as integral components of the hydrological system itself.
- **Limited insights into extreme events and their effects**: The impact of extreme weather events, including droughts, floods, and cyclones, on the dynamics of the water cycle, as well as their modifications under changing climate conditions, are not yet fully understood (Allan et al., 2020). Moreover, the ability to accurately predict the frequency, duration, and intensity of these events within the framework of hydrological processes remains a critical and ongoing challenge (Farazmand and Sapsis, 2019).
- **Uncertainties in the contribution of snow and glacier melt to the water cycle**: The contribution of *snow and glacier melt* to the water cycle, especially in mountainous regions, is not fully quantified (Radić and Hock, 2014). Climate-induced changes in temperature and precipitation are altering melt patterns, but significant uncertainty persists regarding the implications for water availability in glacier- and snow-fed river basins (Pomeroy et al., 2004).
- **Challenges in accurately quantifying evapotranspiration**: Evapotranspiration is a critical component of the water cycle, yet accurate quantification at large scales remains challenging (Pereira et al., 1999). Remote sensing techniques often rely on models that introduce uncertainty, while ground-based measurements are limited, resulting in significant gaps in understanding evapotranspiration dynamics across various climatic conditions and ecosystems (Chen and Liu, 2020).

To address these knowledge gaps, global hydrological modeling can be a valuable approach, integrating diverse data with process knowledge to estimate water fluxes and storage across various compartments. However, while global hydrological modeling has been refined and extended in terms of modeled processes over the last decade, uncertainties in modeling have not necessarily decreased, but are likely better understood (Döll and Fiedler, 2008; Schulze et al., 2024). The wide variability in hydrological model outputs is, in fact, a reflection of the existing knowledge gaps that hinder a holistic understanding of the hydrological system, ultimately limiting our capacity to effectively manage water resources, anticipate floods, and sustainably meet the water needs of ecosystems and communities (Gleick, 2003; Kundzewicz et al., 2007).

1.1 Definition, techniques and their contributions

Inspired by the challenge of limited data in effectively monitoring the intricate global water cycle, spaceborne techniques, particularly spaceborne geodetic sensors, have played a pivotal role over the past three decades (Alsdorf et al., 2007). These sensors provide accurate measurements and insights into fundamental Earth properties such as its geometric shape, gravitational field, and orientation parameters, including their variations over time (Rummel, 2010). With such contributions, their value extends to the thorough observation of the water cycle as well (Alsdorf et al., 2007; Humphrey et al., 2023). They have greatly enhanced our understanding of water availability and have significantly improved our knowledge of water depth, storage volume, and, in general, mass redistribution driven by water (Jaramillo et al., 2024).

As the need for comprehensive hydrological data intensified, the capabilities of spaceborne geodetic sensors, with their expansive coverage and consistent synoptic measurements, have emerged as a promising avenue to address the existing gaps in comprehending hydrological processes (Jaramillo et al., 2024). Through the continuous evolution of new geodetic concepts and the subsequent enhancement of spatiotemporal sampling within the global water cycle, an emerging field typically referred to as ***Hydrogeodesy*** has recently come to the forefront.

Hydrogeodesy is the discipline that uses terrestrial and foremost spaceborne geodetic data, both geometric and gravimetric, in support of global water cycle quantification. By integrating these data sources, hydrogeodesy can offer a holistic perspective on water cycle dynamics, facilitating a better understanding of its intricate processes and aiding in more accurate predictions. As schematically illustrated in Figure 1.1, the key technologies associated with hydrogeodesy are 1) satellite altimetry, 2) satellite gravimetry, 3) satellite imaging, 4) Interferometric Synthetic Aperture Radar (InSAR), 5) Global Navigation Satellite System (GNSS), and 6) GNSS-Reflectometry (GNSS-R), with their various implementations detailed in Table 1.1.

1. **Satellite altimetry**: Over the past three decades, satellite altimetry has been instrumental in monitoring Earth's system, proving effective not only over oceans but also over coastal zones as well as inland water surfaces (Alsdorf and Lettenmaier, 2003; Alsdorf et al., 2007; Calmant and Seyler, 2006; Papa et al., 2006b, 2010a; Crétaux and Birkett, 2006; Calmant and Seyler, 2006; Tourian et al., 2013). Table 1.1 lists all satellite altimetry missions, both laser and radar-based, from 1978 to the present. The satellite altimeter transmits a short pulse with known power toward the water surface along the satellite nadir. The pulse hits the water surface and is reflected to the satellite. Accordingly, the distance between the satellite and the water surface is estimated by measuring the travel time between emission and reception of the pulse (Chelton et al., 1989; Escudier et al., 2017) (See Figure 1.1). The returned signal power can be represented as a time series, referred to as the *waveform*, comprising three primary stages: thermal noise, leading edge, and trailing edge (Brown, 1977). The waveform is sampled in bins with a specific time interval (typically 3.125 ns), which

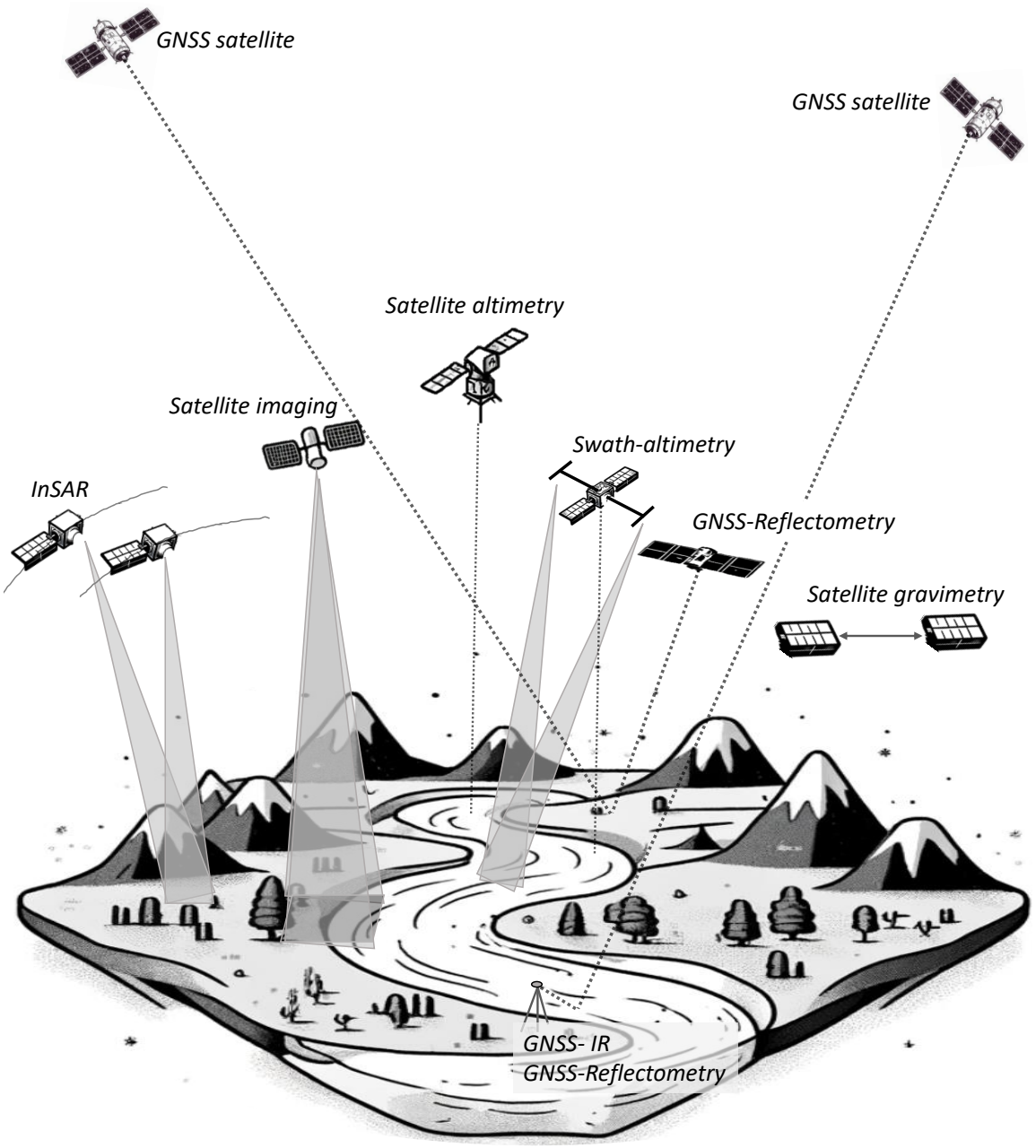

Fig. 1.1: The key technologies associated with hydrogeodesy, including satellite altimetry, both nadir and swath, satellite gravimetry, satellite imaging, Interferometric Synthetic Aperture Radar (InSAR), GNSS, GNSS-Reflectometry (GNSS-R), GNSS-Interferometric Reflectometry (GNSS-IR)

corresponds to a certain distance interval (typically 46.84 cm). The traveling time of the pulse is calculated by defining the midpoint of the leading edge in the waveform as a reference point for the moment that the pulse hits the middle of the water surface (Frappart et al., 1999; Stammer and Cazenave, 2017). This can be properly estimated only if the onboard tracker precisely times the deramping chirp[1] to synchronize with the return signal from the nadir water surface (Chelton et al., 1989). While this synchronization is usually successful over the ocean, it may not be as consistent over coastal zones and inland waters (Rodríguez, 1988). Despite this challenge, satellite altimetry has emerged as a remarkable tool with the capacity to function as virtual gauges for lakes and rivers (Berry et al., 2005; Alsdorf et al., 2007; Papa et al., 2010a).

[1]A chirp signal is a signal in which the frequency continuously increases or decreases over time. In the case of an altimeter, it typically decreases over time. Deramping refers to the process of analyzing or processing the received chirp signal to determine the time delay or phase shift caused by the reflection of a target (in this case, the ground or surface below the altimeter)

Tab. 1.1: Satellite missions and systems that can be potentially used within hydrogeodesy

Satellite altimetry			
Seasat	NASA	1978	1st satellite dedicated to oceanography
GEOSAT	US Navy	1985–1990	Geodetic mission
ERS-1	ESA	1991–2000	Included radar altimeter
TOPEX/Poseidon	NASA/CNES	1992–2006	Joint US-French mission
ERS-2	ESA	1995–2011	Successor to ERS-1
GFO (Geosat Follow-On)	US Navy	1998–2008	Successor to GEOSAT
Jason-1	NASA/CNES	2001–2013	Successor to TOPEX/Poseidon
Envisat (RA2)	ESA	2002–2012	Multi-instrument platform
ICESat	NASA	2003–2010	Focus on ice sheet elevation
Jason-2	NASA/CNES/NOAA/EUMETSAT	2008–2019	Continuation of Jason series
CryoSat-2	ESA	2010–Present	Focus on ice thickness
SARAL/AltiKa	ISRO/CNES	2013–Present	Joint mission with Ka-band altimeter
Sentinel-3A	ESA	2016–Present	Part of Copernicus program, operational
Sentinel-3B	ESA	2018–Present	Part of Copernicus program, operational
ICESat-2	NASA	2018–Present	Follow-on to ICESat
Jason-3	NASA/CNES/NOAA/EUMETSAT	2016–Present	Continuation of Jason series
Sentinel-6 Michael Freilich	ESA/NASA/NOAA/EUMETSAT	2020–Present	Part of Copernicus program, operational
SWOT	NASA/CNES/CSA/UKSA	2022–Present	nadir and swath altimetry
Satellite gravimetry			
CHAMP	DLR	2000–2010	High-Low Satellite to Satellite Tracking
GRACE	NASA, DLR	2002–2017	Low-Low Satellite to Satellite Tracking
GOCE	ESA	2009–2013	satellite gradiometry
GRACE-FO	NASA, DLR	2018–ongoing	Low-Low Satellite to Satellite Tracking
Satellite imaging (optical imaging)			
Landsat	NASA/USGS	1972–Present	Multiple generations
SPOT	CNES	1986–Present	Multiple satellites
QuickBird	DigitalGlobe	2001–2015	Commercial high-resolution satellite
WorldView	Maxar Technologies	2007–Present	Commercial high-resolution satellite constellation
Sentinel	ESA	2014–Present	Part of Copernicus program, multiple missions
Pleiades	CNES	2011–Present	Dual-satellite constellation, Optical imaging
GOES	NOAA	1975–Present	Geostationary weather satellites, multiple generations
MODIS	NASA	1999–Present	Optical and thermal imaging
Suomi NPP	NASA/NOAA	2011–Present	Joint polar-orbiting satellite mission
Himawari	JMA	1977–Present	Geostationary weather satellites, multiple generations
CBERS	CNSA/INPE	1999–Present	Joint Chinese-Multiple generations
SAR imaging and Interferometric Synthetic Aperture Radar (InSAR)			
ERS-1	ESA	1991–2000	Early InSAR mission
ERS-2	ESA	1995–2011	Successor to ERS-1
JERS-1	JAXA	1992–1998	Early Japanese InSAR mission
RADARSAT-1	CSA	1995–2013	First Canadian SAR satellite
RADARSAT-2	CSA	2007–Present	Advanced capabilities, operational
Envisat (ASAR)	ESA	2002–2012	Multi-instrument platform
TerraSAR-X	DLR	2007–Present	High-resolution, operational
TanDEM-X	DLR	2010–Present	Tandem mission with TerraSAR-X, operational
ALOS (Daichi)	JAXA	2006–2011	First ALOS series satellite
ALOS-2	JAXA	2014–Present	Enhanced capabilities, operational
Sentinel-1A	ESA	2014–Present	Part of Copernicus program, operational
Sentinel-1B	ESA	2016–2021	Part of Copernicus program, stopped transmitting data
RADARSAT Constell.	CSA	2019–Present	Constellation for increased coverage, operational
NISAR	NASA/ISRO	2025–Present	Joint NASA-ISRO mission, upcoming
BIOMASS	ESA	Expected 2024	Focus on global forest biomass, upcoming
SAOCOM 1A	CONAE	2018–Present	Part of the SAOCOM constellation, operational
SAOCOM 1B	CONAE	2020–Present	Part of the SAOCOM constellation, operational
COSMO-SkyMed (1st Gen)	ASI	2007–Present	Constellation of four satellites, first-generation
COSMO-SkyMed (2nd Gen)	ASI	2019–Present	Updated constellation, operational
Global Navigation Satellite System (GNSS)			
GPS	USAF	1978–Present	Original and most widely used GNSS
GLONASS	RFSA	1982–Present	Russian GNSS
Galileo	ESA	2011–Present	European GNSS
BeiDou	CNSA	2000–Present	Chinese GNSS
QZSS	JAXA	2010–Present	Regional GNSS for Japan
IRNSS/NavIC	ISRO	2013–Present	Regional GNSS for India
Spaceborne GNSS-Reflectometry (GNSS-R)			
TechDemoSat-1	UKSA	2014–Present	Technology demonstration satellite
CYGNSS	NASA	2016–Present	Cyclone Global Navigation Satellite System
AltiKa	CNES/ISRO	2013–Present	Altimetry mission, includes GNSS reflectometry
ARGOS	NRL	2019–Present	Autonomous Remote Global Observing System, includes GNSS reflectometry
PRETTY	ESA	2023–Present	Passive REflectomeTry and dosimeTrY mission to study various Earth surface properties
HydroGNSS	ESA	Expected 2025–	GNSS Reflectometry mission for hydrological applications, upcoming

The use of satellite altimetry for hydrogeodetic applications has been facilitated by the advent of two recent developments: 1) Open-Loop Tracking Command (OLTC), and 2) Operation in Synthetic

Aperture Radar (SAR) mode. The OLTC was first implemented on the Poseidon-3 altimeter onboard the Jason-2 satellite to improve the onboard tracker through properly setting the reception window of the return echoes. This can be realized by OLTC tables consisting of the overflown surface elevation (Le Gac et al., 2021). The altimeter reads the elevation onboard and uses it together with a navigation bulletin provided by DORIS/DIODE to adjust its tracking window. Such an adjustment helps the altimeter successfully track inland water bodies, especially within rough topography. After the successful experience with Jason-2, OLTC was also implemented in SARAL/AltiKa, Jason-3, and Sentinel-3. On the other hand, inland water monitoring using satellite altimetry has benefited greatly from the Delay Doppler technique or the concept of Synthetic Aperture Radar (SAR), first used in CryoSat-2. The Delay Doppler technique, implemented in two ways—closed-burst and open-burst configurations (Dinardo et al., 2024)—utilizes a wide antenna aperture to accumulate more looks than a conventional altimeter and a relatively small along-track footprint (ca. 250 m) (Raney, 1998). Sentinel-3A was the first mission to operate both in SAR mode (closed-burst) and OLTC. This approach continued in Sentinel-3B, and with the modification of the SAR mode to open-burst, it was implemented in Sentinel-6MF (Dinardo et al., 2024).

Swath altimetry is another emerging technology advancing the use of satellite altimetry for monitoring the water cycle. With its swath altimetry capabilities, the Surface Water and Ocean Topography (SWOT) satellite represents a revolutionary advancement in the field of altimetric satellite missions (Rodriguez et al., 2017; Fu et al., 2024). In addition to its nadir altimeter, SWOT is designed to provide high-resolution measurements of surface water elevations using a Ka-band Radar Interferometer (KaRIn) (Biancamaria et al., 2016). This technology allows SWOT to capture two-dimensional water surface elevations with unprecedented accuracy and spatial resolution. In the future, this capability will be further advanced by the Sentinel-3NG mission (Cretaux et al., 2023).

2. **Satellite gravimetry**: With the help of satellite gravimetry, variations in Earth's gravity field caused by the redistribution of water masses can be monitored. Before 2000, Satellite Laser Ranging (SLR) was the only system available for measuring the time-variable gravity field at global scales. SLR data initially provided observations of the seasonal variations of the low-degree gravity field (up to degree and order 4) (Nerem et al., 2000). However, the spatial resolution of SLR is not appropriate for capturing water storage changes at the catchment scale.

   High-low satellite-to-satellite tracking (hlSST) provides the 3-dimensional coordinates of the position of low Earth orbiting (LEO) satellites using onboard GNSS receivers (Sneeuw et al., 2005). The hlSST technique was employed in the Challenging Minisatellite Payload (CHAMP) mission. Despite the overall success of the CHAMP mission, the quality of the GPS observations and processing standards were insufficient to derive proper time-variable gravity field estimation, and hence, use it for hydrological studies (Reigber et al., 2006). Only on a very large scale of about 2000 km, through a specific processing scheme, meaningful annual signals and long-term trends could be obtained using CHAMP measurements (Weigelt et al., 2013).

   The launch of the Gravity Recovery And Climate Experiment (GRACE) in 2002 (Tapley et al., 2004a) allowed for the recovery of the time-variable gravity field at catchment scales using low-low satellite-to-satellite tracking (llSST). GRACE was the first satellite mission that allowed us to determine continental water storage on short time scales, which was the ambition of hydrologists for a long time (Lettenmaier and Famiglietti, 2006). GRACE has provided a direct measure of the monthly gravity field variations by observing the relative motion of the center-of-mass of the two satellites, measured with a highly precise inter-satellite K-band microwave link (Tapley et al., 2004a). The monthly gravity variations are used to track mass changes in the hydrosphere, cryosphere, and oceans, quantifying Total Water Storage Anomaly (TWSA). GRACE observations paved the way to monitor continental water storage, including deep soil water, for the first time. It contributed to various applications, including determining the natural and anthropogenic footprints in global and regional water changes, ice-sheet mass balance (Chen et al., 2009), ocean circulation, sea-level rise (Chen

et al., 2013; Jacob et al., 2012), atmospheric circulation patterns, drought monitoring (Long et al., 2013; Solander et al., 2017; Saemian et al., 2024), and flood forecasting (Reager et al., 2014).
GRACE Follow-On (GRACE-FO), launched in May 2018, continues GRACE's legacy of monitoring Earth's temporal gravity field using the same constellation as GRACE while additionally being equipped with an experimental Laser Ranging Interferometer (LRI). These missions have enabled the monitoring of shifts in both the global hydrological cycle and oceanic systems (Kusche et al., 2009). Recent achievements highlight the importance of GRACE in better understanding of water storage variability (see, e.g., Sun et al., 2012; Voss et al., 2013; Joodaki et al., 2014; Lorenz et al., 2015; Saemian et al., 2022; Frappart and Ramillien, 2018; Saemian et al., 2020) and even the understanding of the absolute amount of drainable water storage, for which GRACE and GRACE-FO are theoretically blind (cf. Tourian et al., 2018, 2023a).
The success of GRACE and GRACE-FO has created a new demand for scientists and decision-makers for sustained observation of the water storage variations (Pail et al., 2015). In addition, after many successful years of monitoring and investigation, developing near-real-time services and early warning systems is now conceivable and has actually begun (Jäggi et al., 2019). The scope of such services, however, is limited to the coarse spatial resolution of the GRACE and GRACE-FO missions.

3. **Satellite imaging**: Thanks to its ability to cover large and remote areas with high temporal frequency, satellite imaging plays an important role in hydrogeodesy by providing detailed spatiotemporal information about surface water extent (Alsdorf and Lettenmaier, 2003; Papa et al., 2006a; Elmi, 2015). Monitoring surface water extent is crucial for understanding hydrological processes, managing water resources, and assessing environmental changes (Papa et al., 2010b). More specifically, in hydrogeodetic studies, surface water extent is necessary to obtain a holistic view of water volume variation when water level data from altimetry is used and when the derived volume is interpreted together with satellite gravimetry-derived water storage variation.
   Optical satellite sensors, such as those on Landsat and Sentinel-2 satellites, have been widely used for mapping surface water extent, i.e., deriving river width and lake surface area. These sensors capture images in multiple spectral bands, enabling the differentiation of water from other land cover types based on their spectral reflectance properties (McFeeters, 2013). Synthetic Aperture Radar (SAR) sensors, such as those on Sentinel-1 satellites, offer the advantage of all-weather, day-and-night imaging capabilities (Soergel, 2010). SAR is particularly useful for monitoring surface water extent in regions with frequent cloud cover (Martinis et al., 2015).
   While it may seem straightforward to extract surface water extent from satellite imaging, this process is demonstrated to be complex and demanding (Elmi, 2015) and remains an ongoing area of research within hydrogeodesy. A classic approach to extracting water masks from optical images involves pixel-based segmentation algorithms, which define a threshold in the pixel value histogram. While straightforward, these algorithms often fail in complex scenes due to the sensitivity of pixel values to factors like water quality, surface roughness, chemical properties, sediment load, vegetation canopy, and water column depth (Elmi, 2019). This is a challenge, especially along shorelines, where the mix of water, vegetation, and soil complicates threshold determination. On the other hand, region-based segmentation techniques, which use spatial information and treat each pixel as part of a larger region, improve accuracy by relying on the strong spatial correlation in satellite images. Incorporating temporal correlations, influenced by seasonal cycles, further enhances water mask extraction (Elmi and Tourian, 2023).
   The combination of optical and SAR data has also been explored to improve the accuracy and reliability of surface water monitoring (Twele et al., 2016). Recent advancements in hydrogeodesy have seen the integration of satellite image-based surface water estimates with altimetry-based height measurements to derive surface water storage (Yao et al., 2023). Beyond surface water storage, integrating these data with satellite gravimetry measurements allows for a more comprehensive assessment of the water cycle on regional (Tourian et al., 2015) and global scales (van Dijk et al., 2014).

4. **Interferometric Synthetic Aperture Radar (InSAR)**: The InSAR technique exploits the phase difference between radar signals acquired from slightly different viewing geometries to detect ground surface displacement with millimeter precision. This can be realized differently depending on the targeted quantity. Single-Pass InSAR uses two radar antennas on the same platform to capture simultaneous images, which can be realized either across-track to create 3D images for topographic mapping (Zebker and Goldstein, 1986; Madsen and Zebker, 1998), or along-track to detect moving targets and measure ice flow (Goldstein et al., 1993). Repeat-Pass InSAR captures images at different times with the same antenna for monitoring ground deformation and tectonic movements (Massonnet et al., 1993). Differential InSAR (D-InSAR) uses multiple images over time to measure ground displacement, which is useful for monitoring earthquakes and volcanic activity (Massonnet and Feigl, 1998). Recently, it has also been demonstrated to be useful for monitoring water variations in small lakes by using double bounce from nearby vegetation (Aminjafari et al., 2024). Persistent Scatterer InSAR (PS-InSAR) analyzes multiple images to identify stable targets, effective for urban deformation monitoring (Ferretti et al., 2001). Short Baseline Subset (SBAS) InSAR employs a series of images with short temporal and spatial baselines for detailed deformation analysis (Berardino et al., 2002). Wide Swath InSAR utilizes techniques like ScanSAR or TOPS to achieve wide-area coverage, suitable for large-scale mapping and monitoring (De Zan and Monti Guarnieri, 2006).
   With its capability to provide high-resolution, spatially extensive data on ground deformation and subsurface water dynamics, the InSAR technique has emerged as a transformative tool in hydrogeodesy (Jaramillo et al., 2024). It has been effectively applied in various applications, such as monitoring subsidence in urban areas due to groundwater extraction and agricultural activities (Erban et al., 2014; Haghshenas Haghighi and Motagh, 2024), tracking glacier dynamics (Auriac et al., 2014), monitoring soil moisture (Eshqi Molan and Lu, 2020), groundwater changes (Castellazzi et al., 2016), water mass changes in lakes or reservoirs (Darvishi et al., 2021), and ice flow (Palmer et al., 2010). Actually, the InSAR technique implemented in the SWOT mission allows direct measurement of open surface water elevation and surface water extent. In the Ka-band, water (with a certain degree of surface roughness) acts almost as a specular reflector. The KaRIn sensor's near-vertical incidence angles (unlike the more slanted angles used by some other InSAR sensors) enable the backscatter from water to be directed more toward the satellite's nadir. This makes the water appear brighter and easier to distinguish from land (Biancamaria et al., 2016; Rodriguez et al., 2017). This design enables measurement of surface water elevation without the double bounce assistance from nearby vegetation.
5. **Global Navigation Satellite System (GNSS)**: GNSS, including Global Positioning System (GPS), Global Navigation Satellite System (GLONASS), Galileo, BeiDou Navigation Satellite System (Beidou), Quasi-Zenith Satellite System (QZSS), and Indian Regional Navigation Satellite System (IRNSS) (see Table 1.1), enables precise positioning. GNSS plays a crucial role in hydrogeodesy by providing precise measurements of ground displacement, which are essential for understanding water storage and movement in the Earth's crust (van Dam et al., 2001). GNSS networks, such as those maintained by the International GNSS Service (IGS), offer continuous, high-precision positioning data that can detect even minute ground movements caused by changes in groundwater levels, soil moisture, and surface water (Argus et al., 2014; Borsa et al., 2014; van Dam et al., 2001). Through GNSS measurements, water levels in rivers and lakes can be sensed, land subsidence can be monitored, and the movement of glaciers and ice sheets can be tracked (Xue et al., 2021).
   While GNSS network deformation provides insights into effects arising from hydrological, cryospheric, and atmospheric changes, GNSS-based atmospheric sounding has also become a reliable means to monitor water vapor content in the troposphere. Moreover, GNSS-derived vertical displacements have been used to validate and improve hydrological models and GRACE-derived water storage variation (Ferreira et al., 2021). On top of that, within hydrogeodesy, GNSS is instrumental when combined with other geodetic and remote sensing techniques. For example, GNSS data can be

integrated with data from GRACE, allowing for the separation of different components of the water cycle, such as distinguishing between groundwater and surface water contributions to total water storage changes (Carlson et al., 2022).

6. **GNSS-Reflectometry (GNSS-R)**: Radio signals are constantly broadcast to the Earth from GNSS satellites. These signals are partially reflected from the Earth's surface. While surface multipath is one of the main error sources for navigation and positioning, the multipath delay from the Earth's surface can be used to sense the Earth's surface environment (Jin and Komjathy, 2010). Specifically, the delay can be used to produce surface roughness parameters and determine surface characteristics (Ruffini et al., 2004). For instance, the measurements of reflected signals from the ocean surface contain information on the ocean surface height, wind speed, wind direction, and even sea ice conditions (Rodriguez-Alvarez et al., 2023). Given that GNSS signals are continually transmitted and reflected off river basins and water surfaces, including lakes and rivers, placing a receiver on platforms such as ground stations, aircraft, or LEO satellites allows for the measurement of surface water levels, soil moisture, and snow depth. This method offers a cost-effective solution for hydrological monitoring (Larson et al., 2008; Rius et al., 2017; Wang et al., 2021).
   One of the main advantages of the GNSS-R technique is its unprecedented spatiotemporal resolution, which achieves optimal performance when deployed on a spaceborne platform (see Figure 1.3). This high-resolution capability enables detailed observation and monitoring of various hydrological parameters that are not captured by other sensors, positioning it as potentially the most favorable mission for future hydrological studies. The utilization of spaceborne platforms for GNSS-R has advanced significantly over the past decade. One notable mission is TechDemoSat-1, launched by the UK Space Agency (UKSA) in 2014, which served as a technology demonstration satellite showcasing the potential of GNSS-R (Foti et al., 2015). NASA's Cyclone Global Navigation Satellite System (CYGNSS), operational since 2016, employs GNSS-R to study tropical cyclones and improve hurricane forecasting (Ruf and et al., 2016). Additionally, ESA's PRETTY mission, launched in October 2023, aimed to study various Earth surface properties through passive reflectometry and dosimetry (Dielacher et al., 2019). Looking ahead, the European Space Agency (ESA) plans to launch the HydroGNSS mission in 2025, specifically designed for hydrological applications using GNSS reflectometry (Unwin et al., 2021).
   Recently, GNSS-Interferometric Reflectometry (GNSS-IR), a variant of GNSS-R that utilizes interference patterns created by direct and reflected GNSS signals, has been gaining attention. By analyzing these interference patterns, valuable information about the Earth's surface properties can be extracted. One of the primary applications of GNSS-IR is measuring surface water levels, including those of lakes, rivers, and reservoirs. By placing GNSS receivers near water bodies, the interferometric signals can be used to monitor changes in water levels with high precision (Larson, 2016). Moreover, GNSS-IR allows for the measurement of soil moisture content by capturing the phase variation of reflected GNSS signals from the ground surface, which varies depending on the moisture content in the soil (Larson, 2016; Zhang et al., 2021). Additionally, GNSS-IR is used to measure snow depth (Nievinski and Larson, 2014), snowmelt runoff (Altuntas et al., 2022), and shallow sediment compaction (Karegar et al., 2020). This technique offers significant potential in hydrogeodesy by enabling continuous monitoring, allowing for real-time data collection, and even serving as a validation tool for satellite altimetry (Karegar et al., 2022).

The above-mentioned spaceborne geodetic techniques contribute significantly to monitoring the water cycle in various ways. Table 1.2 provides a detailed list of the most geodetically important components of the water cycle, along with the corresponding geodetic techniques for either directly measuring or indirectly estimating each component.

Tab. 1.2: The potential of spaceborne geodetic techniques in monitoring water cycle components

geodetic quantities of water cycle		observed?	by	estimated?	through
river discharge	Q	no		yes	SWOT (e.g., Durand et al., 2014, 2023; Andreadis et al., 2025) satellite altimetry (e.g., Tourian et al., 2013; Paris et al., 2016; Saemian et al., 2025) satellite imaging (e.g., Smith and Pavelsky, 2008; Pavelsky, 2014; Tarpanelli et al., 2013b; Elmi et al., 2021; Scherer et al., 2024)
river surface water height	h	yes	satellite altimetry (Papa et al., 2010a; Tourian et al., 2016) SWOT (e.g., Biancamaria et al., 2016; Fu et al., 2024)		
river surface slope	$\partial h/\partial x$	yes	radar altimetry (e.g., Schwatke et al., 2024) laser altimetry (e.g., Scherer et al., 2023) SWOT (e.g., Biancamaria et al., 2016) GNSS-IR (e.g., Karegar et al., 2022)		
river flow velocity	v	no		yes	satellite imaging (e.g., Everard et al., 2023)
river depth	D	partially	Laser altimetry (e.g., Wang, 2024)	yes	SWOT (e.g., Durand et al., 2009; Yoon et al., 2012) satellite altimetry+imaging (e.g., Tourian et al., 2017a)
river width	W	yes	satellite imaging (e.g., Elmi et al., 2015; Allen and Pavelsky, 2018; Feng et al., 2022) SWOT (e.g., Biancamaria et al., 2016)		
groundwater discharge	Q_{G}	no		no	
absolute total water storage	S	no		no	
Total Drainable Water Storage	S_{D}	no		yes	satellite gravimetry (e.g., Tourian et al., 2018, 2023a)
total water storage anomaly	ΔS	yes	satellite gravimetry (e.g., Wahr et al., 1998)		
snow water storage	S_{S}	no		yes	GNSS (e.g., Capelli et al., 2022; Steiner, 2019)
glacial water storage anomaly	S_{S}	no		yes	GNSS-R (e.g., Steiner et al., 2023)
absolute surface water storage	S_{W}	no		yes	SWOT (+DEM) (e.g., Lee et al., 2010)
surface water storage anomaly	ΔS_{W}	no		yes	SWOT (e.g., Lee et al., 2010) Satellite altimetry+imaging (+DEM) (e.g., Vanthof and Kelly, 2019)
surface water area	A	yes	satellite imaging (e.g., Pekel et al., 2016; Pham-Duc et al., 2017; Elmi and Ahrari, 2025) SWOT (e.g., Fu et al., 2024)		
surface water depth (lakes)	D_{S}	partially	laser altimetry (e.g., Ranndal et al., 2021)		
surface water level change	$\partial h/\partial t$	yes	satellite altimetry (e.g., Birkett, 1995; Crétaux and Birkett, 2006)		
soil moisture depth (top soil)	S_{M}^{t}	no		yes	GNSS-R (e.g., Rodriguez-Alvarez et al., 2009)
soil moisture anomaly (top soil)	$\Delta S_{\mathrm{M}}^{\mathrm{t}}$	no		yes	GNSS-R (e.g., Wu et al., 2021) GNSS-IR (e.g., Larson, 2016) SAR imaging (e.g., Dubois et al., 1995) InSAR (e.g., Karamvasis and Karathanassi, 2023) satellite altimetry (e.g., Uebbing et al., 2017)
soil moisture depth (root zone)	S_{M}^{r}	no		no	
soil moisture anomaly (root zone)	$\Delta S_{\mathrm{M}}^{\mathrm{r}}$	no		no	
absolute groundwater storage	S_{G}	no		no	
groundwater storage anomaly	ΔS_{G}	no		yes	satellite gravimetry+imaging+altimetry (+models) (e.g., Voss et al., 2013)
Hydrological loading effects					
vertical displacement	d_{u}	yes	GNSS (e.g., Fu et al., 2022)	yes	satellite gravimetry (e.g., Argus et al., 2017)
horizontal displacement	d_{n}, d_{e}	yes	GNSS (e.g., Fu et al., 2022)	yes	InSAR (e.g., Hong and Liu, 2021)

Although many components are observed, some remain unobserved due to the limitations of electromagnetic signals (Alsdorf et al., 2007; Jaramillo et al., 2024; Trenberth and Asrar, 2014). One main limitation is that these signals cannot penetrate water bodies to the required depths, hindering the measurement of many components, such as river discharge (Gleason et al., 2017; Gleason and Durand, 2020). River discharge, however, can be estimated by combining river surface height (h), slope ($\partial h/\partial x$), width (W), and cross-sectional area (Durand et al., 2014); by forming a rating curve using any of these variables (Pavelsky, 2014; Tourian et al., 2013); or by exploiting the spectral contrast between water and land in satellite

imagery to derive a reflectance ratio that correlates with discharge (Tarpanelli et al., 2013b). The river surface water height is directly measured by satellite altimetry, both nadir and the SWOT mission (Birkett, 1995; Papa et al., 2010a; Biancamaria et al., 2016). The river surface slope ($\partial h/\partial x$) can be obtained using SWOT and also nadir altimetry, both radar altimetry (Schwatke et al., 2024) and laser altimetry (Scherer et al., 2023). And the river width W can be determined through satellite images (Elmi et al., 2015). With these surface variables, river discharge can be estimated, albeit with some degree of uncertainty (Durand et al., 2014, 2023; Andreadis et al., 2025). The precision of such estimates would be significantly improved if river depth could also be observed. Efforts to achieve this have been made using the SWOT mission, as well as a combination of satellite altimetry and imaging (Yoon et al., 2012; Tourian et al., 2017a).

Another challenge in monitoring hydrological fluxes is that some processes occur in deeper soil layers, making direct measurements nearly impossible. For instance, sub-surface fluxes like groundwater discharge cannot be detected by current spaceborne sensors. However, groundwater models, when calibrated with available surface observations and integrated with remote sensing data, can provide valuable insights into sub-surface hydrological processes (Li et al., 2019).

Spaceborne geodetic sensors are generally more effective at quantifying storage components. As mentioned before, total water storage variations can be obtained using satellite gravimetry (Wahr et al., 1998). Its components, including snow water storage, glacial water storage, surface water storage, soil moisture, and groundwater storage, can also be partially obtained by spaceborne geodetic sensors. It has been demonstrated that snow water storage, S_{S}, can be estimated using GNSS (Capelli et al., 2022; Steiner, 2019). Similarly, glacial water storage anomaly, S_{S}, can be estimated using GNSS-R (Steiner et al., 2023). Surface water storage anomaly, ΔS_{W}, can be obtained by combining height (from altimetry or SWOT) and area with Digital Elevation Model (DEM) (Lee et al., 2010; Vanthof and Kelly, 2019). Surface water area, A, is directly obtained through satellite images (Pekel et al., 2016) and SWOT (Fu et al., 2024). Surface water depth, D_{S}, is partially observed using laser altimetry (Ranndal et al., 2021) and can be indirectly obtained using SWOT (Yoon et al., 2012) and satellite altimetry in combination with satellite images.

Soil moisture anomaly in the topsoil, $\Delta S^{\mathrm{t}}_{\mathrm{M}}$, is not observed, but it can indirectly be estimated using GNSS-R (Wu et al., 2021), GNSS-IR (Larson, 2016), satellite altimetry (Uebbing et al., 2017), SAR imaging (Dubois et al., 1995), and InSAR (Karamvasis and Karathanassi, 2023). It has also been demonstrated that soil moisture depth in the topsoil, S^{t}_{M}, can be estimated using GNSS-R (Rodriguez-Alvarez et al., 2009). However, soil moisture depth in the root zone, S^{r}_{M}, and its anomaly, $\Delta S^{\mathrm{r}}_{\mathrm{M}}$, are neither observed nor estimated. The groundwater storage anomaly, ΔS_{G}, however, can be obtained indirectly using satellite gravimetry in combination with satellite imaging, altimetry, and modeled soil mositure (Voss et al., 2013). However, the absolute groundwater storage, S_{G}, and the absolute total water storage S are not directly observed nor can they be indirectly obtained from any method. The only way to obtain a proxy measure of absolute total water storage is to estimate the Total Drainable Water Storage (TDWS), which requires analyzing the relationship between water storage anomalies from satellite gravimetry and river discharge (Tourian et al., 2018, 2023a).

Moreover, from a geodetic perspective, understanding the impact of hydrological processes on the Earth's physical structure is crucial for effectively monitoring the water cycle. One significant aspect of this impact is the deformation of the Earth's crust due to hydrological mass redistribution. This deformation primarily results from temporal changes in hydrological loads, either imposed by flux changes or storage changes. The consequences of hydrological loading include both vertical and horizontal displacements, which can be monitored using geodetic techniques. Vertical displacement, d_{u}, can be observed using GNSS (Fu et al., 2022) and estimated using satellite gravimetry (Argus et al., 2017). Horizontal displacement, d_{n} and d_{e}, can also be observed using GNSS (Fu et al., 2022) and estimated using InSAR (Hu et al., 2016). These observations provide critical data for understanding and monitoring water-related changes on Earth, thereby enhancing our comprehension of the water cycle.

1.2 Challenges and possible solutions

Despite the progress of spaceborne geodetic sensors and the fact that, for many water cycle components, these sensors provide either a direct measure or an indirect estimate as listed in Table 1.2, hydrogeodesy faces several challenges. Notable challenges include 1) limitations in spatiotemporal resolution, 2) uncertainties in measurements, 3) unobservables, 4) inconsistencies in background models, and 5) the separability of aggregated measurements. Additionally, a challenge of a different nature is 6) integrating diverse data sources. While combining multiple datasets can help address some of these challenges (Kusche, 2003), it introduces its own complexities, requiring the reconciliation of data with differing resolutions, accuracies, and temporal scales. In the following sections, each challenge is discussed, and some avenues for possible solutions to each challenge are described.

1.2.1 Limitation in spatiotemporal resolution

In a logarithmic representation, with the vertical axis indicating spatial resolution in degrees and the horizontal axis indicating temporal resolution in days, Figure 1.2 illustrates the spatiotemporal resolution of various techniques and missions. For satellite altimetry missions, due to the nadir measurement concept, the specified spatial resolution corresponds to the ground track spacing, while the temporal resolution reflects the mission's repeat period. For other missions or mission concepts, including satellite gravimetry, imaging, InSAR, GNSS, GNSS-R, and GNSS-IR, the spatial resolution refers to how finely a signal can be extracted, and the temporal resolution typically depends on the sampling frequency, revisit time, or continuous data availability. The spatiotemporal resolutions of these techniques are represented in Figure 1.2 either as specific points or as approximate regions, depending on the variability across applications.

Satellite altimetry missions, which typically use a nadir-pointing measurement approach and operate with a single satellite in orbit, face limitations in spatiotemporal resolution due to their orbital configurations determining the ground track pattern and revisit frequency. As shown in the logarithmic representation in Figure 1.2, these limitations are evident in the alignment of all missions along a line, indicating an inverse relationship between spatial and temporal resolution. This means that the product of spatial and temporal resolution tends to remain constant, such that improving one (e.g., spatial resolution) generally results in a deterioration of the other (e.g., temporal resolution). The SWOT KaRIn sensor results, either realized in Low Resolution (LR) or High Resolution (HR), benefit from its interferometric measurement concept that enables observations away from the nadir track, delivering spatial resolutions from sub-kilometer down to approximately 30 m, and a temporal resolution of at least 21 days, reaching up to 7 days in some regions (Fu et al., 2024). Among nadir altimetry missions, CryoSat-2 offers the best spatial resolution, with a ground track spacing of approximately 7 km, but has the poorest temporal resolution, approximately one year (Escudier et al., 2017). Such a spatiotemporal resolution highlights that any hydrological cycle phenomenon, such as a flood in smaller rivers, occurring in a spatiotemporal resolution that spans a region below that line will remain unmonitored by altimetry missions.

The spatiotemporal resolution of satellite gravimetry missions, which utilize a different measurement concept than altimetry missions, follows a different yet comparable pattern, where the spatial resolution of GRACE and GRACE-FO is directly dependent on the provided temporal resolution. The best spatial resolution is achieved with a monthly solution, within which the entire Earth is fully covered (Kusche, 2007). On the other hand, the best achieved temporal resolution is 1 day, which comes with a coarse spatial resolution (Kurtenbach et al., 2009). Similarly, for the CHAMP mission, a comparable pattern could be expected. However, given the limitations of CHAMP in terms of the accuracy of GNSS receivers, the typical time-variable solution was a monthly solution with a spatial resolution of about 500–600 km (Weigelt et al.,

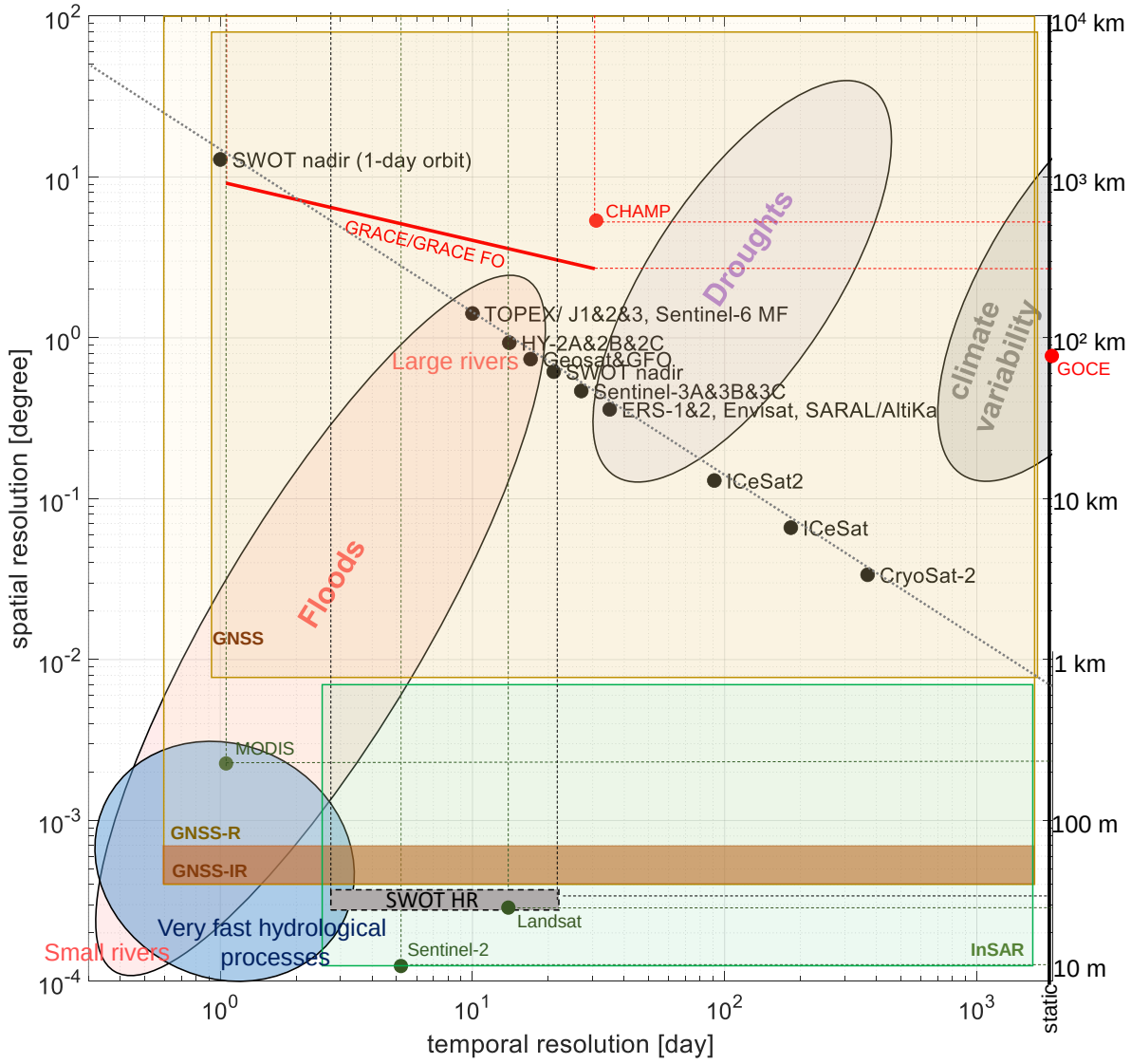

Fig. 1.2: Spatio-temporal coverage of key satellite missions within hydrogeodesy. The figure categorizes mission concepts such as satellite altimetry (e.g., conventional and swath-based, including SWOT HR), satellite gravimetry (e.g., GOCE, CHAMP), Global Navigation Satellite Systems (GNSS), GNSS reflectometry (GNSS-R), GNSS interferometric reflectometry (GNSS-IR), synthetic aperture radar interferometry (InSAR), and optical remote sensing (e.g., MODIS, Landsat, Sentinel-2). These techniques are positioned according to their typical spatial resolution (ranging from $> 10^4\,\mathrm{km}$ to $\sim 10\,\mathrm{m}$) and revisit time (from decadal to sub-daily), illustrating their suitability for capturing hydrological processes across a wide range of spatial and temporal scales—from slow, continental-scale changes to rapid dynamics in small rivers.

2013). The GOCE mission, however, given its orbital configuration, was not suitable for time-variable gravity field estimation and is mostly used for static gravity field determination (Hirt et al., 2011).

Compared to nadir altimetry and satellite gravimetry, satellite imaging is in a better position regarding spatiotemporal resolution. Optical and SAR sensors in the MODIS, Landsat, and Sentinel series provide high-resolution images with pixel sizes ranging from a few meters to tens of meters, capturing detailed spatial information. However, their temporal resolution is often limited by revisit times, typically ranging from days to weeks. For instance, optical satellites like Landsat and Sentinel-2 offer spatial resolutions of 10–30 m but have revisit intervals of 5–16 days, which can limit the frequency of observations needed for continuous monitoring of dynamic processes (Klein et al., 2017; Yao et al., 2019, 2023). SAR satellites, such as Sentinel-1, provide similar spatial resolutions and have the advantage of all-weather, day-and-night imaging capabilities, but also face similar temporal limitations (Wulder et al., 2012). Moreover, the surface

water area of lakes, reservoirs, and river reaches can be extracted from available global inland water datasets such as the Global Inundation Extent from Multiple Satellites (GIEMS) (Papa et al., 2010b), or the Global Surface Water Dataset (GSW) (Pekel et al., 2016). However, the derived surface water estimates are constrained by the temporal and spatial limitations of the initial dataset.

In the case of InSAR, the spatial resolution is determined by the radar's wavelength, the antenna's size, and the distance between successive passes of the satellite. Typically, the spatial resolution of InSAR ranges from about 1–30 m. Temporal resolution, on the other hand, is influenced by the revisit frequency of the satellite. For instance, Sentinel-1 typically has a revisit time of 6 to 12 days. TerraSAR-X can have revisit times as short as 11 days, though specific modes can allow for more frequent monitoring (Karimzadeh and Mastuoka, 2017; Milillo et al., 2017).

GNSS measurements, due to their point-wise measurement concept and relatively well-distributed global network (see IGS stations in Figure 1.3), can offer a moderate spatiotemporal resolution for applications such as monitoring ground displacement due to hydrological loading. However, unlike GNSS-relevant applications that require a dense network, GNSS-R is not network-dependent and provides an unprecedented spatiotemporal resolution. Figure 1.3 illustrates the specular points of GNSS reflections over three days in the Amazon basin, with an elevation angle above 45°. This scenario assumes a GNSS-R receiver on board CryoSat-2, orbiting at an altitude of 700 km with an inclination of 92°, and utilizing a GNSS constellation comprising 24 GLONASS, 24 GPS, and 30 Galileo satellites. Comparing the ground track sampling of CryoSat-2 over three days (black lines) with the GNSS-R sampling highlights the significant benefits of GNSS-R for hydrological applications. However, the accuracy of the measurements still depends on the footprint of the reflected signal, which can be influenced by factors like satellite altitude, elevation angle, and receiver configuration.

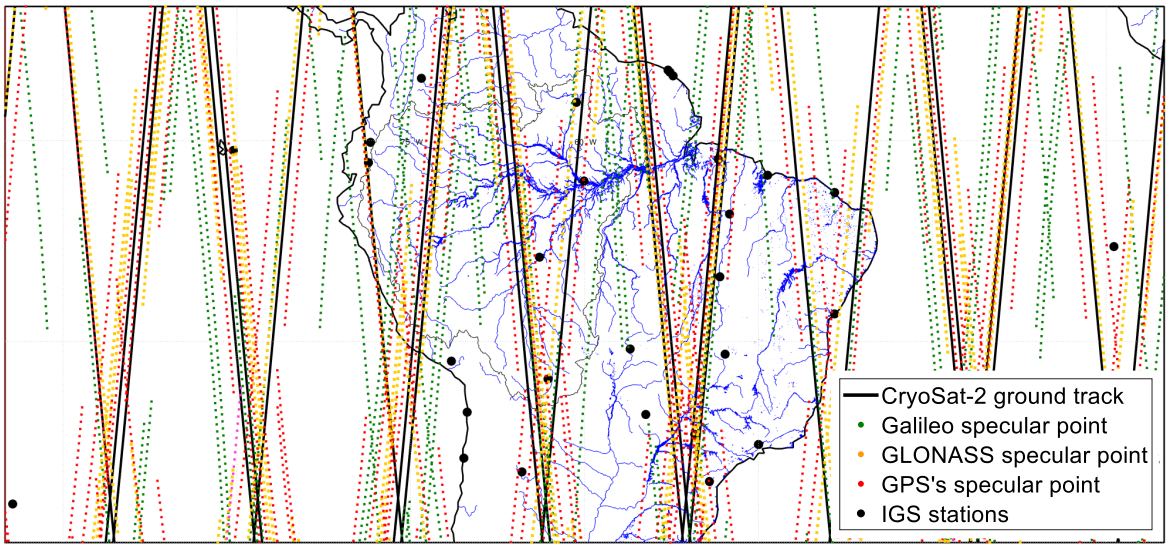

Fig. 1.3: GNSS-R specular points over three days in the Amazon basin, assuming a GNSS-R receiver on board CryoSat-2 at an altitude of 700 km with an inclination of 92°, and a GNSS constellation consisting of 24 GLONASS, 24 GPS, and 30 Galileo satellites. The specular points are filtered to exclude those with elevation angles higher than 45°. Black circles represent IGS stations.

On the other hand, GNSS-IR, which often depends on ground-based receivers, is limited in spatial resolution, providing measurements primarily around the station. However, the temporal resolution of GNSS-IR can be very high, offering measurements with sub-hourly frequency.

It is important to note that what is hidden in Figure 1.2 is the increasing level of uncertainty associated with satellite measurements when they are provided at their highest possible spatiotemporal resolution. However, what is clear in Figure 1.2 is that spaceborne geodetic sensors are limited in their ability to monitor fast

hydrological processes. This limitation hinders the ability to respond properly to natural disasters such as floods, flash droughts, and sudden shifts in water storage. This highlights the need for improvement to effectively track and manage these fast-evolving processes. As emphasized by Cerbelaud et al. (2025), addressing these challenges requires an awareness of the intrinsic trade-offs among spatial and temporal resolution, uncertainty, and interpretability in spaceborne data.

A general solution to the challenge of spatiotemporal resolution involves combining various measurements. This involves the integration of multiple data sources to obtain a more comprehensive representation of hydrological processes. The idea is to combine various data from the same type or different types, such as satellite observations (e.g., GRACE, altimetry), ground-based measurements (e.g., groundwater levels, soil moisture), and model outputs. In such a setup, the goal is to benefit from the strengths of each data source while mitigating their limitations. A classic example of pure data fusion is using multi-mission altimetry to monitor the water level time series of lakes and reservoirs. This approach can deal with the coarse temporal resolution of a single satellite on a water body (Crétaux et al., 2013). Another example is the so-called *densification* procedure that fuses measurements from multiple altimetry along a river occurring at different times to obtain a temporally dense time series at any given location (Tourian et al., 2016; Boergens et al., 2019; Nielsen et al., 2022).

An alternative solution is to assimilate spaceborne geodetic measurements with hydrological data and models, either with or without model coupling. In coupled models, geodetic data can serve as an input to the hydrological model, allowing feedback loops between model parameters within the physical processes. In uncoupled models, there is no dynamic interaction between the geodetic data and the model parameters; instead, the data serves as a constraint for the modeling process. Whether coupled or uncoupled, assimilation is perhaps the most targeted objective within hydrogeodesy. When coupled with models, data assimilation can significantly enhance the simulation of complex hydrological or hydraulic processes by adjusting model parameters and states to align with observed data. In dealing with the coarse spatial resolution of GRACE, many data fusing approaches have been attempted to combine coarse-scale GRACE data with fine-scale hydrological data by either relying on statistical methods (Vishwakarma et al., 2021), or nonlinear machine learning (ML) techniques such as artificial neural networks (ANN) (Miro and Famiglietti, 2018), boosted regression trees (BRT) (Seyoum et al., 2019), random forests (RF) (Jyolsna et al., 2021), and long short-term memory (LSTM) recurrent neural networks (Gorugantula and Kambhammettu, 2022). In such a context, the Bayesian framework also plays a vital role, providing a robust mathematical foundation for integrating prior knowledge, observational data, and model simulations. Bayesian data assimilation techniques, such as the Ensemble Kalman Filter (EnKF) enable the estimation of state variables and model parameters while quantifying uncertainties (Li et al., 2019; Eicker et al., 2014; Neal et al., 2009). These techniques can also update model states and parameters in real-time, improving the accuracy of hydrological predictions (Zaitchik et al., 2008). The Bayesian framework is also practiced and proven to be beneficial in data assimilation without model coupling (Lorenz et al., 2015; Zhong et al., 2021). In this approach, the aim is to integrate observed data, both spaceborne and ground-based, directly into a computational framework or model without explicitly linking model parameters. This method can be more straightforward and less computationally demanding, making it an efficient tool for improving model performance and achieving a better understanding of water cycle parameters.

1.2.2 Uncertainties in measurements

The inherent uncertainties in spaceborne geodetic measurements present significant challenges for accurately assessing hydrological cycles. The uncertainties originate from various sources, including:

- **Orbital errors:** Inaccuracies in orbital data result in errors in the collected data. Nowadays, for almost all spaceborne geodetic techniques, Precise Orbit Determination (POD) techniques are utilized,

which involve the use of GNSS data, laser ranging, and Doppler Orbitography and Radiopositioning Integrated by Satellite (DORIS) to refine the satellite's position and velocity data (Scharroo and Visser, 1998). Thanks to POD, the orbital errors in the current satellite data are typically at the centimeter level (Rudenko et al., 2023). However, even small errors can propagate through the data processing chain, leading to non-negligible uncertainties in measurements. This is particularly critical in applications like sea-level change monitoring, requiring long-term data continuity and high precision, where cumulative errors can significantly impact the reliability of the results. Therefore, continuous advancements in POD techniques and the integration of complementary data sources are essential to further minimize these errors (Montenbruck et al., 2021).

- **Instrumental errors:** These include inaccuracies and noise in the spaceborne and ground-based sensors and instruments. Instrumental drift, thermal effects, and electronic noise can all contribute to measurement uncertainties. For instrumental errors, calibration and validation processes are essential to ensure the accuracy and reliability of the sensors, which often involves comparing satellite data with high-precision ground-based observations within Calibration/Validation (Cal/Val) activities (Bonnefond et al., 2021) or using onboard calibration systems.
- **Atmospheric disturbances:** Variations in the atmosphere, such as changes in temperature, pressure, humidity, and ionospheric conditions, will affect the signals transmitted and received by the satellite, leading to errors in measurements. To deal with atmospheric disturbances, modeling atmospheric delay correction, including tropospheric and ionospheric corrections, is employed (Fu and Cazenave, 2001). In inland altimetry, for instance, this remains a significant challenge, and further advancements are needed to improve the accuracy of these corrections (Fernandes et al., 2014). Continuous improvements in atmospheric modeling and the integration of data from high-resolution meteorological models are vital for reducing these errors and enhancing the reliability of inland altimetry measurements. Furthermore, the development of advanced algorithms and the use of auxiliary data, such as from GNSS receivers, can aid in refining these corrections and addressing the challenges posed by atmospheric disturbances in satellite-based measurements (Arabsahebi et al., 2018a; Alizadeh et al., 2011). In satellite gravimetry, to obtain TWSA, atmospheric tidal and nontidal mass variations must be accurately accounted for. This involves integrating data from global atmospheric models to correct for the gravitational effects of atmospheric mass changes, which can otherwise introduce significant errors into the measurements (Flechtner et al., 2006). For this purpose, high-resolution atmospheric reanalysis data, such as those from the European Centre for Medium-Range Weather Forecasts (ECMWF) or the National Centers for Environmental Prediction (NCEP), are typically employed. These datasets, while crucial for improving accuracy, often add their own uncertainties to TWSA (Zenner et al., 2010).
- **Platform motion-related errors:** Movements of the satellite platform, such as vibrations, tilting, and thermal expansion or contraction, can introduce errors in the data. These movements can affect the alignment and stability of the instruments. To mitigate these errors, precise attitude determination and control systems are employed to monitor and correct the satellite's orientation. These systems use a combination of gyroscopes, star trackers, and reaction wheels to maintain the satellite's stability and ensure that the instruments remain properly aligned. However, depending on the measurement concept, platform motion-related errors can still sometimes be a major source of error. For instance, while pulse-limited radar altimetry is less sensitive to platform motion-related errors due to its corresponding footprint size, laser altimetry is more sensitive to such errors (Abdalati et al., 2010). Also in the SWOT mission, due to the interferometric measurement concept, any baseline roll error is equivalent to a look angle error and, therefore, introduces an interferometric phase error (Peral et al., 2024), which currently poses a challenge for obtaining accurate water levels.
- **Mission constellations:** The mission constellation itself can introduce measurement uncertainty, particularly in satellite gravimetry missions (Sneeuw et al., 2005). In GRACE and GRACE-FO data, the along-track inline formation of the two satellites in a near-polar orbit leads to uncertainty that

predominantly manifests as north-south stripes, contributing to spatially correlated errors. To mitigate this, data are typically filtered to reduce errors, using a destriping filter to minimize correlated errors and either an isotropic filter, such as a Gaussian filter (Jekeli, 1981), or an anisotropic filter (Swenson and Wahr, 2006; Kusche, 2007; Devaraju, 2016) to reduce noise in higher-order coefficients. However, these filters cannot reliably distinguish between true signal and noise, leading to signal alteration—a phenomenon known as *leakage* (Baur et al., 2009). Leakage is most significant where there is high signal contrast in time-variable gravity signal, such as near large water bodies or along coastlines. For example, over lakes, filtering reduces the signal within the lake itself, causing it to extend into adjacent land areas. The leakage presents additional challenges in using GRACE and GRACE-FO data to estimate TWSA, prompting an investigation into several de-leakage algorithms (Long et al., 2015; Vishwakarma et al., 2017).

- **Processing algorithms errors:** The algorithms and models used to process level-1 and level-2 satellite data or ground-based data into usable information can introduce significant errors. Assumptions and approximations made in these algorithms, as well as numerical inaccuracies, can affect the final results. This may be the main source of uncertainty in many spaceborne geodetic techniques. For instance, in inland altimetry, the main source of uncertainty often lies in the processing algorithm to obtain a range estimate from a waveform, the so-called *retracking* procedure (Brown, 1977; Roscher et al., 2017). In the processing of GRACE and GRACE-FO data, as mentioned before, one of the main contributors to an error in the final TWSA estimate is often related to the selected filtering and processing techniques (Swenson et al., 2006; Kusche et al., 2009; Devaraju, 2016). For extracting surface water extent using satellite imaging, the main source of uncertainty often lies in the method for extracting surface water extent (Elmi et al., 2016; Elmi and Tourian, 2023). In line with ongoing efforts to improve processing algorithms, trending Artificial Intelligence (AI)-based techniques, as well as statistical and Bayesian approaches, are being investigated. Here, Bayesian approaches are particularly beneficial as they offer a systematic way to update and refine estimates as new data becomes available (Halimi et al., 2017). Additionally, they are beneficial as they can incorporate multiple sources of uncertainty, including observational errors and model inaccuracies, into a single coherent framework.

1.2.3 Unobservables

As indicated in Table 1.2, many water cycle components, such as river depth and discharge, absolute total water storage, TDWS, and groundwater storage, cannot be observed directly. Instead, these components can often be derived indirectly through surface measurements (Tourian et al., 2017a, 2018). For unobservable variables like groundwater storage, combining different datasets often provides a viable solution. For example, integrating data from GRACE with soil moisture products and altimetry- and images-based surface water storage estimates has proven effective (Voss et al., 2013). However, such an integration poses a challenge due to the differing spatial and temporal resolutions, measurement uncertainties, and processing methodologies of the datasets involved, which will be discussed in Section 1.2.6.

In most cases, obtaining unobservables necessitates solving an inverse problem, which poses a significant challenge due to the nonlinearity and ill-posed nature of the underlying equations, leading to non-unique and unstable solutions (Tarantola, 2005). It is evident that when these variables are derived indirectly, the uncertainties inherent in the measurements and the assumptions within the models propagate through the processing, impacting the final estimates. Consequently, even small errors in the observed data or inaccuracies in the model assumptions can result in significant variations in the derived results.

In deriving unobservable variables, Bayesian approaches are particularly effective, offering a robust framework to incorporate uncertainty and prior information into the estimation process. This probabilistic

framework is especially valuable in handling the non-linearity and ill-posed nature of inverse problems, as it can incorporate various sources of uncertainty and provide a range of plausible solutions rather than a single, potentially unstable estimate (Mariethoz et al., 2010). More specifically, Bayesian approaches are particularly effective for estimating river discharge using data from the SWOT mission. Within reach-scale inverse algorithms, the prior knowledge of river discharge characteristics is combined with observed data from SWOT, resulting in a posterior distribution that fairly represents discharge values and their uncertainties (Durand et al., 2014, 2016; Larnier et al., 2021; Durand et al., 2023).

1.2.4 Inconsistencies of background models

Inconsistencies in background models used in satellite data processing are a major challenge in hydrogeodesy. Background models, such as those for atmospheric delay and pressure, ocean tides, and non-tidal oceanic and atmospheric mass variations, are crucial for obtaining geodetic measurements. Discrepancies among these models can lead to significant variations in derived hydrological parameters (Seo et al., 2008). For instance, GRACE and GRACE-FO require background models to account for atmospheric and oceanic mass variations, both tidal and non-tidal. Inconsistencies in these models can introduce errors in the gravity field solutions, affecting the estimation of TWSA (Tapley et al., 2004b). The challenge lies in the fact that these background models are typically partial, describing individual components of the Earth system without being coupled with other components. Moreover, they are developed using different datasets, methodologies, and assumptions. For example, atmospheric mass changes are modeled using various meteorological data sources and numerical weather prediction models, which may have different spatial and temporal resolutions (Flechtner et al., 2006). Ocean tide models are developed using a combination of satellite altimetry, tide gauge data, and hydrodynamic modeling, each with its inherent limitations and uncertainties (Lyard et al., 2006).

It is necessary to continuously update and improve the models by developing standardized processing schemes and integrating the latest observational data. Specifically, inconsistencies in background models require efforts to harmonize them by coupling different compartments at relevant temporal and spatial scales (Dobslaw et al., 2017). Additionally, validation and intercomparison studies are essential, comparing the outputs of different models against independent observational data to identify and quantify discrepancies (Ray et al., 2011; Seo et al., 2008; Fernandes et al., 2014). Although many efforts have been made, this challenge is not fully resolved and probably will never be tackled. The complexity and variability inherent in the development of background models, combined with the ever-changing nature of the Earth's atmospheric and oceanic systems, indicate that some level of inconsistency will always persist.

1.2.5 Separability of aggregated measurements

The challenge of separating aggregated signals vertically and horizontally is a key obstacle to accurately quantifying different water cycle components. While horizontal separability is rather related to spatial resolution, discussed in Section 1.2.1, vertical separability is primarily attributed to distinguishing between different storage compartments, such as surface water, soil moisture, groundwater, snow, and glaciers. Specifically, GRACE and GRACE-FO, in their estimates of storage variations, are unable to resolve how much of the change comes from different layers of the hydrological system without additional modeling or complementary data (Schmidt et al., 2008). The challenge of vertical separability is further complicated by the fact that different water storage components often have varying temporal and spatial scales. For example, changes in surface water (e.g., lakes and rivers) may occur over shorter periods and more localized regions, whereas groundwater storage variations tend to happen over longer timescales and larger spatial

extents. Soil moisture and snow storage also exhibit distinct temporal dynamics and spatial heterogeneity, making it difficult to differentiate their contributions to the gravimetry-derived signals (Yin et al., 2020).

Combining their data with in-situ measurements, hydrological model outputs, or other spaceborne geodetic sensors (e.g., from altimetry and satellite images) can lead to the separation of some of these components (Voss et al., 2013). Additionally, data assimilation with hydrological models, that describe physical processes between different compartments, provides a solution for estimating the contributions of various compartments (Girotto et al., 2016; Mehrnegar et al., 2023).

The measurement principle of satellite altimetry also presents the challenge of separating aggregated measurements. While the ground track-driven spatial resolution, its consequent limitations, and potential solutions are discussed in Section 1.2.1, the large along-track footprint of altimetry remains a significant challenge. The pulse-limited footprint diameter of altimetry missions is typically between 2–3 km (Raney and Phalippou, 2011), propagating to even more than 10 km in its trailing edge. This leads to the integration of signals from land and water and sometimes even from various water bodies. This complicates the isolation of specific water bodies, especially in regions with complex topography or closely spaced hydrological features. Such issues are typically addressed using a retracking algorithm, as discussed in Section 1.2.2. Another possible solution is to use the Fully Focused Synthetic Aperture Radar (FF-SAR) method, which is an ongoing research area within hydrogeodesy. FF-SAR enhances the spatial resolution of altimetry measurements along the track for SAR altimetry missions, including CryoSat-2, Sentinel-3, and Sentinel-6MF. Unlike the conventional unfocused SAR (UF-SAR) method, FF-SAR can effectively manage different bursts by providing precise delay and phase compensation. This reduces the integration time from about 2 s to 3 ms, resulting in a significant enhancement in along-track resolution (Egido and Smith, 2017). The maximum theoretical resolution achievable is half the length of the antenna, improving the along-track resolution to about 0.5 m compared to 300 m for UF-SAR. The cross-track resolution remains unchanged, as it is controlled by radar bandwidth rather than processing (Egido and Smith, 2017)

1.2.6 Integration of diverse data sources

The integration of diverse data sources, which is a solution to many of the aforementioned challenges, is a challenge in itself. Given the fact that different satellites provide different components of the hydrological cycle, it is essential to combine various datasets for a better understanding of the hydrological cycle (van Dijk et al., 2014). As discussed before, spaceborne geodetic sensors vary in terms of observation type, spatiotemporal resolution, temporal coverage, and measurement techniques (Alsdorf and Lettenmaier, 2003). The challenge is even more prominent when it comes to integrating ground-based observations, such as those from GNSS stations and in-situ hydrological measurements (Tang et al., 2010). Combining these diverse data sources requires sophisticated data fusion techniques that can reconcile differences in resolution, coverage, and measurement methodologies (Zhang, 2010), some of which are discussed in Section 1.2.1. Additionally, the integration of diverse data sources must account for the inherent uncertainties in each dataset, which is a challenge in itself. This challenge is further exacerbated when the uncertainties for several observables (both satellite and in situ) are incompletely known or entirely unknown. To this end, robust and flexible methods with uncertainty quantification frameworks are necessary to assess and propagate these uncertainties through data fusion.

Bayesian data fusion techniques offer a powerful approach for integrating diverse data sources by updating prior knowledge with new observations, resulting in refined estimates incorporating data and model uncertainties. This is especially beneficial in hydrogeodesy, where measurements from various sensors and techniques often have differing levels of uncertainty (Weise and Woger, 1993). In this context, particular attention has been given to the use of EnKF for the assimilation of satellite gravimetry data with other datasets and models (Zaitchik et al., 2010; Eicker et al., 2014; Tangdamrongsub et al., 2020; Khaki

et al., 2020). Despite significant progress in this area, data assimilation approaches face notable challenges. Assimilation in observation space can suffer from numerical instability due to ill-conditioned error covariance matrices, a result of the limited spatial resolution of satellite-based data. In model space, applying coarse satellite gravimetry observations to finer model grids can lead to smoothed spatial details, misallocated mass changes, and suppressed dynamic ranges in complex terrains. Additionally, hydrological processes often exhibit non-Gaussian behaviors—such as skewed soil moisture distributions, log-normal snow water equivalent errors, and non-linear groundwater dynamics—which violate fundamental assumptions of Kalman filtering techniques and introduce biases. These biases can propagate into flux estimates, such as discharge and baseflow, potentially leading to erroneous hydrological assessments. Furthermore, the absence of key physical processes, including those influenced by anthropogenic activities, can exacerbate these biases, complicating the improvement of fluxes like river discharge that depend on temporal storage changes. Consequently, advancing data assimilation and integration methodologies will likely remain a central focus of future research in hydrogeodesy.

Like many other disciplines, hydrogeodesy is witnessing an emerging trend of utilizing AI techniques to integrate diverse datasets and address various challenges (Reichstein et al., 2019; Gou and Soja, 2024). It has been demonstrated that applying AI can uncover patterns and trends previously hidden in complex hydrological datasets (Karpatne et al., 2017). Among the AI techniques employed, ML and, more specifically, Deep Learning (DL) stand out for their remarkable capabilities in extracting meaningful insights from vast amounts of data. ML algorithms, such as Random Forests and Gradient Boosting Machines, are widely used for classification, regression, and clustering tasks in hydrology, enabling predictions of streamflow, groundwater levels, and precipitation patterns with improved accuracy (Zounemat-Kermani et al., 2021). These techniques often serve as a precursor to more advanced DL approaches, where neural networks with multiple layers can automatically extract intricate features from raw data, significantly reducing the need for manual intervention (Janiesch et al., 2021). Within DL, Convolutional Neural Networks (CNNs) are particularly effective in processing spatial data from satellite data, enhancing the monitoring of changes in water bodies, ice caps, and land moisture with unprecedented accuracy (Merchant, 2020). On the other hand, Recurrent Neural Networks (RNNs), including their advanced forms like Long Short-Term Memory (LSTM) networks, excel at analyzing temporal sequences, making them suitable for studying time series data, such as reconstructing pre-satellite records, forecasting river discharge, and detecting long-term trends in water storage (Yu et al., 2021). Additionally, Generative Adversarial Networks (GANs) offer innovative applications in simulating hydrological scenarios and generating high-resolution data from sparse observations (Gu et al., 2024). These capabilities are particularly valuable for addressing data gaps in remote or under-monitored regions, where sparse observations often limit the accuracy of traditional models. They also align with a growing call for empirical, data-driven hydrology at scale, where machine learning serves as a tool for discovery rather than an end in itself, as favored by Gleason and Brown (Gleason and Brown, 2025).

1.3 Rationale and structure of this habilitation thesis

While AI techniques receive significant attention these days, it can be argued that the potential of Bayesian techniques remains underutilized. The extensive data available from different sensors can serve as prior information on the water cycle. These prior insights can be encoded within the Bayesian framework, allowing quantification of water cycle components, even in data-sparse regions or periods (Beven, 2009; Vrugt et al., 2008; Smith, 2010). Bayesian approaches offer a robust framework for handling the vast amounts of data available from different satellites, facilitating the estimation of various hydrological cycle parameters and their associated uncertainties.

Moreover, while AI methods excel in finding unexplored dependencies and predictive modeling, they often struggle with uncertainty quantification (Begoli et al., 2019). Bayesian methods provide a clear advantage in this regard by offering a probabilistic interpretation of results (McMillan et al., 2011). Bayesian techniques can explicitly obtain an uncertainty estimate for parameters. This is particularly important in hydrogeodesy, where the parameters of the hydrological cycle, such as river discharge, soil moisture, and groundwater storage, are often estimated indirectly and are subject to significant uncertainties. Integrating Bayesian techniques with AI-based methods has shown promise in improving the accuracy and efficiency of water cycle modeling and data assimilation processes (Li and Liu, 2025). Bayesian deep learning methods, such as Bayesian neural networks (BNNs), variational autoencoders (VAEs), Bayesian convolutional neural networks (BCNNs), and Bayesian recurrent neural networks (BRNNs), combine the strengths of deep learning with the probabilistic reasoning of Bayesian inference (Wang and Yeung, 2016). BNNs introduce uncertainty estimates into the predictions, providing a measure of confidence in model outputs, which is particularly valuable for hydrogeodesy. VAEs enable efficient encoding and generation of complex hydrological data, facilitating the identification of latent structures and patterns within the data. BCNNs extend Bayesian inference to convolutional neural networks, enhancing uncertainty estimation in image classification and segmentation tasks, while BRNNs apply Bayesian principles to sequential data, improving robustness in time-series predictions (Mo et al., 2022). Therefore, the potential of Bayesian techniques can be explored alongside AI methods or independently, offering enhanced interpretability and reliability in hydrogeodesy.

Inspired by the potential of Bayesian approaches, this habilitation thesis aims to highlight the versatility and power of Bayesian methods in advancing hydrogeodesy, particularly in enhancing water cycle parameters. To this end, first, a fundamental description of Bayesian statistics and modeling is provided, establishing a connection to the classical frequentist approaches typically used in geodesy. Then, the following chapters will discuss three specific studies that utilize Bayesian approaches in different ways. The first study focuses on the use of dynamic models to tackle the challenge of spatiotemporal resolution, demonstrating how Bayesian methods allow for estimating river discharge over a river network. The second study explores downscaling GRACE data using a dedicated Bayesian framework, addressing the issue of coarse spatial resolution and improving the utility of GRACE observations for local-scale hydrological studies. The third study investigates the use of graphical models within a Bayesian framework to improve the estimation of water levels from satellite altimetry.

It is important to note that this thesis does not aim to provide a comprehensive description of all existing Bayesian techniques, nor an overview of all Bayesian techniques in hydrogeodesy, nor a demonstration of all the potential of Bayesian approaches for hydrogeodesy. Instead, along with providing foundational knowledge, it seeks to emphasize the benefit of Bayesian approaches for some of the challenges in hydrogeodesy. These approaches are applicable to many parameters and challenges within hydrogeodesy and demonstrate the effectiveness and versatility of Bayesian methods in improving certain key parameters of the hydrological cycle.

Bayesian statistics and modeling

2

Bayesian statistics presents an approach to analyzing data by relying on the Bayes theorem. In a simple word, this method involves updating initial knowledge about parameters in a statistical model with information obtained from observations (van de Schoot et al., 2021). The initial knowledge is represented as a prior distribution, which is then combined with the observed data using a likelihood function, resulting in the determination of the posterior distribution (Bishop, 2006; Koch, 2007; Aldrich, 2008).

The history of Bayesian statistics can be traced back to the 18th century when mathematicians began to develop methods for estimating the parameters of probability distributions. Thomas Bayes (1701–1761), an English mathematician and theologian, laid the groundwork for Bayesian statistics with his seminal work on probability theory. In his posthumously published essay, *Essay towards solving a problem in the doctrine of chances* in 1764, Bayes introduced what is now known as the Bayes theorem. The solution proposed by Thomas Bayes for the case of a uniform prior was later generalized by Pierre-Simon Laplace (1749–1827), who recognized the broader applicability of Bayesian reasoning. Laplace extended and formalized Bayes' ideas, applying them to various scientific disciplines, including astronomy and biology. His contributions solidified Bayesian statistics as a powerful tool for statistical inference (Aldrich, 2008).

While frequentist statistics received more attention in the early 20th century, Bayesian methods remained relatively obscure until the mid-20th century. Advancements in computational power and the work of statisticians such as Harold Jeffreys and Leonard J. Savage revived interest in Bayesian inference (Jeffreys, 1961; Savage, 1954). The late 20th and early 21st centuries saw a significant increase in the application of Bayesian methods. Today, both frequentist and Bayesian approaches are widely practiced, each providing unique advantages depending on the analysis context and the nature of the data.

2.1 The Bayes theorem and Bayesian probability

Let us consider a pair of random variables, denoted as A and B, with a joint probability distribution $\mathsf{P}(A, B)$, we can write the so-called sum rule and the product rule as:

$$\textbf{sum rule} \qquad \mathsf{P}(A) = \sum_{B} \mathsf{P}(A, B) \tag{2.1}$$

$$\textbf{product rule} \qquad \mathsf{P}(A, B) = \mathsf{P}(A|B)\mathsf{P}(B) \tag{2.2}$$

The sum rule states that the marginal probability of A is the sum of the joint probabilities of A and B over all possible values of B. And the product rule states that the joint probability of A and B is the product of the probability of B and the conditional probability of A given B. In other words, to find the probability of both A and B occurring simultaneously, we multiply the probability of B by the probability of A occurring given that B has occurred.

By combining the product rule of probability with the symmetry rule $\mathsf{P}(A, B) = \mathsf{P}(B, A)$, we obtain the following relationship between conditional probabilities (Bishop, 2006):

$$\mathsf{P}(A|B) = \frac{\mathsf{P}(A,B)}{\mathsf{P}(B)} = \frac{\mathsf{P}(B,A)}{\mathsf{P}(B)} = \frac{\mathsf{P}(B|A)\mathsf{P}(A)}{\mathsf{P}(B)}\,, \tag{2.3}$$

which is called *the Bayes theorem*. By applying the sum rule, it becomes possible to represent the denominator using the variables present in the numerator.

$$\mathsf{P}(B) = \sum_{A} \mathsf{P}(B|A)\mathsf{P}(A)\,, \tag{2.4}$$

which implies that the denominator serves as a normalization factor, guaranteeing that the summation of the conditional probability on the left side of Equation (2.3) across all A values equals one.

The Bayes theorem becomes handy in dealing with obtaining the probability for events that are repeated, and a probability estimate is available. Let us delve into it using a straightforward example. Let's assume we have historical data that tells us the probability of heavy rainfall given that a flood has occurred in the past $\mathsf{P}(\mathrm{Rain}|\mathrm{Flood})$. We also have data on the overall probability of heavy rainfall $\mathsf{P}(\mathrm{Rain})$ regardless of whether a flood happens or not, and the overall probability of a flood $\mathsf{P}(\mathrm{Flood})$. Using the Bayes rule, we can calculate the probability of a flood occurring given the presence of heavy rainfall as:

$$\mathsf{P}(\mathrm{Flood}|\mathrm{Rain}) = \frac{\mathsf{P}(\mathrm{Rain}|\mathrm{Flood})\mathsf{P}(\mathrm{Flood})}{\mathsf{P}(\mathrm{Rain})}\,. \tag{2.5}$$

Let us add some numbers to make it more sensible:

- $\mathsf{P}(\mathrm{Flood})$: Suppose that the probability of a flood occurring in a given year $\mathsf{P}(\mathrm{Flood})$ is 0.1 (10%).
- $\mathsf{P}(\mathrm{Rain}|\mathrm{Flood})$: Suppose that the probability of heavy rainfall given a flood is 0.8 (80%). The probability of heavy rainfall without a flood $\mathsf{P}(\mathrm{Rain}|\neg\mathrm{Flood})$ is 0.2 (20%).

Using the Bayes theorem, we can calculate the probability that a flood occurs given that there has been heavy rainfall. First, we calculate $\mathsf{P}(\mathrm{Rain})$:

$$\mathsf{P}(\mathrm{Rain}) = \mathsf{P}(\mathrm{Rain}|\mathrm{Flood})\mathsf{P}(\mathrm{Flood}) + \mathsf{P}(\mathrm{Rain}|\neg\mathrm{Flood})\mathsf{P}(\neg\mathrm{Flood}) \tag{2.6}$$

$$\mathsf{P}(\mathrm{Rain}) = (0.8 \times 0.1) + (0.2 \times 0.9) = 0.08 + 0.18 = 0.26 \tag{2.7}$$

Then,

$$\mathsf{P}(\mathrm{Flood}|\mathrm{Rain}) = \frac{0.8 \times 0.1}{0.26} \approx 0.3077\,. \tag{2.8}$$

This result shows that given the occurrence of heavy rainfall, the probability of a flood occurring increases to approximately 30.8%, reflecting the impact of both the prior probability and the likelihood of heavy rainfall given a flood.

2.2 Bayesian inference

In the previous example, the exploration of probabilities lies in the concept of frequencies of repeatable random events, which is a classical or frequentist interpretation of probability. Let us shift our focus to the broader Bayesian perspective, where probabilities serve as a means to quantify uncertainty.

Consider an event that is inherently uncertain in nature, such as whether Lake Urmia in Iran will vanish by 2090, a time at which many climate projections indicate the lake will be severely impacted by rising temperatures and increased evapotranspiration (Modaresi and Araghi, 2023). This event cannot be replicated multiple times to establish a probability, as we did with the heavy rain and flood example. However, we often possess some understanding about the rate of Lake Urmia's water loss. And then, when new evidence emerges, such as data from satellite altimetry, satellite imaging, and the GRACE mission (Tourian et al., 2015), our stance on lake water loss might change. In such instances, the ability to precisely gauge uncertainty and recalibrate it based on new measurements becomes crucial, followed by making optimal choices. This can be achieved through the Bayesian interpretation of probability, which provides a framework for updating the probability of a hypothesis as more evidence or information becomes available. This process of updating is known as *Bayesian inference*.

Bayesian inference is the method of deducing properties about a phenomenon from data using the Bayes theorem. The core of Bayesian inference is the likelihood function, which combines prior knowledge with new evidence to form a posterior probability distribution. Given a hypothesis H and observed data D, the Bayes theorem allows us to update the probability of the hypothesis:

$$\mathrm{P}(H|D) = \frac{\mathrm{P}(D|H)\mathrm{P}(H)}{\mathrm{P}(D)}. \tag{2.9}$$

Here, $\mathrm{P}(H|D)$ is the posterior probability, $\mathrm{P}(H)$ is the prior probability, $\mathrm{P}(D|H)$ is the likelihood, and $\mathrm{P}(D)$ is the evidence or marginal likelihood.

The process of Bayesian inference involves the following steps:

- Specifying the prior: This involves defining a prior probability distribution $\mathrm{P}(H)$ that encapsulates our beliefs about the hypothesis before observing any data.
- Calculating the likelihood: Determine the likelihood $\mathrm{P}(D|H)$, which represents the probability of observing the data given the hypothesis.
- Applying the Bayes theorem to update the prior distribution based on the obtained likelihood, resulting in the posterior distribution $\mathrm{P}(H|D)$.

According to Equation (2.9), obtaining the posterior distribution involves multiplying the likelihood by the prior distribution and then normalizing the result (see Figure 2.1). While the prior distribution must be a valid probability distribution (with its integral equal to one), the likelihood function does not have to be a probability distribution. Multiplying the prior by the likelihood yields an unnormalized posterior, which becomes a proper posterior distribution once it is normalized by the denominator.

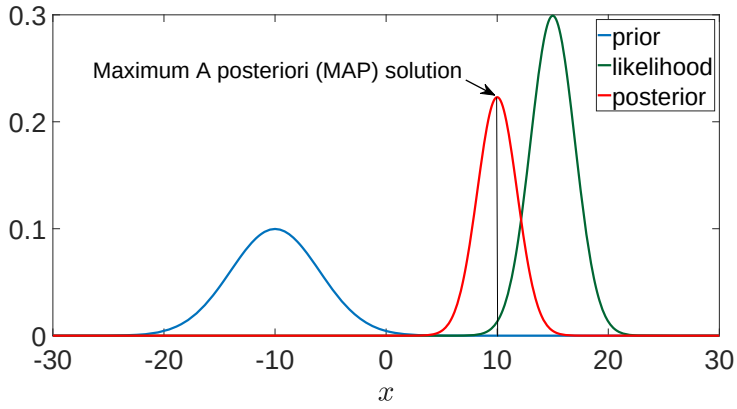

Fig. 2.1: Obtaining the posterior distribution involves multiplying the likelihood by the prior distribution and then normalizing the result. The Maximum A Posteriori (MAP) solution refers to the value of x at which the posterior probability is maximized.

Let us return to the example of Lake Urmia and the question of whether it will vanish by 2090. In this context, the hypothesis H is that the lake will disappear by 2090, meaning that its water level will reach the lowest bathymetry level 1265 m (see the bathymetry of the Lake in Figure 2.2). The observed data D is the measured water level up to 2020 (see Figure 2.2 right). The best way to determine whether the lake will vanish by 2090 is to analyze the water level variations and their long-term behavior. When analyzing the long-term behavior, H refers to the trend parameters of water level variations, and $\mathsf{P}(H)$ is the prior belief about these parameters.

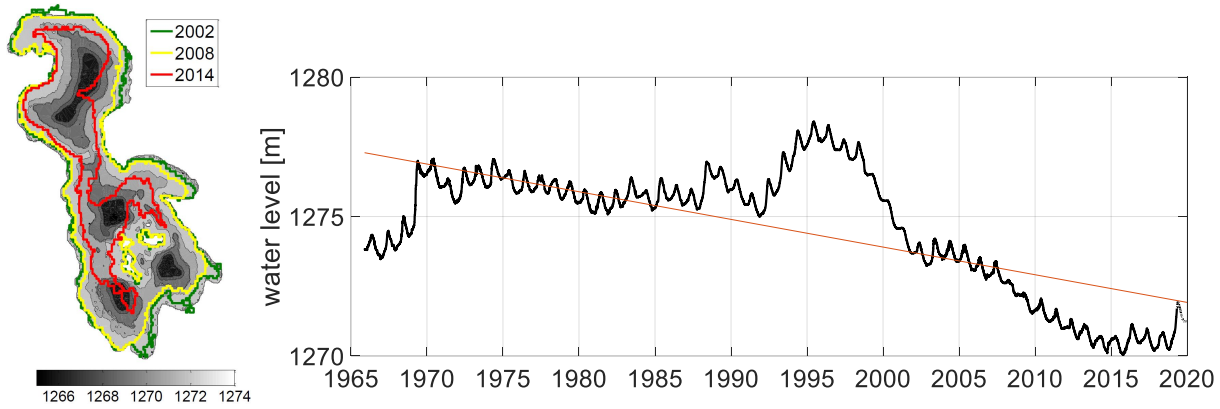

Fig. 2.2: Left) The bathymetry of Lake Urmia varying between 1265 and 1274m, together with the surface water extent of January 2002, 2008, and 2014. Right) Lake Urmia in situ water level time series from 1966 to 2020

We have a set of data with m measurements of the water level, $\boldsymbol{y} = [y_1, \ldots, y_m]^\top$, where $\boldsymbol{t} = [t_1, \ldots, t_m]^\top$ represents the time of the measurements. To analyze the long-term behavior, one common approach is to fit a line to the water level time series $f(\boldsymbol{t}, \boldsymbol{x}) = a + b\boldsymbol{t}$, with $\boldsymbol{x}$ being the unknown parameters $\boldsymbol{x} = [a, b]^\top$. By fitting such a line and extending it to 2090, within an uncertainty range, we can predict whether the water level will reach the lowest possible water level 1265 m. To obtain such an estimate and its uncertainty, the measurements' uncertainty should first be considered. To do this, let us express the uncertainty of observation $\boldsymbol{y}$ using a probability distribution. We assume that, given the value of $\boldsymbol{t}$, the corresponding value of $\boldsymbol{y}$ follows a certain distribution. For simplicity, we assume a normal distribution with a constant variance σ_y^2 for all measurements:

$$\mathsf{P}(\boldsymbol{y}|\boldsymbol{t}, \boldsymbol{x}, \sigma_y^{-2}) = \mathcal{N}(\boldsymbol{y}|f(\boldsymbol{t}, \boldsymbol{x}), \sigma_y^2). \tag{2.10}$$

This means that at any measurement epoch t_i, we assume a normal distribution with the mean being the target function $f(\boldsymbol{t}, \boldsymbol{x})$ to be fitted and standard deviation σ_y. We can use the water level values $\boldsymbol{y}$ measured at $\boldsymbol{t}$ to determine the unknown parameters $\boldsymbol{x}$ using a maximum likelihood estimation. The *likelihood function* is given by the product of probability distributions of all m measurements:

$$\mathsf{P}(\boldsymbol{y}|\boldsymbol{t}, \boldsymbol{x}, \sigma_y^{-1}) = \prod_{i=1}^{m} \mathcal{N}(y_i|f(t_i, \boldsymbol{x}), \sigma_y^2) \tag{2.11}$$

$$= \prod_{i=1}^{m} \frac{1}{\sqrt{2\pi}\sigma_y} \exp\left\{-\frac{1}{2\sigma_y^2}(y_i - f(t_i, \boldsymbol{x}))^2\right\}. \tag{2.12}$$

To maximize this likelihood function, it is convenient to maximize its logarithm:

$$\ln \mathsf{P}(\boldsymbol{y}|\boldsymbol{t},\boldsymbol{x},\sigma_y^{-2}) = -\frac{\sigma_y^{-2}}{2}\sum_{i=1}^{m}(f(t_i,\boldsymbol{x})-y_i)^2 + \frac{m}{2}\ln\sigma_y^2 - \frac{m}{2}\ln(2\pi). \tag{2.13}$$

The solution for the parameter $\hat{\boldsymbol{x}}$ is then obtained by maximizing Equation (2.13) for $\boldsymbol{x}$. For this, we note that the last two terms can be neglected since they do not depend on $\boldsymbol{x}$. Further, it becomes clear that in the first term $\frac{\sigma_y^{-2}}{2}$ is a positive scalar value and does not influence the choice of $\boldsymbol{x}$, therefore replacing $\frac{\sigma_y^{-1}}{2}$ by $\frac{1}{2}$ does not influence the choice of $\boldsymbol{x}$. So maximizing Equation (2.13) corresponds to maximizing the first term only. In fact, instead of maximizing the log-likelihood, we can minimize the negative log-likelihood:

$$\frac{1}{2}\sum_{i=1}^{m}(f(t_i,\boldsymbol{x})-y_i)^2 \rightarrow \text{minimum} \tag{2.14}$$

It becomes immediately evident that maximizing the likelihood is equivalent to minimizing the sum of squared errors, as targeted within least squares estimation.

In a matrix representation of this line fitting exercise, we can write the model as $\boldsymbol{y} = \boldsymbol{A}\boldsymbol{x} + \boldsymbol{e}$, with $\boldsymbol{A}$ being a matrix (design matrix) of size $m \times n$ (here in this example the number of unknowns $n = 2$) with $\boldsymbol{t}$ in its second column and the first column being $\mathbf{1}_m = \begin{bmatrix}1 & 1 & \cdots & 1\end{bmatrix}^\top$. With such a formulation, the cost function in Equation (2.14) can be written as

$$\mathcal{C}(x) = \frac{1}{2}\boldsymbol{e}^\top\boldsymbol{e},$$

for which the minimization means

$$\hat{\boldsymbol{x}} = \min_{\boldsymbol{x}}\mathcal{C}(\boldsymbol{x}) = \min_{\hat{\boldsymbol{x}}}\frac{1}{2}(\boldsymbol{y}-\boldsymbol{A}\boldsymbol{x})^\top(\boldsymbol{y}-\boldsymbol{A}\boldsymbol{x}) = \min_{\boldsymbol{x}}\left(\frac{1}{2}\boldsymbol{y}^\top\boldsymbol{y} - \boldsymbol{y}^\top\boldsymbol{A}\boldsymbol{x} + \frac{1}{2}\boldsymbol{x}^\top\boldsymbol{A}^\top\boldsymbol{A}\boldsymbol{x}\right).$$

The term $\frac{1}{2}y^\top y$ is just a constant that doesn't play a role in the minimization. The minimum occurs at the location where the derivative of $\mathcal{C}$ is zero:

$$\frac{\partial\mathcal{C}}{\partial\boldsymbol{x}}(\hat{\boldsymbol{x}}) = -\boldsymbol{A}^\top\boldsymbol{y} + \boldsymbol{A}^\top\boldsymbol{A}\hat{\boldsymbol{x}} = 0.$$

The solution is then

$$\hat{\boldsymbol{x}} = (\boldsymbol{A}^\top\boldsymbol{A})^{-1}\boldsymbol{A}^\top\boldsymbol{y}, \tag{2.15}$$

with a covariance matrix of $\boldsymbol{Q}_{\hat{\boldsymbol{x}}} = \left(\sigma_y^{-2}\boldsymbol{A}^{\mathrm{T}}\boldsymbol{A}\right)^{-1}$. and the corrected observation $\hat{\boldsymbol{y}}$

$$\hat{\boldsymbol{y}} = \boldsymbol{A}\hat{\boldsymbol{x}}, \tag{2.16}$$

for which the covariance can be obtained through the error propagation

$$\boldsymbol{Q}_{\hat{\boldsymbol{y}}} = \boldsymbol{A}\boldsymbol{Q}_{\hat{\boldsymbol{x}}}\boldsymbol{A}^\top, \tag{2.17}$$

which does not represent the model's goodness of fit, as long as the original σ_y is considered for the weight and no a posteriori variance of unit weight (discussed in Section 2.3) is included (Niemeier, 2008). With the help of the likelihood function, we can provide an estimate of uncertainty $\hat{\sigma}_y^2$ by minimizing the negative of Equation (2.13) for σ_y^{-2}:

$$\frac{\partial\left(-\ln\mathsf{P}(\boldsymbol{y}|\boldsymbol{t},\boldsymbol{x},\sigma_y^{-2})\right)}{\partial\left(\sigma_y^{-2}\right)} = \frac{1}{2}\sum_{i=1}^{m}\{f(t_i,\boldsymbol{x})-y_i\}^2 - \frac{m}{2}\sigma_y^2 = 0,$$

which leads to

$$\hat{\sigma}^2_{y_{\mathrm{ML}}} = \frac{1}{m}\sum_{i=1}^{m}\{y_i - f(t_i,\hat{x})\}^2 = \frac{\boldsymbol{e}^\top \boldsymbol{e}}{m},$$

which is nothing other than the variance of the residuals.

For the Lake Urmia example, a constant uncertainty of $10\,\mathrm{cm}$ ($\sigma_y = 10\,\mathrm{cm}$) is assumed for the in situ water level time series. This value of σ_y indicates that an individual likelihood function for the parameters a and b is associated with each measurement. In this example $m = 19667$. Below is the individual likelihood function of six randomly selected points. Each likelihood function is obtained by considering a single point for fitting the model $y = a + bt$.

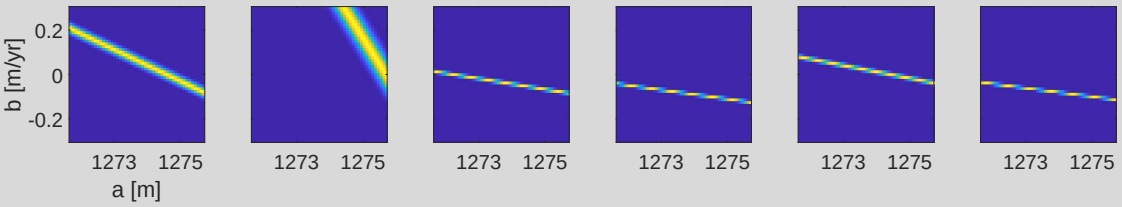

Multiplying all of the likelihood functions for 19,667 daily measurements leads to the following likelihood function:

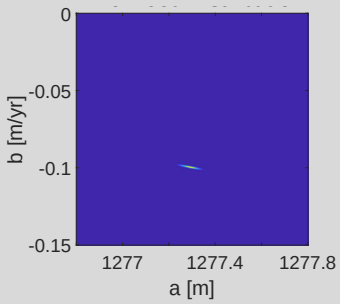

with its maximum being:

$$\hat{\boldsymbol{x}} = \begin{bmatrix}\hat{a}\\ \hat{b}\end{bmatrix} = \begin{bmatrix}1277.289\,\mathrm{m}\\ -0.099\,\mathrm{m/yr}\end{bmatrix}$$

and its dispersion being:

$$Q_{\hat{x}} = \begin{bmatrix}2.03\times10^{-6}\,\mathrm{m}^2 & -1.55\times10^{-10}\,\mathrm{m}^2/\mathrm{yr}\\ -1.55\times10^{-10}\,\mathrm{m}^2/\mathrm{yr} & 1.57\times10^{-14}\,\mathrm{m}^2/\mathrm{yr}^2\end{bmatrix}$$

It should be noted that, from the Equation (2.15), it is clear that choosing σ_y as a constant uncertainty for all observations does not affect the fitted line of the Maximum Likelihood or Least Squares estimate. However, the covariance estimate is influenced by the choice of σ_y.
To evaluate the likelihood of complete desiccation of the lake by 2090, we need to extend the trend line to 2090 using equations (2.16) and (2.17). This results in:

$$\hat{y}_{2090} = 1264.975 \pm 0.005$$

Assuming a normal distribution with the mean 1264.975 m and standard deviation 0.005 m, we can predict that there is a 99% probability that Lake Urmia will reach its lowest water level of 1265 m in 2090:

$$\mathcal{N}(1265|1264.975, 0.005) = 99\%\,.$$

Let us now move to Bayesian inference by introducing a prior distribution over the unknown vector $\boldsymbol{x}$. For simplicity, we consider a normal distribution with a constant variance σ_x^2. We believe a priori that the unknown parameters have a mean value of zero:

$$\mathsf{P}(\boldsymbol{x}|\sigma_x^{-2}) = \mathcal{N}(\boldsymbol{x}|\boldsymbol{0}, \sigma_x^2 \boldsymbol{I}) = \left(\frac{\sigma_x^{-2}}{2\pi}\right)^{n/2} \exp\left(-\frac{\sigma_x^{-2}}{2}\boldsymbol{x}^\top \boldsymbol{x}\right).$$

Using Bayesian inference, we can obtain the posterior distribution for $\boldsymbol{x}$ through the product of the prior distribution and the likelihood function defined in (2.10):

$$\mathsf{P}(\boldsymbol{x}|\boldsymbol{t}, \boldsymbol{y}, \sigma_x^{-2}, \sigma_y^{-2}) \propto \mathsf{P}(\boldsymbol{y}|\boldsymbol{t}, \boldsymbol{x}, \sigma_y^{-2}) \times \mathsf{P}(\boldsymbol{x}|\sigma_x^{-2}) \tag{2.18}$$

$$\text{Posterior} \propto \text{Likelihood} \times \text{Prior}. \tag{2.19}$$

To determine $\boldsymbol{x}$, we find the value of $\boldsymbol{x}$ that maximizes the posterior probability, known as the Maximum A Posteriori (MAP) estimate (see Figure 2.1). This can be achieved by maximizing the logarithm of Equation (2.19) or, equivalently, minimizing its negative. Considering the earlier treatment of the likelihood function, the MAP estimate, $\hat{\boldsymbol{x}}_{\text{MAP}}$, is given by minimizing the following cost function:

$$\hat{\boldsymbol{x}}_{\text{MAP}} = \min_{\boldsymbol{x}} \mathcal{C}_{\text{MAP}}(\boldsymbol{x}) = \frac{\sigma_y^{-2}}{2} \sum_{i=1}^{m} \left(f(t_i, \boldsymbol{x}) - y_i\right)^2 + \frac{\sigma_x^{-2}}{2}\boldsymbol{x}^\top \boldsymbol{x}. \tag{2.20}$$

Comparing Equation (2.20) with the cost function of a classical regularization problem:

$$\mathcal{C}_{\text{reg}}(\boldsymbol{x}) = \frac{1}{2}\sum_{i=1}^{m} \left(f(t_i, \boldsymbol{x}) - y_i\right)^2 + \frac{\lambda}{2}\boldsymbol{x}^\top \boldsymbol{x}, \tag{2.21}$$

we see that maximizing the posterior distribution when both the prior and the likelihood are normally distributed is equivalent to a regularization problem with the regularization parameter given by:

$$\lambda = \frac{\sigma_x^{-2}}{\sigma_y^{-2}} = \frac{\sigma_y^2}{\sigma_x^2}. \tag{2.22}$$

Since the normal distribution is a conjugate prior, multiplying it by the likelihood results in a posterior density function that belongs to the same family of distributions as the prior density function (Koch, 2007). Therefore, the posterior distribution will also be normally distributed, given by:

$$\mathsf{P}(\boldsymbol{x}|\boldsymbol{t}, \boldsymbol{y}) \sim \mathcal{N}(\boldsymbol{x}|\hat{\boldsymbol{x}}_{\text{MAP}}, \boldsymbol{Q}_{\hat{\boldsymbol{x}}_{\text{MAP}}}^{-1}), \tag{2.23}$$

where

$$\hat{\boldsymbol{x}}_{\text{MAP}} = (\boldsymbol{A}^\top \boldsymbol{A} + \frac{\sigma_x^{-2}}{\sigma_y^{-2}}\boldsymbol{I})^{-1}\boldsymbol{A}^\top \boldsymbol{y}. \tag{2.24}$$

The MAP estimate is the value of $\boldsymbol{x}$ that maximizes the posterior distribution. In the case of a normal distribution, this corresponds to the mean of the posterior distribution, with the dispersion being represented by the covariance matrix:

$$\boldsymbol{Q}_{\hat{\boldsymbol{x}}_{\text{MAP}}} = \left(\sigma_y^{-2}\boldsymbol{A}^\top \boldsymbol{A} + \sigma_x^{-2}\boldsymbol{I}\right)^{-1}. \tag{2.25}$$

For the Lake Urmia example, we again assume a constant uncertainty of $10\,\mathrm{cm}$ ($\sigma_y = 10\,\mathrm{cm}$) for the in situ water level time series. For the sake of experimentation, we deliberately chose an incorrect prior (see figure below). Specifically, mean values of zero are assumed for both a and b, with a constant uncertainty of $\sigma_x = 0.1$ for each, which is intentionally inaccurate. In particular, we assign an uncertainty of $0.1\,\mathrm{m}$ to the unknown parameter a and an uncertainty of $0.1\,\mathrm{m/yr}$ to the unknown parameter b. This prior implies a belief that the trend is zero and the water level remains constant. Since a and b have different units, applying a constant uncertainty is even more inappropriate. Applying Equation (2.24) using these numbers, we obtain:

$$\hat{x}_{\mathrm{MAP}} = \begin{bmatrix} \hat{a}_{\mathrm{MAP}} \\ \hat{b}_{\mathrm{MAP}} \end{bmatrix} = \begin{bmatrix} 1277.030\,\mathrm{m} \\ -0.091\,\mathrm{m/yr} \end{bmatrix}$$

We see that the prior shifts the MAP solution toward zero. In other words, from the estimated trend of $-0.099\,\mathrm{m/yr}$ obtained using the least squares method on page 30, the MAP estimate is adjusted to $-0.091\,\mathrm{m/yr}$. The covariance matrix is given as:

$$Q_{\hat{x}_{\mathrm{MAP}}} = \begin{bmatrix} 2.03 \times 10^{-6}\,\mathrm{m}^2 & -5.7 \times 10^{-8}\,\mathrm{m}^2/\mathrm{yr} \\ -5.7 \times 10^{-8}\,\mathrm{m}^2/\mathrm{yr} & 2.10 \times 10^{-9}\,\mathrm{m}^2/\mathrm{yr}^2 \end{bmatrix}$$

Comparing these numbers with those on page 30, we observe that such an inaccurate prior not only alters the estimates of $\hat{a}$ and $\hat{b}$, but also increases the uncertainty. However, this increase cannot be visually observed in the plots below. Note that in the plots below, the x-axis of the prior distribution is different than the likelihood and the posterior to show the zero mean for a.

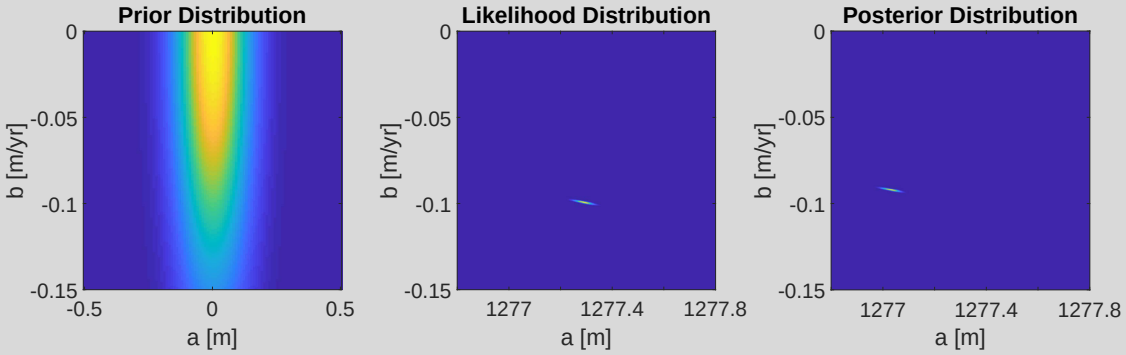

Extending the estimated trend to 2090, we obtain:

$$\hat{y}_{2090} = 1265.613 \pm 0.004$$

Assuming a normal distribution with a mean of 1265.613 m and a standard deviation of 0.004 m, we can predict that there is a 0% probability that Lake Urmia will reach its lowest water level of 1265 m in 2090.

$$\mathcal{N}(1265|1265.613, 0.004) = 0\%$$

Comparing these results with those on page 30, we observe that the prediction is influenced by the inaccurate prior. Although the selected σ_y and σ_x result in a regularization parameter of $\lambda = \frac{\sigma_y^2}{\sigma_x^2} = 1$, and the likelihood plays a major role in obtaining the posterior, the prior assumption of a zero mean for a and b implies a belief that there is no trend in the lake. This assumption drastically reduces the probability of complete desiccation from 99% to zero.

Now let us consider a more general case where the prior follows a multivariate normal distribution with mean $\boldsymbol{\mu}$ and covariance matrix Σ_x:

$$\mathsf{P}(\boldsymbol{x}|\Sigma_x^{-1}) = \mathcal{N}(\boldsymbol{x}|\boldsymbol{\mu}, \Sigma_x)\,,$$

and the likelihood function also follows a multivariate normal distribution, where the model represents the mean and the dispersion is represented by Σ_y. Combining the prior and the likelihood, the posterior distribution becomes:

$$\mathsf{P}(\boldsymbol{x}|\boldsymbol{y}) \propto \exp\left(-\frac{1}{2}(\boldsymbol{y}-\boldsymbol{A}\boldsymbol{x})^\top \Sigma_y^{-1}(\boldsymbol{y}-\boldsymbol{A}\boldsymbol{x}) - \frac{1}{2}(\boldsymbol{x}-\boldsymbol{\mu})^\top \Sigma_x^{-1}(\boldsymbol{x}-\boldsymbol{\mu})\right).$$

Expanding the terms in the exponent, for the likelihood term, we have

$$(\boldsymbol{y}-\boldsymbol{A}\boldsymbol{x})^\top \Sigma_y^{-1}(\boldsymbol{y}-\boldsymbol{A}\boldsymbol{x}) = \boldsymbol{y}^\top \Sigma_y^{-1}\boldsymbol{y} - 2\boldsymbol{y}^\top \Sigma_y^{-1}\boldsymbol{A}\boldsymbol{x} + \boldsymbol{x}^\top \boldsymbol{A}^\top \Sigma_y^{-1}\boldsymbol{A}\boldsymbol{x},$$

and for the prior term: $(\boldsymbol{x}-\boldsymbol{\mu})^\top \Sigma_x^{-1}(\boldsymbol{x}-\boldsymbol{\mu}) = \boldsymbol{\mu}^\top \Sigma_x^{-1}\boldsymbol{\mu} - 2\boldsymbol{\mu}^\top \Sigma_x^{-1}\boldsymbol{x} + \boldsymbol{x}^\top \Sigma_x^{-1}\boldsymbol{x}$.

By grouping the quadratic, linear, and constant terms, we have:

$$\mathsf{P}(\boldsymbol{x}|\boldsymbol{y}) \propto \exp\left(-\frac{1}{2}\boldsymbol{x}^\top(\boldsymbol{A}^\top \Sigma_y^{-1}\boldsymbol{A} + \Sigma_x^{-1})\boldsymbol{x} + \boldsymbol{x}^\top(\boldsymbol{A}^\top \Sigma_y^{-1}\boldsymbol{y} + \Sigma_x^{-1}\boldsymbol{\mu}) + \text{constants}\right).$$

The MAP estimate $\hat{\boldsymbol{x}}_{\text{MAP}}$ maximizes the posterior. Ignoring constants, this is equivalent to minimizing the negative quadratic form: $-\frac{1}{2}\boldsymbol{x}^\top(\boldsymbol{A}^\top \Sigma_y^{-1}\boldsymbol{A} + \Sigma_x^{-1})\boldsymbol{x} + \boldsymbol{x}^\top(\boldsymbol{A}^\top \Sigma_y^{-1}\boldsymbol{y} + \Sigma_x^{-1}\boldsymbol{\mu})$.

Taking the gradient with respect to $\boldsymbol{x}$ and setting it to zero:

$$(\boldsymbol{A}^\top \Sigma_y^{-1}\boldsymbol{A} + \Sigma_x^{-1})\hat{\boldsymbol{x}}_{\text{MAP}} = \boldsymbol{A}^\top \Sigma_y^{-1}\boldsymbol{y} + \Sigma_x^{-1}\boldsymbol{\mu},$$

which leads to the MAP solution:

$$\hat{\boldsymbol{x}}_{\text{MAP}} = (\boldsymbol{A}^\top \boldsymbol{\Sigma}_y^{-1}\boldsymbol{A} + \boldsymbol{\Sigma}_x^{-1})^{-1}(\boldsymbol{A}^\top \boldsymbol{\Sigma}_y^{-1}\boldsymbol{y} + \boldsymbol{\Sigma}_x^{-1}\boldsymbol{\mu})\,, \tag{2.26}$$

with the dispersion being:

$$\mathsf{D}(\boldsymbol{x}|\boldsymbol{y}) = \boldsymbol{Q}_{\hat{\boldsymbol{x}}_{\text{MAP}}} = (\boldsymbol{A}^\top \boldsymbol{\Sigma}_y^{-1}\boldsymbol{A} + \boldsymbol{\Sigma}_x^{-1})^{-1}\,. \tag{2.27}$$

In essence, this Bayesian estimation is analogous to adding the prior information as an additional constraint in a classical least squares adjustment:

$$\bar{\boldsymbol{A}} = \begin{bmatrix}\boldsymbol{A}\\ \boldsymbol{I}\end{bmatrix}, \bar{\boldsymbol{y}} = \begin{bmatrix}\boldsymbol{y}\\ \boldsymbol{\mu}\end{bmatrix}, \bar{\boldsymbol{P}} = \begin{bmatrix}\boldsymbol{P} & 0\\ 0 & \boldsymbol{\Sigma}_x^{-1}\end{bmatrix}.$$

The system of equations can be written as:

$$\begin{cases}\boldsymbol{y} = \boldsymbol{A}\boldsymbol{x} + \boldsymbol{e}\\ \boldsymbol{\mu} = \boldsymbol{x} + \boldsymbol{v}\end{cases}$$

The solution to the system is:

$$\hat{\boldsymbol{x}} = (\bar{\boldsymbol{A}}^\top \bar{\boldsymbol{P}}\bar{\boldsymbol{A}})^{-1}\bar{\boldsymbol{A}}^\top \bar{\boldsymbol{P}}\bar{\boldsymbol{y}}\,.$$

Substituting back, we obtain:

$$\hat{\boldsymbol{x}} = (\boldsymbol{A}^\top \Sigma_y^{-1}\boldsymbol{A} + \Sigma_x^{-1})^{-1}(\boldsymbol{A}^\top \Sigma_y^{-1}\boldsymbol{y} + \Sigma_x^{-1}\boldsymbol{\mu})\,.$$

Now let's define a realistic prior for the Lake Urmia example. Let's assume from a climate projection that there is an estimate of -0.14 m/yr for b and a we take 1277 m:

$$\boldsymbol{\mu} = \begin{bmatrix} 1277\,\mathrm{m} \\ -0.14\,\mathrm{m/yr} \end{bmatrix}$$

with

$$\Sigma_x = \begin{bmatrix} 0.4^2\,\mathrm{m}^2 & 0 \\ 0 & 0.036^2\,\mathrm{m}^2/\mathrm{yr}^2 \end{bmatrix}$$

For the observation, for simplicity we assume a constant uncertainty of 10 cm ($\sigma_y = 10\,\mathrm{cm}$) for the in situ water level time series, leading to

$$\Sigma_y = \begin{bmatrix} 0.1^2 & 0 & \cdots & 0 \\ 0 & 0.1^2 & \cdots & 0 \\ \vdots & \vdots & \ddots & \vdots \\ 0 & 0 & \cdots & 0.1^2 \end{bmatrix}$$

In this case, following (2.26), we obtain:

$$\hat{x}_{\mathrm{MAP}} = \begin{bmatrix} \hat{a}_{\mathrm{MAP}} \\ \hat{b}_{\mathrm{MAP}} \end{bmatrix} = \begin{bmatrix} 1277.290\,\mathrm{m} \\ -0.099\,\mathrm{m/yr} \end{bmatrix},$$

with the covariance matrix:

$$Q_{\hat{x}_{\mathrm{MAP}}} = \begin{bmatrix} 2.03 \times 10^{-6}\,\mathrm{m}^2 & -5.65 \times 10^{-8}\,\mathrm{m}^2/\mathrm{yr} \\ -5.65 \times 10^{-8}\,\mathrm{m}^2/\mathrm{yr} & 2.10 \times 10^{-9}\,\mathrm{m}^2/\mathrm{yr}^2 \end{bmatrix},$$

which indicates that the maximum likelihood estimate (box on page 30) remains unchanged (as seen in the blots below). This outcome is understandable, as the prior does not deviate significantly from the likelihood, and since the uncertainty of the likelihood function is smaller, it predominantly dictates the estimation of the posterior.

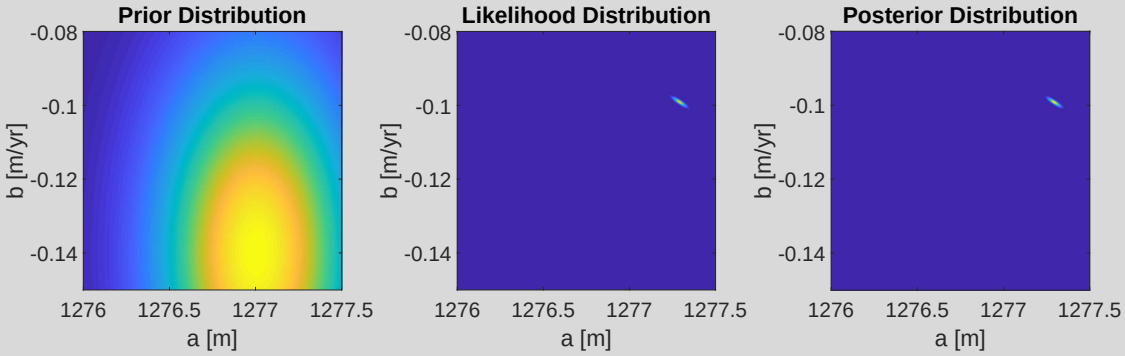

Extending the estimated trend to 2090, we obtain:

$$\hat{y}_{2090} = 1264.975 \pm 0.004$$

leading to a prediction of 99% probability that Lake Urmia will reach its lowest water level of 1265 m in 2090:

$$\mathcal{N}(1265|1264.975, 0.004) = 99\%$$

Comparing the results with $\boldsymbol{\mu}$ equal to zero (previous box on page 32), we see that having a prior of $-0.14\,\mathrm{m/yr}$ for the trend with a precision of $0.036^2\,\mathrm{m}^2/\mathrm{yr}^2$ suggests a larger estimated trend, increasing the probability that the lake will disappear by 2090.

2.3 A posteriori variance factor (unit weight variance) in Bayesian inference

In least squares adjustment, the a posteriori variance factor (often denoted as $\hat{\sigma}_0^2$) plays a crucial role in scaling the covariance matrix of the observations to reflect the actual dispersion observed in the data:

$$\hat{\sigma}_0^2 = \frac{\boldsymbol{e}^\top \boldsymbol{\Sigma}_y^{-1} \boldsymbol{e}}{m-n}\,.$$

The adjusted covariance matrix $\hat{\boldsymbol{Q}}_{\hat{x}}$ for the estimated parameters $\hat{\boldsymbol{x}}$ can then be scaled by this a posteriori variance factor to reflect the true variability observed:

$$\hat{\boldsymbol{Q}}_{\hat{x}} = \hat{\sigma}_0^2 (\boldsymbol{A}^\top \boldsymbol{\Sigma}_y^{-1} \boldsymbol{A})^{-1}\,.$$

The variance of unit weight $\hat{\sigma}_0^2$ helps assessing the quality of observations, the model's overall fit, and the choice of $\boldsymbol{\Sigma}_y$. If $\hat{\sigma}_0^2 \approx 1$, the model fits the observations well, and $\boldsymbol{\Sigma}_y$ accurately represents the observation uncertainty. If $\hat{\sigma}_0^2$ is much greater than 1, the observations are more dispersed than expected, indicating potential issues with the data or the model. If there are no issues with the model or observations, $\hat{\sigma}_0^2 > 1$ suggests an overly optimistic choice of $\boldsymbol{\Sigma}_y$. Conversely, if $\hat{\sigma}_0^2 < 1$, it suggests an overly pessimistic choice of $\boldsymbol{\Sigma}_y$.

For the Lake Urmia example, with

$$\Sigma_y = \begin{bmatrix} 0.1^2 & 0 & \cdots & 0 \\ 0 & 0.1^2 & \cdots & 0 \\ \vdots & \vdots & \ddots & \vdots \\ 0 & 0 & \cdots & 0.1^2 \end{bmatrix}$$

we obtain the variance of unit weight as

$$\hat{\sigma}_0^2 = 254.04$$

Such a large $\hat{\sigma}_0^2$ is primarily due to mismodeling and fitting a line to data with seasonal variation. With this $\hat{\sigma}_0^2$ the covariance matrix will be updated

$$\hat{\boldsymbol{Q}}_{\hat{x}} = \hat{\sigma}_0^2 (\boldsymbol{A}^\top \Sigma_y^{-1} \boldsymbol{A})^{-1} = \begin{bmatrix} 5.16 \times 10^{-4} & -3.94 \times 10^{-8} \\ -3.94 \times 10^{-8} & 4.01 \times 10^{-12} \end{bmatrix} \mathrm{m}^2$$

which leads to

$$\hat{y}_{2090} = 1264.975 \pm 0.072$$

and unlike the results without considering the variance of unit weight on page 30, the estimate with an uncertainty 7 cm leads to a probability of 63% that Lake Urmia will disappear in 2090:

$$\mathcal{N}(1265 | 1274.975, 0.072) = 63\%\,.$$

2.3.1 Case 1: Known variance of unit weight

To bring the variance of unit weight into a Bayesian context, consider a parametric model:

$$\boldsymbol{y} = \boldsymbol{A}\boldsymbol{x} + \boldsymbol{e}\,.$$

Assume that our inference of dispersion for the prior and the likelihood function is well-established, and we know the variance factor σ^2:

$$\mathsf{D}(\boldsymbol{y}) = \sigma^2\boldsymbol{\Sigma}_y\,,$$

with the likelihood function given by:

$$\mathsf{P}(\boldsymbol{y}|\boldsymbol{x}, \sigma^{-2}\boldsymbol{\Sigma}_y) \sim \mathcal{N}(\boldsymbol{A}\boldsymbol{x}, \sigma^2\boldsymbol{\Sigma}_y)\,.$$

The prior distribution is:

$$\boldsymbol{x} \sim \mathcal{N}(\boldsymbol{\mu}_0, \sigma^2\boldsymbol{\Sigma}_x)\,.$$

The posterior distribution, which also follows a normal distribution, takes the form:

$$\mathsf{P}(\boldsymbol{x}|\boldsymbol{y}) \sim \mathcal{N}(\boldsymbol{\mu}, \sigma^2(\boldsymbol{A}^\top\boldsymbol{\Sigma}_y^{-1}\boldsymbol{A} + \boldsymbol{\Sigma}_x^{-1})^{-1})\,,$$

with the Maximum A Posteriori (MAP) estimate of $\boldsymbol{x}$:

$$\hat{\boldsymbol{x}}_{\mathrm{MAP}} = (\boldsymbol{A}^\top\boldsymbol{\Sigma}_y^{-1}\boldsymbol{A} + \boldsymbol{\Sigma}_x^{-1})^{-1}(\boldsymbol{A}^\top\boldsymbol{\Sigma}_y^{-1}\boldsymbol{y} + \boldsymbol{\Sigma}_x^{-1}\boldsymbol{\mu})\,, \tag{2.28}$$

with the dispersion being:

$$\mathsf{D}(\boldsymbol{x}|\boldsymbol{y}) = \boldsymbol{Q}_{\hat{\boldsymbol{x}}_{\mathrm{MAP}}} = \sigma^2(\boldsymbol{A}^\top\boldsymbol{\Sigma}_y^{-1}\boldsymbol{A} + \boldsymbol{\Sigma}_x^{-1})^{-1}\,.$$

Like the least squares adjustment, the variance factor σ^2 does not affect the estimation itself but influences its uncertainty.

2.3.2 Case 2: Unknown variance of unit weight

Let the variance factor σ^2 be a random variable and unknown. To obtain a conjugate prior for our unknown parameters $\boldsymbol{x}$ and σ^2, we first define τ as the reciprocal of σ^2:

$$\tau = \frac{1}{\sigma^2}\,. \tag{2.29}$$

We assume an a priori expected value for σ^2 as follows:

$$\mathsf{E}(\sigma^2) = \sigma_p^2\,. \tag{2.30}$$

Given τ, we consider the prior distribution of $\boldsymbol{x}$ under the condition that a value for τ is known. The prior distribution for $\boldsymbol{x}$, with mean $\boldsymbol{\mu}$ and covariance $\tau^{-1}\boldsymbol{V}$, follows a normal distribution:

$$\mathsf{P}(\boldsymbol{x}|\boldsymbol{\mu}, \tau\boldsymbol{V}^{-1}) = \mathcal{N}(\boldsymbol{\mu}, \tau^{-1}\boldsymbol{V})\,. \tag{2.31}$$

Next, we assume that τ itself is Gamma distributed, denoted as $\tau \sim \mathsf{G}(b,p)$, where b is the shape parameter and p is an inverse scale parameter (Koch, 2007). Thus, the joint density function $\mathsf{P}(\boldsymbol{x},\tau|\boldsymbol{\mu},\boldsymbol{V}^{-1},b,p)$ for $\boldsymbol{x}$ and τ follows a Normal-Gamma distribution:

$$\mathsf{P}(\boldsymbol{x},\tau|\boldsymbol{\mu},\boldsymbol{V}^{-1},b,p) = \mathsf{P}(\boldsymbol{x}|\boldsymbol{\mu},\tau^{-1}\boldsymbol{V})\mathsf{P}(\tau|b,p) = \mathsf{NG}(\boldsymbol{\mu},\boldsymbol{V},b,p)\,. \tag{2.32}$$

This joint density function can be explicitly written as:

$$\begin{aligned}\mathsf{P}(\boldsymbol{x},\tau|\boldsymbol{\mu},\boldsymbol{V}^{-1},b,p) =& (2\pi)^{-n/2}(\det \boldsymbol{V})^{-1/2} b^p (\Gamma(p))^{-1} \\ & \tau^{n/2+p-1}\exp\left\{-\frac{\tau}{2}\left[2b+(\boldsymbol{x}-\boldsymbol{\mu})^{\mathrm{T}}\boldsymbol{V}^{-1}(\boldsymbol{x}-\boldsymbol{\mu})\right]\right\},\end{aligned} \tag{2.33}$$

for $b>0$, $p>0$, $0<\tau<\infty$, and $-\infty<x_i<\infty$. Furthermore, if $\boldsymbol{x}$ and τ have a Normal-Gamma distribution, then $\boldsymbol{x}$ has a marginal distribution of a multivariate t-distribution:

$$\mathsf{P}(\boldsymbol{x}) \sim t(\boldsymbol{\mu}, b\boldsymbol{V}/p, 2p)\,, \tag{2.34}$$

where the dispersion of $\boldsymbol{x}$ is determined by the scale matrix $\frac{b\boldsymbol{V}}{p}$, but because the multivariate t-distribution has heavier tails than the normal distribution, its actual covariance matrix (when it exists) is:

$$\mathsf{D}(\boldsymbol{x}) = \frac{2p}{2p-2}\cdot\frac{b\boldsymbol{V}}{p} = \frac{b\boldsymbol{V}}{p-1}, \quad \text{for } p>1\,. \tag{2.35}$$

On the other hand, the marginal distribution of τ is a Gamma distribution:

$$\mathsf{P}(\tau) \sim \mathsf{G}(b,p)\,. \tag{2.36}$$

The Gamma distribution can be expressed as:

$$\mathsf{P}(\tau|b,p) = \mathsf{G}(b,p) = \frac{b^p}{\Gamma(p)}\tau^{p-1}e^{-b\tau}\,, \tag{2.37}$$

with the Gamma function $\Gamma(p)$ defined for integer p as:

$$\Gamma(p) = (p-1)!\ \ p\in\mathcal{N}\,, \tag{2.38}$$

and for half-integer values as:

$$\Gamma(p+\frac{1}{2}) = \frac{(2p-1)(2p-3)\cdots 5\times 3\times 1}{2^p}\sqrt{\pi}\,. \tag{2.39}$$

The expected value and variance of τ are given by:

$$\mathsf{E}(\tau) = \frac{p}{b}, \qquad \mathrm{Var}(\tau) = \frac{p}{b^2}\,. \tag{2.40}$$

Prior distribution: Now with the setup defined above, for the prior distribution, we choose the Normal-Gamma distribution with $\boldsymbol{\mu}_0$ as the mean of the prior and $\boldsymbol{\Sigma}_{\boldsymbol{x}}$ as its uncertainty, together with the shape b_0 and the inverse scale p_0 for τ

$$\mathsf{P}(\boldsymbol{x},\tau) \sim \mathsf{NG}(\boldsymbol{\mu}_0, \boldsymbol{\Sigma}_{\boldsymbol{x}}, b_0, p_0)\,. \tag{2.41}$$

Following the property of the Normal-Gamma distribution, the marginal distribution of $\boldsymbol{x}$ follows the t-distribution

$$\boldsymbol{x} \sim t(\boldsymbol{\mu}_0, b_0\Sigma_x/p_0, 2p_0) \tag{2.42}$$

with $\mathsf{E}(\boldsymbol{x}) = \boldsymbol{\mu}_0$ and following Equation (2.35)

$$\mathrm{D}(\boldsymbol{x}) = \frac{b_0}{p_0 - 1}\Sigma_x = \sigma_p^2\Sigma_x \,. \tag{2.43}$$

This implies:

$$\frac{b_0}{p_0 - 1} = \sigma_p^2 \quad \Rightarrow \quad b_0 = \sigma_p^2(p_0 - 1) \,. \tag{2.44}$$

On the other hand the prior marginal distribution of $\tau \sim \mathrm{G}(b_0, p_0)$, which implies an *inverse Gamma* prior on the variance $\sigma^2 \sim \mathrm{IG}(b_0, p_0)$.

with

$$\mathsf{E}(\sigma^2) = \frac{b_0}{p_0 - 1} = \sigma_p^2 \tag{2.45}$$

$$\mathrm{Var}(\sigma^2) = \frac{b_0^2}{(p_0 - 1)^2(p_0 - 2)} = V_{\sigma^2} \tag{2.46}$$

Substitute b_0 from Equation (2.44) in the above equation, we have:

$$V_{\sigma^2} = \frac{\left[\sigma_p^2(p_0 - 1)\right]^2}{(p_0 - 1)^2(p_0 - 2)} = \frac{(\sigma_p^2)^2}{p_0 - 2} \tag{2.47}$$

Solving for p_0:

$$p_0 = \frac{(\sigma_p^2)^2}{V_{\sigma^2}} + 2 \tag{2.48}$$

Substitute into b_0:

$$b_0 = \left(\frac{(\sigma_p^2)^2}{V_{\sigma^2}} + 1\right)\sigma_p^2 \tag{2.49}$$

Likelihood function: The above choice of prior, which combines a normal distribution for $\boldsymbol{x}$ with a Gamma distribution for τ, constitutes a conjugate prior that simplifies the derivation of the posterior when combined with a normally distributed likelihood:

$$\mathsf{P}(\boldsymbol{y}|\hat{\boldsymbol{y}}, \sigma^{-2}{\boldsymbol{\Sigma}_{\boldsymbol{y}}}^{-1}) = \frac{1}{(2\pi)^{m/2}(\det(\sigma^2\boldsymbol{\Sigma}_{\boldsymbol{y}}))^{1/2}} \exp\left\{-\frac{1}{2}(\boldsymbol{y} - \hat{\boldsymbol{y}})^{\mathrm{T}}\sigma^{-2}{\boldsymbol{\Sigma}_{\boldsymbol{y}}}^{-1}(\boldsymbol{y} - \hat{\boldsymbol{y}})\right\}, \tag{2.50}$$

where $\hat{\boldsymbol{y}} = \boldsymbol{A}\boldsymbol{\mu} = \boldsymbol{A}\hat{\boldsymbol{x}}_{\mathbf{MAP}}$. Using the property of the determinant, we can transform the likelihood as follows:

$$\begin{aligned}(\det(\sigma^2\boldsymbol{\Sigma}_{\boldsymbol{y}}))^{-1/2} &= (\det(\tau^{-1}\boldsymbol{\Sigma}_{\boldsymbol{y}}))^{-1/2} \\ &= (\det({\boldsymbol{\Sigma}_{\boldsymbol{y}}}^{-1}))^{1/2}\tau^{m/2},\end{aligned} \tag{2.51}$$

thus the likelihood becomes:

$$\mathsf{P}(\boldsymbol{y}|\boldsymbol{x},\tau) = (2\pi)^{-m/2}(\det(\boldsymbol{\Sigma_y}^{-1}))^{1/2}\tau^{m/2}\exp\left[-\frac{\tau}{2}(\boldsymbol{y}-\hat{\boldsymbol{y}})^{\mathrm{T}}\boldsymbol{\Sigma_y}^{-1}(\boldsymbol{y}-\hat{\boldsymbol{y}})\right]. \tag{2.52}$$

Posterior distribution: Since the prior is conjugate, the posterior distribution will also follow a Normal-Gamma distribution:

$$\mathsf{P}(\boldsymbol{x},\tau|\boldsymbol{y}) \sim \mathsf{NG}(\boldsymbol{\mu},\boldsymbol{\Lambda},b,p). \tag{2.53}$$

This posterior distribution is derived from the product of the prior and likelihood:

$$\begin{aligned} p(\boldsymbol{x},\tau|\boldsymbol{y}) &\propto \tau^{n/2+p_0-1}\exp\{-\frac{\tau}{2}[2b_0+(\boldsymbol{x}-\boldsymbol{\mu}_0)^{\mathrm{T}}\boldsymbol{\Lambda}^{-1}(\boldsymbol{x}-\boldsymbol{\mu}_0)]\} \\ &\quad \tau^{m/2}\exp\{-\frac{\tau}{2}(\boldsymbol{y}-\hat{\boldsymbol{y}})^{\mathrm{T}}\boldsymbol{\Sigma}_y^{-1}(\boldsymbol{y}-\hat{\boldsymbol{y}})\} \\ &\propto \tau^{m/2+n/2+p_0-1}\exp\{-\frac{\tau}{2}[2b_0+(\boldsymbol{x}-\boldsymbol{\mu}_0)^{\mathrm{T}}\boldsymbol{\Lambda}^{-1}(\boldsymbol{x}-\boldsymbol{\mu}_0) \\ &\quad +(\boldsymbol{y}-\hat{\boldsymbol{y}})^{\mathrm{T}}\boldsymbol{\Sigma}_y^{-1}(\boldsymbol{y}-\hat{\boldsymbol{y}})]\}. \end{aligned} \tag{2.54}$$

with

$$\boldsymbol{\mu} = \hat{\boldsymbol{x}}_{\mathbf{MAP}} = (\boldsymbol{A}^{\mathrm{T}}\boldsymbol{\Sigma_y}^{-1}\boldsymbol{A}+\boldsymbol{\Sigma_x}^{-1})^{-1}(\boldsymbol{A}^{\mathrm{T}}\boldsymbol{\Sigma_y}^{-1}\boldsymbol{y}+\boldsymbol{\Sigma_x}^{-1}\boldsymbol{\mu}_0), \tag{2.55}$$

and the covariance matrix with the a posteriori $\hat{\sigma}_{\mathrm{B}}$:

$$\boldsymbol{\Lambda} = \boldsymbol{Q}_{\hat{\boldsymbol{x}}_{\mathbf{MAP}}} = \hat{\sigma}_{\mathrm{B}}^2(\boldsymbol{A}^{\mathrm{T}}\boldsymbol{\Sigma_y}^{-1}\boldsymbol{A}+\boldsymbol{\Sigma_x}^{-1})^{-1}, \tag{2.56}$$

To obtain the *a posteriori* variance of unit weight $\hat{\sigma}_{\mathrm{B}}^2$, the parameters p and b in Equation (2.33) must be derived. By comparing Equation (2.54) with Equation (2.33), we find that $p = p_0 + m/2$, and consequently according to Equation (2.48):

$$p = \frac{m+2(\sigma_p^2)^2/V_{\sigma^2}+4}{2}. \tag{2.57}$$

Further by comparing equations (2.54) and (2.33), we can derive b as:

$$b = \frac{1}{2}\left\{2\left[\frac{(\sigma_p^2)^2}{V_{\sigma^2}}+1\right]\sigma_p^2+(\boldsymbol{x}-\boldsymbol{\mu}_0)^{\mathrm{T}}\boldsymbol{\Sigma_x}^{-1}(\boldsymbol{x}-\boldsymbol{\mu}_0)+(\boldsymbol{y}-\hat{\boldsymbol{y}})^{\mathrm{T}}\boldsymbol{\Sigma_y}^{-1}(\boldsymbol{y}-\hat{\boldsymbol{y}})\right\}. \tag{2.58}$$

As mentioned above, the posterior marginal distribution for $\boldsymbol{x}$ is the multivariate t-distribution:

$$\mathsf{P}(\boldsymbol{x}|\boldsymbol{y}) \sim t(\boldsymbol{\mu},\frac{b\boldsymbol{\Lambda}}{p},2p), \tag{2.59}$$

with the expected value vector:

$$\mathsf{E}(\boldsymbol{x}|\boldsymbol{y}) = \boldsymbol{\mu}. \tag{2.60}$$

The marginal posterior distribution of τ is a Gamma distribution:

$$\mathsf{P}(\tau|b,p) = \mathsf{G}(b,p). \tag{2.61}$$

Since $\sigma^2 = \tau^{-1}$, the posterior distribution of σ^2 is an Inverse Gamma distribution $\mathsf{P}(\sigma^2|\boldsymbol{y}) \sim \mathsf{IG}(b,p)$ with expectation of σ^2 as

$$\mathsf{E}(\sigma^2|\boldsymbol{y}) = \frac{b}{p-1}\,. \tag{2.62}$$

Using equations (2.57) and (2.58) , the expectation of σ^2 can be explicitly written as:

$$\begin{aligned}\mathsf{E}(\sigma^2|\boldsymbol{y}) = \hat{\sigma}_{\mathrm{B}}^2 = \left(m + 2\frac{(\sigma_p^2)^2}{V_{\sigma^2}} + 2\right)^{-1} \Bigg\{ 2\left[\frac{(\sigma_p^2)^2}{V_{\sigma^2}} + 1\right]\sigma_p^2 \\ + (\boldsymbol{\mu} - \boldsymbol{\mu}_0)^{\mathrm{T}} {\boldsymbol{\Sigma}_{\boldsymbol{x}}}^{-1} (\boldsymbol{\mu} - \boldsymbol{\mu}_0) + (\boldsymbol{y} - \hat{\boldsymbol{y}})^{\mathrm{T}} {\boldsymbol{\Sigma}_{\boldsymbol{y}}}^{-1} (\boldsymbol{y} - \hat{\boldsymbol{y}}) \Bigg\},\end{aligned} \tag{2.63}$$

with the variance:

$$\mathrm{Var}(\sigma^2|\boldsymbol{y}) = \frac{2(\hat{\sigma}_B^2)^2}{1 + 2\frac{(\sigma_p^2)^2}{V_{\sigma^2}}}\,. \tag{2.64}$$

Therefore, the updated covariance matrix is:

$$\hat{\boldsymbol{Q}}_{\hat{\boldsymbol{x}}_{\mathbf{MAP}}} = \hat{\sigma}_B^2 (\boldsymbol{A}^{\mathrm{T}} {\boldsymbol{\Sigma}_{\boldsymbol{y}}}^{-1} \boldsymbol{A} + {\boldsymbol{\Sigma}_{\boldsymbol{x}}}^{-1})^{-1}\,. \tag{2.65}$$

Prior

$$\mathsf{P}(\boldsymbol{x}|\sigma_p^{-2} {\boldsymbol{\Sigma}_{\boldsymbol{x}}}^{-1}) = \mathcal{N}(\boldsymbol{\mu}_0, \sigma_p^2 \boldsymbol{\Sigma}_{\boldsymbol{x}}) \tag{2.66}$$

Likelihood

$$\mathsf{P}(\boldsymbol{y}|\boldsymbol{x}, \sigma_p^{-2} {\boldsymbol{\Sigma}_{\boldsymbol{y}}}^{-1}) = \mathcal{N}(\hat{\boldsymbol{y}}, \sigma_p^2 \boldsymbol{\Sigma}_{\boldsymbol{y}}) \tag{2.67}$$

Posterior

$$\mathsf{P}(\boldsymbol{x}|\boldsymbol{y}, \hat{\sigma}_{\mathrm{B}}^{-2} {\boldsymbol{\Sigma}_{\boldsymbol{x}}}^{-1}, \hat{\sigma}_{\mathrm{B}}^{-2} {\boldsymbol{\Sigma}_{\boldsymbol{y}}}^{-1}) \sim \mathcal{N}(\boldsymbol{\mu}, \boldsymbol{\Lambda}) \tag{2.68}$$

$$\hat{\boldsymbol{x}}_{\mathbf{MAP}} = \boldsymbol{\mu} = (\boldsymbol{A}^{\mathrm{T}} {\boldsymbol{\Sigma}_{\boldsymbol{y}}}^{-1} \boldsymbol{A} + {\boldsymbol{\Sigma}_{\boldsymbol{x}}}^{-1})^{-1} (\boldsymbol{A}^{\mathrm{T}} {\boldsymbol{\Sigma}_{\boldsymbol{y}}}^{-1} \boldsymbol{y} + {\boldsymbol{\Sigma}_{\boldsymbol{x}}}^{-1} \boldsymbol{\mu}_0) \tag{2.69}$$

$$\hat{\boldsymbol{Q}}_{\hat{\boldsymbol{x}}_{\mathbf{MAP}}} = \hat{\sigma}_{\mathrm{B}}^2 (\boldsymbol{A}^{\mathrm{T}} {\boldsymbol{\Sigma}_{\boldsymbol{y}}}^{-1} \boldsymbol{A} + {\boldsymbol{\Sigma}_{\boldsymbol{x}}}^{-1})^{-1} \tag{2.70}$$

$$\begin{aligned}\hat{\sigma}_{\mathrm{B}}^2 = \left(m + 2\frac{(\sigma_p^2)^2}{V_{\sigma^2}} + 2\right)^{-1} \Bigg\{ 2\left[\frac{(\sigma_p^2)^2}{V_{\sigma^2}} + 1\right]\sigma_p^2 \\ + (\boldsymbol{\mu} - \boldsymbol{\mu}_0)^{\mathrm{T}} {\boldsymbol{\Sigma}_{\boldsymbol{x}}}^{-1} (\boldsymbol{\mu} - \boldsymbol{\mu}_0) + (\boldsymbol{y} - \hat{\boldsymbol{y}})^{\mathrm{T}} {\boldsymbol{\Sigma}_{\boldsymbol{y}}}^{-1} (\boldsymbol{y} - \hat{\boldsymbol{y}}) \Bigg\}\end{aligned} \tag{2.71}$$

For the Lake Urmia example, with Σ_y, $\boldsymbol{\mu}$, and Σ_x defined on page 34, assuming $\sigma_p^2 = 1$ and $V_{\sigma^2} = 0.01$, according to Equation (2.3.2), $\hat{\sigma}_{\mathrm{B}}^2$ will be 230.64, which is comparable to $\hat{\sigma}_0^2 = 254.04$ on page 35. The difference, however, is that in this case, the prior values $\boldsymbol{\mu}$ and their uncertainty Σ_x, together with the variance considered for the a priori factor V_{σ^2}, also play a role and will be gauged.
With $\hat{\sigma}_{\mathrm{B}}^2$ the covariance is then will be

$$\hat{\boldsymbol{Q}}_{\hat{\boldsymbol{x}}_{\mathbf{MAP}}} = \begin{bmatrix} 4.68 \times 10^{-4}\,\mathrm{m}^2 & -1.31 \times 10^{-5}\,\mathrm{m}^2/\mathrm{yr} \\ -1.31 \times 10^{-5}\,\mathrm{m}^2/\mathrm{yr} & 4.8 \times 10^{-7}\,\mathrm{m}^2/\mathrm{yr}^2 \end{bmatrix}$$

Extending the estimated trend to 2090, we obtain:

$$\hat{y}_{2090} = 1264.975 \pm 0.068$$

leading to a prediction of 64% probability that Lake Urmia will reach its lowest water level of 1265 m in 2090:

$$\mathcal{N}(1265|1264.97, 0.068) = 64\%$$

Comparing the results with those on page 34, where a 99% probability of the lake disappearing by 2090 was obtained, the inclusion of the variance of unit weight leads to an uncertainty estimate of approximately 7 cm, which results in a probability of 64% that Lake Urmia will disappear by 2090.

The main benefit of $\hat{\sigma}_{\mathrm{B}}^2$ would be observed in cases where the prior and the likelihood deviate significantly from each other, as in the example on page 32, where the prior values of a and b are defined as 0. In this case, $\hat{\sigma}_{\mathrm{B}}^2 = 7758.15$, leading to:

$$\hat{\boldsymbol{Q}}_{\hat{\boldsymbol{x}}_{\mathbf{MAP}}} = \begin{bmatrix} 0.015\,\mathrm{m}^2 & -1.20 \times 10^{-6}\,\mathrm{m}^2/\mathrm{yr} \\ -1.20 \times 10^{-6}\,\mathrm{m}^2/\mathrm{yr} & 1.22 \times 10^{-10}\,\mathrm{m}^2/\mathrm{yr}^2 \end{bmatrix}$$

making the posterior as shown below, which represents a realistic estimate given such an inaccurate prior. To better understand the effect, compare the posterior below with the one on page 32.

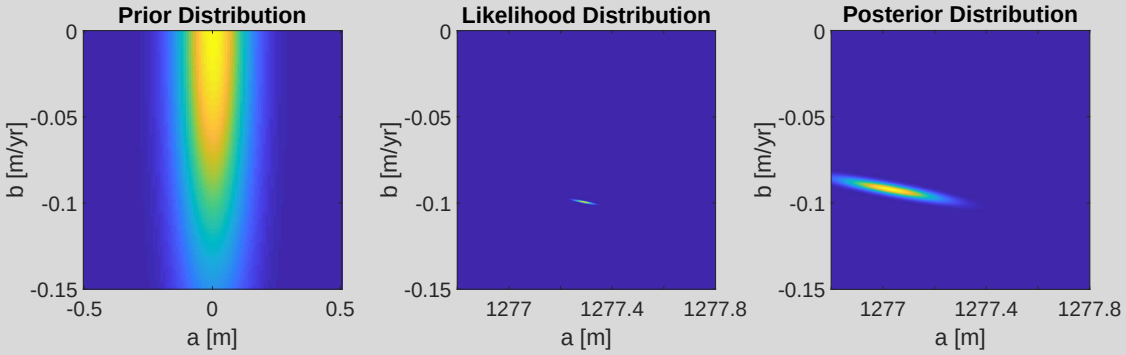

$$\hat{y}_{2090} = 1265.613 \pm 0.39$$

leading to a prediction of 6% probability that Lake Urmia will reach its lowest water level of 1265 m in 2090:

$$\mathcal{N}(1265|1265.613, 0.39) = 6\%$$

2.4 Dynamic system within Bayesian inference

In the discussion in Section 2.2, the unknown parameters of the linear models are assumed to remain constant over time. We will now introduce parameters for dynamical systems, which vary with time. Building on the formulation derived in the previous section, we will explore how the Bayesian framework, specifically the derivation of the MAP solution, can be applied to a dynamic system.

Let us consider that $\boldsymbol{x}_t$ is the $n \times 1$ random vector of unknown parameters at time t. A matrix $\boldsymbol{\Phi}_{n\times n}$ is the transition matrix from $t \to t+1$:

$$\boldsymbol{x}_{t+1} = \boldsymbol{\Phi}\boldsymbol{x}_t\,.$$

Now, let us add a random vector $\boldsymbol{e}_t$ of size $n \times 1$ as disturbances. $\boldsymbol{e}_t$ is independent of $\boldsymbol{x}_t$:

$$\boldsymbol{x}_{t+1} = \boldsymbol{\Phi}\boldsymbol{x}_t + \boldsymbol{e}_t\,.$$

Let $\mathsf{E}(\boldsymbol{e}_t) = 0$ and $\mathsf{D}(\boldsymbol{e}_t) = \boldsymbol{Q}_t$, where $\boldsymbol{Q}_t$ is the covariance matrix of size $n \times n$. Let us assume $\boldsymbol{Q}_t$ is known. If N different moments are considered, the linear dynamic system is:

$$\boldsymbol{x}_{t+1} = \boldsymbol{\Phi}(t+1,t)\boldsymbol{x}_t + \boldsymbol{e}_t\,,$$

with $\mathsf{E}(\boldsymbol{e}_t) = 0$ and $\mathsf{D}(\boldsymbol{e}_t) = \boldsymbol{Q}_t$, for $t \in \{1,\ldots,N-1\}$. Now, we bring the observations $\boldsymbol{y}_t$ that contain information on the unknown state vectors. The relations between m observations of $\boldsymbol{y}_t$ and $\boldsymbol{x}_t$ are given by:

$$\boldsymbol{y}_t = \boldsymbol{H}_t\boldsymbol{x}_t + \boldsymbol{v}_t\,,$$

where $\boldsymbol{v}_t$ is the observation noise, which is normally distributed:

$$\boldsymbol{v}_t \sim \mathcal{N}(0, \sigma^2\boldsymbol{\Sigma}_y)\,,$$

and $\boldsymbol{H}_t$ is a matrix of size $m \times n$ with:

$$\boldsymbol{H}_t\boldsymbol{x}_t = \mathsf{E}(\boldsymbol{y}_t|\boldsymbol{x}_t)\,.$$

$\boldsymbol{y}_t$ is the vector of observations of size $m \times 1$, and $\boldsymbol{\Sigma}_y$ is the positive definite covariance matrix of observations of size $m \times m$.

Now, let $\boldsymbol{e}_t$ and $\boldsymbol{y}_t$ be independent and normally distributed:

$$\boldsymbol{e}_t \sim \mathcal{N}(0, \boldsymbol{Q}_t)\,,$$

and the likelihood function being

$$\mathsf{P}(\boldsymbol{y}_t|\boldsymbol{x}_t) \sim \mathcal{N}(\boldsymbol{H}_t\boldsymbol{x}_t, \sigma^2\boldsymbol{\Sigma}_y)\,.$$

Based on this likelihood function and following Bayesian inference discussed in Section 2.2, the posterior density function of the unknown random vector $\boldsymbol{x}_t$ shall be determined. Since we are dealing with a dynamic scenario, the prior information at epoch t can be defined as the posterior distribution at epoch $t-1$ denoted as $\hat{\boldsymbol{x}}_{t,t-1}$.

Within such a formulation, the Bayes theorem can be applied recursively. Since the prior is normally distributed and the likelihood is also normally distributed, the posterior is also normally distributed. In general, we can write the prior density function as:

$$\mathsf{P}(\boldsymbol{x}_t|\boldsymbol{y}_1,\ldots,\boldsymbol{y}_{t-1}) \sim \mathcal{N}(\hat{\boldsymbol{x}}_{t,t-1}, \sigma^2\boldsymbol{\Sigma}_{\boldsymbol{x}_{t,t-1}})$$

which leads to a posterior:

$$\mathsf{P}(\boldsymbol{x}_t|\boldsymbol{y}_1,\ldots,\boldsymbol{y}_t) \sim \mathcal{N}(\boldsymbol{\mu},\sigma^2\boldsymbol{\Lambda})\,.$$

Following Equation (2.26), given the defined prior and likelihood, the MAP solution will be

$$\boldsymbol{\mu} = (\boldsymbol{H}_t^\top \boldsymbol{\Sigma}_{\boldsymbol{y}_t}^{-1}\boldsymbol{H}_t + \boldsymbol{\Sigma}_{\boldsymbol{x}_{t,t-1}}^{-1})^{-1}(\boldsymbol{H}_t^\top \boldsymbol{\Sigma}_{\boldsymbol{y}_t}^{-1}\boldsymbol{y}_t + \boldsymbol{\Sigma}_{\boldsymbol{x}_{t,t-1}}^{-1}\hat{\boldsymbol{x}}_{t,t-1})$$

and according to Equation (2.27)

$$\boldsymbol{\Lambda} = (\boldsymbol{H}_t^\top \boldsymbol{\Sigma}_{\boldsymbol{y}_t}^{-1}\boldsymbol{H}_t + \boldsymbol{\Sigma}_{\boldsymbol{x}_{t,t-1}}^{-1})^{-1}$$

Therefore, we can write

$$\hat{\boldsymbol{x}}_{t,t} = (\boldsymbol{H}_t^\top \boldsymbol{\Sigma}_{\boldsymbol{y}_t}^{-1}\boldsymbol{H}_t + \boldsymbol{\Sigma}_{\boldsymbol{x}_{t,t-1}}^{-1})^{-1}(\boldsymbol{H}_t^\top \boldsymbol{\Sigma}_{\boldsymbol{y}_t}^{-1}\boldsymbol{y}_t + \boldsymbol{\Sigma}_{\boldsymbol{x}_{t,t-1}}^{-1}\hat{\boldsymbol{x}}_{t,t-1}) \tag{2.72}$$

and

$$\mathsf{D}(\boldsymbol{x}_t|\boldsymbol{y}_1,\ldots,\boldsymbol{y}_t) = \sigma^2\boldsymbol{\Sigma}_{\boldsymbol{x}_{t,t}}$$

where

$$\boldsymbol{\Sigma}_{\boldsymbol{x}_{t,t}} = (\boldsymbol{H}_t^\top \boldsymbol{\Sigma}_{\boldsymbol{y}_t}\boldsymbol{H}_t + \boldsymbol{\Sigma}_{\boldsymbol{x}_{t,t-1}})^{-1}\,.$$

The above formulation can be simplified by using the identities:

$$(A - BD^{-1}C)^{-1} = A^{-1} + A^{-1}B(D - CA^{-1}B)^{-1}CA^{-1}$$

$$D^{-1}C(A - BD^{-1}C)^{-1} = (D - CA^{-1}B)^{-1}CA^{-1}$$

which allows us to write

$$(\boldsymbol{H}^\top \boldsymbol{\Sigma}_{\boldsymbol{y}}^{-1}\boldsymbol{H} + \boldsymbol{\Sigma}_{\boldsymbol{x}}^{-1})^{-1} = \boldsymbol{\Sigma}_{\boldsymbol{x}} - \boldsymbol{\Sigma}_{\boldsymbol{x}}\boldsymbol{H}^\top(\boldsymbol{H}\boldsymbol{\Sigma}_{\boldsymbol{x}}\boldsymbol{H}^\top + \boldsymbol{\Sigma}_{\boldsymbol{y}})^{-1}\boldsymbol{H}\boldsymbol{\Sigma}_{\boldsymbol{x}}$$

$$(\boldsymbol{H}^\top \boldsymbol{\Sigma}_{\boldsymbol{y}}^{-1}\boldsymbol{H} + \boldsymbol{\Sigma}_{\boldsymbol{x}}^{-1})^{-1}\boldsymbol{H}^\top\boldsymbol{\Sigma}_{\boldsymbol{y}} = \boldsymbol{\Sigma}_{\boldsymbol{x}}\boldsymbol{H}^\top(\boldsymbol{H}\boldsymbol{\Sigma}_{\boldsymbol{x}}\boldsymbol{H}^\top + \boldsymbol{\Sigma}_{\boldsymbol{y}})^{-1}\,.$$

By replacing them into (2.72), we have:

$$\begin{aligned}\hat{\boldsymbol{x}}_{t,t} &= (\boldsymbol{H}_t^\top \boldsymbol{\Sigma}_{\boldsymbol{y}_t}^{-1}\boldsymbol{H}_t + \boldsymbol{\Sigma}_{\boldsymbol{x}_{t,t-1}}^{-1})^{-1}\boldsymbol{H}_t^\top \boldsymbol{\Sigma}_{\boldsymbol{y}_t}^{-1}\boldsymbol{y}_t + (\boldsymbol{H}_t^\top \boldsymbol{\Sigma}_{\boldsymbol{y}_t}^{-1}\boldsymbol{H}_t + \boldsymbol{\Sigma}_{\boldsymbol{x}_{t,t-1}}^{-1})^{-1}\boldsymbol{\Sigma}_{\boldsymbol{x}_{t,t-1}}^{-1}\hat{\boldsymbol{x}}_{t,t-1} \\ &= \boldsymbol{\Sigma}_{\boldsymbol{x}_{t,t-1}}\boldsymbol{H}_t^\top(\boldsymbol{H}_t\boldsymbol{\Sigma}_{\boldsymbol{x}_{t,t-1}}\boldsymbol{H}_t^\top + \boldsymbol{\Sigma}_{\boldsymbol{y}_t})^{-1}\boldsymbol{y}_t + (\boldsymbol{H}_t^\top \boldsymbol{\Sigma}_{\boldsymbol{y}_t}^{-1}\boldsymbol{H}_t + \boldsymbol{\Sigma}_{\boldsymbol{x}_{t,t-1}}^{-1})^{-1}\boldsymbol{\Sigma}_{\boldsymbol{x}_{t,t-1}}^{-1}\hat{\boldsymbol{x}}_{t,t-1}\,.\end{aligned}$$

With

$$J = \boldsymbol{\Sigma}_{\boldsymbol{x}_{t,t-1}}\boldsymbol{H}_t^\top(\boldsymbol{H}_t\boldsymbol{\Sigma}_{\boldsymbol{x}_{t,t-1}}\boldsymbol{H}_t^\top + \boldsymbol{\Sigma}_{\boldsymbol{y}_t})^{-1}\boldsymbol{y}_t\,,$$

we have

$$\begin{aligned}\hat{\boldsymbol{x}}_{t,t} &= J + \hat{\boldsymbol{x}}_{t,t-1} - \boldsymbol{\Sigma}_{\boldsymbol{x}_{t,t-1}}\boldsymbol{H}_t^\top(\boldsymbol{H}_t\boldsymbol{\Sigma}_{\boldsymbol{x}_{t,t-1}}\boldsymbol{H}_t^\top + \boldsymbol{\Sigma}_{\boldsymbol{y}_t})^{-1}\boldsymbol{H}_t\boldsymbol{\Sigma}_{\boldsymbol{x}_{t,t-1}}\boldsymbol{\Sigma}_{\boldsymbol{x}_{t,t-1}}^{-1}\hat{\boldsymbol{x}}_{t,t-1} \\ &= \hat{\boldsymbol{x}}_{t,t-1} + \boldsymbol{\Sigma}_{\boldsymbol{x}_{t,t-1}}\boldsymbol{H}_t^\top(\boldsymbol{H}_t\boldsymbol{\Sigma}_{\boldsymbol{x}_{t,t-1}}\boldsymbol{H}_t^\top + \boldsymbol{\Sigma}_{\boldsymbol{y}_t})^{-1}(\boldsymbol{y}_t - \boldsymbol{H}_t\hat{\boldsymbol{x}}_{t,t-1})\,.\end{aligned}$$

Finally, we can write

$$\hat{\boldsymbol{x}}_{t,t} = \hat{\boldsymbol{x}}_{t,t-1} + \boldsymbol{F}_t(\boldsymbol{y}_t - \boldsymbol{H}_t\hat{\boldsymbol{x}}_{t,t-1})\,,$$

where

$$\boldsymbol{F}_t = \boldsymbol{\Sigma}_{\boldsymbol{x}_{t,t-1}}\boldsymbol{H}_t^\top(\boldsymbol{H}_t\boldsymbol{\Sigma}_{\boldsymbol{x}_{t,t-1}}\boldsymbol{H}_t^\top + \boldsymbol{\Sigma}_{\boldsymbol{y}_t})^{-1}\,,$$

and

$$\boldsymbol{\Sigma}_{\boldsymbol{x}_{t,t}} = (\boldsymbol{I} - \boldsymbol{F}_t\boldsymbol{H}_t)\boldsymbol{\Sigma}_{\boldsymbol{x}_{t,t-1}}\,. \tag{2.73}$$

Thus, the estimation of $\hat{\boldsymbol{x}}_{t,t}$ and $\boldsymbol{\Sigma}_{\boldsymbol{x}_{t,t}}$ is recursively computed from $\hat{\boldsymbol{x}}_{t,t-1}$ and $\boldsymbol{\Sigma}_{\boldsymbol{x}_{t,t-1}}$. In fact, with such a setup, the prior is always obtained from the previous posterior:

$$\mathsf{P}(\boldsymbol{x}_{t-1}|\boldsymbol{y}_1,\ldots,\boldsymbol{y}_{t-1}) \sim \mathcal{N}(\hat{\boldsymbol{x}}_{t-1,t-1}, \boldsymbol{\Sigma}_{\boldsymbol{x}_{t-1,t-1}}),$$

and by the linear dynamic system, the state vector $\boldsymbol{x}_{t-1}$ is transformed to $\boldsymbol{x}_t$. The prior distribution for $\boldsymbol{x}_t$ can therefore be obtained since $\boldsymbol{x}_{t-1}$ and $\boldsymbol{e}_{t-1}$ are independent.

$$\mathsf{P}(\boldsymbol{x}_t|\boldsymbol{y}_1,\ldots,\boldsymbol{y}_{t-1}) \sim \mathcal{N}(\hat{\boldsymbol{x}}_{t,t-1}, \boldsymbol{\Sigma}_{\boldsymbol{x}_{t,t-1}}),$$

with

$$\hat{\boldsymbol{x}}_{t,t-1} = \boldsymbol{\Phi}_{t,t-1}\hat{\boldsymbol{x}}_{t-1,t-1},$$

and

$$\sigma^2\boldsymbol{\Sigma}_{\boldsymbol{x}_{t,t-1}} = \sigma^2\boldsymbol{\Phi}_{t,t-1}\boldsymbol{\Sigma}_{\boldsymbol{x}_{t-1,t-1}}\boldsymbol{\Phi}_{t,t-1}^\top + \boldsymbol{Q}_{t-1},$$

and finally obtaining $\hat{\sigma}_t^2\boldsymbol{\Sigma}_{\boldsymbol{x}_{t,t}}$ using Equation (2.73), where $\hat{\sigma}_t^2$ is obatained based equations (2.63) and (2.64) as

$$\begin{aligned}\hat{\sigma}_t^2 = \left(m + 2\frac{(\hat{\sigma}_{t-1}^2)^2}{v_{\hat{\sigma}_{t-1}^2}} + 2\right)^{-1} \Bigg\{ 2\left[\frac{(\hat{\sigma}_{t-1}^2)^2}{v_{\hat{\sigma}_{t-1}^2}} + 1\right]\hat{\sigma}_{t-1}^2 + (\hat{\boldsymbol{x}}_{t,t} - \hat{\boldsymbol{x}}_{t,t-1})^\top \boldsymbol{\Sigma}_{\boldsymbol{x}_{t,t}}^{-1}(\hat{\boldsymbol{x}}_{t,t} - \hat{\boldsymbol{x}}_{t,t-1}) \\ + (\hat{\boldsymbol{y}}_t - \boldsymbol{H}_t\hat{\boldsymbol{x}}_{t,t})^\top \boldsymbol{\Sigma}_{\boldsymbol{y}_t}^{-1}(\hat{\boldsymbol{y}}_t - \boldsymbol{H}_t\hat{\boldsymbol{x}}_{t,t}) \Bigg\},\end{aligned}$$

$$v_{\hat{\sigma}_t^2} = \frac{2(\hat{\sigma}_t^2)^2}{m + 2(\hat{\sigma}_{t-1}^2)^2 / v_{\hat{\sigma}_{t-1}^2}}. \tag{2.74}$$

The linear state-space representation is:

$$\begin{cases} \boldsymbol{x}_t = \boldsymbol{\Phi}\boldsymbol{x}_{t-1} + \boldsymbol{e}_t \\ \boldsymbol{y}_t = \boldsymbol{H}_t\boldsymbol{x}_t + \boldsymbol{v}_t \end{cases} \tag{2.75}$$

with

$$\mathsf{D}(\boldsymbol{e}_t) = \boldsymbol{Q}_t$$

$$\mathsf{D}(\boldsymbol{v}_t) = \sigma^2\boldsymbol{\Sigma}_{\boldsymbol{y}_t} \quad (\sigma_{p_1}^2 = 1)$$

$$\mathsf{E}(\boldsymbol{e}_t\boldsymbol{v}_t^\top) = 0$$

Prediction Step

$$\hat{\boldsymbol{x}}_{t,t-1} = \boldsymbol{\Phi}_{t,t-1}\hat{\boldsymbol{x}}_{t-1,t-1} \tag{2.76}$$

$$\sigma^2\boldsymbol{\Sigma}_{\boldsymbol{x}_{t,t-1}} = \sigma^2\boldsymbol{\Phi}_{t,t-1}\boldsymbol{\Sigma}_{\boldsymbol{x}_{t-1,t-1}}\boldsymbol{\Phi}_{t,t-1}^\top + \boldsymbol{Q}_{t-1} \tag{2.77}$$

For the initial state, we can assume $\boldsymbol{\Sigma}_{\boldsymbol{x}_{0,0}}$ as the identity matrix.

Estimation Step

$$\hat{\boldsymbol{x}}_{t,t} = \hat{\boldsymbol{x}}_{t,t-1} + \boldsymbol{F}_t(\boldsymbol{y}_t - \boldsymbol{H}_t\hat{\boldsymbol{x}}_{t,t-1}) \tag{2.78}$$

$$\boldsymbol{F}_t = \boldsymbol{\Sigma}_{\boldsymbol{x}_{t,t-1}}\boldsymbol{H}_t^\top(\boldsymbol{H}_t\boldsymbol{\Sigma}_{\boldsymbol{x}_{t,t-1}}\boldsymbol{H}_t^\top + \boldsymbol{\Sigma}_{\boldsymbol{y}_t})^{-1} \tag{2.79}$$

$$\boldsymbol{\Sigma}_{\boldsymbol{x}_{t,t}} = (\boldsymbol{I} - \boldsymbol{F}_t\boldsymbol{H}_t)\boldsymbol{\Sigma}_{\boldsymbol{x}_{t,t-1}} \tag{2.80}$$

with

$$\mathsf{D}(\boldsymbol{x}_t|\boldsymbol{y}_1,\ldots,\boldsymbol{y}_t) = \hat{\sigma}_t^2\boldsymbol{\Sigma}_{\boldsymbol{x}_{t,t}}$$

$$\hat{\sigma}_t^2 = \left(m + 2\frac{(\hat{\sigma}_{t-1}^2)^2}{v_{\hat{\sigma}_{t-1}^2}} + 2 \right)^{-1} \left\{ 2 \left[\frac{(\hat{\sigma}_{t-1}^2)^2}{v_{\hat{\sigma}_{t-1}^2}} + 1 \right] \hat{\sigma}_{t-1}^2 + (\hat{\boldsymbol{x}}_{t,t} - \hat{\boldsymbol{x}}_{t,t-1})^\top \boldsymbol{\Sigma}_{\boldsymbol{x}_{t,t}}^{-1} (\hat{\boldsymbol{x}}_{t,t} - \hat{\boldsymbol{x}}_{t,t-1}) \right.$$
$$\left. + (\hat{\boldsymbol{y}}_t - \boldsymbol{H}_t \hat{\boldsymbol{x}}_{t,t})^\top \boldsymbol{\Sigma}_{\boldsymbol{y}_t}^{-1} (\hat{\boldsymbol{y}}_t - \boldsymbol{H}_t \hat{\boldsymbol{x}}_{t,t}) \right\}$$
$$v_{\hat{\sigma}_t^2} = \frac{2(\hat{\sigma}_t^2)^2}{m + 2(\hat{\sigma}_{t-1}^2)^2 / v_{\hat{\sigma}_{t-1}^2}} \tag{2.81}$$

The MAP solution we derived above is known as the Kalman filter, a recursive algorithm that provides efficient solutions to linear estimation problems (Kalman, 1960; Welch and Bishop, 1995; Koch, 2007). The Kalman filter has been widely applied across various disciplines, including engineering, economics, and environmental sciences. Within hydrogeodetic studies, the Kalman filter is particularly valuable for its ability to assimilate real-time data and update predictions of dynamic systems. It is frequently employed in the monitoring and forecasting of hydrological variables, such as groundwater levels, streamflows, and precipitation patterns (Ghil and Malanotte-Rizzoli, 1991).

For systems with non-linear models, the linearized version of the Kalman filter, namely the Extended Kalman Filter (EKF), offers a potential solution. However, while EKF is computationally efficient, it may introduce errors due to the linearization required to handle non-linear dynamics, particularly in systems with pronounced non-linearity (Brown and Hwang, 1997). To address the limitations of EKF, the Ensemble Kalman Filter (EnKF) has emerged as a widely adopted alternative, particularly in hydrogeodetic studies. Unlike EKF, EnKF uses a Monte Carlo-based approach to represent the probability distribution of the system state through an ensemble of model simulations. This ensemble-based methodology avoids the need for linearization, making it better suited for systems with complex, non-linear dynamics. Additionally, EnKF inherently provides uncertainty estimates by analyzing the spread of the ensemble, offering valuable insights into the reliability of the predictions (Evensen, 2003).

In addition to EnKF, alternative approaches such as the Unscented Kalman Filter (UKF) and Cubature Kalman Filter (CKF) have been developed to address the limitations of linearization inherent in the Extended Kalman Filter. The UKF uses a deterministic sampling technique, known as the unscented transform, to approximate the mean and covariance of the system state. By selecting a set of carefully chosen points (sigma points) around the current state estimate, the UKF captures the effects of non-linear transformations more accurately than the EKF without requiring explicit linearization (Wan and Van Der Merwe, 2000). Similarly, the Cubature Kalman Filter (CKF) offers an alternative approach for handling nonlinear systems. It is based on cubature rules for numerical integration, which provide a third-order accurate approximation of the mean and covariance propagation in Gaussian filtering. The CKF improves upon the UKF by ensuring symmetry and reducing potential numerical instabilities associated with higher-order approximations (Arasaratnam and Haykin, 2009). This method is particularly advantageous in systems where accurate representation of non-linear dynamics is critical, and it has been successfully applied in various geophysical and hydrological contexts (Sun et al., 2023).

While both the UKF and CKF offer improvements over the EKF in handling non-linear systems, their higher computational demands compared to the EKF and EnKF can be a limiting factor, particularly in real-time or large-scale applications. The EKF and EnKF have recently attracted significant attention for their use in data assimilation involving GRACE and GRACE-FO data. The EnKF, in particular, has demonstrated its effectiveness in various applications, such as improving soil moisture estimates through the joint assimilation of GRACE/-FO water storage and soil moisture observations (Girotto et al., 2019; Tangdamrongsub et al., 2020; Khaki et al., 2020) and refining estimates of water balance components (Lorenz et al., 2015; Wu et al., 2022) using GRACE and GRACE-FO data.

It is worth noting that in the implemented Kalman filters, calculating the variance of unit weight, $\hat{\sigma_t}^2$, and evaluating its impact has not been a primary focus in hydrogeodetic studies to date. The emphasis is typically on state estimation and updating processes, with the variance of unit weight often assumed or derived from a priori information rather than recalculated at each step. This indicates a potential area for further research, particularly in improving the accuracy and reliability of state estimates in dynamic systems.

2.5 Sampling techniques

So far, we have explored linear models and assumed normal distributions for both the prior and likelihood, for which analytical solutions can be obtained. However, in most cases, in the Bayesian framework, obtaining an analytical solution is not feasible, and one must indirectly obtain the posterior distribution. In real-world applications, the posterior distributions usually do not have closed-form solutions and are computationally challenging, especially in high-dimensional parameter spaces. Consequently, performing Bayesian inference in many practical scenarios would be nearly impossible. In such cases, sampling techniques are required to approximate posterior distributions (Bishop, 2006).

In obtaining the posterior distribution, the key issue is how to compute the expectation of a function $f(\boldsymbol{x})$ given a probability distribution $\mathsf{P}(\boldsymbol{x})$

$$\mathsf{E}(f) = \int f(\boldsymbol{x})\mathsf{P}(\boldsymbol{x})\, d\boldsymbol{x}\,. \tag{2.82}$$

Sampling methods aim to generate a set of samples x_i (for $i = 1, \ldots, N$) independently drawn from the distribution $\mathsf{P}(\boldsymbol{x})$, such that it allows to approximate the expectation in (2.82) by

$$\hat{f} = \frac{1}{N}\sum_{i=1}^{N} f(x_i)\,.$$

As long as the samples x_i come from the distribution $\mathsf{P}(x)$, then $\mathsf{E}(\hat{f}) = \mathsf{E}(f)$, ensuring that $\hat{f}$ is an unbiased estimator. Notably, the estimator's accuracy does not depend on the dimensionality of x, and a relatively small number of samples, typically ten or twenty, might suffice to achieve accurate estimates. However, samples x_i might not always be independent, reducing the effective sample size. Additionally, if $f(x)$ is small in regions where $\mathsf{P}(x)$ is large and vice versa, larger sample sizes may be needed for sufficient accuracy.

Table 2.1 presents an overview of some prominent sampling techniques, including Markov Chain Monte Carlo (MCMC), Sequential Monte Carlo (SMC), and Variational Inference (VI). MCMC methods are a class of algorithms designed to generate random samples from a probability distribution by constructing a Markov chain that has the desired distribution. In the recent past, different versions of MCMC have been developed and used, including:

- **Metropolis-Hastings algorithm:** The Metropolis-Hastings algorithm generates random samples using a general proposal distribution and includes an acceptance/rejection step for the proposed parameter values (van de Schoot et al., 2021; Metropolis et al., 1953).
- **Gibbs Sampling:** is particularly useful when the joint distribution is challenging to sample from, but the conditional distributions are easier to sample from (Geman and Geman, 1984).
- **Hamiltonian Monte Carlo (HMC):** leverages gradient information from the log-posterior to propose new samples more efficiently than traditional MCMC methods (Neal, 2011).

- **The No-U-Turn Sampler (NUTS):** is an adaptive version of HMC that automatically tunes the algorithm parameters, enhancing efficiency and performance (Hoffman and Gelman, 2014).

Sequential Monte Carlo (SMC) methods, such as particle filters, are another class of algorithms where particles are propagated over time and weighted based on their likelihood, providing a powerful framework for dynamic models (Doucet et al., 2000).

Tab. 2.1: Sampling Techniques in Bayesian Statistics

Technique	Description
Markov Chain Monte Carlo (MCMC) Methods	
Metropolis-Hastings Algorithm	An algorithm designed to generate random samples from a probability distribution that utilizes a general proposal distribution and includes an acceptance/rejection step for the proposed parameter values (van de Schoot et al., 2021; Metropolis et al., 1953).
Gibbs Sampling	MCMC method useful when the joint distribution is difficult to sample from directly, but the conditional distributions are easier to sample from (Geman and Geman, 1984).
Hamiltonian Monte Carlo (HMC)	MCMC method that uses gradient information from the log-posterior to propose new samples efficiently (Neal, 2011).
No-U-Turn Sampler (NUTS)	Adaptive version of HMC that automatically tunes the algorithm parameters (Hoffman and Gelman, 2014).
Sequential Monte Carlo (SMC)	
Particle Filters	SMC method where particles are propagated over time and weighted based on their likelihood (Doucet et al., 2000).
Variational Inference (VI)	
Mean-Field Variational Inference	Approximates the posterior by factorizing it into independent distributions and optimizing a lower bound on the marginal likelihood (Jordan et al., 1999).
Stochastic Variational Inference	Extension of VI that uses stochastic optimization for large datasets (Hoffman et al., 2013).
Other Techniques	
Rejection Sampling	Samples are generated from a proposal distribution and accepted or rejected based on a criterion involving the target distribution (Smith and Gelfand, 1992).
Importance Sampling	Samples are drawn from a proposal distribution and weighted to approximate the target distribution (Rubinstein, 1981).
Nested Sampling	Estimates the evidence (marginal likelihood) in Bayesian statistics, useful for model comparison (Skilling, 2006).
Approximate Bayesian Computation (ABC)	Used when the likelihood function is intractable; approximates the posterior by simulating data and comparing it to observed data (Beaumont, 2010).
Slice Sampling	MCMC method that samples uniformly from the region under the graph of the target distribution (Neal, 2003).
Langevin Dynamics	MCMC method using gradient information with added Gaussian noise to propose new samples (Roberts and Tweedie, 1996).
Bayesian Bootstrap	Non-parametric Bayesian method that resamples data to create a posterior distribution of an estimator (Rubin, 1981).

Variational Inference (VI) techniques offer deterministic alternatives to MCMC by approximating the posterior distribution through optimization. Mean-Field Variational Inference approximates the posterior by factorizing it into independent distributions and optimizing a lower bound on the marginal likelihood (Jordan et al., 1999). Stochastic Variational Inference, an extension of VI, employs stochastic optimization to handle large datasets efficiently (Hoffman et al., 2013).

Several other sampling techniques are also noteworthy. Rejection Sampling generates samples from a proposal distribution and accepts or rejects them based on a criterion involving the target distribution (Smith and Gelfand, 1992). Importance Sampling draws samples from a proposal distribution and weights them to approximate the target distribution (Rubinstein, 1981). Nested Sampling is useful for estimating the evidence (marginal likelihood) in Bayesian statistics, aiding in model comparison (Skilling, 2006). Approximate Bayesian Computation (ABC) is employed when the likelihood function is intractable; ABC approximates the posterior by simulating data and comparing it to observed data (Beaumont, 2010). Slice Sampling is an MCMC method that samples uniformly from the region under the graph of the target distribution (Neal, 2003). Langevin Dynamics uses gradient information with added Gaussian noise to

propose new samples in an MCMC framework (Roberts and Tweedie, 1996). Finally, the Bayesian Bootstrap is a non-parametric Bayesian method that resamples data to create a posterior distribution of an estimator (Rubin, 1981).

Within hydrogeodesy, different sampling methods have been practiced for various applications. For instance, in estimating river discharge MCMC was utilized by Paris et al. (2016) to obtain nonlinear stage-discharge rating curves based on satellite altimetry and modeled discharge. The Metropolis-Manning (MetroMan) algorithm, which is one of the standard river discharge algorithms of SWOT data, uses the Metropolis-Hastings algorithm to obtain flow law parameters from the nonlinear Strickler-Manning equation (Durand et al., 2014). The Bayesian At-many-stations hydraulic geometry-Manning's (BAM) algorithm and its successor geoBAM, also standard river discharge algorithms of the SWOT mission, make use of the HMC sampling scheme to estimate river discharge (Hagemann et al., 2017; Brinkerhoff et al., 2020). In downscaling GRACE water storage change, Mehrnegar et al. (2021) used MCMC to generate groundwater and soil water storage changes at approximately 12.5 km resolution. In reconstructing GRACE mass change time series, Rateb et al. (2022) utilized MCMC to sample posterior distributions, based on which TWSA and its uncertainty are obtained. Additionally, a variant of MCMC was used by Forootan et al. (2024) to merge TWSA from GRACE and GRACE-FO with water storage estimations derived from a water balance model. These examples, while representing only a subset of many applications, illustrate the use of sampling methods in estimating water cycle parameters from complex, nonlinear, non-Gaussian models.

2.6 Graphical models

In Bayesian statistics, the above-described sampling techniques are frequently utilized to approximate complex posterior distributions. However, as the probabilistic model's complexity increases—particularly in the context of high-dimensional data—these methods can become computationally demanding and difficult to implement. A primary challenge lies in efficiently capturing and representing the intricate dependencies among a large number of random variables within these sophisticated models.

This is where *graphical models* come into play. Graphical models provide a powerful framework, offering a visual and mathematical way to represent and analyze the dependencies among random variables. They can significantly simplify the complexity of the probabilistic structures, allowing for more efficient computation of posterior distributions, even in high-dimensional spaces. By encoding dependencies graphically, these models enable more tractable forms of sampling and inference, reducing computational burdens that might otherwise hinder the application of Bayesian techniques (Bishop, 2006).

Based on their structure and the types of dependencies they capture, graphical models can be categorized into 1) Bayesian Networks, 2) Markov Random Fields (MRFs), 3) Conditional Random Fields (CRFs), 4) Factor Graphs, 5) Chain Graphs, 6) Dynamic Graphical Models, and 7) Relational Models. Each type of graphical model brings its strengths suitable for different applications, which are listed Table 2.2.

This section discusses two types of graphical models listed in Table 2.2 that are frequently used in hydrogeodesy and could benefit from Bayesian inference (Bishop, 2006), namely 1) Bayesian networks and 2) Markov random fields (MRFs).

2.6.1 Bayesian Networks

Bayesian networks, also known as belief networks or directed acyclic graphs (DAGs), are a class of graphical models where nodes represent random variables, and edges denote conditional dependencies. Each node in

Tab. 2.2: Summary of different types of graphical models

Type of graphical model	Description	Key feature
Bayesian Networks (DAGs)	Directed graphs where nodes represent random variables and edges denote conditional dependencies (Pearl, 1988).	Factorization of joint probability into a product of conditional probabilities.
Markov Random Fields (MRFs)	Undirected graphs where nodes represent random variables and edges denote symmetric dependencies (Kindermann and Snell, 1980).	Factorization of joint probability into a product of potential functions.
Conditional Random Fields (CRFs)	Undirected models for structured prediction, directly modeling conditional distributions (Lafferty et al., 2001).	Incorporates complex features without assuming independence among observations.
Factor Graphs	Bipartite graphs with variable and factor nodes, connecting variables to the factors that involve them (Kschischang et al., 2001).	Unifies directed and undirected graphical models.
Chain Graphs	Graphs that contain both directed and undirected edges (Lauritzen, 1996).	Represents both causal and associative relationships.
Dynamic Graphical Models	Models with nodes indexed by time, representing time-evolving processes (Murphy, 2002).	Captures temporal dependencies.
Relational Models	Graphs that represent entities and the relationships between them (Getoor and Taskar, 2007).	Handles structured data with multiple types of entities and relationships.

a Bayesian network is associated with a conditional probability distribution, specifying how the variable depends on its parents in the graph.

The power of Bayesian networks lies in their ability to model joint probability distributions concisely. The joint distribution of a set of variables $\boldsymbol{X} = \{X_1, X_2, \ldots, X_n\}$ in a Bayesian network is given by

$$\mathsf{P}(\boldsymbol{X}) = \prod_{i=1}^{n} \mathsf{P}(X_i \mid \mathrm{Pa}(X_i)), \tag{2.83}$$

where $\mathrm{Pa}(X_i)$ denotes the parents of X_i in the network. This factorization simplifies the computation of the joint distribution and makes Bayesian networks suitable for tasks such as inference and learning. Let us consider an example involving Heavy Rain (H), Rain (R), Soil Moisture (S), Groundwater Recharge (G), and Flood (F):

- Heavy Rain (H): Whether there is heavy rain or not. $\mathrm{H} \in \{\text{True, False}\}$
- Rain (R): Whether it rains or not. $\mathrm{R} \in \{\text{True, False}\}$
- Soil Moisture (S): The moisture level in the soil. $\mathrm{S} \in \{\text{High, Low}\}$
- Groundwater Recharge (G): Whether there is groundwater recharge or not. $\mathrm{G} \in \{\text{True, False}\}$
- Flood (F): Whether there is a flood or not. $\mathrm{F} \in \{\text{True, False}\}$

In such an example the dependencies can be defined as

- Heavy rain can cause rain.
- Rain affects soil moisture.
- Soil moisture affects groundwater recharge.
- Heavy rain can also directly influence groundwater recharge.
- Heavy rain can directly influence floods.
- Soil moisture and groundwater recharge influence the likelihood of a flood.

Based on the above dependencies, the structure of the Bayesian network will be:

- Heavy Rain (H) influences Rain (R).
- Rain (R) influences Soil Moisture (S).
- Soil Moisture (S) influences Groundwater Recharge (G).
- Heavy Rain (H) directly influences Groundwater Recharge (G).

- Heavy Rain (H) directly influences Flood (F).
- Soil Moisture (S) and Groundwater Recharge (G) influence Flood (F).

This can be visualized in a DAG with 5 nodes as shown in Figure 2.3. With such a graph, the joint probability

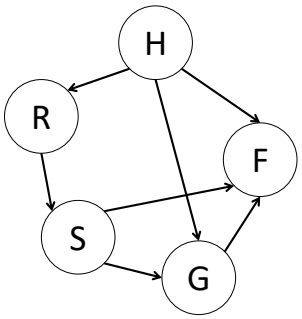

Fig. 2.3: Example of a directed acyclic graph describing the joint distribution over 5 variables Heavy Rain (H), Rain (R), Soil Moisture (S), Groundwater Recharge (G), and Flood (F)

distribution can easily be written in terms of the product of a set of conditional distributions, one for each node in the graph

$$\mathsf{P}(\mathrm{H},\mathrm{R},\mathrm{S},\mathrm{G},\mathrm{F}) = \mathsf{P}(\mathrm{H}) \cdot \mathsf{P}(\mathrm{R}|\mathrm{H}) \cdot \mathsf{P}(\mathrm{S}|\mathrm{R}) \cdot \mathsf{P}(\mathrm{G}|\mathrm{S},\mathrm{H}) \cdot \mathsf{P}(\mathrm{F}|\mathrm{S},\mathrm{G},\mathrm{H})$$

Now suppose we want to calculate the probability of flood (F) given that we know there is heavy rain (H). We need to obtain:

$$\mathsf{P}(\mathrm{F}|\mathrm{H}) = \sum_{\mathrm{R},\mathrm{S},\mathrm{G}} \mathsf{P}(\mathrm{F},\mathrm{R},\mathrm{S},\mathrm{G}|\mathrm{H}),$$

which can be expanded using the chain rule for Bayesian networks:

$$\mathsf{P}(\mathrm{F}|\mathrm{H}) = \sum_{\mathrm{R},\mathrm{S},\mathrm{G}} \mathsf{P}(\mathrm{F}|\mathrm{S},\mathrm{G},\mathrm{H}) \cdot \mathsf{P}(\mathrm{G}|\mathrm{S},\mathrm{H}) \cdot \mathsf{P}(\mathrm{S}|\mathrm{R}) \cdot \mathsf{P}(\mathrm{R}|\mathrm{H})$$

Or consider a more complex scenario where we have evidence about soil moisture (S) and we want to update our belief about the likelihood of a flood (F). Suppose we know the soil moisture is high ($\mathrm{S} = \text{High}$). In this case, we want to compute:

$$\mathsf{P}(\mathrm{F}|\mathrm{S} = \text{High}).$$

Using the Bayes theorem, we can write this as:

$$\mathsf{P}(\mathrm{F}|\mathrm{S} = \text{High}) = \frac{\mathsf{P}(\mathrm{S} = \text{High}|\mathrm{F}) \cdot \mathsf{P}(\mathrm{F})}{\mathsf{P}(\mathrm{S} = \text{High})},$$

we can obtain $\mathsf{P}(\mathrm{S} = \text{High}|\mathrm{F})$ using the dependencies in the network:

$$\mathsf{P}(\mathrm{S} = \text{High}|\mathrm{F}) = \sum_{\mathrm{H},\mathrm{R},\mathrm{G}} \mathsf{P}(\mathrm{S} = \text{High}|\mathrm{R}) \cdot \mathsf{P}(\mathrm{R}|\mathrm{H}) \cdot \mathsf{P}(\mathrm{H}) \cdot \mathsf{P}(\mathrm{G}|\mathrm{S},\mathrm{H}).$$

Apart from the above examples, the line fitting example over the Lake Urmia water level can also be represented using DAGs. For the unknown variables $\boldsymbol{x}$ and observed data $\boldsymbol{y} = [y_1, \ldots, y_m]^\top$, we can construct a DAG as shown in Figure 2.4. The joint distribution $\mathsf{P}(\boldsymbol{x}, \boldsymbol{y})$ is given by:

$$\mathsf{P}(\boldsymbol{x}, \boldsymbol{y}) = \mathsf{P}(\boldsymbol{x}) \prod_{i=1}^{m} \mathsf{P}(y_i|\boldsymbol{x}).$$

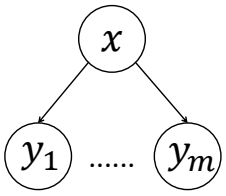

Fig. 2.4: DAG of the line fitting example with random variables $\boldsymbol{x}$ and $\boldsymbol{y} = [y_1, \ldots, y_m]^\top$

By applying the Bayes theorem, this can be transformed into:

$$\mathsf{P}(\boldsymbol{x}|\boldsymbol{y}) \propto \mathsf{P}(\boldsymbol{x}) \prod_{i=1}^{m} \mathsf{P}(y_i|\boldsymbol{x}) \,.$$

This formulation is similar to what we had before in (2.19), where we find the posterior distribution $\mathsf{P}(\boldsymbol{x}|\boldsymbol{y})$ by multiplying the prior distribution $\mathsf{P}(\boldsymbol{x})$ with the likelihood function.

In addition, the Bayesian network eases the procedure of indirectly sampling the posterior, discussed in 2.5. For directed graphs without observed variables, sampling from the joint distribution is straightforward if conditional distributions can be sampled at each node. This is done using ancestral sampling using (2.83). To sample from the joint distribution, one can iterate through variables $X_1, \ldots, X_M$, sampling from $\mathsf{P}(X_i \mid \mathrm{Pa}_i)$. When some nodes in a directed graph have observed values, this approach can be extended to logic sampling (Henrion, 1988), a special case of importance sampling. If a sampled value for X_i matches its observed value, the sample is retained; otherwise, the sample is discarded, and the process restarts. This ensures correct posterior sampling, but becomes inefficient with a large number of observed variables.

2.6.2 Markov Random Fields

Markov random fields (MRFs), or undirected graphical models, represent variables as nodes and use undirected edges to denote dependencies. Unlike Bayesian networks, MRFs do not imply a directional relationship but instead indicate that variables are conditionally independent of all others given their neighbors. The Gibbs-Boltzmann distribution provides a way to represent the joint probability distribution of an MRF using clique-based potential functions. A clique is a subset of nodes in the graph such that an edge directly connects every pair of nodes within the subset. Specifically, the joint probability distribution of a set of random variables $\boldsymbol{X}$ in an MRF can be expressed as

$$\mathsf{P}(\boldsymbol{X}) = \frac{1}{Z} \prod_{C \in \mathcal{C}} \psi_C(X_C) \,, \tag{2.84}$$

where $\mathcal{C}$ is the set of all cliques in the graph, ψ_C is a potential function over the clique C. This means that all variables are mutually dependent within a clique, forming a fully connected subgraph. Z is the partition function ensuring the distribution sums to one.

$$Z = \sum_{x} \prod_{C \in \mathcal{C}} \psi_C(X_C) \,.$$

Unlike Bayesian networks, MRFs are not inherently Bayesian but can be used within a Bayesian framework when spatial or contextual dependencies are modeled using prior distributions. The distinction lies in whether the Bayes theorem and prior/posterior distributions are utilized, which is not necessarily a requirement for MRFs (Besag, 1974; Geman and Geman, 1984).

In the formulation of an MRF, observations can be incorporated through the use of observed variables in conjunction with the hidden (or latent) variables. This is commonly done by defining a joint probability distribution that includes both the hidden variables $\boldsymbol{X}$ and the observed variables $\boldsymbol{Y}$ (see Figure 2.5):

$$\mathsf{P}(\boldsymbol{X},\boldsymbol{Y}) = \frac{1}{Z}\exp\left(-\sum_{C\in\mathcal{C}}\psi_C(\boldsymbol{X}_C,\boldsymbol{Y}_C)\right),$$

with

$$Z = \sum_{X,Y}\exp\left(-\sum_{C\in\mathcal{C}}\psi_C(\boldsymbol{X}_C,\boldsymbol{Y}_C)\right).$$

In practice, the potentials $\psi_C(X_C,Y_C)$ often decompose into terms involving individual variables and pairs of variables (or higher-order cliques). For instance:

$$\psi_C(X_C,Y_C) = \sum_i \phi_i(X_i,Y_i) + \sum_{(i,j)\in E}\phi_{ij}(X_i,X_j,Y_i,Y_j).$$

Here, $\phi_i(X_i,Y_i)$ is a unary potential function that incorporates the influence of the observation Y_i on the hidden variable X_i, and $\phi_{ij}(X_i,X_j,Y_i,Y_j)$ is a pairwise potential function that can incorporate both the dependencies between hidden variables and their relationships with the observations (see Figure 2.5).

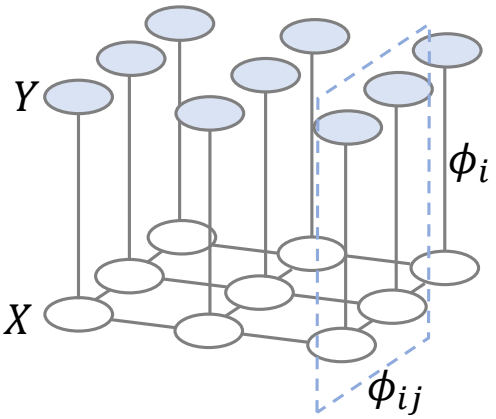

Fig. 2.5: A schematic illustration of MRF with the hidden variables $\boldsymbol{X}$ and the observed variables $\boldsymbol{Y}$. The unary potential function $\phi_i(X_i,Y_i)$ incorporates the influence of the observation Y_i on the hidden variable X_i, and the pairwise potential function $\phi_{ij}(X_i,X_j,Y_i,Y_j)$ incorporates both the dependencies between hidden variables and their relationships with the observations.

By incorporating the observed variables $\boldsymbol{Y}$ into the potential functions, the MRF can model the joint distribution of the hidden and observed variables, allowing for inference and learning to be performed with respect to the observed data.

The MAP-MRF Framework

The Maximum A Posteriori estimation in the Markov Random Fields (MAP-MRF) framework is a specific inference task aimed at finding the most probable configuration of the hidden variables $\boldsymbol{X}$ given the observed data $\boldsymbol{Y}$. This approach seeks to maximize the posterior distribution $\mathsf{P}(\boldsymbol{X}|\boldsymbol{Y})$, which is expressed using the Bayes theorem as:

$$\mathsf{P}(\boldsymbol{X}|\boldsymbol{Y}) = \frac{\mathsf{P}(\boldsymbol{X},\boldsymbol{Y})}{\mathsf{P}(\boldsymbol{Y})},$$

where $\mathsf{P}(\boldsymbol{Y})$ is the marginal likelihood of the observations, acting as a normalizing constant. The goal in MAP estimation is to find the configuration $\hat{\boldsymbol{X}}$ that maximizes this posterior probability:

$$\hat{\boldsymbol{X}} = \arg\max_{\boldsymbol{X}} \mathsf{P}(\boldsymbol{X}|\boldsymbol{Y}).$$

Substituting the joint probability into this equation gives:

$$\hat{\boldsymbol{X}} = \arg\max_{\boldsymbol{X}} \frac{\mathsf{P}(\boldsymbol{X},\boldsymbol{Y})}{\mathsf{P}(\boldsymbol{Y})} = \arg\max_{\boldsymbol{X}} \mathsf{P}(\boldsymbol{X},\boldsymbol{Y}) = \arg\max_{\boldsymbol{X}} \frac{1}{Z} \exp\left(-\sum_{C\in\mathcal{C}} \psi_C(\boldsymbol{X}_C,\boldsymbol{Y}_C)\right).$$

Since $\mathsf{P}(\boldsymbol{Y})$ is constant with respect to $\boldsymbol{X}$, and Z is the partition function which does not affect the location of the maximum, the MAP estimate simplifies to:

$$\hat{\boldsymbol{X}} = \arg\max_{\boldsymbol{X}} \exp\left(-\sum_{C\in\mathcal{C}} \psi_C(\boldsymbol{X}_C,\boldsymbol{Y}_C)\right),$$

or equivalently,

$$\hat{\boldsymbol{X}} = \arg\min_{\boldsymbol{X}} \sum_{C\in\mathcal{C}} \psi_C(\boldsymbol{X}_C,\boldsymbol{Y}_C).$$

Solving the MAP-MRF problem involves finding the configuration of hidden variables $\boldsymbol{X}$ that minimizes the sum of the potential functions over all cliques, conditioned on the observed data $\boldsymbol{Y}$. To better understand the hidden layer $\boldsymbol{X}$, and observation $\boldsymbol{Y}$, and the MAP-MRF framework, let's consider an example that will be explored in more detail in Chapter 5. There, a MAP-MRF problem is formulated to retrack altimetry waveforms and enhance water level estimation from satellite altimetry. Rather than identifying a retracking point in a single waveform, the objective is to identify a retracking line within an image, generated by aligning all consecutive waveforms within a virtual station, known as a *radargram*. This retracking line divides the radargram into two segments: the left (*Front*) and the right (*Back*) of the retracking line. This segmentation approach can be interpreted as a binary image segmentation problem. There, in the defined MAP-MRF, $\boldsymbol{X}$ represents the labels *Front* and *Back*, which are indeed hidden states and must be sought. $\boldsymbol{Y}$ represents the pixel intensities of the radargram, corresponding to the measured reflected power of the waveforms from satellite altimetry.

The Bayesian aspect of the MAP-MRF framework involves incorporating prior knowledge and using the Bayes theorem to update beliefs about the hidden variables based on observed data. Prior beliefs about the hidden variables $\boldsymbol{X}$ are encoded in a prior distribution $\mathsf{P}(\boldsymbol{X})$, and the likelihood function $\mathsf{P}(\boldsymbol{Y}|\boldsymbol{X})$ quantifies how probable the observed data $\boldsymbol{Y}$ is given a particular configuration of the hidden variables $\boldsymbol{X}$. Inference in the Bayesian MAP-MRF framework involves finding the configuration $\hat{\boldsymbol{X}}$ that maximizes the posterior probability, which is equivalent to minimizing the energy function given by the sum of potential functions. Practically, solving the MAP-MRF problem involves finding the configuration of hidden variables $\boldsymbol{X}$ that minimizes the sum of the potential functions over all cliques, conditioned on the observed data $\boldsymbol{Y}$. Several optimization techniques can be employed to solve the MAP-MRF problem, including:

- **Graph Cuts**: This method is particularly effective for binary and multi-label problems in computer vision, where the problem can be transformed into a minimum cut problem on a graph. The graph cuts method is utilized to obtain the solution for the MRF-MAP problem defined in Chapter 5.
- **Belief Propagation**: An iterative algorithm that computes marginal distributions of the nodes, which can be adapted to find the most probable configuration.
- **Simulated Annealing**: A probabilistic technique that explores the solution space by accepting worse solutions with a certain probability to escape local minima.
- **Iterated Conditional Modes (ICM)**: An iterative algorithm that updates each variable to minimize the local energy function, assuming other variables are fixed.

Within hydrogeodesy, MRF-MAP has been practiced mostly when classification or denoising is targeted. For instance, it has been employed to solve the height estimation problem in InSAR imaging (Ferraiuolo et al., 2004). Additionally, it has been utilized to obtain surface water extent from optical images (Elmi et al., 2016; Elmi, 2019) and in retrieving time series of river water extent from global inland water datasets (Elmi and Tourian, 2023). Moreover, it has also been used to detect water in SWOT HR images (Lobry et al., 2019). In general, as spaceborne data continue to evolve, especially SWOT-type data, the role of probabilistic methods like MRF-MAP is expected to grow, contributing to more refined insights into Earth's water systems.

3 A Bayesian approach to estimating daily river discharge from space

River discharge is one of the most crucial hydrological parameters, serving as a major link in the global hydrologic cycle and as a critical climate component (Dingman and Bjerklie, 2006). Accurate measurements of river discharge are essential for flood hazard management, water resource planning, climate and ecological studies, and adherence to transboundary water agreements (Smith and Pavelsky, 2008). However, the global publicly available discharge database is declining steadily over the past few years (Fekete and Vörösmarty, 2007; Fekete et al., 2012; Tourian et al., 2013; Sneeuw et al., 2014; Elmi et al., 2024; Saemian et al., 2025). To address this issue, there has been a growing interest in using spaceborne methods to estimate discharge (Alsdorf et al., 2007; McCabe et al., 2017; Tourian et al., 2017a; Gleason and Durand, 2020; Tarpanelli et al., 2018, 2021; Domeneghetti et al., 2021; Elmi et al., 2021).

Recent studies show that altimetric water height or image-based river width over rivers can sensibly be used to deal with the growing lack of discharge (da Silva et al., 2010; Calmant et al., 2012; Getirana and Peters-Lidard, 2012; Tourian et al., 2013; Tarpanelli et al., 2013a; Maillard et al., 2015; Elmi et al., 2015, 2024). These studies estimated river discharge through a one-on-one functional relationship of discharge and altimetric water level time series or image-based river width, the so-called *rating curve*. This model is typically derived from a non-linear regression of simultaneous discharge vs. river width or water level at the crossing of altimetry groundtrack and river, the so-called *virtual station*. However, the onset of the decline of the Global Runoff Data Center (GRDC) database around the 70ies coincides with the beginning of the satellite era (Elmi et al., 2024). Hence, synchronous time series of sufficient duration are only available for a limited set of discharge gauges. This limitation was alleviated to a great extent by Tourian et al. (2013), who estimate discharge through quantile function mapping. Thus, the statistics of pre-altimetry discharge data can be employed for discharge prediction in the satellite altimetry or satellite imaging time frame under a weak assumption of stationarity for discharge. The method is further improved by Elmi et al. (2021) to infer a nonparametric model for estimating the river discharge and its uncertainty. The algorithm employs a stochastic quantile mapping function scheme by iteratively generating realizations of river discharge and height (width) time series using a Monte Carlo simulation, obtaining a collection of quantile mapping functions by matching all possible permutations of simulated river discharge and height (width) quantile functions and adjusting the measurement uncertainties according to the point cloud scatter.

However, a general problem of all estimated altimetric and image-based discharge is their coarse temporal resolution, which is dictated by the repeat period of the satellite orbit. Moreover, the original time series from individual missions carries noise and data outages, predominantly due to the neighboring topography and heterogeneity of the reflecting surface. Such limitations inhibit the operational use of altimetric water level time series in hydrological and hydrodynamic models. Recently, in terms of qualitative and quantitative improvement of altimetry for rivers, Tourian et al. (2016); Boergens et al. (2019); Nielsen et al. (2022) developed methods, by which the altimetric water level time series along a river are connected hydraulically and statistically to improve the temporal resolution of water level time series. Such methods can be used to generate dense water level time series at any given location along the river and consequently generate a dense discharge time series through corresponding one-on-one rating curves.

Apart from direct discharge modeling approaches, various assimilation methods have been employed to estimate river discharge, especially for ungauged basins. For instance, Andreadis et al. (2007) used synthetic surface water elevation data integrated into a raster-based river hydrodynamic model with an ensemble Kalman filter to estimate river discharge. Similarly, Yoon et al. (2012) applied a data assimilation algorithm, which also utilized an ensemble Kalman filter and a hydrodynamic model, to derive river bathymetry and discharge from the SWOT satellite mission. Neal et al. (2009) combined water level information from fused satellite SAR images and a digital terrain model (DTM) with simulations from a coupled hydrological and hydrodynamic model to estimate discharge, assuming substantial channel information is available. Additionally, Emery et al. (2018) developed a platform that calibrates a hydrological model of river storage and discharge using satellite altimetry-based discharge data. Moreover, Ishitsuka et al. (2021) employed the Mass-conserved Flow Law Inversion (McFLI) method, derived from satellite imaging and combined with hydrological models in a global data assimilation framework, to estimate discharge in ungauged basins. Gejadze et al. (2022) devised a robust discharge estimation method using Variational Data Assimilation based on the complete Saint-Venant hydraulic model. Paiva et al. (2013) proposed a data assimilation framework for both gauged and radar altimetry-based discharge and water levels, applied to a large-scale hydrologic-hydrodynamic model for forecasting streamflow in the Amazon River basin. Huang et al. (2018) demonstrated the use of satellite imaging and altimetry data combined with sparse gauge data on the Tibetan plateau to estimate river discharge using power function equations. Lastly, Emery et al. (2020) utilized a hydrodynamic model, based on the work of David et al. (2011), to assimilate daily averaged in situ discharge measurements and correct daily averaged runoff using a classical Kalman filter, tested over a four-year case study of two rivers in Texas.

The launch of the SWOT satellite on December 16, 2022, shall lead to a significant improvement in obtaining the first global estimates of river discharge (Durand et al., 2023). SWOT delivers consistent data on the spatial distribution of river storage and discharge (Biancamaria et al., 2016). The satellite observes most mid-latitude locations twice during its 21-day repeat cycle, resulting in around 35 observations per year, with a higher frequency at higher latitudes (Biancamaria et al., 2016; Durand et al., 2023). While this frequency is adequate for monitoring the global water cycle, it may not sufficiently capture the temporal dynamics required for local-scale river studies (Durand et al., 2016). Therefore, even with SWOT, it seems necessary to make efforts to improve temporal resolution.

3.1 A Kalman Filter based method to estimate river discharge

As discussed in Section 2.4, the use of Bayesian approaches in dynamic systems, particularly the Kalman Filter, is a well-established methodology that has been used in many disciplines for various purposes, such as navigation, control systems, and signal processing. It has also been applied in hydrogeodetic studies. In hydrogeodetic studies, the use of the Kalman Filter and dynamic systems is particularly beneficial when representing a river system. The Kalman Filter allows for the integration of multiple data sources and the continuous updating of estimates as new measurements become available. This is crucial for accurately modeling and predicting the behaviour of river systems, which are dynamic and influenced by numerous factors such as rainfall, evaporation, and human activities. By using a dynamic system approach, we can create a more accurate representation of the river's state over time. The Kalman Filter helps in this by combining geodetic measurements, such as water surface elevation and river width obtained from satellites, with hydrological models that describe the river's flow and discharge. This integration allows for real-time updating and correction of the model based on new observations, leading to more reliable predictions of river discharge and other hydrological parameters (Lorenz and Kunstmann, 2012).

Inspired by the existing challenge of monitoring river discharge from space and the opportunity offered by the Kalman Filter, a method is proposed here that goes beyond the conventional one-on-one relationship

and single-reach approach, estimating daily river discharge using a multitude of altimetric time series. A linear dynamic system is implemented to (1) provide a scheme for data assimilation of multiple altimetric discharges along a river, (2) estimate daily discharge, (3) deal with data outages in altimetric discharge, and (4) smooth the discharge estimation. As discussed in Section 2.4, the linear dynamic system consists of a stochastic process model that benefits from the cyclostationary behaviour of the discharge. The covariance and cross-covariance information of river discharge along the river stream are included within the process model. Multiple altimetric discharge time series are combined with the process model to form a linear dynamic system. The linear dynamic system is solved using the Kalman filter and a smoother. Such a methodology is flexible to integrate all kinds of satellite altimetry data as well as SWOT data.

The starting point of developing a stochastic process model is to define the time series of residual daily discharge $\boldsymbol{r}_t$ by

$$\boldsymbol{r}_t = \boldsymbol{Q}_t - \widetilde{\boldsymbol{Q}}_t \ , \tag{3.1}$$

with $\boldsymbol{Q}_t$ as the daily discharge time series and $\widetilde{\boldsymbol{Q}}$ as the mean daily discharge (Figure 3.2). Both $\boldsymbol{Q}_t$ and $\widetilde{\boldsymbol{Q}}$ can represent time series of several stations/locations along the river. The $\widetilde{\boldsymbol{Q}}$ represents the cyclostationary behaviour of daily river discharge, which is computed as

$$\widetilde{\boldsymbol{Q}}_k = \frac{1}{T/365} \sum_{i}^{T/365} \boldsymbol{Q}_{i,k} \ , \tag{3.2}$$

in which k is the day of the year, varying from 1 to 365. After removing the cyclostationary behaviour from the daily discharge time series, one can assume that the remaining residual does not change drastically from time $t-1$ to t. Given such an assumption, a linear process model can be formed by

$$\boldsymbol{r}_t = \boldsymbol{A}\boldsymbol{r}_{t-1} + \boldsymbol{e} \ , \tag{3.3}$$

where,

$$\mathrm{E}\{\boldsymbol{r_t}\} = 0 \ . \tag{3.4}$$

In the above process model (3.3), the process dynamics $\boldsymbol{A}$ is unknown and it should be estimated by minimizing the process error $\boldsymbol{e}$. An approximation of process dynamic $\hat{\boldsymbol{A}}$ is then a linear estimator of the state $\boldsymbol{r}_t$ given $\boldsymbol{r}_{t-1}$ (Gelb, 1974; Kurtenbach, 2011)

$$\hat{\boldsymbol{r}}_t = \hat{\boldsymbol{A}}\boldsymbol{r}_{t-1} \ . \tag{3.5}$$

Consequently, the process error can be quantified as,

$$\boldsymbol{e} = \hat{\boldsymbol{r}}_t - \boldsymbol{r}_t \quad \text{with} \quad \mathrm{C}\{\boldsymbol{e}\} = \boldsymbol{\Sigma}_{\mathrm{P}} = \mathrm{E}\{\boldsymbol{e}\boldsymbol{e}^{\mathsf{T}}\} \ . \tag{3.6}$$

With the above formulation, the minimum error variance occurs when

$$\mathrm{tr}[C\{\boldsymbol{e}\}] = \min \ . \tag{3.7}$$

Since the equation (3.4) is valid for all $\boldsymbol{A}$, the expectation can be justified (Moritz, 1989; Kurtenbach, 2011)

$$\mathrm{E}\{\hat{\boldsymbol{r}}_t\} = \mathrm{E}\{\hat{\boldsymbol{A}}\boldsymbol{r}_{t-1}\} = \hat{\boldsymbol{A}}\mathrm{E}\{\boldsymbol{r}_{t-1}\} = 0 = \mathrm{E}\{\boldsymbol{r}_t\} \ . \tag{3.8}$$

To determine the minimum variance estimator, first, the outer product of the error vector from equation (3.6) is calculated

$$\boldsymbol{e}\boldsymbol{e}^{\mathsf{T}} = (\hat{\boldsymbol{r}}_t - \boldsymbol{r}_t)(\hat{\boldsymbol{r}}_t - \boldsymbol{r}_t)^{\mathsf{T}} \ . \tag{3.9}$$

Then by substituting $\hat{r}_t$ from (3.5) and multiplying the terms:

$$\boldsymbol{e}\boldsymbol{e}^{\mathsf{T}} = (\hat{\boldsymbol{A}}\boldsymbol{r}_{t-1} - \boldsymbol{r}_t)(\hat{\boldsymbol{A}}\boldsymbol{r}_{t-1} - \boldsymbol{r}_t)^{\mathsf{T}} \tag{3.10}$$

$$= \hat{\boldsymbol{A}}\boldsymbol{r}_{t-1}\boldsymbol{r}_{t-1}^{\mathsf{T}}\hat{\boldsymbol{A}}^{\mathsf{T}} - \boldsymbol{r}_t\boldsymbol{r}_{t-1}^{\mathsf{T}} - \hat{\boldsymbol{A}}\boldsymbol{r}_{t-1}\boldsymbol{r}_t^{\mathsf{T}} + \boldsymbol{r}_t\boldsymbol{r}_t^{\mathsf{T}} \ . \tag{3.11}$$

The auto-covariance and cross-covariance are then defined as

$$\text{Auto-covariance:} \quad \boldsymbol{\Sigma} = \mathrm{C}\{\boldsymbol{r}_t\} = \mathrm{E}\{\boldsymbol{r}_t\boldsymbol{r}_t^{\mathsf{T}}\} \tag{3.12}$$

$$\text{Cross-covariance:} \quad \boldsymbol{\Sigma}_\Delta = \mathrm{C}\{\boldsymbol{r}_t, \boldsymbol{r}_{t-1}\} = E\{\boldsymbol{r}_t\boldsymbol{r}_{t-1}^{\mathsf{T}}\} \tag{3.13}$$

Then the error covariance matrix of the process model is

$$\mathrm{C}\{\boldsymbol{e}\} = \mathrm{E}\{\boldsymbol{e}\boldsymbol{e}^{\mathsf{T}}\} = \boldsymbol{A}\boldsymbol{\Sigma}\boldsymbol{A}^{\mathsf{T}} - \boldsymbol{\Sigma}_\Delta\boldsymbol{A}^{\mathsf{T}} - \boldsymbol{A}\boldsymbol{\Sigma}_\Delta^{\mathsf{T}} + \boldsymbol{\Sigma} \ , \tag{3.14}$$

which can be rearranged into

$$\mathrm{C}\{\boldsymbol{e}\} = \boldsymbol{\Sigma} - \boldsymbol{\Sigma}_\Delta\boldsymbol{\Sigma}^{-1}\boldsymbol{\Sigma}_\Delta^{\mathsf{T}} + (\boldsymbol{A} - \Sigma_\Delta\Sigma^{-1})\boldsymbol{\Sigma}(\boldsymbol{A} - \boldsymbol{\Sigma}_{\boldsymbol{\Delta}}\boldsymbol{\Sigma}^{-1})^{\mathsf{T}}. \tag{3.15}$$

The first term is independent of $\boldsymbol{A}$

$$\boldsymbol{\Sigma} - \boldsymbol{\Sigma}_\Delta\boldsymbol{\Sigma}^{-1}\boldsymbol{\Sigma}_\Delta^{\mathsf{T}} \ = \ \mathrm{c}. \tag{3.16}$$

Therefore, the trace of the error covariance matrix is minimum if the second term disappears, leading to the definition

$$\hat{\boldsymbol{A}} = \boldsymbol{\Sigma}_\Delta\boldsymbol{\Sigma}^{-1}, \tag{3.17}$$

and a covariance matrix

$$C\{\boldsymbol{e}\} = \boldsymbol{\Sigma} - \boldsymbol{\Sigma}_\Delta\boldsymbol{\Sigma}^{-1}\boldsymbol{\Sigma}_\Delta^{\mathsf{T}} \ . \tag{3.18}$$

In the common Kalman notation this is referred to as the covariance matrix of the prediction noise.

The process dynamics $\hat{\boldsymbol{A}}$ is a matrix that acts in the time and spatial domain at the same time. Since it is derived from the statistics of residual daily time series, it transfers the information about random errors, climatic variability, and extreme events from $t-1$ to t and from any given station to other stations.

Since the true auto- and cross-covariances between the residuals of daily river discharge are unknown, they are approximated by the empirical sample covariance matrices using legacy discharge data available at gauging stations

$$\boldsymbol{\Sigma} = C\{\boldsymbol{r}_t\} = E\{\boldsymbol{r}_t\boldsymbol{r}_t^{\mathsf{T}}\} = \frac{1}{T}\sum_{t=1}^{T}\boldsymbol{r}_t^{\mathsf{T}}\boldsymbol{r}_t \tag{3.19}$$

$$\boldsymbol{\Sigma}_\Delta = C\{\boldsymbol{r}_t, \boldsymbol{r}_{t-1}\} = E\{\boldsymbol{r}_t\boldsymbol{r}_{t-1}^{\mathsf{T}}\} = \frac{1}{T-1}\sum_{t=2}^{T}\boldsymbol{r}_{t-1}^{\mathsf{T}}\boldsymbol{r}_t \tag{3.20}$$

Such an approximation for the auto- and cross-covariance matrices means that the residual of daily river discharge is considered as a stationary stochastic process. In essence, this implies that the residual daily discharge does not change its statistical properties with time and that its statistical properties can be deduced from a single, sufficiently long realization of the process. In this case, this is not necessarily true, and it might lead to uncertainty for the process model. However, since the process model can be combined with available in situ or spaceborne discharge measurements, such limitations will have a weak influence on our final solutions.

Now by combining (3.3) and (3.1) the stochastic process model for daily discharge is obtained

$$\begin{aligned}(\boldsymbol{Q}_t - \widetilde{\boldsymbol{Q}}_t) &= \hat{\boldsymbol{A}}(\boldsymbol{Q}_{t-1} - \widetilde{\boldsymbol{Q}}_{t-1}) + \boldsymbol{e} \\ (\boldsymbol{Q}_t - \widetilde{\boldsymbol{Q}}_t) &= \hat{\boldsymbol{A}}\boldsymbol{Q}_{t-1} - \hat{\boldsymbol{A}}\widetilde{\boldsymbol{Q}}_{t-1} + \boldsymbol{e} \\ \boldsymbol{Q}_t &= \hat{\boldsymbol{A}}\boldsymbol{Q}_{t-1} - \hat{\boldsymbol{A}}\widetilde{\boldsymbol{Q}}_{t-1} + \widetilde{\boldsymbol{Q}}_t + \boldsymbol{e}\end{aligned} \tag{3.21}$$

which can be rewritten in the form of

$$\boldsymbol{Q}_t = \hat{\boldsymbol{A}}\boldsymbol{Q}_{t-1} + \boldsymbol{G}\boldsymbol{U}_{t-1} + \boldsymbol{e}, \tag{3.22}$$

where,

$$\boldsymbol{G} = \begin{bmatrix} -\hat{\boldsymbol{A}} & \boldsymbol{I} \end{bmatrix} \quad \& \quad \boldsymbol{U}_{t-1} = \begin{bmatrix} \widetilde{\boldsymbol{Q}}_{t-1} \\ \widetilde{\boldsymbol{Q}}_t \end{bmatrix} . \tag{3.23}$$

The form obtained in (3.22) is the stochastic process model of discharge that estimates at $\boldsymbol{Q}_t$ by having the discharge at $t-1$ relying on information provided by auto-covariance, cross-covariance, and daily mean of discharge.

The process model can benefit from available observations of the process occurring at discrete points in time, which allows for controlling and improving the discharge estimation of the stochastic process model. For this, one can use estimated discharge from satellite altimetry or *in situ* discharge measurements. The linear observation equation reads

$$\boldsymbol{Z}_t = \boldsymbol{O}\boldsymbol{Q}_t + v_t \quad \text{with} \quad \boldsymbol{v}_t \sim \mathcal{N}(\boldsymbol{0}, \boldsymbol{Q}_{xt}), \tag{3.24}$$

where $\boldsymbol{Z}_t$ denotes all available discharge measurements. Here, $\boldsymbol{O}$ is an identity matrix. The observation equation setup will be explained in detail in Section 3.2.3.

The process model (3.22) and observation model (3.24) are independent. Together they form a linear dynamic system. The state Q_t will be estimated using the prior information from the process model and the likelihood function obtained from available discharge estimation from altimetry. The formulation described in Chapter 2 will be used to obtain a posterior and the MAP solution, which is summarized in Table 3.1.

Tab. 3.1: Overview of the Kalman filter and the smoothing procedure

Parameter	Equation
Prediction step	$\boldsymbol{Q}_t^- = \widehat{\boldsymbol{A}}\boldsymbol{Q}_{t-1}^+ + \boldsymbol{G}\boldsymbol{U}_{t-1} + \boldsymbol{e}$ with $\boldsymbol{e} \sim \mathcal{N}(\boldsymbol{0}, \boldsymbol{\Sigma}_\Sigma)$
State prediction covariance	$\boldsymbol{\Sigma}_t^- = \widehat{\boldsymbol{A}}\boldsymbol{\Sigma}_{t-1}^-\widehat{\boldsymbol{A}}^\mathsf{T} + \boldsymbol{\Sigma}_\mathrm{P}$
Observation innovations	$\boldsymbol{V}_t = \boldsymbol{Z}_t - \boldsymbol{O}_t\boldsymbol{Q}_t^- + \boldsymbol{\nu}_{t,d}$ with $\boldsymbol{\nu}_t \sim \mathcal{N}(\boldsymbol{0}, \boldsymbol{Q}_{\mathrm{x},t})$
Measurement prediction covariance	$\boldsymbol{S}_t = \boldsymbol{O}_t\boldsymbol{P}_t^-\boldsymbol{O}_t^\mathsf{T} + \boldsymbol{Q}_{xt}$
Kalman gain	$\boldsymbol{K}_t = \boldsymbol{\Sigma}_t^-\boldsymbol{O}_t^\mathsf{T}\boldsymbol{S}_t^{-1}$
Correction step	$\boldsymbol{Q}_t^+ = \boldsymbol{Q}_t^- + \boldsymbol{K}_t\boldsymbol{V}_t$
Updated state covariance	$\boldsymbol{\Sigma}_t^+ = \boldsymbol{\Sigma}_t^- - \boldsymbol{K}_t\boldsymbol{S}_t\boldsymbol{K}_t^\mathsf{T}$
Smoothing gain	$\boldsymbol{K}_t^* = \boldsymbol{\Sigma}_t^+\widehat{\boldsymbol{A}}\left(\boldsymbol{\Sigma}_{t+1}^-\right)^{-1}$
Smoothing step	$\boldsymbol{Q}_t = \boldsymbol{Q}_t^+ + \boldsymbol{K}_t^*\left(\boldsymbol{Q}_{t+1} - \boldsymbol{Q}_{t+1}^-\right)$
Smoothed covariance	$\boldsymbol{\Sigma}_t^* = \boldsymbol{\Sigma}_t^+ + \boldsymbol{K}_t^*\left(\boldsymbol{\Sigma}_{t+1}^* - \boldsymbol{\Sigma}_t^-\right)\boldsymbol{K}_t^{*\mathsf{T}}$

3.2 Implementation

The algorithm is employed over the Niger Basin, located in western Africa, which covers 7.5% of the continent and spans ten countries (Figure 3.1). The Niger River flows in a crescent through Mali and Niger, along the border with Benin, and then through Nigeria, discharging through the massive Niger Delta into the Gulf of Guinea in the Atlantic Ocean. Additionally, two tributaries, the Bani and Benue rivers, are considered. The Benue River, located in Nigeria, is the most important tributary of the Niger, merging with the river at Lokoja in Nigeria (Figure 3.1). The Bani River, the principal tributary of the Niger River in Mali, merges with the Niger near Mopti (Gleick, 2000). The Niger River runs with relatively high flow velocity until it reaches the Inner Niger Delta, where the river's gradient suddenly decreases (Figure 3.2). Consequently, a vast region of braided streams, marshes, and lakes is formed, resulting in a loss of the river's potential flow due to seepage and evaporation (Figure 3.1). To better represent the river dynamics, two dams, Kainji and Jebba, which are used to generate hydropower in Nigeria, are also considered (Figure 3.1).

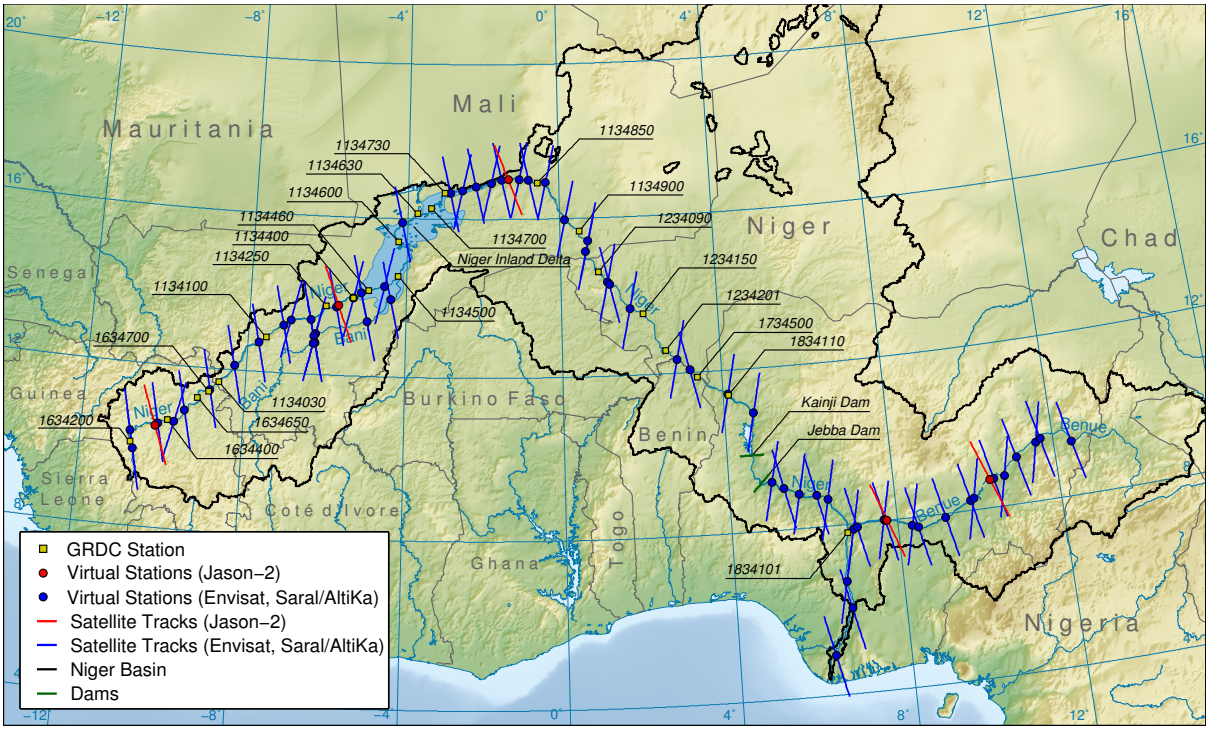

Fig. 3.1: The Niger River flows through 5 countries: Guinea, Mali, Niger, Benin, Nigeria, and its two major tributaries, Bani and Benue. Red and blue lines and dots represent the groundtrack and the selected virtual stations from Jason-2 and ENVISAT, SARAL/AltiKa, respectively.

3.2.1 In situ river discharge over the Niger River

Table 3.2 lists the in situ data, sorted according to river streamflow, taken from GRDC, with the locations of these stations along the Niger River indicated in Figure 3.1. The Koulikoro, Dire, Niamey, and Lokoja are the only gauging stations for which the data is available after 2002. To represent the magnitude of river discharge at the different gauging stations, the mean daily discharge of different stations is plotted in a Hovmöller diagram (Figure 3.2). This diagram indicates a clear seasonal behaviour of discharge with a time lag pattern along the streamflow. The river flows with high velocity from August to October between the longitudes of $-9°$ and $-4°$, which is slowed down when the river reaches the Inner Niger Delta. The

Tab. 3.2: Available *in situ* river discharge stations over the Niger basin from the Global Runoff Data Center (GRDC)

station	country	lat	long	area	station No.	start	end
Faranah	Guinea	10.03	−10.75	71054	1634200	1955	2001
Kouroussa	Guinea	10.65	−9.87	596423	1634400	1923	2002
Tiguibery	Guinea	11.25	−9.17	118415	1634650	1952	1979
Dialakoro	Guinea	11.42	−8.91	2069197	1634700	1954	1980
Banankoro	Mali	11.68	−8.67	1542735	1134030	1967	2001
Koulikoro	Mali	12.87	−7.55	667686	1134100	1907	2006
Kirango Aval	Mali	13.72	−6.05	3209	1134250	1925	2001
Ke-Macina	Nali	13.95	−5.37	715793	1134400	1953	1992
Tilembeya	Mali	14.15	−4.98	132864	1134460	1922	1992
Nantaka (Mopti)	Mali	14.53	−4.22	16756	1134500	1922	2001
Akka	Mali	15.4	−4.23	133668	1134600	1987	1990
Tonka	Mali	16.13	−3.75	134465	1134630	1954	1992
Dire	Mali	16.27	−3.38	275389	1134700	1924	2003
Koryoume	Mali	16.67	−3.03	1266556	1134730	1963	2001
Tossaye	Mali	16.93	−0.58	301846	1134850	1954	1992
Ansongo	Mali	15.67	0.50	340103	1134900	1950	2001
Kandadji	Niger	14.62	0.98	68078	1234090	1975	2002
Niamey	Niger	13.52	2.08	68809	1234150	1929	2006
W	Niger	12.58	2.62	362037	1234201	1985	2002
Malanville	Benin	11.87	3.38	378835	1734500	1952	2000
Yidere Bode	Nigeria	11.38	4.13	416723	1834110	1984	2002
Lokoja	Nigeria	7.80	6.77	529977	1834101	1970	2006

increase in mean daily discharge at Lokoja station happens due to the inflow contribution of the Benue River.

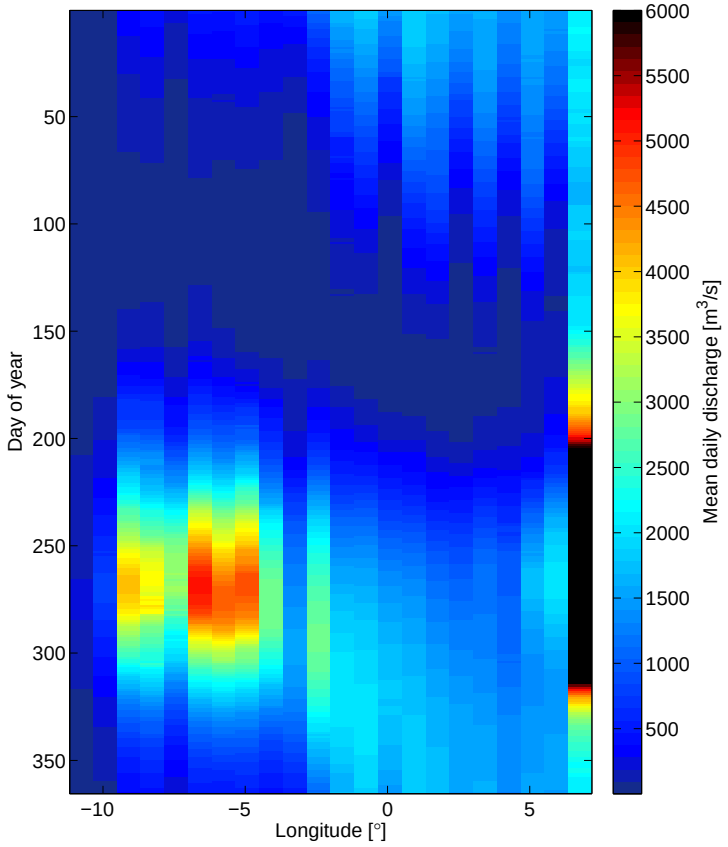

Fig. 3.2: Hovmöller diagram of mean daily discharge of 22 gauging stations along the Niger River

The discharge values are converted to runoff quantities in mm/day by dividing them by the corresponding basin area and multiplying by 86,400 (Table 3.2). Figure 3.3 illustrates the available time series of *in situ* discharge, expressed in mm/day, from 1970 to 2016.

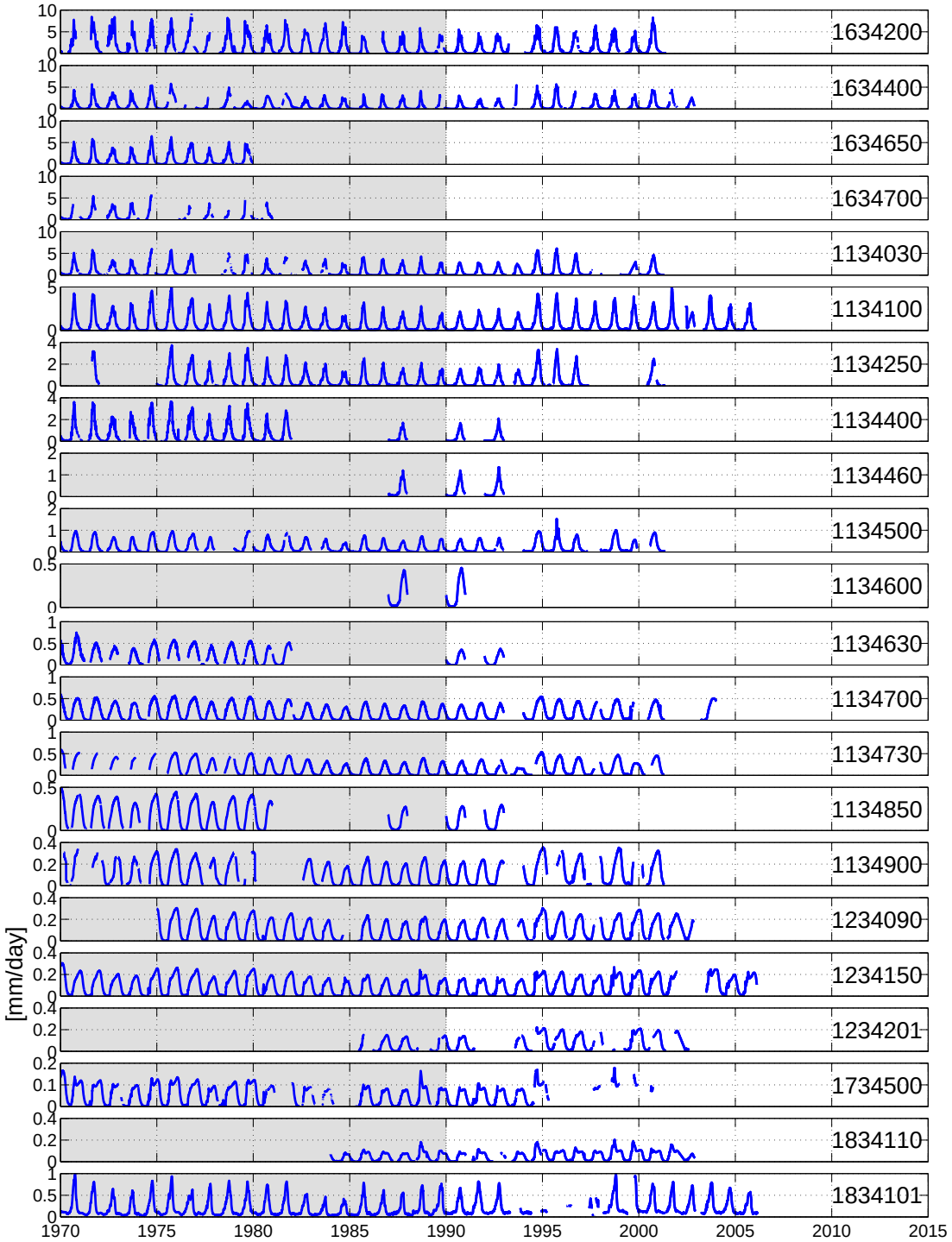

Fig. 3.3: Available *in situ* discharge time series from GRDC along the Niger River. The time period with a gray background indicates the training period.

3.2.2 Altimetric water level time series over the Niger River

Water level time series for 68 virtual stations along the Niger River, Bani River, and Banue River are obtained using the satellite altimeter mission ENVISAT (ENV) (ESA, 2007), Jason-2 (JA2) (CNES, 2011), and SARAL/AltiKa (SAR) (CNES, 2013). Table 3.3 lists all 68 virtual stations along the Niger, Bani, and Benue rivers.

Tab. 3.3: Available water level time series from altimetry

km	ID	Lon	Lat	Avg. Height	Amp.	Points	ENV.	JA2	SAR	Quality
Niger River										
50	1560	−10.67	9.87	426.49	5.40	100	+	—	+	0.93
113	1559	−10.77	10.31	404.74	3.94	100	+	—	+	0.86
233	1557	−10.16	10.47	371.21	4.14	171	—	+	—	0.85
244	1556	−10.10	10.53	363.58	5.47	96	+	—	+	0.85
310	1555	−9.71	10.62	358.24	5.82	94	+	—	+	0.87
358	1554	−9.47	10.92	349.71	5.62	102	+	—	+	0.90
476	1553	−8.87	11.46	335.18	6.35	96	+	—	+	0.82
579	1489	−8.30	12.11	326.62	5.65	93	+	—	+	0.89
691	1487	−7.73	12.73	299.64	8.06	107	+	—	+	0.89
781	1486	−7.11	13.18	287.63	6.45	104	+	—	+	0.84
809	1485	−6.94	13.33	286.04	5.20	103	+	—	+	0.87
863	1484	−6.43	13.36	282.84	4.35	108	+	—	+	0.81
2514	1482	−5.79	13.72	275.20	6.79	107	+	—	+	0.87
2520	1510	−5.73	13.75	275.09	6.45	271	—	+	—	0.88
2575	1481	−5.36	13.95	271.84	5.88	108	+	—	+	0.89
2600	1480	−5.16	14.08	270.54	6.32	108	+	—	+	0.84
2671	1479	−4.57	14.27	267.03	5.38	96	+	—	+	0.90
2941	1495	−4.14	15.89	260.68	5.15	108	+	—	+	0.93
3151	1492	−2.88	16.67	258.52	4.86	107	+	—	+	0.97
3189	1491	−2.56	16.73	258.06	4.80	98	+	—	+	0.89
3236	1490	−2.20	16.83	257.26	4.91	109	+	—	+	0.96
3287	1475	−1.80	16.92	256.79	4.71	108	+	—	+	0.93
3318	1474	−1.52	17.01	256.28	4.36	104	+	—	+	0.97
3337	1404	−1.35	17.01	256.65	3.12	216	—	+	—	0.95
3373	1403	−1.06	17.01	254.93	3.09	103	+	—	+	0.96
3401	1405	−0.81	17.00	253.16	3.95	102	+	—	+	0.94
3458	1406	−0.36	16.94	251.21	4.66	82	+	—	—	0.91
3580	1407	0.13	15.97	245.75	3.97	108	+	—	+	0.97
3682	1408	0.72	15.42	236.59	4.10	103	+	+	+	0.91
3716	1409	0.66	15.15	232.75	3.16	106	+	—	+	0.93
3832	1410	1.19	14.35	204.12	4.21	104	+	—	+	0.93
3836	1411	1.25	14.31	203.54	3.52	101	+	—	+	0.92
3937	1496	1.76	13.66	184.24	3.79	75	+	—	+	0.89
4183	1515	2.89	12.33	163.18	2.94	102	+	—	+	0.78
4227	1516	3.20	12.07	159.78	5.12	102	+	—	+	0.79
4363	1517	4.12	11.40	148.25	7.34	102	+	—	+	0.78
4459	1519	4.72	10.90	137.99	7.48	109	+	—	+	0.91
4711	1520	5.06	9.17	70.14	6.32	109	+	—	+	0.59
4749	1521	5.33	8.99	65.25	3.87	90	+	—	+	0.57
4798	1283	5.69	8.83	59.27	5.44	102	+	—	+	0.52
4845	1522	6.10	8.76	54.14	4.66	102	+	—	+	0.70
4883	1523	6.37	8.65	49.97	6.36	107	+	—	+	0.66
5130	1571	6.65	6.65	22.38	8.45	110	+	—	+	0.84
5205	1524	6.72	6.01	15.23	7.89	108	+	—	+	0.89
5352	1528	6.23	4.92	2.85	5.84	106	+	—	+	0.84
Benue River										
278	1586	12.44	9.31	153.04	5.09	84	+	—	+	0.72
377	1585	11.69	9.49	132.71	5.34	108	+	—	+	0.85
392	1584	11.57	9.41	129.50	6.67	83	+	—	+	0.85
458	1280	11.06	9.13	117.04	6.58	109	+	—	+	0.87
522	1583	10.69	8.72	107.14	7.09	100	+	—	+	0.87
557	1582	10.43	8.69	102.29	7.72	108	+	—	+	0.87
567	1581	10.33	8.68	101.69	7.83	263	—	+	—	0.87
644	1580	9.89	8.28	89.30	6.67	112	+	—	+	0.92
654	1279	9.81	8.23	87.85	6.85	109	+	—	+	0.91
735	1578	9.16	7.91	75.21	9.57	76	+	—	+	0.87
821	1278	8.481	7.76	63.66	7.02	105	+	—	+	0.92
835	1277	8.341	7.81	61.09	7.12	110	+	—	+	0.92
906	1576	7.742	8.01	51.41	8.51	258	—	+	—	0.92
909	1575	7.702	8.012	50.96	7.47	95	+	—	+	0.92
912	1574	7.672	8.022	49.85	6.86	106	+	—	+	0.93
990	1573	7.01	7.92	39.72	8.56	82	+	—	+	0.89
1000	1572	6.92	7.86	38.97	8.12	52	+	—	+	0.90
Bani River										
72	1497	−4.99	13.37	268.68	7.22	105	+	—	+	0.85
178	1509	−4.41	13.94	266.22	6.38	106	+	—	+	0.89
611	1504	−6.35	12.78	276.91	6.68	90	+	—	+	0.87
616	1503	−6.30	12.79	276.43	5.73	93	+	—	+	0.90
638	1501	−6.34	12.95	275.81	7.68	106	+	—	+	0.83
644	1500	−6.29	13.01	275.58	7.06	101	+	—	+	0.89

3.2.3 Altimetric discharge as observation

To estimate altimetric discharge at 22 gauging stations and incorporate them into the linear dynamic system, a dense time series of water levels at the gauging stations is first generated by merging the water level

time series of individual Virtual Stations (VSs), i.e., by densifying (Tourian et al., 2016). The water level time series and legacy discharge measurements at the gauges are then turned into quantile functions, from which the corresponding rating curves are obtained using the quantile matching approach (Tourian et al., 2013). To achieve a proper estimation of uncertainty for the estimated discharge, the Gauss-Helmert Model is employed to estimate the rating curve parameters. The subsequent sections provide a detailed description of the densification process and the discharge estimation steps.

Densification of water level time series

The individual water level time series along the Niger River and two tributaries of Benue and Bani are densified using the method developed by Tourian et al. (2016). They suggested a geodetic approach by which all VSs of several satellite altimeters are connected hydraulically and statistically to produce water-level time series at any location along the river. By this, one can generate water level time series with an improved temporal resolution of $\sim$ 3-5 days at any given location along the Niger River.

Densified altimetric water level time series are generated at the locations of *in situ* gauging stations listed in Table 3.2 to be incorporated into the observation equation of the linear process model. Various data selection setups are employed to obtain these densified water level time series, taking into account

- Case 1: all VSs along the Niger River (45 VSs)
- Case 2: all VSs of Niger including those over the Bani tributary (51 VSs)
- Case 3: all VSs of Niger including those over the Benue tributary (62 VSs)
- Case 4: all VSs of Niger including those over the both Bani and Benue tributaries (68 VSs)
- Case 5: similar to case 4 but with dam consideration
- Case 6: similar to case 5 but also with consideration of Niger inner delta

For Case 5, VSs located upstream of the two major dams, Kainji and Jebba, are used to densify the altimetric water level time series for the 21 gauging stations situated upstream of these dams. Conversely, for the gauging station at Lokoja, located downstream of the dams, corresponding VSs are utilized. In Case 6, the densification process is differentiated based on location: 1) Upstream of the Niger inner delta, 2) Downstream of the inner delta and upstream of the dam, and 3) Downstream of the dams. Due to the availability of a relatively high number of VSs for these cases, the densified time series are obtained with a temporal resolution of 1–2 days, derived from individual time series with original sampling intervals of 10 or 35 days.

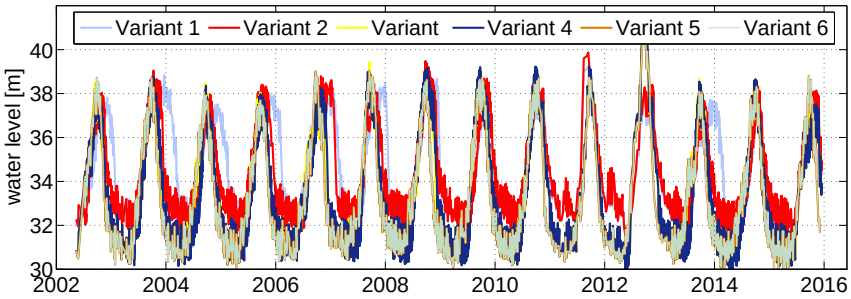

Fig. 3.4: Densified altimetric water level time series at Lokoja station, GRDC no. 1834101, using five different setups for the selection of VS

Figure 3.4 shows the densified altimetric water level time series at Lokoja GRDC station using the aforementioned six different variants for the selection of VSs. The time series of cases 1 and 2 show different characters in comparison to those for cases 3,4, 5, and 6. This is predominantly because water level

variation of the tributary Benue is not considered for cases 1 and 2. The tributary Benue matters for the Lokoja station since it is located downstream of the confluence point of the Benue and Niger.

Estimation of altimetric river discharge and its uncertainty

To estimate river discharge $\boldsymbol{Q}$ from altimetric water level time series $\boldsymbol{H}$, one has to obtain a functional relationship, the so-called rating curve, which maps water level variation $\boldsymbol{\Delta H}$ to river discharge discharge $\boldsymbol{Q}$ (Gleason and Smith, 2014)

$$\boldsymbol{Q} + \boldsymbol{e} = a(\boldsymbol{\Delta H})^b \ . \tag{3.25}$$

The water level variation $\boldsymbol{\Delta H}$ can be derived by defining a reference level H_0: $\boldsymbol{\Delta H} = \boldsymbol{H} - H_0$. The parameters a and b are estimated by minimizing the norm of model inconsistencies $\boldsymbol{e}$ in (3.25). For such minimization, often the water level and river discharge time series are treated as noise-free data sets, which is not the case neither for water level from altimetry nor for the measured discharge at the gauge. Such limitation is lifted by implementing a Gauss-Helmert Model (GHM). In the GHM, two parameters of $\boldsymbol{e}_{\mathrm{Q}}$ and $\boldsymbol{e}_{\mathrm{H}}$ are added to the equation (3.25), representing the error in discharge and error in water level time series, respectively

$$\boldsymbol{Q} - \boldsymbol{e}_{\mathrm{Q}} - a(\boldsymbol{\Delta H} - \boldsymbol{e}_{\mathrm{H}})^b = f(a, b, \boldsymbol{e}_{\mathrm{Q}}, \boldsymbol{e}_{\mathrm{H}}) = 0 \ . \tag{3.26}$$

With such formulation a functional relatinship $f(.)$ with unknown parameters of $a, b, \boldsymbol{e}_{\mathrm{Q}}, \boldsymbol{e}_{\mathrm{H}}$ is obtained. It can be linearized by splitting up the quantities

$$\begin{aligned} a &= a_0 + \Delta a, \ \ b = b_0 + \Delta b \\ e_{\mathrm{Q}} &= \boldsymbol{e}^{\mathrm{o}}_{\mathrm{Q}} + \Delta e_{\mathrm{Q}}, \ \ e_{\mathrm{H}} = \boldsymbol{e}^{\mathrm{o}}_{\mathrm{H}} + \Delta e_{\mathrm{H}} \end{aligned} \tag{3.27}$$

and choose a Taylor point related to both parameters and uncertainties: a_0, b_0, $\boldsymbol{e}^{\mathrm{o}}_{\mathrm{Q}}$ and $\boldsymbol{e}^{\mathrm{o}}_{\mathrm{H}}$.

After linearizing Equation (3.26) using a Taylor series expansion and minimizing the objective function, the rating curve parameters a and b are estimated. The covariance matrix is then used to estimate the uncertainties for these parameters, denoted as $\sigma_{\hat{a}}$ and $\sigma_{\hat{b}}$. A detailed description of the Gauss-Helmert Model is provided in Appendix A. For the implementation of the Gauss-Helmert Model, 10% of the measured discharge is used as the error for discharge ($\mathrm{e_Q}$), and the estimated error from the altimetry processing is used for $\mathrm{e_H}$.

Uncertainty estimation

By solving the Gauss-Helmert model and deriving the covariance matrix, the parameters a and b are obtained along with their uncertainties. These uncertainties are then used to propagate errors, allowing for the estimation of the error in the estimated discharge.

$$\sigma^2_{\hat{\mathrm{Q}},t} = \boldsymbol{\Delta H_t}^{2\hat{b}} \sigma^2_{\hat{\mathrm{a}}} + (\hat{a}\hat{b}\boldsymbol{\Delta H_t}^{\hat{b}-1})^2 \sigma^2_{\Delta \mathrm{H_t}} + [\hat{a}\boldsymbol{H}^{\hat{b}} \log(\boldsymbol{\Delta} H_t)]^2 \sigma^2_{\hat{\mathrm{b}}} \tag{3.28}$$

Figure 3.5 shows the estimated uncertainty of discharge using water level time series from all cases of densification for the outlet gauge of the Niger basin at Lokoja. Similar to this gauge, the estimated errors $\sigma^2_{\hat{\mathrm{Q}}}$ for all other gauges are also proportional to the estimated discharge and vary on average 10–20% of discharge.

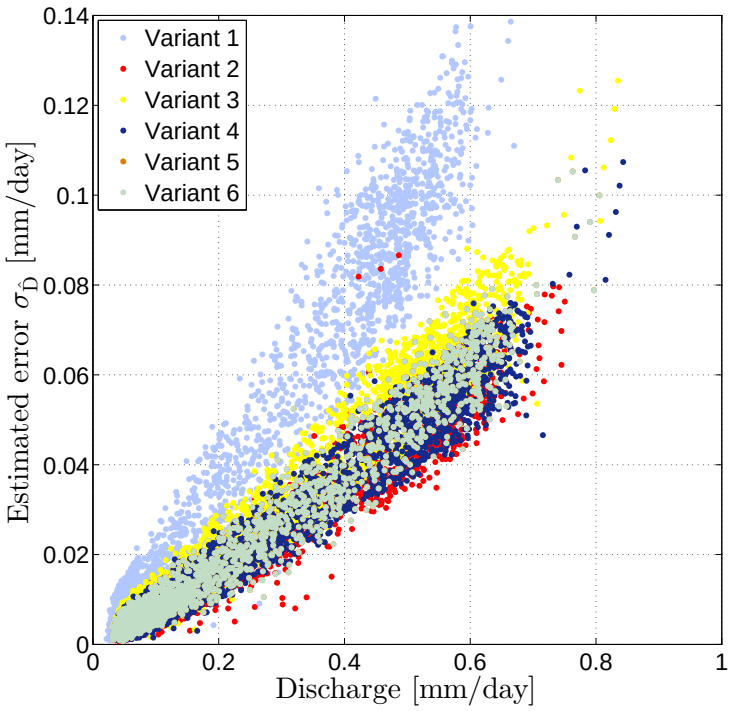

Fig. 3.5: Estimated uncertainty of discharge using water level time series from all cases of densification for the outlet gauge of Niger basin at Lokoja

Dealing with non-simultaneous measurements of discharge and water level

Above all the aforementioned formulation, one has to form rating curve model using corresponding measurements of water level and discharge. However, synchronous time series of sufficient duration are only available for a limited set of discharge gauges. This limitation was dealt with to a great extent by Tourian et al. (2013) who predicted discharge through quantile function mapping. By their method, the statistics of pre-altimetry discharge data can in principle be employed for discharge prediction in the altimetry time frame. This means the rating curve parameters can be derived from the corresponding quantile functions of water level measurements $\boldsymbol{q}_{\mathrm{H}}$ and legacy discharge $\boldsymbol{q}_{\mathrm{Q}}$, rather than from their time series. In other words, in equation (3.29), $\boldsymbol{H}$ can be replaced with $\boldsymbol{q}_{\mathrm{H}}$ and $\boldsymbol{Q}$ can be replaced with $\boldsymbol{q}_{\mathrm{Q}}$

$$\boldsymbol{q}_{\mathrm{Q}} + i = a(\boldsymbol{q}_{\mathrm{H}} - H_0)^b \quad . \tag{3.29}$$

Figure 3.6 shows obtained rating curves from quantile matching, all cases shown in gray, and fitted rating curve models with consideration of Gauss-Helmert using water level time series from all cases of densification for six selected gauges. As can be seen in the figure, quantile matching-driven rating curves of some gauges show peculiar behaviour with a bulge in the middle for some of the cases. This is because of densifying, inconsistent altimetric time series at the selected gauge. For instance, for the gauges of 1134700 and 1234150, which are located between the Inner Niger Delta and dams, only water level time series from case 6 of densification lead to a meaningful rating curve.

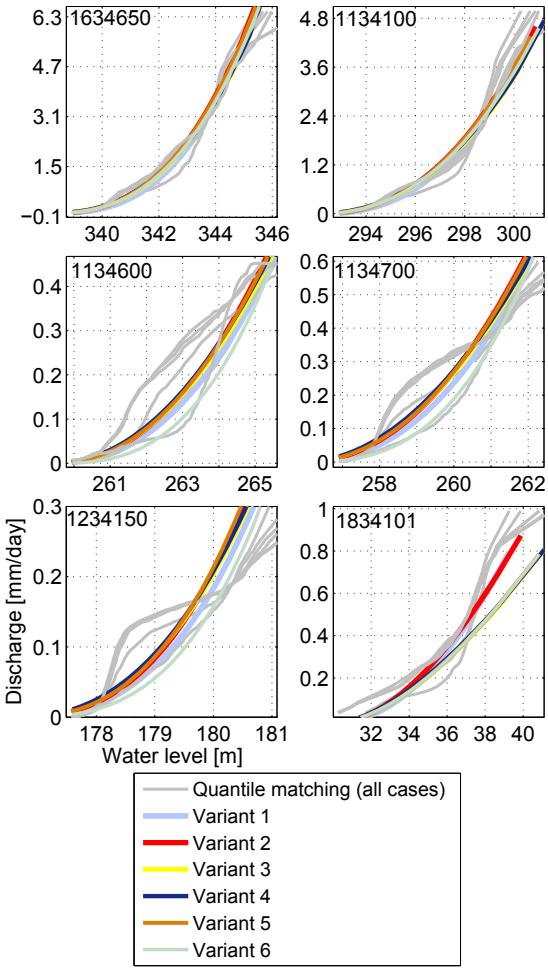

Fig. 3.6: Obtained rating curves from quantile matching for all cases (gray) and fitted rating curve models using Gauss-Helmert consideration using water level time series from all cases of densification for six selected gauges

3.2.4 Forming observation equations

In general the observation vector $\boldsymbol{Z}_t$, formulated in equation (3.24), can contain *in situ* measurements of discharge $\boldsymbol{Q}_{\mathrm{ins},t}$ together with the estimated altimetric discharge $\boldsymbol{Q}_{\mathrm{alt},t}$:

$$\boldsymbol{Z}_t = \begin{bmatrix} \boldsymbol{Q}_{\mathrm{alt},t} \\ \boldsymbol{Q}_{\mathrm{ins},t} \end{bmatrix}, \tag{3.30}$$

So that the design matrix is populated with unit matrices

$$\boldsymbol{O} = \begin{bmatrix} \boldsymbol{I} \\ \boldsymbol{I} \end{bmatrix}. \tag{3.31}$$

The estimated error, estimated in (3.28), can then be assigned to the $\boldsymbol{\Sigma}_{x,t}$ matrix, which contains the covariance information of observations at each time t

$$\boldsymbol{\Sigma}_{x,t} = \begin{bmatrix} \sigma^2_{\hat{\mathrm{Q}},t} & 0 \\ 0 & \sigma^2_{\mathrm{ins},t} \end{bmatrix} \tag{3.32}$$

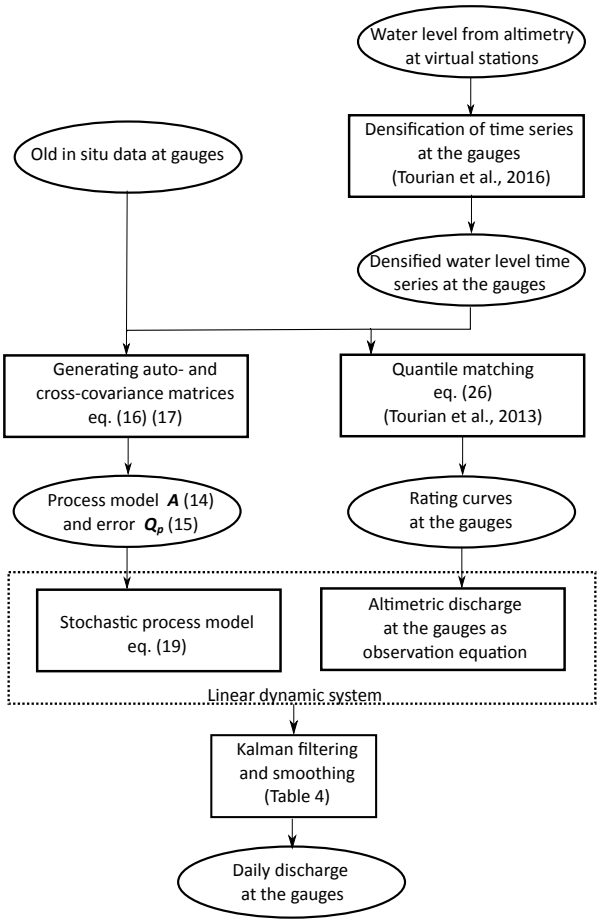

Fig. 3.7: Flow diagram of the proposed methodology to estimate daily discharge time series over an entire river basin

$\sigma_{\mathrm{ins},t}$ refers to uncertainties of available *in situ* measurements of discharge, and the observations from different sources can be assumed to be uncorrelated.

Here, since the *in situ* data are used solely for validation purposes, they are not incorporated into the observation equation. Therefore, the observation vector is defined as:

$$\boldsymbol{Z}_t = \left[\boldsymbol{Q}_{\mathrm{alt},t}\right], \tag{3.33}$$

and covariance matrix consists of

$$\boldsymbol{\Sigma}_{x,t} = \left[\sigma^2_{\hat{\mathrm{Q}},t}\right], \tag{3.34}$$

The matrix $\boldsymbol{O}$ in the equation (3.24) is then an identity matrix with the size of the observation vector.

Figure 3.7 summarizes the proposed algorithm to estimate daily discharge time series over an entire river basin.

3.3 Results and validation

To estimate daily river discharge along the Niger River and implement the proposed methodology, a training period between 1970–1990 and a validation period from 1990–2016 are defined (Figure 3.3). The available *in situ* daily discharge is utilized to train the stochastic process model, forming the linear dynamic system with the help of altimetric discharge. Since only one year of discharge data is available during the

training period for two gauging stations (1134460 and 1134600), these stations are excluded from the investigations.

To build the stochastic process model described in Section 3.1, the time series of residual daily discharge $\boldsymbol{r}_t$ is first derived, for which mean daily discharge is removed from daily values. Using equation (3.2), mean daily values are estimated from all available data until the end of the training period (until the end of 1989). From the obtained residual time series of 20 gauging stations, $\widehat{\boldsymbol{A}}$ and $\boldsymbol{\Sigma}_{\mathrm{P}}$ are derived by estimating $\boldsymbol{\Sigma}$ and $\boldsymbol{\Sigma}_{\Delta}$ (3.17). Figure 3.8 shows the estimated process model $\widehat{\boldsymbol{A}}$, representing both spatial and temporal covariance of residual daily discharge along the Niger River. In other words, the matrix indicates how the residual daily river discharge at different stations along the Niger at time t can be estimated from the residual daily river discharge at $t-1$.

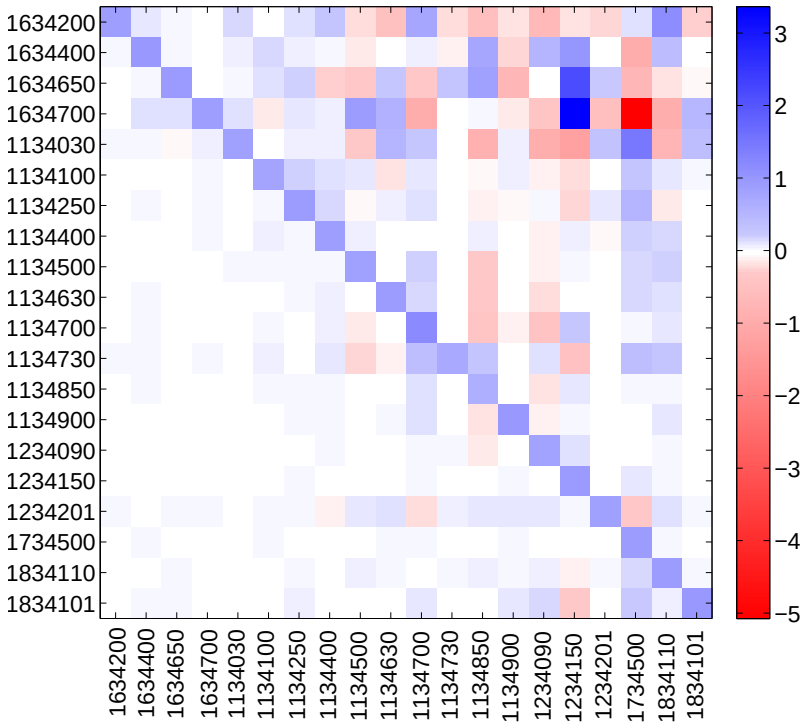

Fig. 3.8: Estimated process model $\widehat{\boldsymbol{A}}$ of residual daily river discharge for 20 gauging stations along the Niger River

To generate the prior, the stochastic process model evolves with the help of its predictor $\widehat{\boldsymbol{A}}$ (Figure 3.8) under the control of $\boldsymbol{G}\boldsymbol{U}_{t-1}$. The control input $\boldsymbol{G}\boldsymbol{U}_{t-1}$ adds the mean daily discharge at time t minus $\widehat{\boldsymbol{A}}\widetilde{\boldsymbol{Q}}_{t-1}$ to the process model, which leads to adding a prediction for residual discharge to the legacy mean daily discharge $\widetilde{\boldsymbol{Q}}_{t-1}$ (see equation (3.21)). In essence, the process model is allowed to estimate discharge within the range of process noise $\boldsymbol{\Sigma}_{\mathrm{P}}$. Figure 3.9 shows the process noise $\boldsymbol{\Sigma}_{\mathrm{P}}$, estimated from residual daily river discharge of 20 gauging stations along the Niger River. In this matrix, the diagonal elements refer to the variance of process noise for river discharge estimation. After obtaining the initial prediction, the state prediction covariance is computed by adding the process noise to the propagated error of the process model (see Table 3.1).

By bringing the observation equation with corresponding covariance information $\boldsymbol{\Sigma}_{x,t}$ into the dynamic system, the predicted discharge by the prior is updated through the estimation of prediction covariance $\boldsymbol{S}_t$ and Kalman gains $\boldsymbol{K}_t$, which essentially generate the likelihood function. The prediction covariance $\boldsymbol{S}_t$ is formed by adding the covariance matrix of observation $\boldsymbol{\Sigma}_{x,t}$ to the propagated covariance matrix of the observation equation, considering the state prediction covariance $\boldsymbol{P}_t^-$ for discharge (Table 3.1). The estimated discharge is then corrected by adding the multiplication of Kalman gain and observation innovations. Since the Kalman filtering is used in this study for assimilation purposes and not for prediction

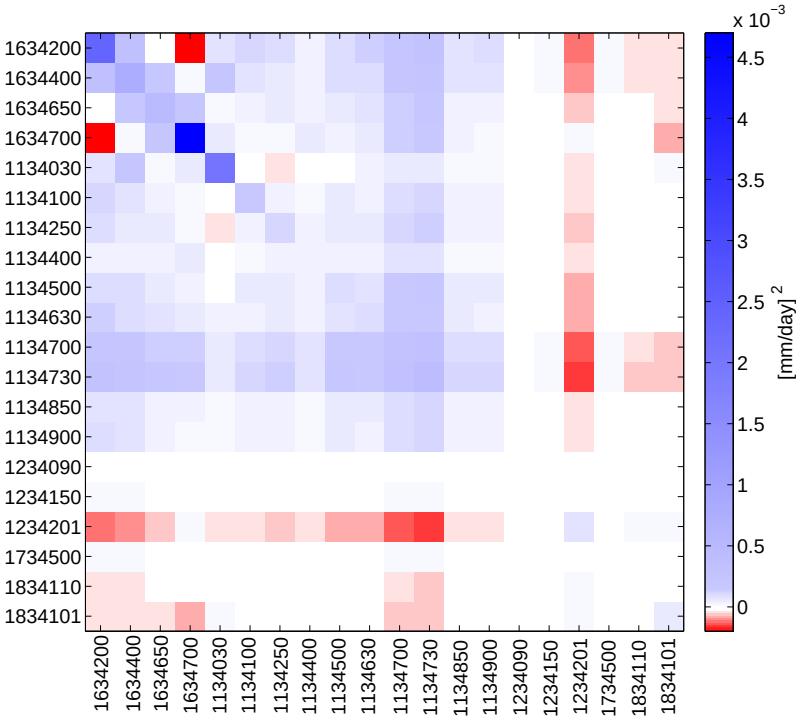

Fig. 3.9: Estimated state prediction covariance $\boldsymbol{\Sigma}_{\mathrm{P}}$ of residual daily river discharge for 20 gauging stations along the Niger River

purposes, the discharge estimation is smoothed by the backward estimation of smoothing gain $\boldsymbol{K}_t^*$ as indicated in Table 3.1.

Figure 3.10 shows the estimated daily river discharge from Kalman filtering and consecutive smoothing. For the results in Figure 3.10, the observation from case 6 of densification is used. Obviously, with the choice of ENVISAT, Jason 2, and SARAL/AltiKa for altimetry, the estimated altimetric discharge time series are only available after 2002. Since the *in situ* data were excluded from observation for validation purposes, the Kalman filtering and smoothing results before 2002 primarily relied on the process model itself. This is evident from the left panel of Figure 3.11. This figure provides a zoomed-in version of 6 stations of Figure 3.10. By comparing the smoothed discharge (red curve) with the mean daily discharge (gray curve), it becomes evident that when altimetric discharge data is not available, the estimated discharge largely depends on the control input (mean daily discharge) combined with an additional term derived from the spatial correlation of residual daily discharge.

The estimated discharge for stations 1134400 and 1734500 emphasizes the fact that even a process model that considers the spatiotemporal covariance information along an entire river system cannot properly capture the daily river discharge in the absence of altimetry. In the right panel of Figure 3.11, three examples illustrate the impact of assimilating altimetric discharge with the stochastic process model. For gauge 1134100, the estimated discharge demonstrates a clear improvement over the mean daily discharge from legacy data due to the incorporation of altimetric discharge. This enhancement is evident when comparing the estimated discharge with *in situ* measurements and the mean daily discharge. For gauge 1234150, shown in a zoomed-in view before and after the availability of altimetric discharge, the effect is even more noticeable. A systematic time delay between the estimated and *in situ* discharge is apparent until October 2002. This discrepancy is partially addressed by incorporating altimetric discharge data. However, discrepancies persist, primarily due to complex reaches with abrupt changes in slope or morphology between consecutive VSs in the densification scheme.

Further findings from the results of gauge 12345150 include the importance of performing a smoothing procedure after the Kalman filtering. The undesirable outcome of Kalman filtering for March to April 2003 was resolved after applying the smoothing procedure. This is also the case for stations that are located downstream of the Inner Niger Delta and upstream of dams in winter 2012. Such noisy estimation happens due to a significant difference between the control input (mean daily discharge) and the altimetric discharge.

To validate the estimated time series $\boldsymbol{Q}$ of river discharge against *in situ* data $\boldsymbol{Q}_{\mathrm{ins}}$, the following metrics are used:

- Correlation Coefficient (CC), which represents the agreement of time series in terms of temporal behaviour
- Relative Root Mean Squared Error (Rel. RMSE)

$$\mathrm{Rel.\,RMSE} = \frac{\mathrm{RMSE}}{\mathrm{RMS}(\boldsymbol{Q}_{\mathrm{ins}})} \tag{3.35}$$

- Relative bias

$$\mathrm{Rel.\,bias} = \frac{(\overline{\boldsymbol{Q}} - \overline{\boldsymbol{Q}}_{\mathrm{ins}})}{\mathrm{RMS}(\boldsymbol{Q}_{\mathrm{ins}})} \tag{3.36}$$

- Nash-Sutcliffe Efficiency (NSE) coefficient

$$\mathrm{NSE}_{\mathrm{mean}} = 1 - \frac{\sum(\boldsymbol{Q}_{\mathrm{ins}} - \boldsymbol{Q})^2}{\sum(\boldsymbol{Q}_{\mathrm{ins}} - \overline{\boldsymbol{Q}}_{\mathrm{ins}})^2}$$

- An alternative formulation of the NSE coefficient, which takes the legacy mean daily cycle of a variable into account. This metric is introduced to evaluate the estimated discharge against available mean daily values of old data $\tilde{\boldsymbol{Q}}_{\mathrm{ins}}$

$$\mathrm{NSE}_{\mathrm{cycle}} = 1 - \frac{\sum(\boldsymbol{Q}_{\mathrm{ins}} - \boldsymbol{Q})^2}{\sum(\boldsymbol{Q}_{\mathrm{ins}} - \tilde{\boldsymbol{Q}}_{\mathrm{ins}})^2} \tag{3.37}$$

  A positive $\mathrm{NSE}_{\mathrm{cycle}}$ indicates that the estimated discharge $\boldsymbol{Q}$ outperforms the mean daily values of old data $\tilde{\boldsymbol{Q}}_{\mathrm{ins}}$.

Using these performance metrics, the estimated discharge (smoothed version) is validated against *in situ* data. For the validation, two gauges, Tiguibery (1634650) and Dialakoro (1634700), are excluded since the discharge was not measured between 1990–2016. Figure 3.12 shows different performance metrics along the Niger River for different cases of densification of time series from satellite altimetry. Overall, the validation results show an average CC of 0.9, an average relative RMSE and relative bias of 15%, $\mathrm{NSE}_{\mathrm{mean}}$ greater than 0.5 for 15 gauges, and almost $\mathrm{NSE}_{\mathrm{cycle}}$ above 0 for all gauges.

The high $\mathrm{NSE}_{\mathrm{mean}}$ coefficients (around 0.8) for many gauges indicate that the method provides an acceptable daily discharge time series. However, for three gauges—1134400, 1134630, and 1134850—the $\mathrm{NSE}_{\mathrm{mean}}$ values are not as favorable, which aligns with the observed relative bias values for these gauges. Such large relative biases can be explained by a biased control input (mean daily discharge) in the process model for these gauges, which can be described by the non-stationary behaviour of discharge. Since these stations are located around the Inner Niger Delta, regime changes upstream or downstream due to possible river management are highly expected. On the other hand, for these stations, the available daily discharge time series during the validation period is scant and discontinuous, which hinders us from further interpretations.

From an operational standpoint, the estimated discharge must surpass the mean daily discharge derived from historical data. The metric $\mathrm{NSE}_{\mathrm{cycle}}$ is specifically designed to evaluate this performance by comparing the estimated discharge with the mean daily values of older data. Although $\mathrm{NSE}_{\mathrm{cycle}}$ and $\mathrm{NSE}_{\mathrm{mean}}$ share

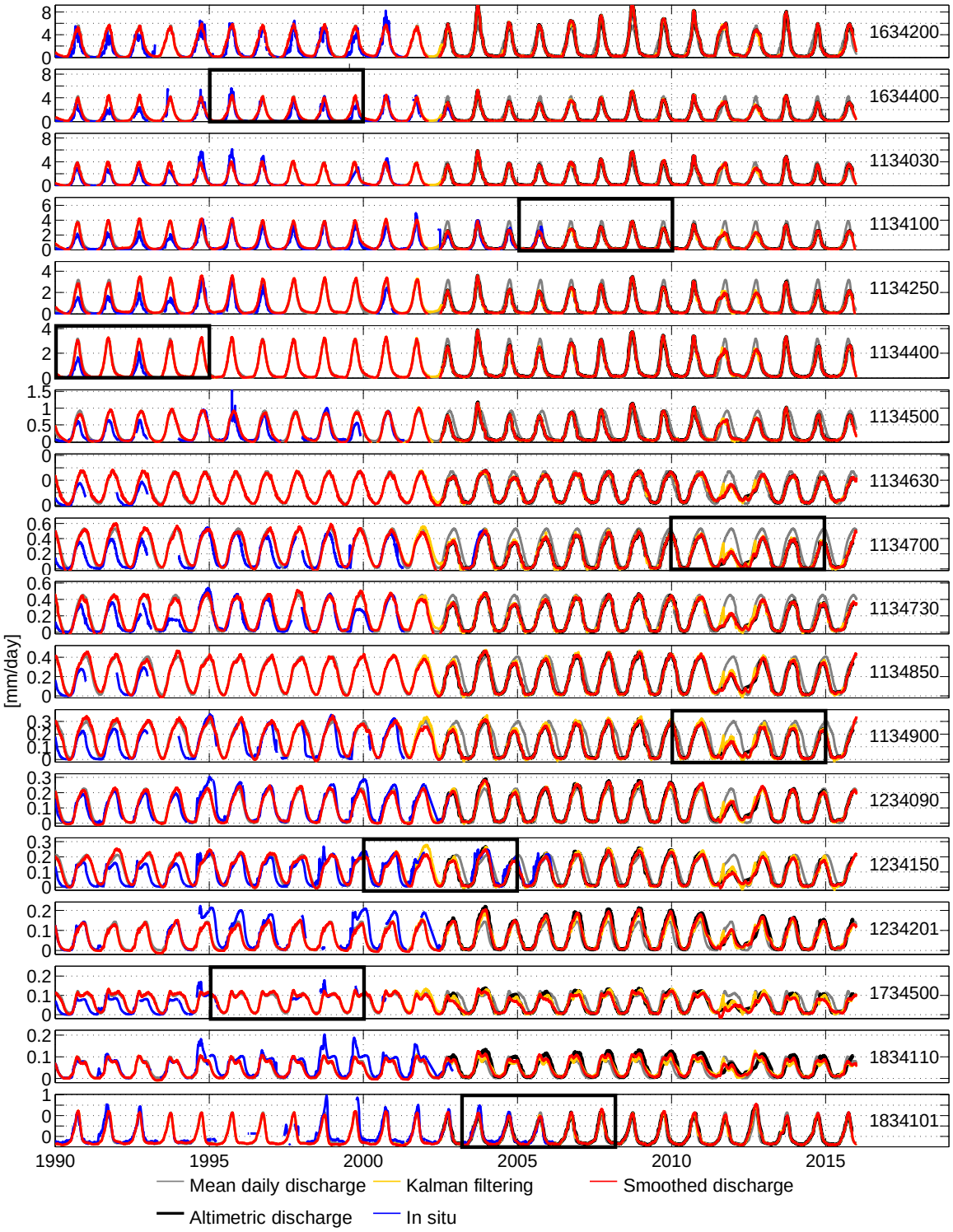

Fig. 3.10: Estimated daily river discharge at 18 gauging stations along the Niger River

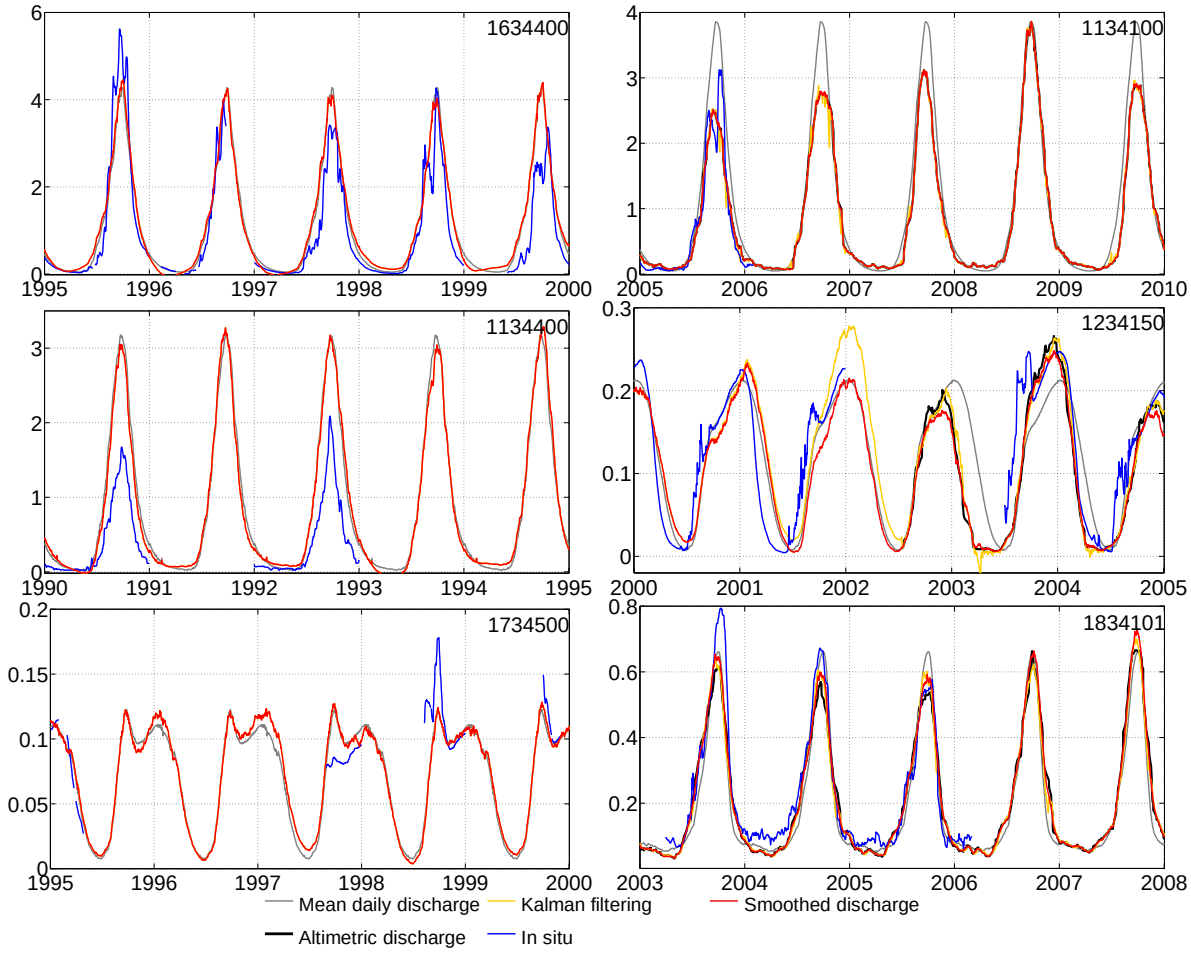

Fig. 3.11: Zoom in of estimated daily river discharge for 6 stations shown in Figure 3.10

similar names, they are interpreted differently. A $\mathrm{NSE}_{\mathrm{cycle}}$ value greater than 0 indicates that the estimated discharge exceeds the performance of the mean daily discharge, whereas a $\mathrm{NSE}_{\mathrm{mean}}$ value greater than 0.5 suggests acceptable performance. Among all the metrics used, only $\mathrm{NSE}_{\mathrm{cycle}}$ effectively captures the performance of different densification approaches. When using the results from case 1 in the observation equation, contributions from the Bani and Benue rivers, as well as the effects of dams and the Niger Inner Delta, are not considered. This case involves densifying 45 VSs along the Niger River, leading to a negative $\mathrm{NSE}_{\mathrm{cycle}}$ at Lokoja (1834101). This negative value arises because the Benue River, which significantly influences the discharge at Lokoja, is not included. Similarly, including only the Bani River in case 2 does not yield a positive $\mathrm{NSE}_{\mathrm{cycle}}$. A positive $\mathrm{NSE}_{\mathrm{cycle}}$ for this gauge is achieved only when incorporating the Benue River's contribution, which merges with the Niger River at Lokoja.

For the three problematic gauges—1134400, 1134630, and 1134850—positive $\mathrm{NSE}_{\mathrm{cycle}}$ values indicate that the estimated daily discharge surpasses the legacy mean daily data. Despite this, as illustrated for gauge 1134400 in Figure 3.11, the improvement is minimal. Given the limited *in situ* data available for these stations during the validation period, caution should be exercised in interpreting these modest improvements.

Overall, better performance metrics are received with case 6, which distinguishes between VSs of different river reaches with different flow characteristics. In case 6, even the Inner Niger Delta is considered, distinguishing between VSs located upstream and downstream of it, differentiating it from case 5. This consideration significantly influences the $\mathrm{NSE}_{\mathrm{cycle}}$ values of 1634400, 1134100, 11346700, 1234090, and 1234150. This emphasizes the need for a careful analysis and understanding of the river system for a successful densification process. Compared to the densification setup implemented by Tourian et al. (2016), an additional step is taken here by considering the effect of tributaries along the Niger River. However, as discussed by Tourian et al. (2016), proper densification is realized when a time-variable flow velocity is estimated instead of average flow velocity and when the channel geometry is properly characterized.

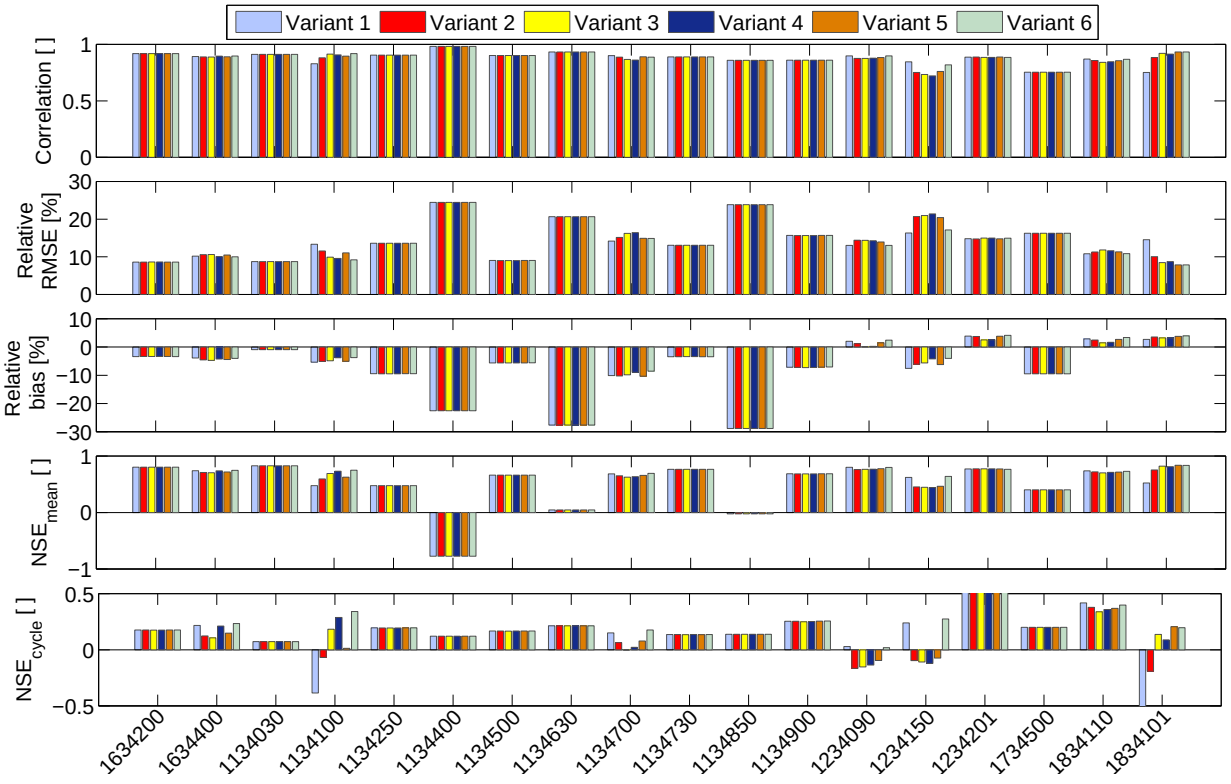

Fig. 3.12: Performance metrics of estimated discharge time series at 18 gauging stations along the Niger River for different cases of densification of altimetry

All in all, the validation results demonstrate that the algorithm can be confidently used to estimate daily discharge time series for an entire river basin. The validation results show that this method can even be used for operational purposes, as it delivers better estimates than the legacy mean daily data. Furthermore, within the developed methodology, an ensemble of SWOT discharge values from various existing estimation algorithms (Durand et al., 2023), along with altimetry-based and image-based discharge data of different river locations, can be ingested into the observation equation. This leads to an assimilated (combined) estimation of daily river discharge out of SWOT measurements at the full catchment scale.

4

A Bayesian framework for spatial downscaling of GRACE-derived terrestrial water storage data

The Gravity Recovery and Climate Experiment (GRACE) and its successor, the GRACE Follow-On (GRACE-FO), have significantly advanced our ability to measure Earth's gravity field variations and monitor large-scale water storage changes. However, these missions face inherent limitations related to spatial resolution. As discussed in Section 1.2.1, the highest spatial resolution achieved with GRACE and GRACE-FO is approximately 300–400 km, obtained with a monthly solution (Vishwakarma et al., 2018). Despite their valuable contribution to understanding large-scale hydrological processes, the spatial resolution of GRACE and GRACE-FO data constrains their utility primarily to large river basins and catchments (Lorenz et al., 2014; Tourian et al., 2015; Yi et al., 2017; Springer, 2019). The observed gravity signal from GRACE integrates mass changes over relatively large areas, making it difficult to detect localized variations, like river systems (see Figure 4.1).

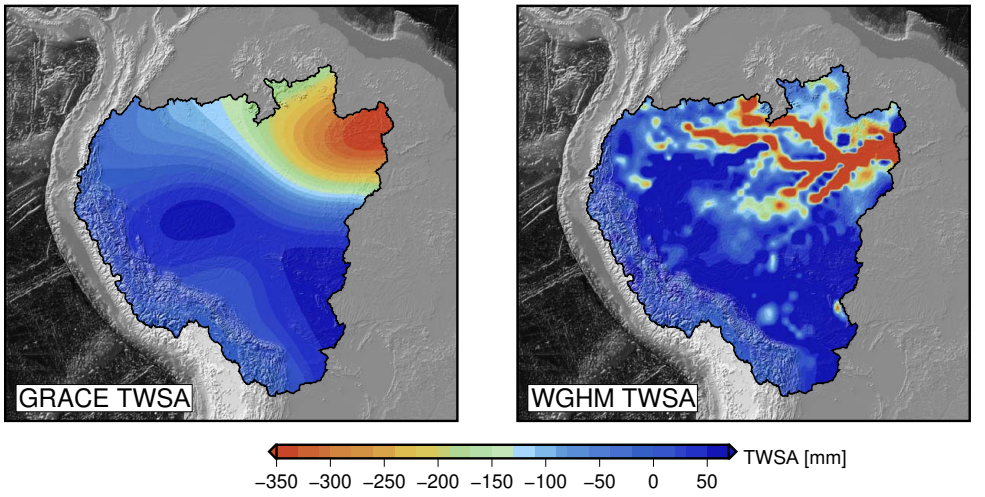

Fig. 4.1: Terrestrial Water Storage Anomaly (TWSA) over the Amazon Basin as obtained by GRACE after filtering (left) and by the WaterGAP Global Hydrology Model (WGHM) (right) for January 2005.

The resolution challenge is particularly significant in areas where water storage changes are influenced by smaller-scale hydrological processes, such as in small catchments, mountainous regions, or coastal aquifers. These regions often exhibit critical variations in water storage that are crucial for local ecosystems, agricultural activities, and human water consumption. The current spatial resolution limits the utility of GRACE-derived Terrestrial Water Storage Anomaly (TWSA) and its time derivative Terrestrial Water Storage Flux (TWSF) to large catchments. This limited spatial resolution also hinders a detailed understanding of water cycle dynamics and may overlook important hydrological changes in vulnerable areas where populations heavily depend on water resources.

To overcome the low spatial resolution of GRACE, it is required to use an additional dataset or a model with a better resolution. Many studies have addressed this limitation by assimilating or jointly evaluating GRACE

with a fine-scale dataset based on either statistical approaches, frequentist or Bayesian inference, or, more recently, machine learning methods.

In a purely statistical approach to downscaling, one can rely on multi- or bivariate linear relationships between a coarse-scale and fine-scale dataset(s) to obtain downscaled products. Following this approach, Yin et al. (2018) relied on the linear relationship between GRACE and fine-scale evapotranspiration data to improve the spatial resolution of GRACE-derived groundwater storage anomalies. With a similar perspective, Vishwakarma et al. (2021) benefited from th multivariate linear regression model to downscale GRACE water storage anomaly by relying on its linear relationship with water storage fields from the WaterGAP Global Hydrology Model (WGHM), three precipitation datasets, evapotranspiration, and two different runoff models. However, the linear statistical approaches usually face two problems 1) they ignore existing nonlinear relationships between fine- and coarse-scale datasets, and 2) they determine the downscaled products without taking the marginal or joint distribution of the datasets into account. The latter leads to the limitation that no distribution or, more precisely, no proper uncertainty can be derived for the obtained downscaled results.

While the first problem cannot be easily tackled, the Bayesian framework as described in Chapter 2 offers a solution to the second problem, which involves obtaining a posterior distribution for the target variable. For instance, Bayesian Model Averaging (BMA) has been employed to assimilate diverse GRACE products, integrating a priori knowledge, consolidating information from multiple models, and generating an uncertainty estimate (Long et al., 2017). Within the Bayesian framework, to obtain the posterior distribution, one possible solution is to make use of the Kalman Filter (see Chapter 3), where at each time point, the prior is determined by a process model, and the likelihood function is defined by the observation equation. Such a setup offers the possibility of either using coarse data within the process model to generate a prior or using it as an observation to generate the likelihood function. The latter has been practiced in several studies to downscale GRACE, where GRACE is assimilated with a land surface model (Zaitchik et al., 2008) or with WGHM (Eicker et al., 2014; Schumacher et al., 2018).

While the Kalman filter provides a posterior distribution for the target variable and thus uncertainty, it is limited by the fact that both the likelihood and the prior are assumed to be normally distributed, and being a conjugate prior, the posterior is also normally distributed. Therefore, the estimated uncertainty may be at most a proxy for the actual uncertainty. Indeed, in the Bayesian framework, it is possible to predetermine the distribution in advance and to draw indirect inferences about the posterior distribution. This is typically done by using a Markov chain to obtain a set of parameter values from the posterior distribution and using Monte Carlo integration to obtain a distribution estimate of the posterior distribution and the associated statistics with sampled parameters, the so-called Markov Chain Monte Carlo (MCMC)-based sampling techniques (described in Chapter 2) (van de Schoot et al., 2021). Such a technique has recently been employed to downscale GRACE water storage change data and generate groundwater and soil water storage changes at approximately 12.5 km resolution (Mehrnegar et al., 2021), as well as for the purpose of reconstructing GRACE mass changes time series to bridge the gap between GRACE and GRACE-FO (Rateb et al., 2022).

Although the second problem is somehow tackled in the Bayesian framework, the first problem, representing the nonlinear relationship between datasets, remains a challenge. Inspired by such a problem, various nonlinear Machine Learning (ML) algorithms have been used to downscale GRACE data, such as Artificial Neural Network (ANN) (Miro and Famiglietti, 2018), or Boosted Regression Trees (BRT) (Seyoum et al., 2019) or Random Forest (RF) (Jyolsna et al., 2021) or, very recently, Long Short-Term Memory (LSTM) recurrent neural networks (Gorugantula and Kambhammettu, 2022). The ML-based methods have even exhibited notable efficacy in bridging the gap between GRACE and GRACE-FO measurements (Sun et al., 2021) or even in producing water storage estimates using land surface model outputs (Yu et al., 2021). Nevertheless, beyond the overarching issue of ML-based methodologies lacking physical interpretability in

the derived relationships, they often fail to provide a comprehensive uncertainty estimation for the target variable. Therefore, alternative methods should be sought.

4.1 A Bayesian approach for downscaling GRACE data

In a $0.5° \times 0.5°$ grid cell, x_D is sought, which represents a downscaled GRACE data. To be specific, let's assume that here the aim is to downscale TWSF. For downscaling x_D, one can make use of fine-scale TWSF x_M and soil moisture change (SMC) x_S available at $0.5° \times 0.5°$. Here, soil moisture change was chosen as it is generally a better proxy for water storage variation than individual hydrologic fluxes such as precipitation (P), evapotranspiration (ET), or runoff (R), which would provide a comparable storage flux quantity only if $P - ET - R$ is determined. Soil moisture serves as an essential component of the hydrological cycle, influencing various processes such as evapotranspiration, groundwater recharge, and surface runoff (Brocca et al., 2010). Changes in soil moisture content reflect variations in the amount of water stored in the soil, impacting the overall water balance and availability within the basin (Tromp-van Meerveld and McDonnell, 2006). Tian et al. (2017) specifically investigated the contributions of soil moisture to various water compartments, revealing substantial influences on groundwater and terrestrial water storage (cf. Tian et al., 2017, Fig. 2). Long et al. (2013) showed that even in the presence of extreme drought conditions, soil moisture storage changes in Texas exert a predominant influence on the majority of water storage variations. This justification is further substantiated over the Amazon region, given that in a shallow catchment like the Amazon Basin, where approximately 65% of all drainable water is stored in the upper layers (Tourian et al., 2018; Frappart et al., 2019), soil moisture serves as a representative quantity for assessing variations in water storage.

For the methodology developments, the following data serve as the foundation: For x_M, the WGHM model $\dot{M}_\mathrm{W}$, PCR-GLOBWB model $\dot{M}_\mathrm{P}$, SURFEX-TRIP model $\dot{M}_\mathrm{U}$, and an ensemble of water balance components $\dot{M}_\mathrm{F}$. More detail can be found in Section 4.2.1. For x_S, soil moisture fluxes from ASCAT $\dot{S}_\mathrm{A}$ and from GLEAM $\dot{S}_\mathrm{L}$ are utilized. To derive TWSF from GRACE data, spherical harmonic coefficients from ITSG-Grace2018 were used, following the processing steps outlined by Tourian et al. (2022) to obtain TWSA. Gaps in TWSA values for each grid cell were filled with the mean monthly value for the respective grid cell and month. Finally, the TWSA was numerically differentiated using a central difference scheme to derive TWSF $\dot{M}_\mathrm{G}$.

To obtain x_D, the aim is not only to use the available high-resolution data, but also the stochastic information within the covariance structure of different datasets. Therefore, the problem is reformulated as finding the conditional probability $\mathrm{P}(x_\mathrm{D}|x_\mathrm{M},x_\mathrm{S})$ of x_D given x_M and x_S, which provides a measure for the likelihood of x_D given x_M and x_S. This formulation allows the problem to be placed within the Bayesian framework as follows:

$$\mathrm{P}(x_\mathrm{D}|x_\mathrm{M},x_\mathrm{S}) = \frac{\mathrm{P}(x_\mathrm{M}|x_\mathrm{D},x_\mathrm{S})\mathrm{P}(x_\mathrm{S}|x_\mathrm{D})\mathrm{P}(x_\mathrm{D})}{\mathrm{P}(x_\mathrm{M},x_\mathrm{S})} \quad . \tag{4.1}$$

In the Bayesian framework $\mathrm{P}(x_\mathrm{M}|x_\mathrm{D},x_\mathrm{S})$ and $\mathrm{P}(x_\mathrm{S}|x_\mathrm{D})$ are the likelihood functions representing the likelihood of x_M given x_D and x_S, and of x_S given x_D. Let's recall that the likelihood functions are not probability distributions over x_D and x_S, and their integral with respect to x_D and x_S does not equal one. The $\mathrm{P}(x_\mathrm{D})$ is the prior of the downscaled TWSF, which can be inferred via the prior beliefs about the TWSF. The joint probability in the denominator $\mathrm{P}(x_\mathrm{M},x_\mathrm{S})$ acts as a normalization constant, ensuring that the posterior $\mathrm{P}(x_\mathrm{D}|x_\mathrm{M},x_\mathrm{S})$ is a valid probability density and integrates to one. In the above-formulated framework, $\hat{x}_\mathrm{D}$ can then be obtained by finding the Maximum A Posteriori (MAP) estimate (see Section 2.2)

$$\hat{x}_\mathrm{D} = \arg\max_{x_\mathrm{D}\in\mathcal{X}} \mathrm{P}(x_\mathrm{M}|x_\mathrm{D},x_\mathrm{S})\mathrm{P}(x_\mathrm{S}|x_\mathrm{D})\mathrm{P}(x_\mathrm{D}), \tag{4.2}$$

where $\hat{x}_{\mathrm{D}}$ would represent a fine-scale TWSF realized at each $0.5^\circ \times 0.5^\circ$ grid cell given the data from the hydrological measurements and the model.

By such a formulation of the problem, the fine-scale TWSF can be determined if the likelihood functions $\mathrm{P}(x_{\mathrm{M}}|x_{\mathrm{D}}, x_{\mathrm{S}})$ and $\mathrm{P}(x_{\mathrm{S}}|x_{\mathrm{D}})$ and the prior $\mathrm{P}(x_{\mathrm{D}})$ are known. In other words, knowing the likelihood functions and the prior, a posterior can be obtained whose maximum gives the solution to the problem.

In Bayesian statistics, the primary focus is on the estimation of the entire posterior distribution. Since the mathematical equation describing the posterior distribution is usually very complicated and high-dimensional, with the number of dimensions corresponding to the number of parameters, a direct inference of the posterior distribution is usually not possible, requiring sampling methods such as MCMC (van de Schoot et al., 2021). Here, however, the aim is to directly obtain the posterior distribution through non-parametric likelihood functions and the prior defined by the data itself. In other words, $\hat{x}_{\mathrm{D}}$ is obtained by maximizing the product of non-modeled, non-parametric likelihood functions and the prior. The challenge then lies in obtaining a likelihood function that reliably describes how probable the data from fine-scale TWSF and SMC are for different values of downscaled TWSF x_{D}. Note that if the likelihood function is not representative of the stochastics of the data, the Bayesian inference will give biased estimates (Koch, 2007). Moreover, it is important to include an appropriate prior to the proposed Bayesian framework, which best reflects the prior beliefs on TWSF. These are further explained in the following sub-sections.

4.1.1 Prior $\mathrm{P}(x_{\mathrm{D}})$

The coarse-scale TWSF from GRACE can provide the best prior for TWSF because it is the only source that provides measurements of the TWSF without relying on modeling assumptions. Therefore, the GRACE data $\dot{M}_{\mathrm{G}}$ itself is chosen as the prior. To this end, GRACE estimates are realized on a $0.5^\circ \times 0.5^\circ$ grid cell, which are overly smooth realizations of TWSF x_{D}. Depending on the signal strength, GRACE estimates could provide a relatively fair estimate of TWSF. To form a prior distribution, the distribution of TWSF in each grid cell must be known. Given the seasonality of the GRACE-TWSF time series, the distribution in each grid cell is rather platykurtic, with kurtosis larger than 3. Therefore, assuming a normal distribution for the prior would not be adequate. Instead, the Pearson system, a flexible parametric family of distributions that encompasses a wide range of distribution shapes, is relied upon (Johnson et al., 1995). This approach makes it possible to find a distribution that best represents the data based on the mean, standard deviation, skewness, and kurtosis of the data.

Therefore, for each $0.5^\circ \times 0.5^\circ$ grid cell Ω at time t (month m Jan., Feb., Mar.,... and year y), a distribution from the Pearson system is fitted centered around the GRACE estimate $\dot{M}_{\mathrm{G}}(t, \Omega)$, with the standard deviation σ_Ω^m and kurtosis β_Ω^m of all GRACE values of the month m within the grid cell Ω. For instance, σ_Ω^1 and β_Ω^1 are the standard deviation and kurtosis of all TWSF values in January in the grid cell Ω, respectively. Such a choice for the prior allows us to represent the temporal characteristics of each grid cell in each specific month m separately.

4.1.2 Likelihood functions $\mathrm{P}(x_{\mathrm{M}}|x_{\mathrm{D}}, x_{\mathrm{S}})$ and $\mathrm{P}(x_{\mathrm{S}}|x_{\mathrm{D}})$

The likelihood function, used in both Bayesian and frequentist inference, generally quantifies the strength of support provided by the observed data for possible values of the unknown parameter(s) (van de Schoot et al., 2021). In general, specifying a likelihood function can be straightforward, especially in physics-based problems where a model is assumed to connect the observation y and the unknowns x (e.g., $y = Ax$). With such a model, the likelihood function $\mathrm{P}(y|x)$ can be obtained by assuming a certain distribution (e.g., normal distribution). In the context of frequentist inference, such an assumption enables the solution if

the information about the first two moments of the likelihood function $\mathsf{P}(y|x)$ is available, where the first moment is assumed to be $E(y) = Ax$ and the second moment is assumed to be $D(y) = \Sigma_y$.

Here, the derivation of $\mathsf{P}(x_\mathrm{M}|x_\mathrm{D},x_\mathrm{S})$ and $\mathsf{P}(x_\mathrm{S},x_\mathrm{D})$ will be difficult since finding a suitable model for $x_\mathrm{M} = f(x_\mathrm{D},x_\mathrm{S})$ and $x_\mathrm{S} = f(x_\mathrm{D})$ involves a high level of uncertainty. To this end, $\mathsf{P}(x_\mathrm{M}|x_\mathrm{D},x_\mathrm{S})$ and $\mathsf{P}(x_\mathrm{S},x_\mathrm{D})$ must be empirically determined from the datasets. This brings us to two challenges:

1. How to empirically obtain $\mathsf{P}(x_\mathrm{M}|x_\mathrm{D},x_\mathrm{S})$ and $\mathsf{P}(x_\mathrm{S},x_\mathrm{D})$?

2. How to deal with the problem that there is no data for x_D on which to determine the conditional probabilities?

These issues are addressed in the following subsections, respectively.

How to empirically obtain $\mathsf{P}(x_\mathrm{M}|x_\mathrm{D},x_\mathrm{S})$ and $\mathsf{P}(x_\mathrm{S},x_\mathrm{D})$?

To obtain $\mathsf{P}(x_\mathrm{M}|x_\mathrm{D},x_\mathrm{S})$ and $\mathsf{P}(x_\mathrm{S},x_\mathrm{D})$, empirical multivariate distributions $\mathsf{P}(x_\mathrm{M},x_\mathrm{D},x_\mathrm{S})$ and $\mathsf{P}(x_\mathrm{S},x_\mathrm{D})$ are first obtained using Copulas. Copulas C are multivariate distributions defined on the unit hypercube with uniform marginals (Nelsen, 2007).

$$C : [0,1]^n \rightarrow [0,1]\,, \tag{4.3}$$

in which n is the dimension. For instance, $n = 2$ leads to a bivariate copula. Copulas allow us to describe the dependence of multivariate distributions with any kind of marginal distributions (Nelsen, 2007). According to Sklar (1973), each multivariate distribution $\mathsf{F}(x_1,\ldots,x_n)$ can be represented with the help of a copula

$$\mathsf{F}(x_1,\ldots,x_n) = C(\mathsf{F}_1(x_1),\ldots,\mathsf{F}_n(x_n)) \tag{4.4}$$

in which $\mathsf{F}_i(x_i)$ is the i-th one dimensional marginal distribution of the multivariate distribution. The cumulative probability values of the marginal distribution $U := \mathsf{F}(x)$ of any variable span $[0,1]$. For every $u \in [0,1]$ (Czado, 2019):

$$\mathsf{P}(U \leq u) = \mathsf{P}(F(x) \leq u) = \mathsf{P}(x \leq F^{-1}(u)) = F(F^{-1}(u)) = u\,, \tag{4.5}$$

which means that $U := \mathsf{F}(x)$ is uniformly distributed. Following (4.4) and knowing that the copula is obtained from $\mathsf{F}_i(x_i)$, one can state that a copula expresses the dependence between datasets without the influence of their marginal distributions. For a bivariate case, one can obtain an empirical copula $\tilde{C}$ by first converting x_1 and x_2 into their normalized rank domain, obtaining u_{1j} and u_{2j}. Then for each $u_1 \in [0,1]$ and $u_2 \in [0,1]$, simply obtain a cumulative sum of the number of cases in which u_{1j} u_{2j} is less than u_1 and u_2, respectively:

$$\tilde{C}(u_1,u_2) := \frac{1}{L+1}\sum_{j=1}^{L} 1_{[u_{1j}\leq u_1, u_{2j}\leq u_2]} \text{ for all } 0 \leq u_1,u_2 \leq 1\,, \tag{4.6}$$

where L is the length of the data. Assuming that C is absolutely continuous, the copula density $c(u_1,\ldots,u_n)$ can be written as

$$c(u_1,\ldots,u_n) = \frac{\partial^n C(u_1,\ldots,u_n)}{\partial u_1 \ldots \partial u_n} \tag{4.7}$$

A copula density represents a probability that a set of uniform variables u_i $i = 1,...,n$ would be located within a particular region of [0,1]^n space, which corresponds to the level of dependency of variables. Therefore, the joint probability density of x_S and x_D reads

$$\mathsf{P}(x_\mathrm{S},x_\mathrm{D}) = c(\mathsf{F}_\mathrm{S}(x_\mathrm{S}),\mathsf{F}_\mathrm{D}(x_\mathrm{D}))\mathsf{P}(x_\mathrm{S})\mathsf{P}(x_\mathrm{D})\,. \tag{4.8}$$

By building C_{SD} and C_{MDS}, which are empirical copulas between x_{S}, x_{D} and x_{M} generated by Eq. (4.6),one can then obtain the corresponding likelihood by (Czado, 2019)

$$\mathsf{P}(x_{\mathrm{S}}|x_{\mathrm{D}}) = \frac{\partial}{\partial u_{\mathrm{D}}}\left(\frac{\partial}{\partial x_{\mathrm{S}}} C_{\mathrm{SD}}(\mathsf{F}_{\mathrm{S}}(x_{\mathrm{S}}), u_{\mathrm{D}})\right)\Big|_{u_{\mathrm{D}}=\mathsf{F}_{\mathrm{D}}(x_{\mathrm{D}})}. \tag{4.9}$$

For the trivariate case, the likelihood can be obtained by

$$\mathsf{P}(x_{\mathrm{M}}|x_{\mathrm{D}}, x_{\mathrm{S}}) = \frac{\partial^2}{\partial u_{\mathrm{D}} \partial u_{\mathrm{S}}}\left(\frac{\partial}{\partial x_{\mathrm{M}}} C_{\mathrm{MDS}}(\mathsf{F}_{\mathrm{S}}(x_{\mathrm{M}}), u_{\mathrm{D}}, u_{\mathrm{S}})\right)\Big|_{\substack{u_{\mathrm{D}} = \mathsf{F}_{\mathrm{D}}(x_{\mathrm{D}}) \\ u_{\mathrm{S}} = \mathsf{F}_{\mathrm{S}}(x_{\mathrm{S}})}} \tag{4.10}$$

How to generate copulas and deal with the problem that x_{D} is not available?

For generating both copulas C_{SD} and C_{MDS}, realizations of fine-scale water storage flux x_{D} are required. As this data is not available, it is the focus of this study to obtain it. Due to the coarse resolution of GRACE and its inability to capture the full distribution, GRACE data at a $0.5° \times 0.5°$ resolution cannot serve as a representative basis for forming copulas C_{SD} and C_{MDS}. Therefore, it is essential to analyze the empirical copula density of GRACE data alongside the selected fine-scale models. Figure 4.2 shows the empirical copula density for all pairs of data considered here. $\dot{M}_{\mathrm{P}}$ and $\dot{M}_{\mathrm{U}}$ show the strongest dependence among all pairs, which may be due to a similar modeling approach. As expected, given that they are two different quantities, the TWSF and soil moisture data show less dependence and more scatter in their empirical copulas.

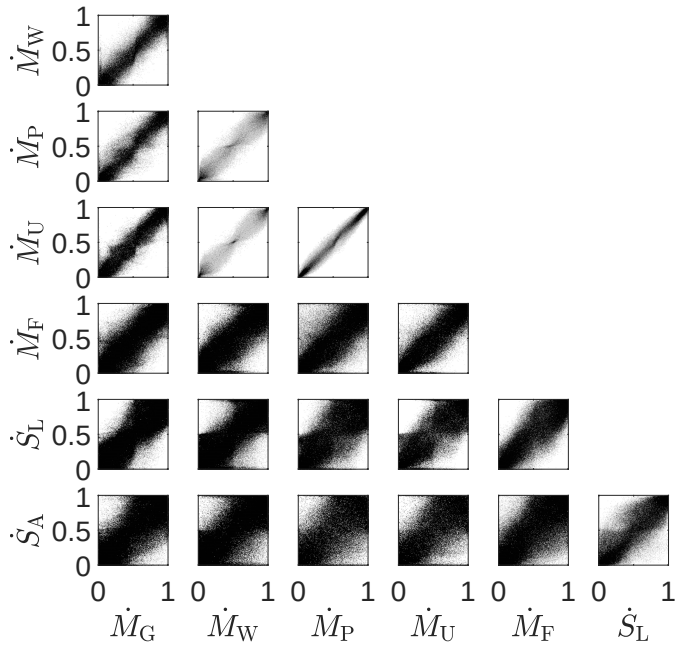

Fig. 4.2: Empirical copula density for all pairs of data considered in this study.

Some of the copula densities including, for example, $\dot{M}_{\mathrm{W}}$-$\dot{M}_{\mathrm{P}}$, $\dot{M}_{\mathrm{W}}$-$\dot{M}_{\mathrm{U}}$, $\dot{S}_{\mathrm{L}}$-$\dot{S}_{\mathrm{A}}$ show a strong tail dependency, which can be explained by the fact that stronger signals are better correlated to each other. In essence, this is an important property of a copula that can express whether the corresponding dependence varies for different quantiles of the variable. In the pairs with GRACE (first column), a general pattern is observed that the copula densities are scattered, which represents less correlated behavior in different quantiles. For the $\dot{M}_{\mathrm{G}}$-$\dot{S}_{\mathrm{L}}$ and $\dot{M}_{\mathrm{G}}$-$\dot{S}_{\mathrm{A}}$ data pairs, perfect correlation is not expected, as these copula

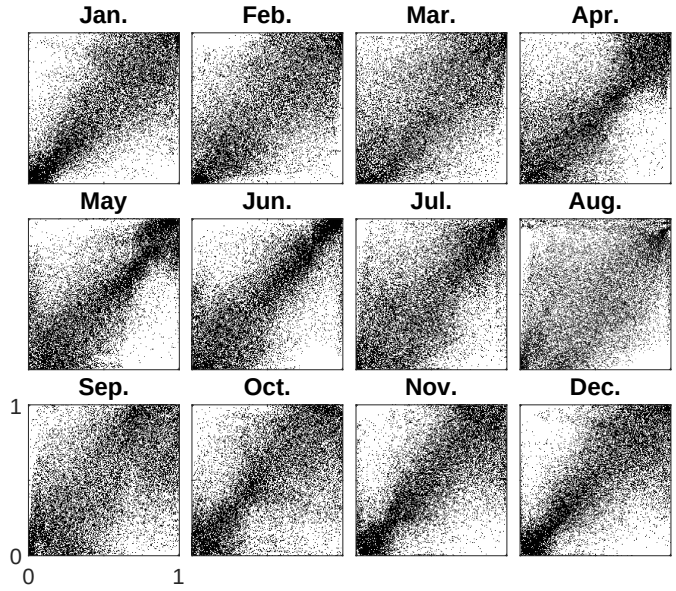

Fig. 4.3: Monthly empirical copula of $\dot{M}_{\mathrm{W}}$ versus $\dot{M}_{\mathrm{G}}$ for all grid cells of Amazon Basin

densities involve different quantities. However, for TWSF data pairs, ideally, copula densities with the data points aligned along the diagonal are expected, similar to the data pair $\dot{M}_{\mathrm{P}}$-$\dot{M}_{\mathrm{U}}$. A reason for the deviation from an ideal case is the fact that different datasets represent TWSF differently and with different spatial resolutions. In the case of pairs with GRACE, the main reason for the scatter in copula densities is that GRACE generally provides a meaningful signal for lower-degree spherical harmonic coefficients, and its estimates for higher-degree coefficients (i.e., shorter wavelengths) are overly smooth. This can be seen in Figure 4.4, which shows the average degree variance (averaged over all months) of TWSF and SMC. Comparing the degree variances of GRACE with those of $\dot{M}_{\mathrm{W}}$ and $\dot{M}_{\mathrm{U}}$, it is clear that GRACE has by far the lowest information content for the shorter wavelength (small features), due to the omission error.

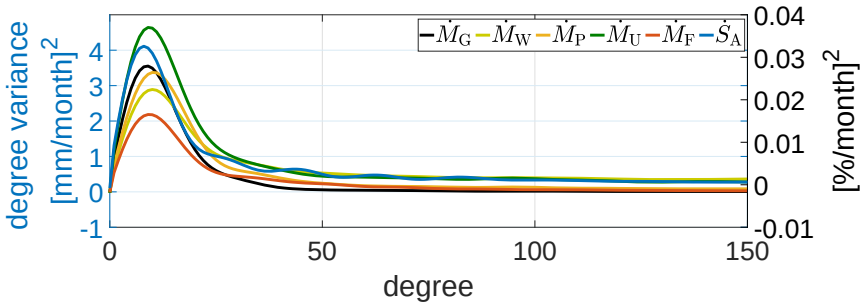

Fig. 4.4: Average of monthly degree variances for $\dot{M}_{\mathrm{G}}$, $\dot{M}_{\mathrm{W}}$,$\dot{M}_{\mathrm{P}}$, $\dot{M}_{\mathrm{U}}$, $\dot{M}_{\mathrm{F}}$ and $\dot{S}_{\mathrm{A}}$

To obtain copula densities that are not contaminated by noise or excessive smoothness in the data, one solution is to obtain copula densities from long wavelengths only. This would mean converting the grid data to a spherical-harmonic representation to focus on the longer wavelengths to generate copula densities. One important advantage of using the copula is that it is invariant to monotonic transformations of the marginal variables. This is a major advantage compared to approaches using covariances, as those strongly depend on the marginal distributions. Thus, by converting grid-based data into spherical harmonic coefficients, the dependency between datasets can still be represented by generating copulas from these spherical harmonic coefficients. This is possible since the equation (4.11), that turns the spatial data into spherical harmonic

representation (i.e., spherical harmonic analysis) can be considered as a monotonic transformation (i.e., a larger field $f(\Omega)$ would lead to larger spherical harmonic coefficients ΔC_{lm} and ΔS_{lm}).

$$\begin{Bmatrix} \Delta C_{lm} \\ \Delta S_{lm} \end{Bmatrix} = \frac{1}{4\pi} \iint_{\Omega} f(\Omega) \bar{P}_{lm}(\cos\theta) \begin{Bmatrix} \cos m\lambda \\ \sin m\lambda \end{Bmatrix} d\Omega \tag{4.11}$$

Therefore, copulas C_{SD} and C_{MDS} can be constructed using spherical harmonic coefficients from GRACE TWSF and fine-scale data. By assuming that dependencies captured in lower spherical harmonic degrees apply to higher degrees, copulas can be generated from truncated datasets. This truncation mitigates potential deterioration of dependencies caused by the imperfect resolution of $0.5^\circ \times 0.5^\circ$ datasets, particularly for GRACE data. Additionally, generating copulas in the spectral domain rather than the spatial domain helps avoid undesirable field variations resulting from truncation errors.

To distinguish the truncated data from the non-truncated one, the truncated data are symbolized with *. An experimental analysis (not shown here) showed that the best degree for the truncation is $l_{\mathrm{tr}} = 30$. Figure 4.5 shows bivariate empirical copulas directly generated from spherical harmonics coefficients up to degree 30 for all pairs of data, in which the tail dependency between datasets is much more visible due to less influence of noise from higher degrees. Here, different patterns are observed in the empirical copulas

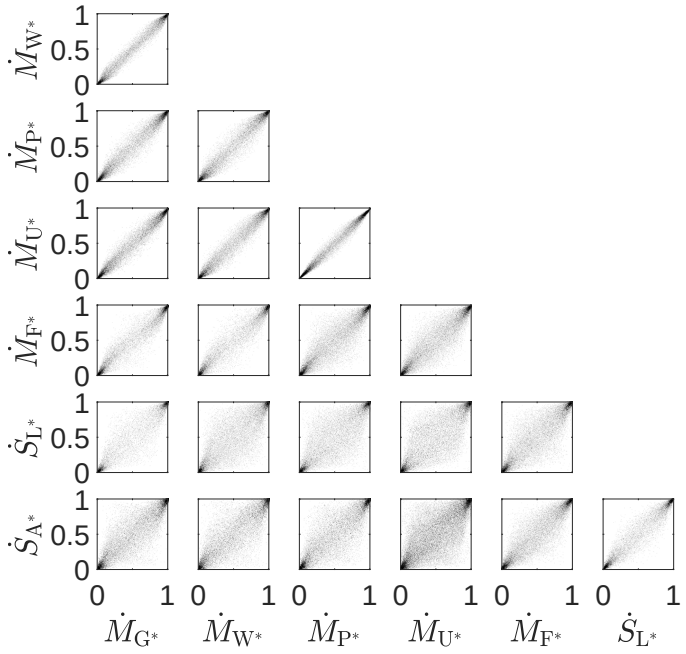

Fig. 4.5: Empirical bivariate copula density for all pairs of truncated data considered in this study.

for various months (Figure 4.6).

Copula models and likelihood functions

Given the tail dependencies observed in the empirical copulas, the Student's t copula is fitted, as it allows for effective modeling of tail dependencies between variables and is straightforward to simulate and calibrate. To this end, C_{SD} and C_{MDS} are constructed using the Student's t copula for each month, resulting in a total of 24 copulas: 12 for C_{SD} (Figure 4.7) and 12 for C_{MDS} (copula densities not shown here). Figure 4.7 illustrates the copula density for C_{SD}, demonstrating similar patterns to those observed in Figure 4.3.

,

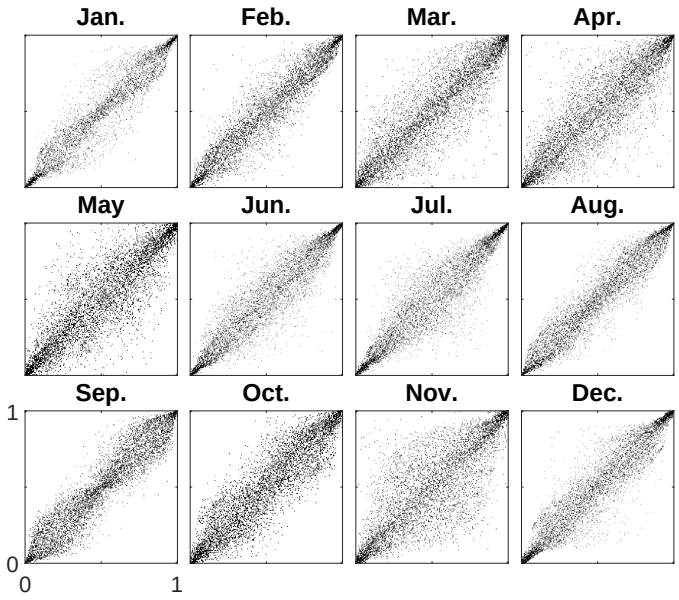

Fig. 4.6: Monthly empirical copula of $\dot{M}_{\mathrm{W}^*}$ versus $\dot{M}_{\mathrm{G}^*}$ for all grid cells of Amazon Basin

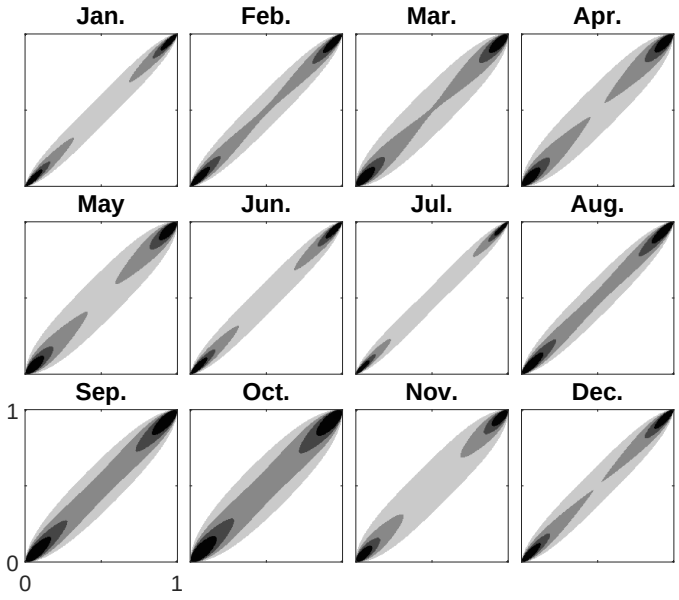

Fig. 4.7: Modelled monthly copula between $\dot{M}_{\mathrm{W}}$ versus $\dot{M}_{\mathrm{G}}$ for all grid cells of Amazon Basin

With the constructed copulas, for each $0.5^\circ \times 0.5^\circ$ grid cell Ω at time t within month m and year y, the required likelihood functions are obtained by taking the derivative of a given quantile:

$$\mathsf{P}(x_{\mathrm{S}}|x_{\mathrm{D}};t,\Omega) = \frac{\partial}{\partial u_{\mathrm{D}}}\left(\frac{\partial}{\partial x_{\mathrm{S}}} C^m_{\mathrm{SD}}(\mathsf{F}_{\mathrm{S}_\Omega}(x_{\mathrm{S}}), u^r_{\mathrm{D}})\right)\Big|_{u^r_{\mathrm{D}}=\mathsf{F}_{\mathrm{G}_\Omega}(\dot{M}_{\mathrm{G}}(t,\Omega))} \tag{4.12}$$

and

$$\mathsf{P}(x_{\mathrm{M}}|x_{\mathrm{D}},x_{\mathrm{S}};t,\Omega) = \frac{\partial^2}{\partial u_{\mathrm{D}}\partial u_{\mathrm{S}}}\left(\frac{\partial}{\partial x_{\mathrm{M}}} C^m_{\mathrm{MDS}}(\mathsf{F}_{\mathrm{W}_\Omega}(x_{\mathrm{M}}), u^r_{\mathrm{D}}, u^r_{\mathrm{S}})\right)\Big|_{\substack{u^r_{\mathrm{D}} = \mathsf{F}_{\mathrm{G}_\Omega}(\dot{M}_{\mathrm{G}}(t,\Omega)) \\ u^r_{\mathrm{S}} = \mathsf{F}_{\mathrm{S}_\Omega}(\dot{S}_{\mathrm{L,A}}(t,\Omega))}} \tag{4.13}$$

$\mathsf{F}_{\mathrm{G}_\Omega}$ is the empirical cumulative distribution function of GRACE data $\dot{M}_{\mathrm{G}}$ in the grid cell Ω, using which u_{D}^r (a value between 0 and 1) is obtained by $\dot{M}_{\mathrm{G}}(t,\Omega)$ as a realization of x_{D}. It should be noted that the $\mathsf{F}_{\mathrm{G}_\Omega}$ is empirically derived from all monthly estimates of GRACE from 2002 to 2017 in the grid cell Ω. Similarly, $\mathsf{F}_{\mathrm{S}_\Omega}$ is the empirical cumulative distribution function of SMC data $\dot{S}_{\mathrm{L}}$ or $\dot{S}_{\mathrm{A}}$ in the grid cell Ω.

4.1.3 MAP estimate and its uncertainty

Once the prior and likelihood functions are derived for each $0.5^\circ \times 0.5^\circ$ grid cell Ω and at time t, the posterior is attained by

$$\mathsf{P}(x_{\mathrm{D}}|x_{\mathrm{M}},x_{\mathrm{S}};t,\Omega) = \frac{\mathsf{P}(x_{\mathrm{M}}|x_{\mathrm{D}},x_{\mathrm{S}};t,\Omega)\mathsf{P}(x_{\mathrm{S}}|x_{\mathrm{D}};t,\Omega)\mathsf{P}(x_{\mathrm{D}};t,\Omega)}{\int \mathsf{P}(x_{\mathrm{M}}|x_{\mathrm{D}},x_{\mathrm{S}};t,\Omega)\mathsf{P}(x_{\mathrm{S}}|x_{\mathrm{D}};t,\Omega)\mathsf{P}(x_{\mathrm{D}};t,\Omega)} \tag{4.14}$$

from which the MAP is estimated through

$$\hat{x}_{\mathrm{D}}(t,\Omega) = \arg\max_{\mathrm{D}\in\mathcal{D}} \mathsf{P}(x_{\mathrm{D}}|x_{\mathrm{M}},x_{\mathrm{S}};t,\Omega), \tag{4.15}$$

which represents TWSF value with maximum posterior probability in each month at each grid cell. The uncertainty of TWSF is then derived as the interquartile range (IQR) of the posterior distribution

$$\sigma_{\hat{x}_{\mathrm{D}}} = Q_3 - Q_1\,, \tag{4.16}$$

where the lower quartile Q_1 corresponds with the 25th percentile and the upper quartile Q_3 corresponds with the 75th percentile of the posterior distribution. Figure 4.8 shows the overall flowchart of the proposed method for downscaling.

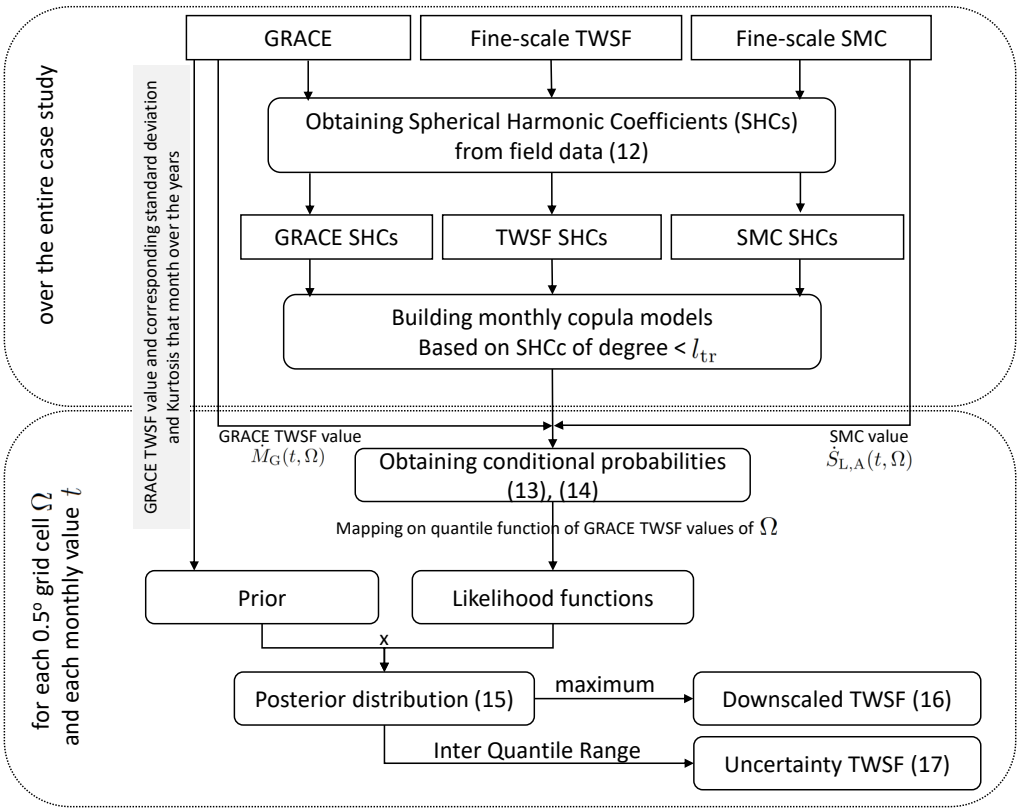

Fig. 4.8: Flowchart of proposed copula-supported Bayesian framework

4.1.4 Mass-conserved MAP estimate

On large scales, say over the entire Amazon, GRACE should provide the best representation of total mass change. Because of the uncertainty of individual measurements, neither of the selected fine-scale TWSF data can deliver a realistic representation of total mass change over a large basin. As a result, the downscaled result, obtained from the data and statistical distribution of fine-scale TWSF and SMC in combination with GRACE in each grid cell, is not expected to maintain the mass conservation property. Moreover, the proposed Bayesian framework is set for each grid cell and each month individually and is not designed to be constrained by a condition for the whole basin. A statistical approach that does not interfere with the Bayesian framework is relied upon to fulfill the mass conservation over a large basin. To this end, a mass-conserved downscaled field is derived by assuming that the cumulative distribution of downscaled TWSF $\hat{x}_{\mathrm{D}}$ should obey F_{G} (CDF from GRACE) over a large basin. Therefore, a classical CDF matching (Verhoest et al., 2015) is applied, which transforms $\mathsf{F}(x_{\mathrm{D}}|x_{\mathrm{M}}, x_{\mathrm{S}})$ to F_{G}, leading to an estimate $\hat{x}_{\mathrm{MD}}$ whose distribution follows the distribution of GRACE throughout the Amazon Basin. Through such an approach, it is ensured that the spatial distribution pattern of the TWSF remains intact, and only the distribution of the data in terms of their quantiles changes.

4.2 Results and validation

A portion of the Amazon Basin, upstream of Óbidos, Brazil, was selected as the study area. It has an area of 4,702,314 km^2 and contributes to draining the largest volume of liquid freshwater on land. The Amazon Basin has the highest amount of freshwater discharge into the ocean, with about 20% of the total water carried to the oceans by rivers. The method is applied across the nine sub-basins outlined in Table 4.1 (Figure 4.9). The Amazon Basin was selected due to its significant recharge and water storage variation (Figure 4.9 bottom panel). This region, characterized by extensive surface water storage and diverse freshwater wetlands, provides an opportunity to validate the downscaled results using independent data.

Tab. 4.1: Sub-basins of Amazon Basin used in this study with their area and climate classification.

Basin	Area [10^6 km^2]	Climate
Upper Japurá River	0.12	fully humid
Upper Solimões River	1.22	partially humid
Juruá River	0.16	partially humid
Upper Negro River	0.28	fully humid
Purus River	0.37	tropical monsoon
Upper Branco River	0.17	tropical monsoon
Lower Solimões River	0.32	fully humid
Madeira River	1.31	savanna
Manacapuru-Óbidos	0.74	fully humid[a]

[a]: partially tropical monsoon

As mentioned before, the method is supported by fine-scale 1) TWSF and 2) SMC datasets from different sources listed in Table 4.2.

4.2.1 Fine-scale Total Water Storage Flux

Fine-scale Total Water Storage Flux (TWSF) data are obtained in two different ways:

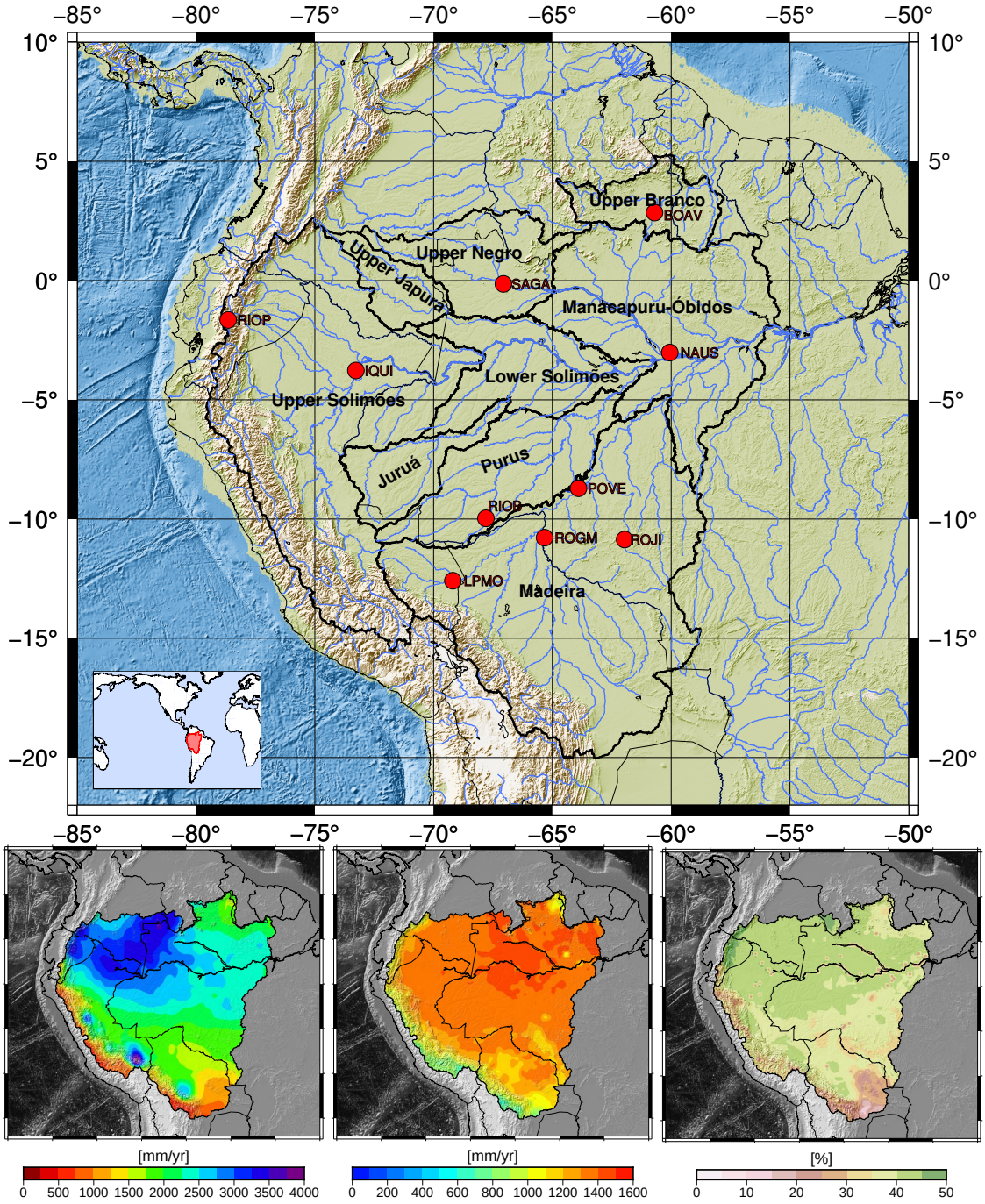

Fig. 4.9: Top panel) Study area containing nine sub-basins of the Amazon Basin with 10 selected GPS stations (red circles). Bottom panels: left) Mean annual precipitation over the Amazon Basin within the GRACE period (2002–2016) from the ensemble mean of selected datasets; middle) same as before, however, for evapotranspiration, and right) average soil moisture from GLEAM 3.5a within the GRACE period (2002–2016).

Tab. 4.2: Summary of datasets used in this study for downscaling and validation purposes.

Data	symbol
Terrestrial Water Storage Flux (TWSF)	
GRACE	$\dot{M}_{\mathrm{G}}$
WGHM	$\dot{M}_{\mathrm{W}}$
PCR-GLOBWB	$\dot{M}_{\mathrm{P}}$
SURFEX-TRIP	$\dot{M}_{\mathrm{U}}$
Ensemble water flux	$\dot{M}_{\mathrm{F}}$
Soil Moisture Change (SMC)	
GLEAM	$\dot{S}_{\mathrm{L}}$
ASCAT	$\dot{S}_{\mathrm{A}}$
Data for validation	
Vertical Surface Displacement Change (VCDR)	
Surface Water Storage Change (SWSC)	

1. Using TWSF models, and

2. through water balance equation.

TWSF models

For the fine-scale TWSF models, 12 models listed in Table 4.3 were considered. To avoid erroneous models, an evaluation of model performance was conducted by comparing the aggregated TWSF time series over the Amazon Basin. The evaluation concluded that three models—WGHM $\dot{M}_{\mathrm{W}}$, PCR-GLOBWB $\dot{M}_{\mathrm{P}}$, and SURFEX-TRIP $\dot{M}_{\mathrm{U}}$—demonstrated superior performance, with a correlation coefficient (CC) greater than 0.82, Kling-Gupta efficiency (KGE) greater than 0.53, and root-mean-square error (RMSE) less than 8.6 cm. Consequently, these three models were utilized for the implementation of the downscaling method.

Tab. 4.3: Summary of the models that provide TWSA over the Amazon Basin. LSM: Land Surface Model, GHM: Global Hydrological Model; AM: Atmospheric Model.

Model	Type	Spatial Resolution	Time period	Reference
CLM5-CRUNCEP	LSM	$0.9425^\circ \times 1.25^\circ$	1850–2014	Lawrence et al. (2019); Oleson et al. (2019)
CLM5-GSWP3	LSM	$0.9425^\circ \times 1.25^\circ$	1850–2014	Lawrence et al. (2019); Oleson et al. (2019)
ERA5	AM	$0.25^\circ \times 0.25^\circ$	1979–present	Hersbach et al. (2020)
HBV-SIMREG	GHM	$0.5^\circ \times 0.5^\circ$	1979–2012	Lindström et al. (1997)
HTESSEL	LSM	$0.25^\circ \times 0.25^\circ$	1980–2014	Balsamo et al. (2015)
LISFLOOD	GHM	$0.25^\circ \times 0.25^\circ$	1980–2014	Van Der Knijff et al. (2010)
ORCHIDEE	LSM	$0.25^\circ \times 0.25^\circ$	1980–2014	Polcher et al. (2011)
PCR-GLOBWB	GHM	$0.25^\circ \times 0.25^\circ$	1979–2014	Sutanudjaja et al. (2018); Wada et al. (2014)
SURFEX-TRIP	LSM	$0.5^\circ \times 0.5^\circ$	1979–2012	Decharme et al. (2013)
SWBM	GHM	$0.5^\circ \times 0.5^\circ$	1979–2012	Koster and Mahanama (2012); Orth and Seneviratne (2013)
W3RA	GHM	$0.5^\circ \times 0.5^\circ$	1979–2012	Van Dijk (2010)
WaterGap Global Hydrology Model	GHM	$0.5^\circ \times 0.5^\circ$	1901–2016	Müller Schmied et al. (2021)

TWSF through water balance equation over Amazon

At basin-scale, TWSF $\dot{M}_{\mathrm{F}}$ can be determined through the terrestrial water balance equation, given as:

$$\dot{M}_{\mathrm{F}} = \{\bar{P}\} - \{\bar{ET}\} - \{\bar{R}\}. \tag{4.17}$$

In Eq. (4.17), $\{\bar{P}\}$ is the ensemble mean of thirteen precipitation datasets, $\{\bar{ET}\}$ is the ensemble mean of four evapotranspiration datasets, and $\{\bar{R}\}$ is the ensemble mean of three runoff datasets, listed in Table 4.4. The filter $[\frac{1}{4}\ \frac{1}{2}\ \frac{1}{4}]$ is then convolved with the obtained $\dot{M}_{\mathrm{F}}$ time series to enhance compatibility with the GRACE TWSF, which is derived using the central difference scheme (Tourian, 2013).

Tab. 4.4: Summary of the datasets used in this study to compute the ensemble mean of the water balance fluxes. G: Gauge, S: Satellite, R: Reanalysis, GHM: Global Hydrological Model.

	Dataset	Method/Source(s)	Spatial Resolution	Time period	Reference
Precipitation	AgCFSR	G, R	$0.25° \times 0.25°$	1980–2010	Ruane et al. (2015)
	AgMERRA	G, S, R	$0.25° \times 0.25°$	1980–2010	Ruane et al. (2015)
	CHIRPS	G, S, R	$0.05° \times 0.05°$	1981–present	Funk et al. (2015)
	CRUv4.04	G	$0.5° \times 0.5°$	1901–2019	Harris et al. (2020)
	GPCCv2020	G	$0.25° \times 0.25°$	1982–2019	Schneider et al. (2020)
	GPCPv2.3	G, S	$2.5° \times 2.5°$	1979–present	Adler et al. (2003)
	GPCP 1DD	G, S	$1.0° \times 1.0°$	1996–present	Huffman et al. (2001)
	GPM IMERG v6 Final	G, S	$0.1° \times 0.1°$	2000–present	Huffman et al. (2019)
	MSWEP v2.8	G, S, R	$0.1° \times 0.1°$	1979–2020	Beck et al. (2019)
	PERSIANN-CDR	G, S	$0.25° \times 0.25°$	1983–present	Ashouri et al. (2015)
	PREC/L	G	$0.5° \times 0.5°$	1948–present	Chen et al. (2002)
	TRMM-3B42-adj	G, S	$0.25° \times 0.25°$	1998–2019	Huffman et al. (2007)
	UDELv5.01	G	$0.5° \times 0.5°$	1900–2017	Willmott and Matsuura (1995)
ET	ERA5	R	31 km	1979–present	Hersbach et al. (2020)
	FluxCom	G, S	$0.5° \times 0.5°$	2001–2013	Jung et al. (2019)
	P-LSH	G, S	$0.083° \times 0.083°$	1982–2013	Zhang et al. (2009, 2010)
	PML-v2	G, S	$0.05° \times 0.05°$	2002–2019	Zhang et al. (2019, 2016)
Runoff	G-RUN-Ensemble	G, S, R	$0.5° \times 0.5°$	1979–present	Ghiggi et al. (2021)
	SURFEX-TRIP	GHM	$0.5° \times 0.5°$	1979–2012	Lindström et al. (1997)
	W3RA	GHM	$0.5° \times 0.5°$	1979–2012	Van Dijk (2010)

4.2.2 Soil moisture data over Amazon

Available soil moisture products can generally be categorized into three main classes: (i) satellite-based products obtained from active- or passive-microwave satellite observations; (ii) hydrological and land surface models without data assimilation; and (iii) hydrological and land surface models assimilated with external satellite data, such as soil moisture or brightness temperature. Two soil moisture products were selected: 1) the satellite-based product of the Advanced Scatterometer (ASCAT) for the period 2007–2016 (Wagner et al., 2013), and 2) the Global Land Evaporation Amsterdam Model (GLEAM) version 3.5a (Martens et al., 2017) for the period 2002–2016, which is a model assimilated with satellite data including SMOS L3 and ESA CCI SM v2.3. ASCAT represents the liquid water content in a surface soil layer as a percentage of total saturation at a 25 km resolution (Wagner et al., 2013), while GLEAM represents the volumetric soil moisture in the root-zone layer (0–10 cm).

These datasets were chosen based on the recent study by Beck et al. (2021), which evaluated the performance of 18 satellite- and model-based soil moisture products using 826 ground stations. In their study, AMSR2 and SMAPL3E slightly outperformed ASCAT. However, these products only cover a few years of the GRACE period (AMSR2 covers 2012–2016, and SMAPL3E covers 2015–2016). Additionally, they (ibid) demonstrated that among assimilated products, ESA-CCI SM V04.4 COMBINED delivered comparable performance to GLEAM. However, due to a significant number of missing values over the Amazon Basin, this dataset was not included in the analysis.

To obtain a flux-like variable, the soil moisture data from the two selected sources were then converted into Soil Moisture Change (SMC) by applying numerical differentiation to each grid cell.

4.2.3 The downscaled TWSF fields

Based on the proposed methodology and using fine-scale TWSF and SMC datasets, monthly downscaled TWSF x_{D} and mass-conserved downscaled TWSF x_{MD} on a $0.5° \times 0.5°$ grid are obtained. Within the proposed Bayesian framework, GRACE data is always relied upon for the prior, as described in Subsection 5.2.1. The likelihood functions were determined by generating copula densities using four different TWSF and two different SMC datasets. As a result, eight realizations of downscaled TWSF were obtained (Table 4.5).

Tab. 4.5: Input datasets of fine-scale TWSF and SMC for 8 realizations of downscaling

		fine-scale SMC	
fine-scale TWSF		GLEAM $\dot{S}_{\mathrm{L}}$	ASCAT $\dot{S}_{\mathrm{A}}$
WGHM	$\dot{M}_{\mathrm{W}}$	1	2
PCR-GLOBWB	$\dot{M}_{\mathrm{P}}$	3	4
SURFEX-TRIP	$\dot{M}_{\mathrm{U}}$	5	6
ensemble flux	$\dot{M}_{\mathrm{F}}$	7	8

Figure 4.10 shows empirical CDFs of GRACE monthly TWSF $\dot{M}_{\mathrm{G}}$ (bottom) and fine-scale input TWSF $\dot{M}_{\mathrm{W}}$, $\dot{M}_{\mathrm{F}}$, $\dot{M}_{\mathrm{P}}$, $\dot{M}_{\mathrm{U}}$ along with empirical CDFs of the downscaled TWSF $\hat{x}_{\mathrm{D}}$ (light coral) and the mass-conserved downscaled TWSF $\hat{x}_{\mathrm{MD}}$ (turquoise) of the 8 realizations. Larger tails in CDFs of fine-scale TWSF reveal that they contain more details in comparison to GRACE, which generally shows a smooth transition to the tails. There, all fine-scale datasets have a relatively symmetric distribution, with the exception of the flux ensemble dataset $\dot{M}_{\mathrm{F}}$ exhibiting a rather skewed distribution.

The downscaled TWSF's CDF shows less heavy tails and, in general, less similar behaviour to the input fine-scale datasets in terms of their details in tails. Almost all realizations cover a different range of TWSFs from what is represented by their input fine-scale data. This is the result of the counteraction of the prior and the likelihood functions $\mathrm{P}(x_{\mathrm{S}}|x_{\mathrm{D}})$ and $\mathrm{P}(x_{\mathrm{M}}|x_{\mathrm{D}}, x_{\mathrm{S}})$, which potentially helps to reduce the effect of over- and underestimation by models. This can also be seen in the time series of downscaled TWSF for the first realization (Figures 4.11) that, in terms of dynamics, it is a trade-off between GRACE, WGHM, and the dynamics of SMC.

The mass-conserved downscaled TWSF $\hat{x}_{\mathrm{MD}}$ is the result of the CDF matching of the downscaled data with the GRACE CDF, thus yielding the same CDFs as GRACE (Figure 4.10). Such a CDF matching leads to having very similar time series with GRACE (Figures 4.11). Over the sub-basins, however, they are not necessarily the same, since $\hat{x}_{\mathrm{MD}}$ is conditioned over the entire Amazon and not over each sub-basin. It is important to recall that CDF matching affects only the distribution in terms of quantiles, without altering the spatial distribution of the data. Figure 4.12 highlights this fact, where for both realizations shown, the downscaled TWSF and mass-conserved downscaled TWSF exhibit a similar spatial pattern, with the mass-conserved product contrasting more (or sometimes less) to ensure GRACE distribution. Comparing GRACE (top row, left) and fine-scale TWSF data (realization 1: WGHM model, realization 3: PCR-GLOBWB model) (top row, middle) for both realizations, a consistent TWSF range is observed. However, the two fields represent different TWSF patterns in the river system of the Amazon Basin. In realization 1, while WGHM clearly distinguishes the river system, GRACE senses it as a smoothed field centered somewhere in the river.

At each grid cell, downscaled TWSF (Figure 4.12, bottom row, left) represents the value with maximum posterior probability obtained within the developed Bayesian framework. In fact, it represents the most plausible TWSF when considering SMC and fine-scale TWSF data as well as prior information from GRACE data. Its pattern shows that it is actually much more detailed in comparison to GRACE data, where for

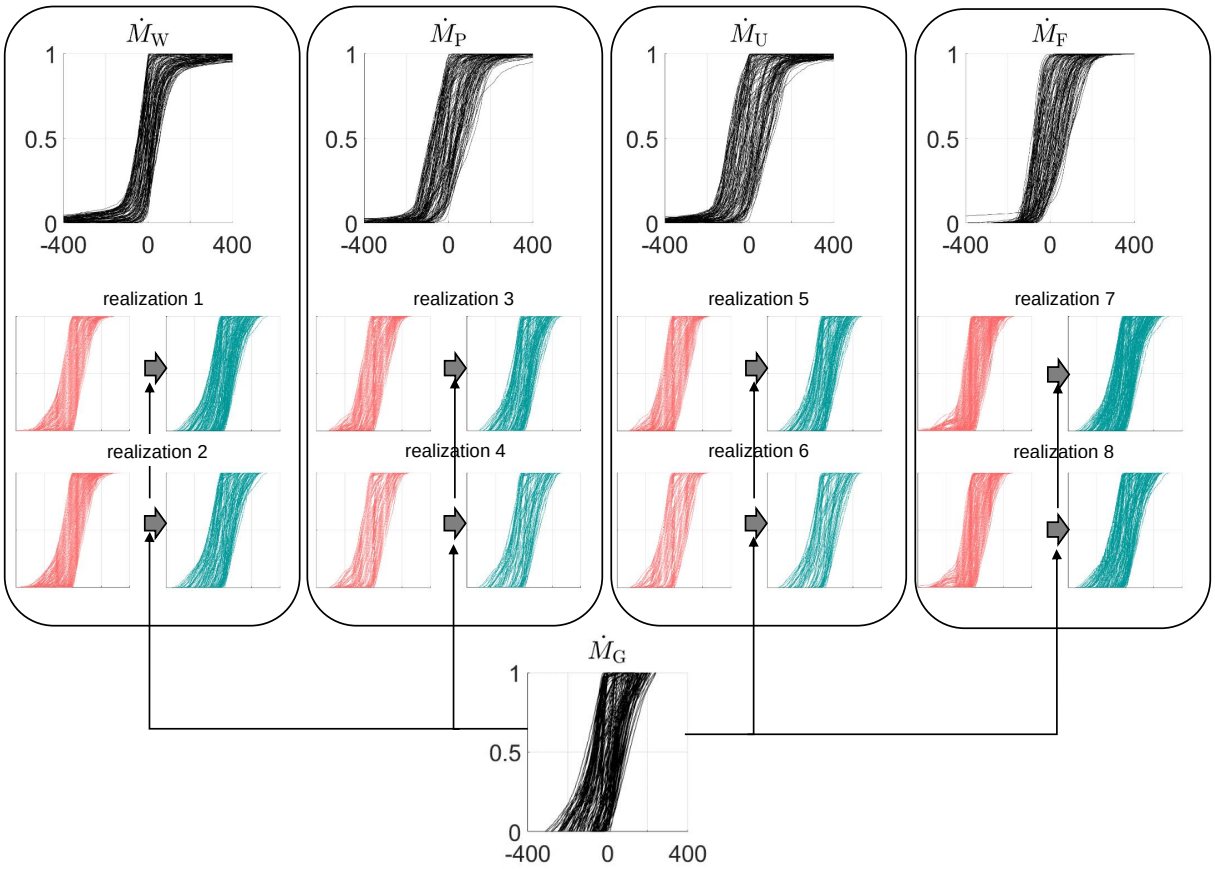

Fig. 4.10: Empirical CDF of monthly fine-scale TWSF (top row) and those from GRACE (bottom row) together with empirical CDF of monthly downscaled TWSF (light coral) and mass-conserved downscaled TWSF (turquoise) for all 8 realizations over the entire Amazon

instance, in realization 1, the river system is recognized, and some local patterns are captured, including those over the Andes Mountains. However, the downscaled TWSF can also be dominated by the prior information (GRACE), leading to a positive TWSF in the presence of negative estimates by WGHM. Such a difference in likelihood functions and the prior leads to a wider posterior distribution and, thus, to a larger uncertainty. The uncertainty map in Figure 4.12 (second row, right) shows indeed a larger value of about 50 mm/month over grid cells where prior and fine-scale models deviate from each other. The mass-conserved downscaled estimate provides an even more detailed TWSF in comparison to the downscaled field. For instance, large TWSF values in the Ucayali River, seen in the WGHM data, are also partially captured in the mass-conserved downscaled field.

To assess the relevance of the gained details, longitudinal profile lines at specific latitudes are examined (Figure 4.13), focusing on the first realization with GLEAM as the SMC and WGHM as the fine-scale TWSF. The high fluctuation of the WGHM model profile lines in Figure 4.13 should not be interpreted as noise, but rather as a positive feature, as it reveals details provided in the WGHM. For instance, in latitude $-4.25\,^{\circ}$ around the longitude $-55\,^{\circ}$–$-67\,^{\circ}$ strong changes in WGHM belong to the river network in the Lower Solimões River. These changes are seamlessly represented by the filtered GRACE field. As can be seen in figures 4.14, 4.15, and 4.16, soil moisture change data partially represent the TWSF field, which is also visible in the profile lines. The downscaled TWSF results represent a general compromise between input datasets, with the important characteristic that they capture relevant fluctuations and show a general agreement with TWSF from GRACE. The results of October 2016 (last column) can be read simultaneously with Figure 4.14, where for all selected latitudes, the downscaled TWSF seems to

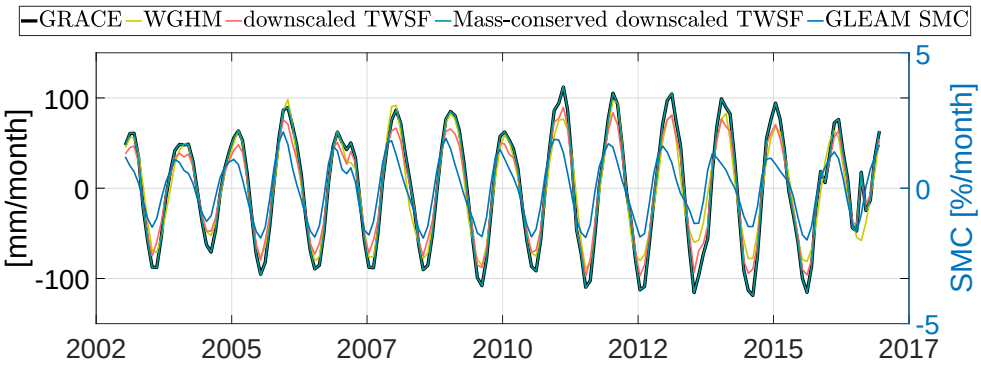

Fig. 4.11: Time series of aggregated TWSF from GRACE, WGHM, downscaled and mass-conserved downscaled products together with SMC over the Amazon Basin

follow the pattern of WGHM model and $\dot{S}_{\mathrm{L}}$ and simultaneously follows the decay in $\dot{M}_{\mathrm{G}}$. Examining the corresponding likelihoods and prior distribution for longitude $-63.25\,^{\circ}$ in the bottom panel of Figure 4.13, it is evident how all components contribute to the final posterior. Contributions are influenced by the likelihood functions in some cases, while others reflect a stronger alignment with the prior or a compromise between the two. For instance, in October 2016, when the TWSF shows stronger dynamics towards the downstream part of the basin, especially in the Manacapuru-Óbidos sub-basin, results successfully traced the detailed spatial variations (Figure 4.14). Moreover, results in Figure 4.14 show the recognition of significant negative TWSF in the Upper Branco sub-basin. In case of realization 1, due to inconsistencies between the likelihood functions and the prior data, the uncertainty estimates within the floodplain valleys increase up to 60 mm/month. The results of realization 8, for which the ensemble flux data is used as input for fine-scale TWSF, the river system is not represented in downscaled products, obviously, since the input did not represent it.

Based on the above results, it can be concluded that the downscaled products reflect TWSF characteristics derived from both GRACE and fine-scale TWSF data. However, a critical question remains: Do these downscaled products yield meaningful results when compared to an independent dataset? Direct validation against in situ TWSF measurements is not possible due to their absence. Instead, validation is performed using 1) satellite-based estimates of surface water storage variations (Sub-section 4.2.5), and 2) vertical crustal displacements derived from GPS measurements (Sub-section 4.2.6).

4.2.4 Examples of downscaled TWSA fields

To demonstrate the applicability of the proposed method, this section shows some examples where downscaling of the Terrestrial Water Storage Anomaly (TWSA) is targeted instead of TWSF. In such a case, the fine-scale TWSA is used as input instead of the fine-scale TWSF model, and the fine-scale soil moisture itself instead of the fine-scale soil moisture change (SMC). All the results shown in this section are from Realization 1, where the fine-scale TWSA is taken from WGHM and the fine-scale SM is from GLEAM.

4.2.5 Validation against surface water storage

Surface water storage is a major component of water storage variations in the Amazon Basin (Frappart et al., 2019; Fassoni-Andrade et al., 2021; Papa and Frappart, 2021). Surface water storage variations from (Frappart et al., 2019) are utilized, derived by combining surface water extent estimates from the Global Inundation Extent Multi-Satellite (GIEMS) dataset (Prigent et al., 2007) with approximately 1,000

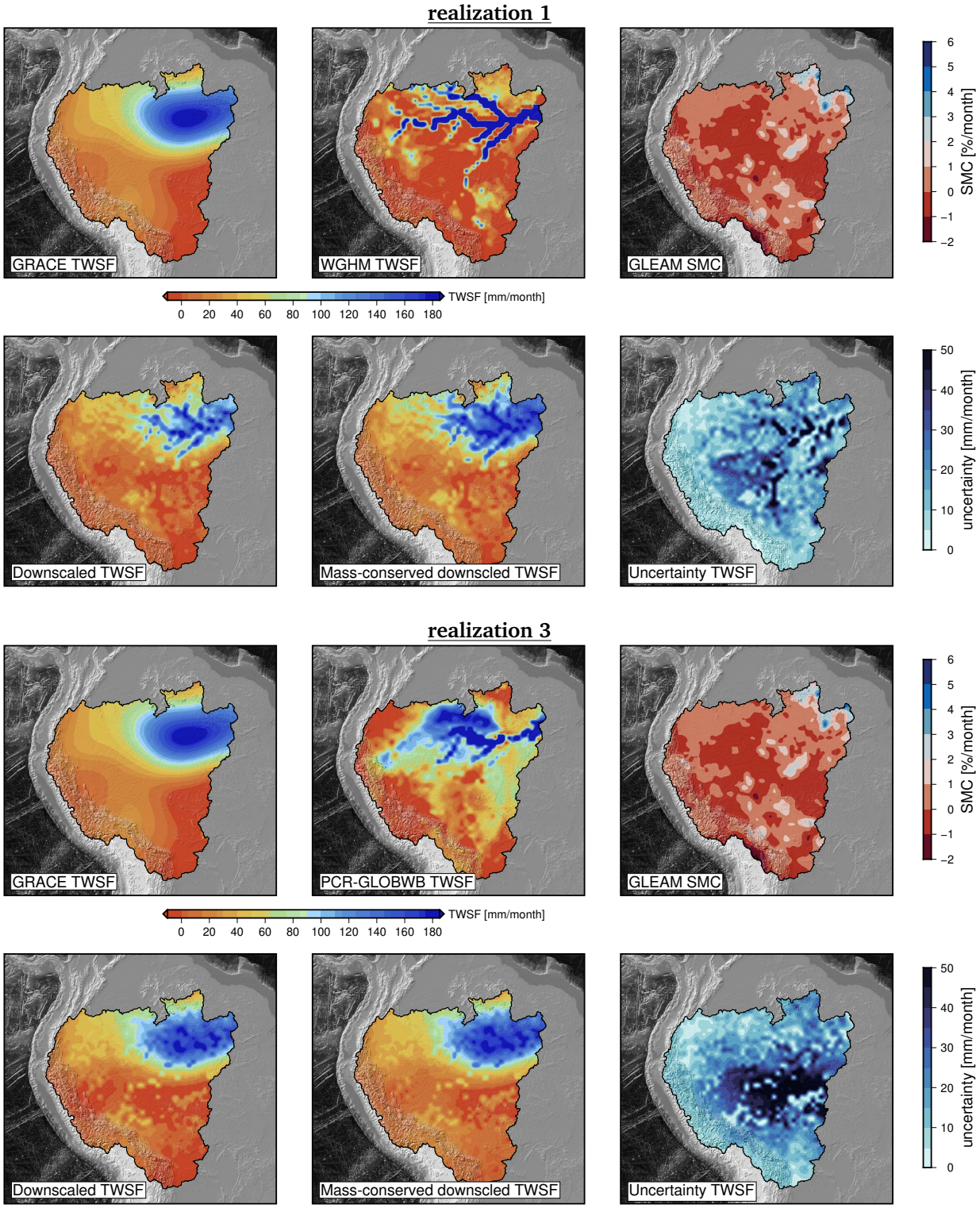

Fig. 4.12: Inputs and outputs of realization 1 (top panel) and realization 3 (bottom panel) for March 2012. The first row in each panel represents the inputs: GRACE as prior, input fine-scale TWSF (WGHM for realization 1 and PCR-GLOBWB for realization 3), and SMC from GLEAM. The second row represents the output: downscaled TWSF, mass-conserved downscaled TWSF, and the corresponding uncertainty estimates.

altimetry-based water levels from ENVISAT, manually constructed (Da Silva et al., 2010; Normandin et al., 2018) and available through Hydroweb (`http://hydroweb.theia-land.fr/`).

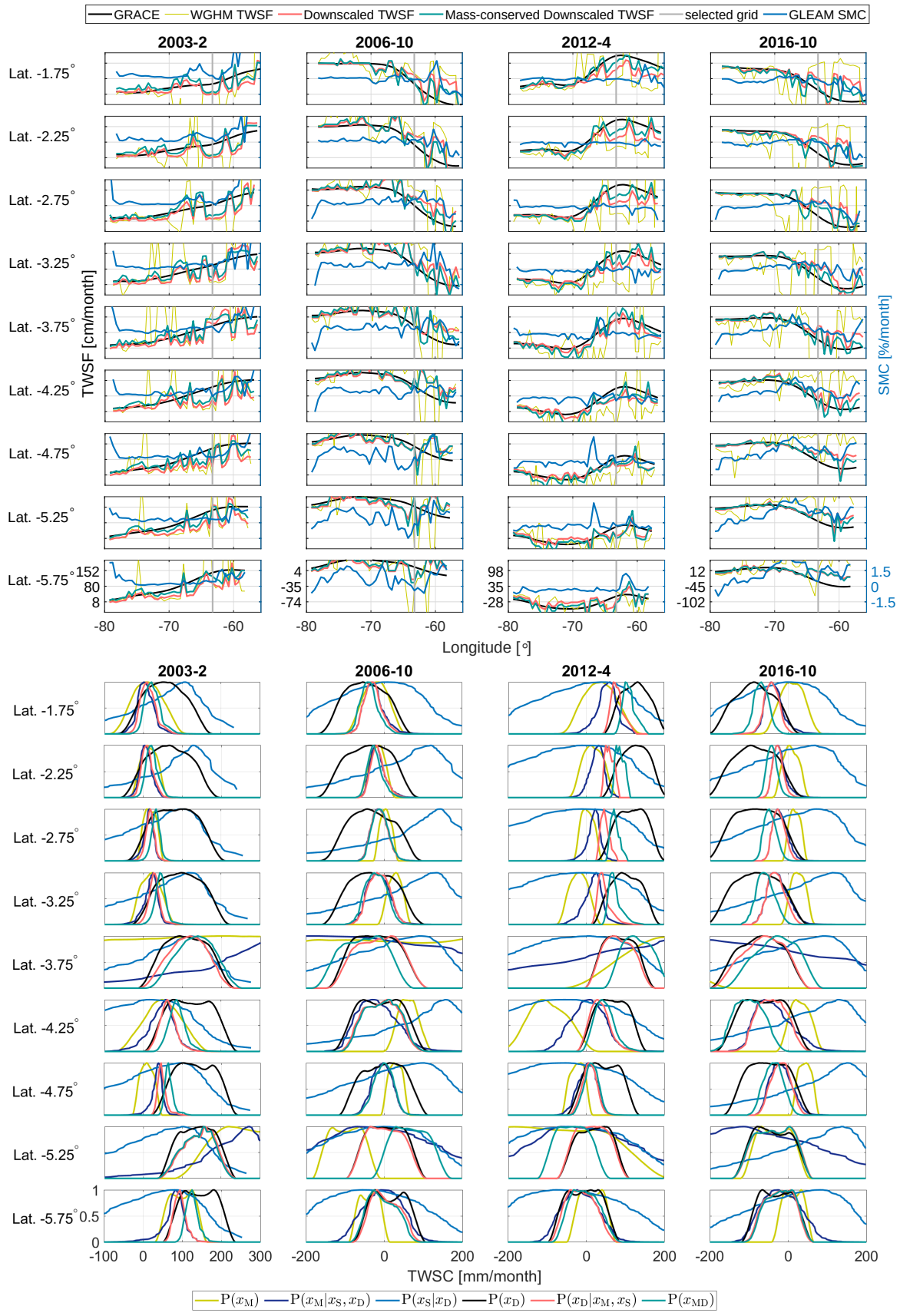

Fig. 4.13: Top panel: Profile lines of TWSF from GRACE $\dot{S}_G$, hydrological measurements $\dot{S}_{SM}$, WGHM model $\dot{S}_W$ together with downscaled products for 9 selected latitudes along the Amazon Basin Bottom panel: For the selected grid cells indicated as grey vertical lines in the top panel $P(x_M|x_D,x_S)$ is the likelihood function of fine-scale TWSF given x_D and x_S. $P(x_S|x_D)$ is the likelihood function of SMC given x_D, $P(x_D)$ is the prior distribution obtained from the distribution of GRACE TWSF in a grid cell for a certain month and the posterior distribution is obtained by $P(x_D|x_M,x_S) = P(x_M|x_D,x_S)P(x_S|x_D)P(x_D)$. $P(x_M)$ is the fine-scale TWSF distribution for the selected grid cell, allowing a comparison with the corresponding distribution from GRACE $P(x_D)$.

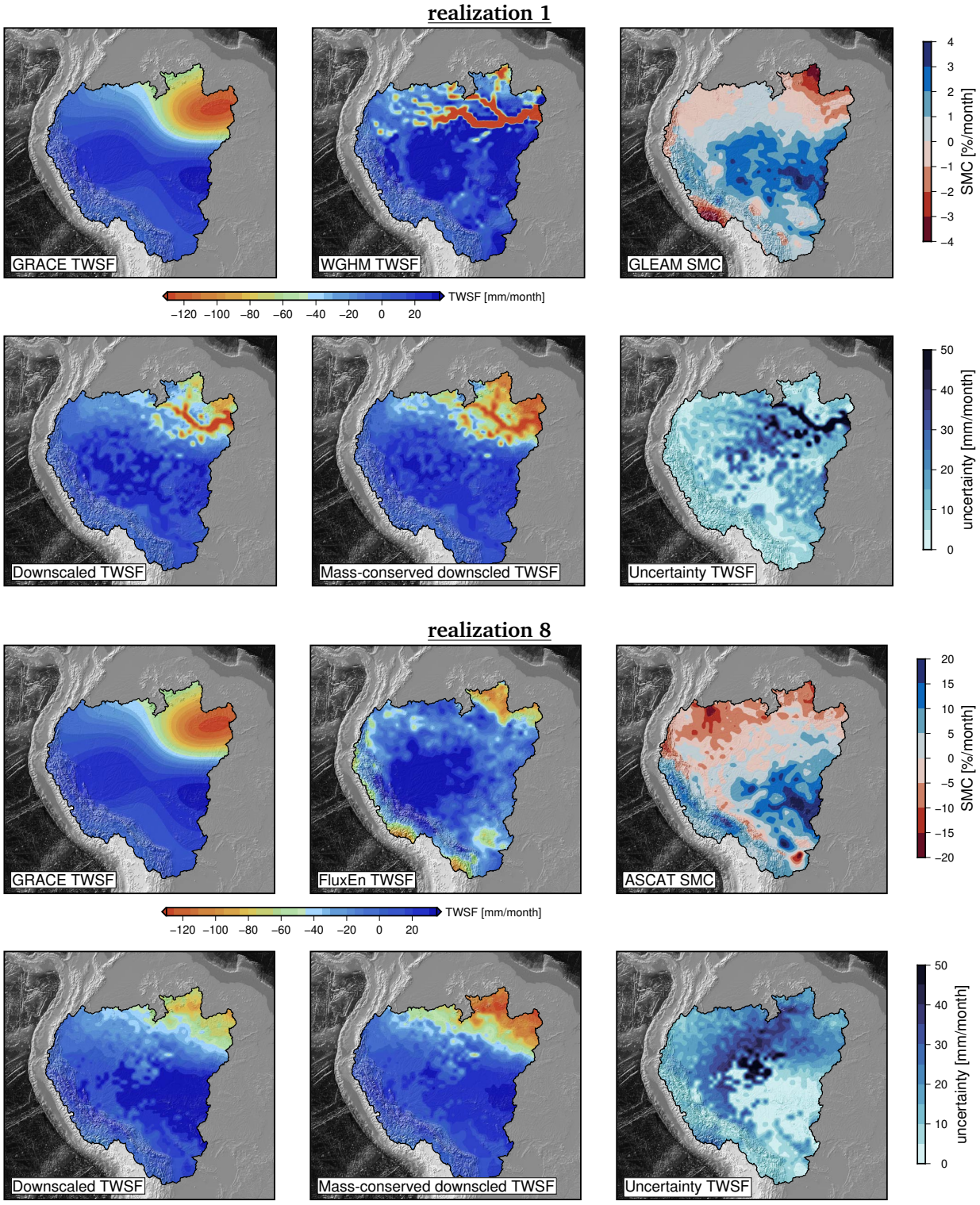

Fig. 4.14: Inputs and outputs of realization 1 (top panel) and realization 8 (bottom panel) for October 2016. The first row in each panel represents the inputs: GRACE as prior, input fine-scale TWSF (WGHM for realization 1 and PCR-GLOBWB for realization 8), and SMC (GLEAM for realization 1 and ASCAT for realization 8). The second row represents the output: downscaled TWSF, mass-conserved downscaled TWSF, and the corresponding uncertainty estimates.

For validation purposes, the surface water storage change (SWSC) was determined as the time derivative of SWSA. SWSC profiles were then extracted along nine river branches in the Amazon Basin and compared with the TWSF profiles from GRACE, the fine-scale model, and downscaled products.

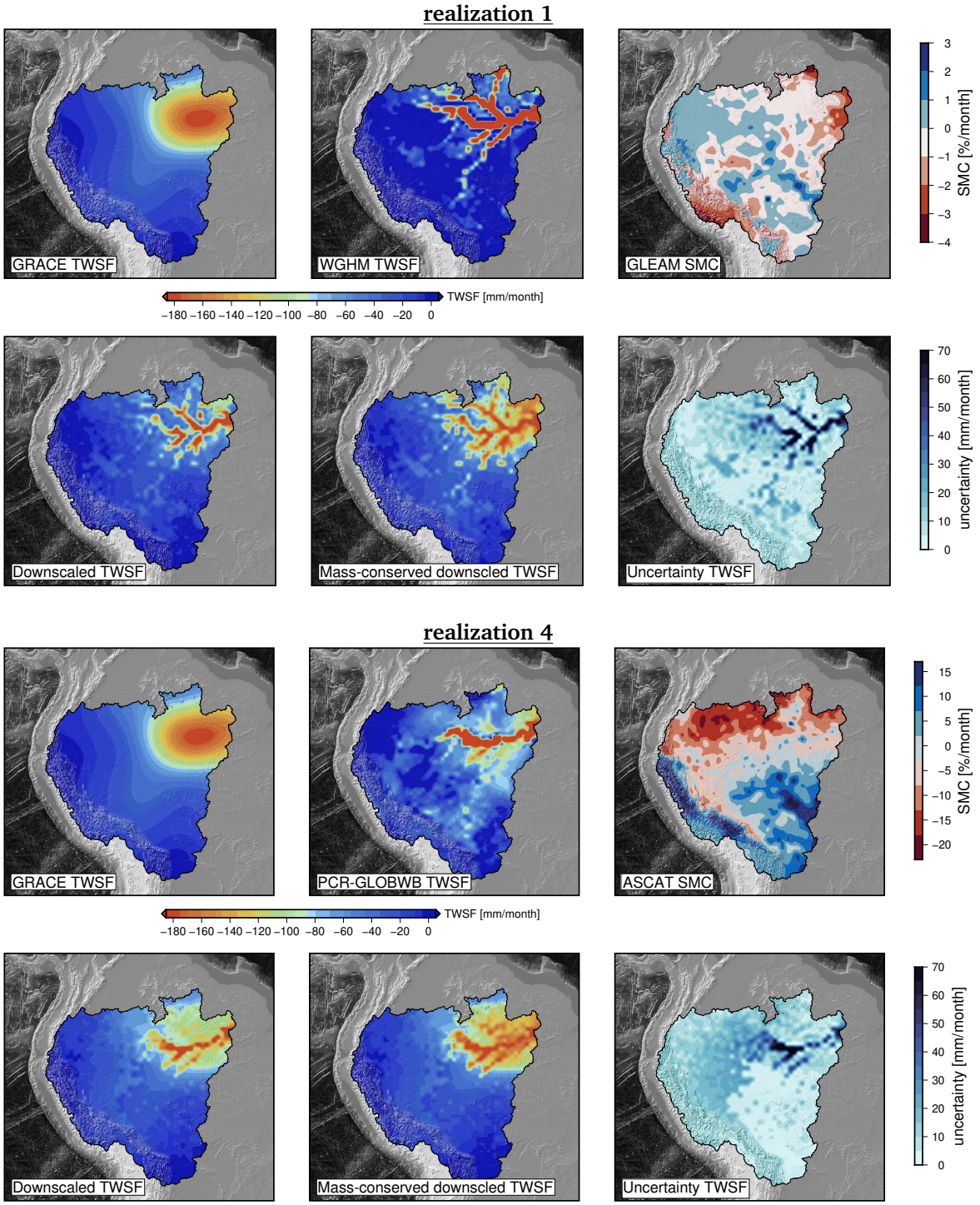

Fig. 4.15: Inputs and outputs of realization 1 (top panel) and realization 4 (bottom panel) for September 2007. The first row in each panel represents the inputs: GRACE as prior, input fine-scale TWSF (WGHM for realization 1 and PCR-GLOBWB for realization 4), and SMC (GLEAM for realization 1 and ASCAT for realization 4). The second row represents the output: downscaled TWSF, mass-conserved downscaled TWSF, and the corresponding uncertainty estimates.

SWSC profiles for nine river branches within the Amazon Basin were extracted for the period 2003–2010. Assuming that the contribution of other storage components in the river is negligible, the SWSC profiles are then compared to the TWSF profiles from GRACE, the fine-scale model, and the downscaled products. Figure 4.19 shows SWSC and TWSF profiles of some randomly selected months along the main stem of the Amazon River out of realization 1, showing generally good agreement of the GRACE and downscaled

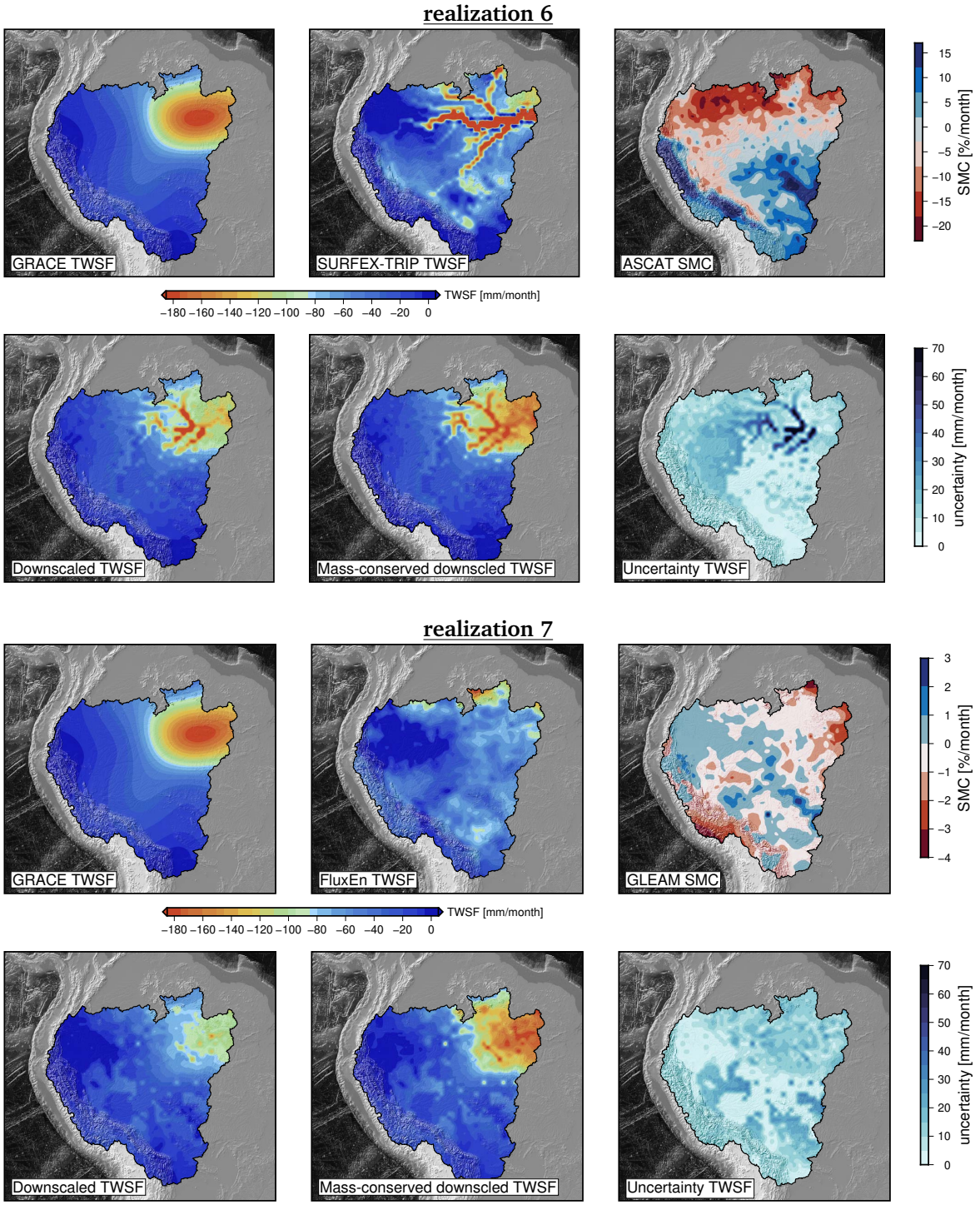

Fig. 4.16: Inputs and outputs of realization 6 (top panel) and realization 7 (bottom panel) for September 2007. The first row in each panel represents the inputs: GRACE as prior, input fine-scale TWSF (SURFEX-TRIP for realization 6 and FluxEn for realization 7), and SMC (ASCAT for realization 6 and GLEAM for realization 7). The second row represents the output: downscaled TWSF, mass-conserved downscaled TWSF, and the corresponding uncertainty estimates.

products with the SWSC profiles. Visual inspection reveals that the downscaled products follow variation details in the river system, which are not represented by GRACE. (That is, GRACE shows a relatively smooth variation along the profiles, omitting high-frequency information.) On the other hand, WGHM TWSF shows both overestimated and underestimated values with different behavior, resulting in lower CCs. Putting all CCs obtained for each month together and representing them in the form of CDF (Figure 4.20) it is

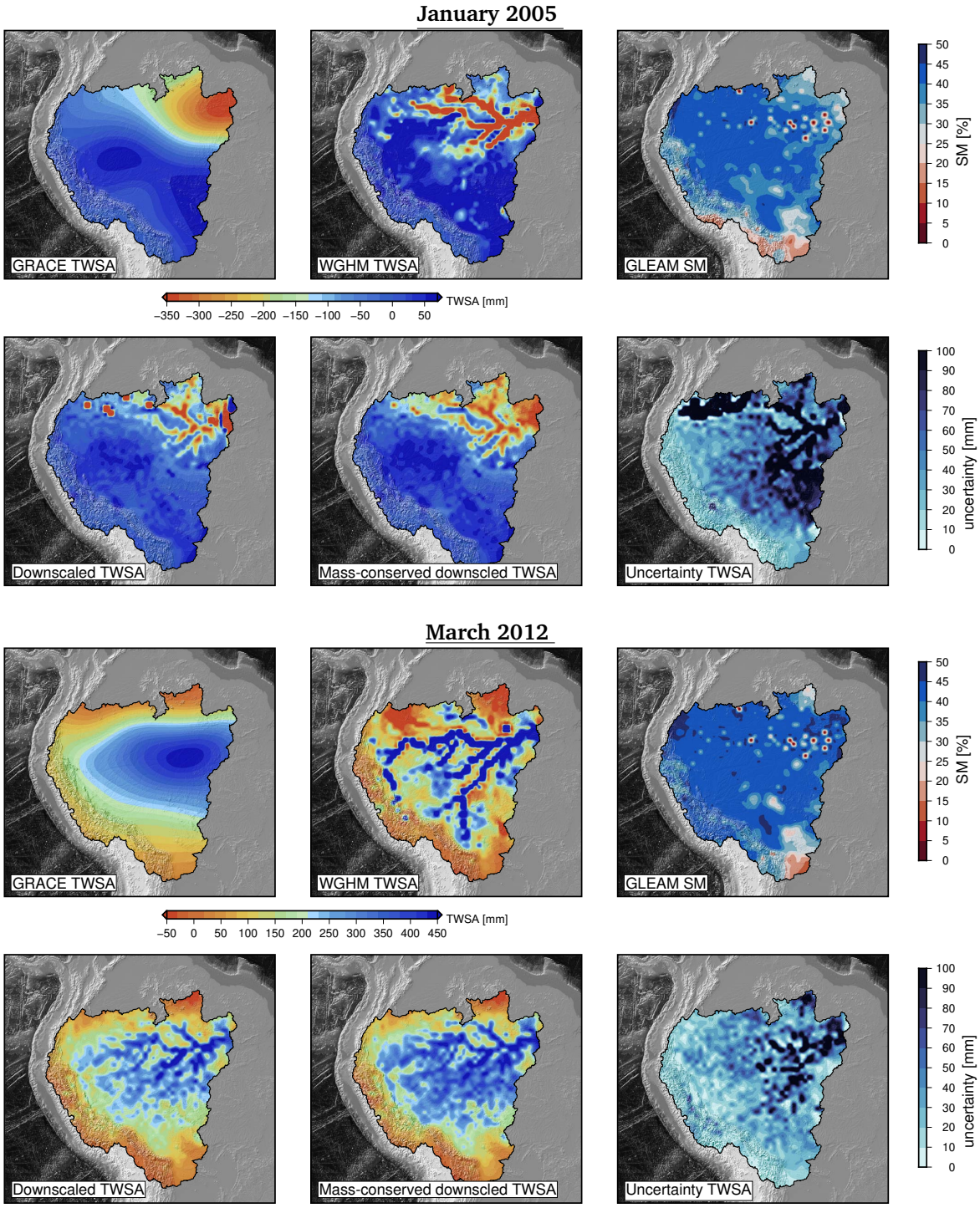

Fig. 4.17: Inputs and outputs of realization 1 for January 2005 (top panel) and March 2012 (bottom panel). The first row in each panel represents the inputs: GRACE TWSA as prior, input fine-scale TWSA (SURFEX-TRIP for realization 6 and FluxEn for realization 7), and soil moisture from GLEAM. The second row represents the output: downscaled TWSA, mass-conserved downscaled TWSA, and the corresponding uncertainty estimates.

clear that GRACE always outperforms the input fine-scale TWSF and also SMC. GRACE is closely followed by the downscaled TWSF and downscaled mass-conserved TWSF for all realizations. The downscaled products, which are fed by fine-scale TWSF and SMC outperform both of them in all realizations over the Amazon main stem. However, such a conclusion on CC of the Amazon River cannot be generalized for all rivers. Examining the median of monthly spatial correlations (Figure 4.21, top, for all nine rivers and all

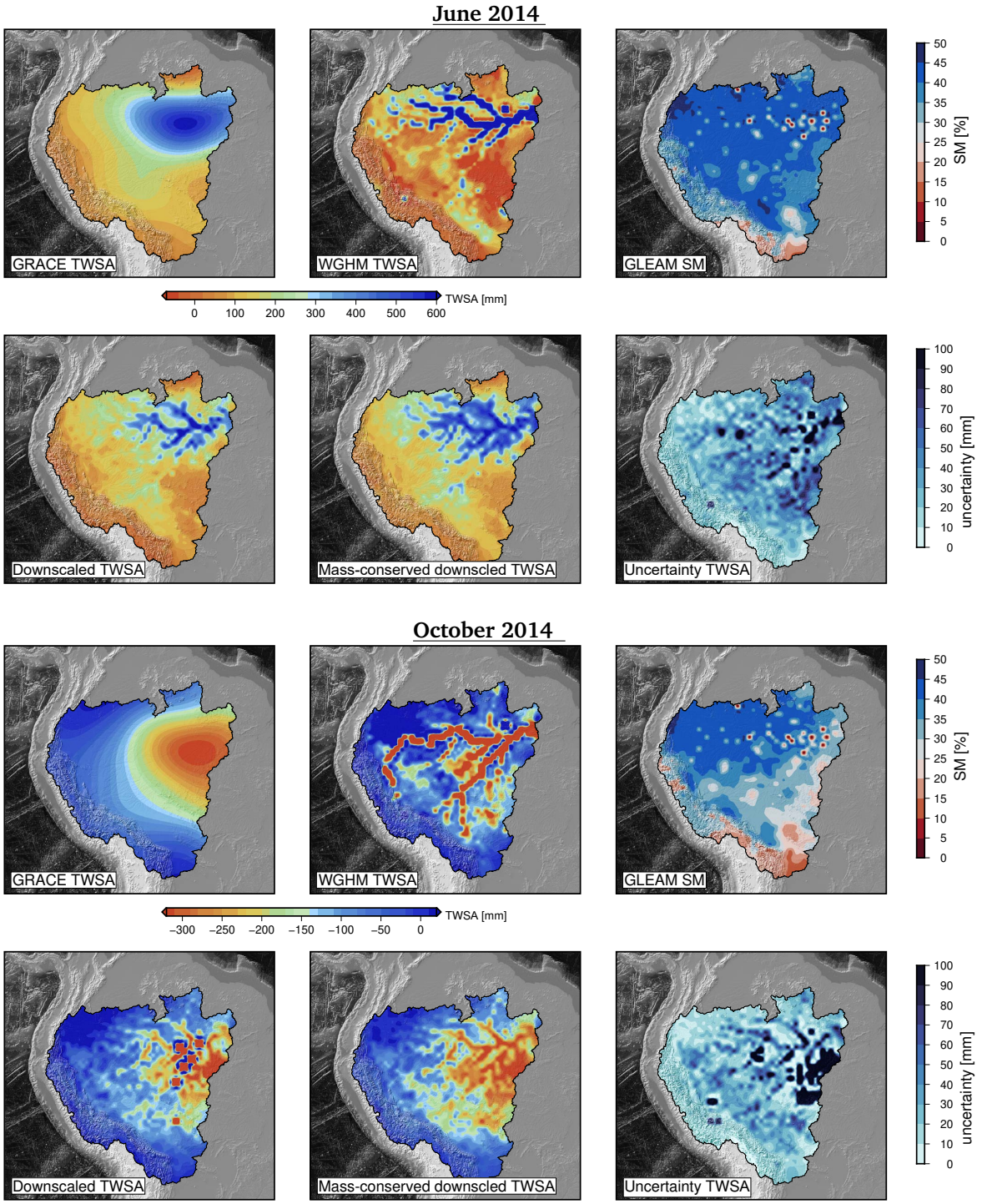

Fig. 4.18: Inputs and outputs of realization 1 for June 2014 (top panel) and October 2014 (bottom panel). The first row in each panel represents the inputs: GRACE TWSA as prior, input fine-scale TWSA (SURFEX-TRIP for realization 6 and FluxEn for realization 7), and soil moisture from GLEAM. The second row represents the output: downscaled TWSA, mass-conserved downscaled TWSA, and the corresponding uncertainty estimates.

realizations), it is observed that the downscaled product for the Madeira River does not outperform the fine-scale TWSF, except for realization 7. However, in terms of relative RMSE (Figure 4.21 bottom), as also evident from Figure 4.19, the input fine-scale TWSF profiles exhibit a large error in capturing variations in river storage. For instance, the WGHM model shows a large relative RMSE of up to 100% over rivers like Amazon, Japura, Madeira, Putamayo, and Ucayali. The downscaled products, on the other hand,

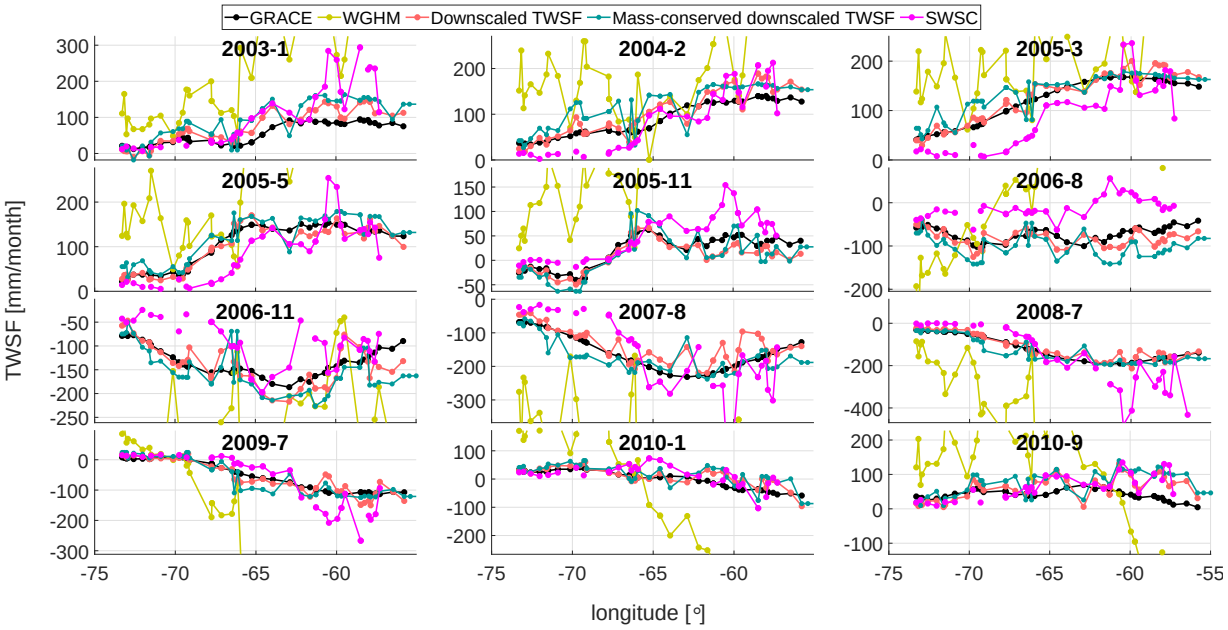

Fig. 4.19: SWSC and TWSF profiles of some randomly selected months along the main stem of the Amazon River for GRACE, WGHM, and downscaled products from the realization 1. Note that the y-axis was chosen to better show the fluctuations, resulting in the overestimated or underestimated WGHM TWSF profiles not being fully displayed.

provide a similar relative RMSE to GRACE despite being so much more detailed in the variations of river storage change. Overall, the median relative RMSE across all rivers and all realizations results in 24% for GRACE, 70% for the input fine-scale TWSF, 26% for the downscaled TWSF, and 28% for the mass-conserved downscaled result.

Overall, from Figures 4.20 and 4.21, it can be concluded that realizations 7 and 8, which use ensemble flux data as the input fine-scale TWSF, exhibit the lowest performance in capturing the details of river storage variation. This is due to the inherent error in the water balance elements preventing the acquisition of a meaningful spatial pattern in TWSF, which can also be identified in Figures 4.14 and 4.16. Overall, realization 5 with SURFEX-TRIP as input TWSF and GLEAM as input SMC shows the best performance with a mean CC of 0.44 (mean across all rivers), followed by realizations 6 and 1 with a similar CC of 0.41.

4.2.6 Validation against GPS data

For comparison purposes, 10 GPS sites (Figure 4.9, top panel) within the spatial and temporal domains of the downscaled TWSF were selected. The dataset consists of monthly vertical crustal displacements covering the period from January 2009 to December 2015. The daily GPS raw dataset, processed by the Nevada Geodetic Laboratory (NGL) at the University of Nevada, was utilized. This dataset is publicly available at `http://geodesy.unr.edu/`, with further information and caveats provided by Blewitt et al. (2018). The GPS data consists of daily precise point positioning solutions, and the contribution of the ocean loading to the stations' motion was considered during the processing. Therefore, the daily GPS series is still contaminated with geophysical signals such as the tidal and nontidal atmospheric loadings and the nontidal ocean loadings. Thus, the atmospheric (tidal and nontidal) and oceanic (nontidal) loads provided by the Global Geophysical Fluids Center of the German Research Centre for Geosciences (Dill and Dobslaw, 2013) were used to remove such contributions from the respective GPS stations. Furthermore, the "trajectory model" proposed by Bevis and Brown (2014) was applied to detect and remove the contributions due to potential jumps (e.g., antenna changes) and co/post-seismic. At this stage, the 10 GPS station series for

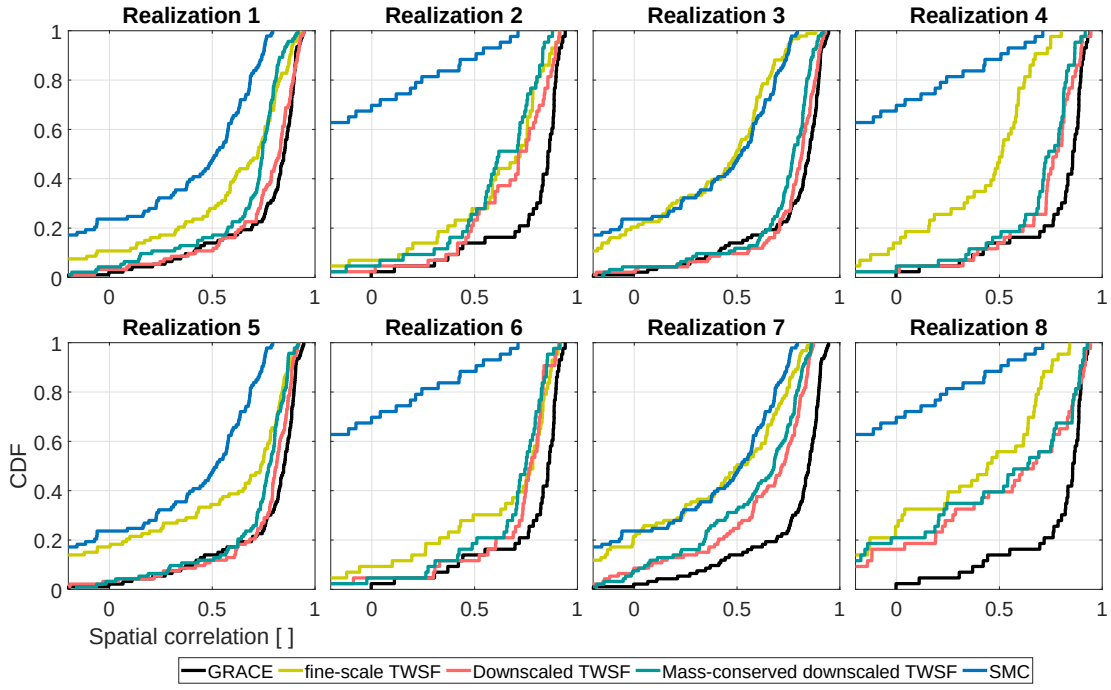

Fig. 4.20: CDF of monthly spatial CCs of Amazon River profiles from SWSC with those from GRACE, fine-scale TWSF, downscaled products, and SMC for all realizations

Vertical Crustal Displacements (VCD) primarily reflect the hydrological loadings. The time derivative of the VCD series is then computed using the central difference scheme, resulting in VCD changes (VCDR) expressed in mm/month.

The VCDR time series are used for validation in two ways: 1) comparing them with TWSF based vertical displacement, which is obtained by convolving the TWSF loading (mm/month) with the Green function, and 2) direct comparison with the TWSF of the grid cell where the GPS station is located.

The downscaled TWSF fields based on the eight realizations (cf. Table 4.5) were convolved with Green's function to estimate the respective Vertical Crustal Displacements (VCD) changes (VCDR), which are equivalent to the temporal derivative of VCD. Using Green's function to compute the VCDR from the different TWSF realizations would require estimating the deformation field considering all water masses of the world (excluding the oceans and atmosphere). Overall, the impact reduces with increasing distances due to the reciprocal distance appearing in Newton's integral. However, the downscaled fields only cover the Amazon Basin (Figure 4.9). Since the comparisons are relative to the datasets (TWSF based on eight realizations) covering the same spatial domain, the omission of the far zone fields would impact all data products in the same way when compared to GPS-based results. Hence, the assessment performed here may indicate internal validation and is valid only among the evaluated products. That said, the estimated VCDR series were then compared with the GPS observed VCDR throughout the period Jan 2009 to Dec 2015, and the results are summarized in Figure 4.22 in terms of RMSE values.

Overall, the RMSE values range from approximately 2 to 14 mm/month for all realizations for all GPS sites (Figure 4.22). Within the respective realizations, the exception is the estimated VCDR based on input fine-scale TWSF, which underperforms the VCDR for almost all GPS stations. For the other solutions (GRACE, downscaled TWSF, and mass-conserved downscaled TWSF), these figures are between 2.27–5.65 mm/month. Considering this maximum range for the RMSE values seen in Figure 4.22, it would be equivalent to approximately 4 mm, if VCD would be considered instead of VCDR. Consequently, given the overall root-mean-square (RMS) of the GPS series, this figure would be equivalent to an RMS reduction (cf.

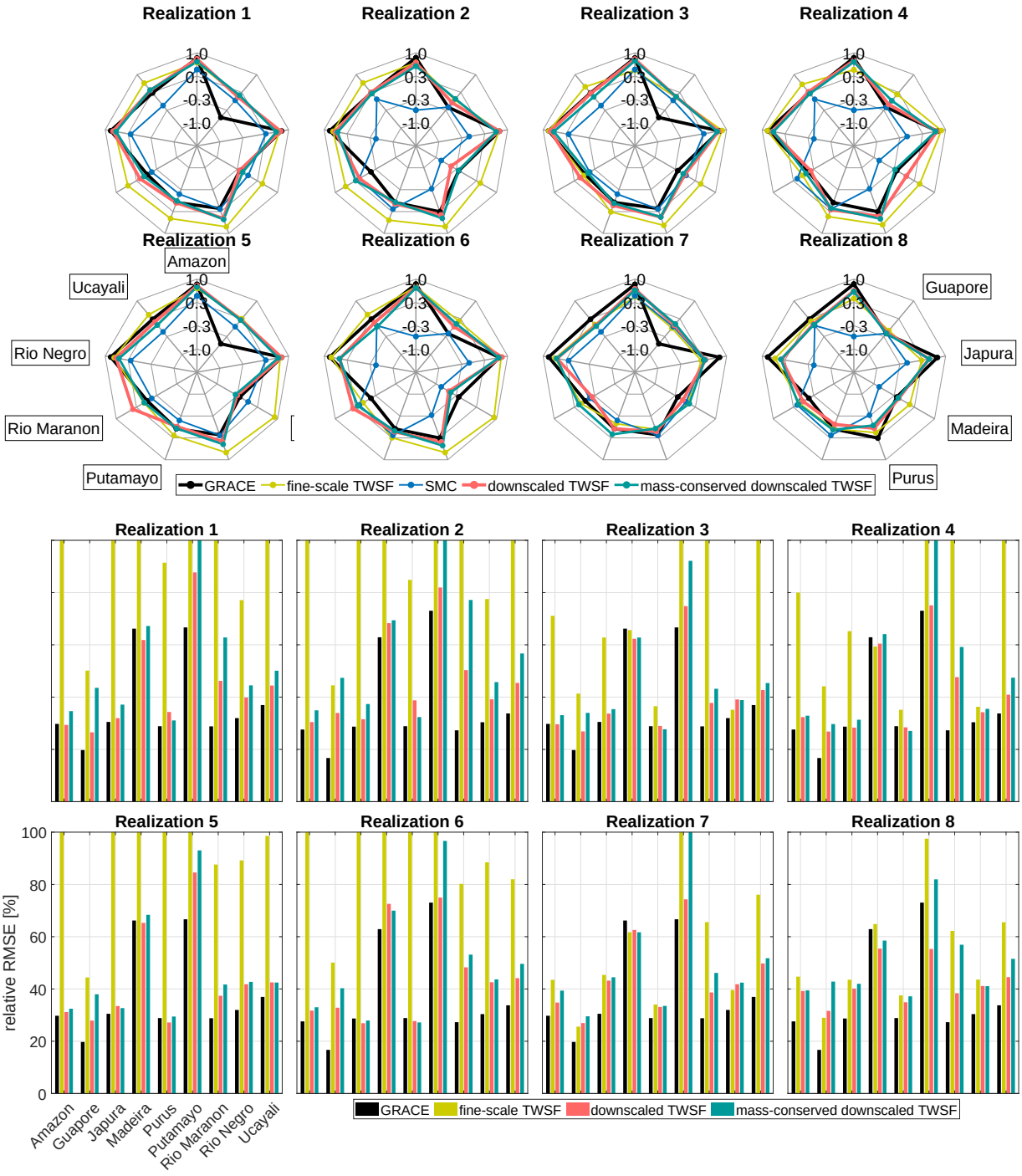

Fig. 4.21: Top: median of spatial CCs of SWSC river profiles with SMC and different TWSF estimates (GRACE, input fine-scale, downscaled, and mass-conserved downscaled) for 9 rivers in the Amazon Basin. Bottom: median of relative RMSE of SWSC river profiles with respect to different TWSF estimates

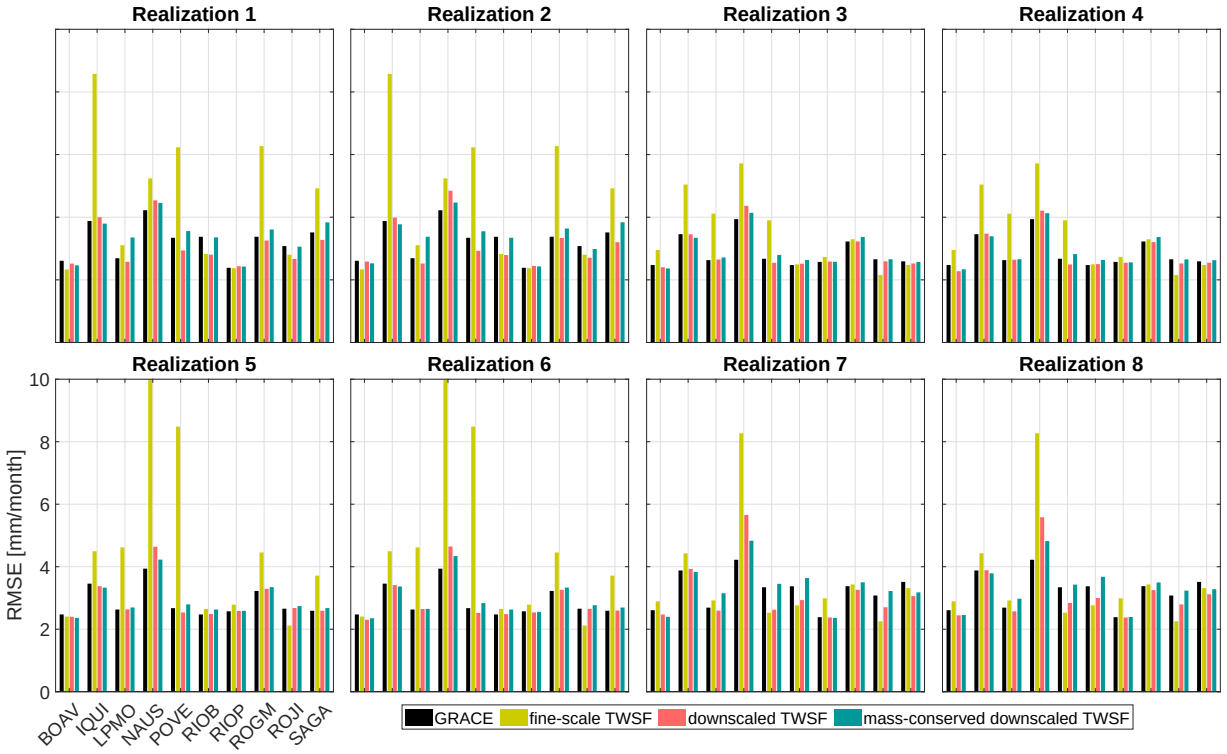

Fig. 4.22: RMSE values of the respective realizations of TWSF-based VCDR and GPS-based VCDR for the 10 GPS sites within the Amazon Basin.

Moreira et al., 2016) of VCD of approximately 63%, which agrees with previous studies (e.g., Moreira et al., 2016; Ferreira et al., 2019).

Specifically for the different realizations, the summary of the RMSE values as the median for all GPS sites (10) through the different downscaled products, realization 4 with PCR-GLOBWB and ASCAT performs the best overall. However, this is closely followed by realizations 3, 6, and 5, respectively. Specifically for the four solutions (i.e., GRACE, fine-scale TWSF, downscaled TWSF, and mass-conserved downscaled TWSF) over the 10 GPS sites, the best performance is for downscaled TWSF followed by GRACE. (The difference between their RMSE values is approximately 7.6%.) Generally, if the downscaled results outperform those from GRACE and the fine-scale TWSF, it is an indication of the advantages brought by SMC data. Overall, the fine-scale TWSF (see Table 4.5 for the input datasets) provides the worst performance in terms of RMSE through the different realizations (Figure 4.22). The highest RMSE value for the fine-scale TWSF for the 10 GPS sites is seen for the NAUS station (evident in realizations 5 to 8). It is located in the city of Manaus, Brazil, at the confluence of the Solimões (the upper Amazon River) and the Negro (Figure 4.9). Regarding the RMSE for the NAUS station, it indicates that realizations 7 and 8, based on the ensemble flux data (cf. Table 4.5), might not capture the river water level changes adequately. This agrees with the assessment presented in Sub-section 4.2.5 based on surface water storage.

A direct comparison between GPS-VCDR and TWSF at a given cell where the GPS site lies allows us to quantify the overall relationship between the loading and displacement. For instance, Birhanu and Bendick (2015) reported that the reciprocal correlation between the GRACE-derived TWSA and GPS-observed VCD (VCDR) could be explored in such a way that one could estimate absolute changes in the TWSA (TWSF) from vertical surface displacements (their time derivative) and vice versa. Likewise, Chew and Small (2014) pointed out that GPS-based VCD data could be used to monitor drought induced by the variations in TWSA. Hence, Figure 4.23 shows the CC between the GPS-VCDR and the respective TWSF products over the 10 GPS locations throughout the different realizations. Averaging all CCs over all 10 GPS stations leads to

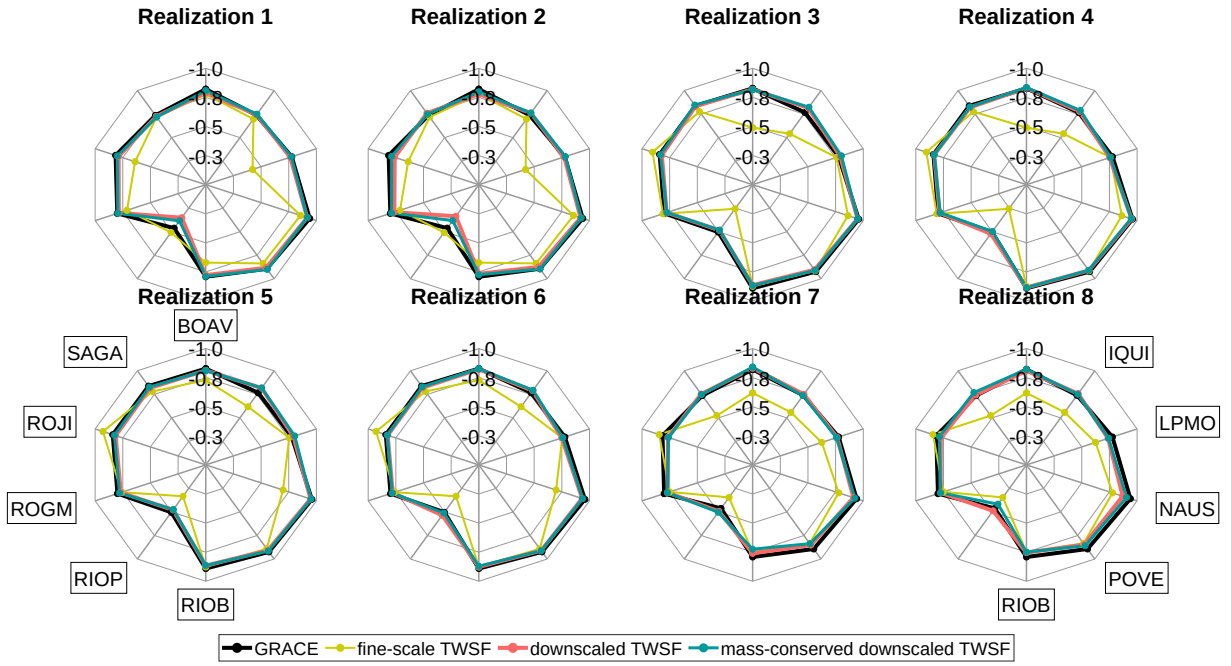

Fig. 4.23: Correlation coefficients between the respective realizations of TWSF and GPS-based VCDR for the 10 GPS sites.

-0.80 for GRACE, -0.81 for downscaling products, and -0.73 for input fine-scale TWSF. Overall, the fine-scale TWSF presents the lowest correlation (anti-correlation) over the GPS sites through all realizations (Figure 4.23). These agree with the results presented in the previous sub-section as well as the RMSE values presented in Figure 4.22. Among the different realizations, realization 4 shows the strongest anti-correlation with an average CC of -0.82, closely followed by realizations 3, 5, and 6 with an average CC of -0.81, which is a similar result to the RMSE analysis.

4.3 Discussion

As mentioned in the introduction to this chapter, linear statistical approaches typically encounter two main issues: 1) they overlook the nonlinear relationships between fine- and coarse-scale datasets, and 2) they generate downscaled products without considering the marginal or joint distribution of the datasets. As a result, the second issue limits these methods, as they do not allow for the derivation of a distribution or, more specifically, proper uncertainty estimates for the downscaled results. Here, both of these problems are addressed by proposing a copula-supported Bayesian framework. To this end, a copula-based method is used, enabling the modeling of dependencies, both linear and nonlinear, between random variables without information about the marginal distributions. This approach allows the direct obtaining of a posterior probability of the downscaled Terrestrial Water Storage Flux (TWSF) (the time derivative of TWSA) in the context of fine-scale data of available TWSF and Soil Moisture Change (SMC) fields. The downscaled TWSF is estimated by taking the maximum of the posterior distribution, and more importantly, the uncertainty for the estimate is determined by relying on the extent of the posterior. The Bayesian ingredients, including the likelihood functions and the prior, are obtained from the data itself. For the likelihood functions, conditional probability functions are derived from the joint distribution function defined by the copula.

The proposed copula-supported Bayesian framework was evaluated using fine-scale data for TWSF and SMC from various sources not previously combined in such studies. Therefore, a direct comparison of results for a comparative assessment of the proposed methodology against previous studies is not possible.

Despite numerous studies devoted to the downscaling of GRACE data, the literature is rather scant with respect to the validation of outcome products (see, e.g., Zaitchik et al., 2008; Eicker et al., 2014; Reager et al., 2015; Schumacher et al., 2018; Yin et al., 2018; Miro and Famiglietti, 2018; Seyoum et al., 2019; Jyolsna et al., 2021; Vishwakarma et al., 2021; Mehrnegar et al., 2021; Gorugantula and Kambhammettu, 2022). In most studies, either no independent validation was performed, or validation was performed using storage compartment data such as groundwater (Jyolsna et al., 2021), for which surface water storage and soil moisture must first be modeled and removed, adding uncertainty to the validation results.

The two independent validation datasets presented here can be leveraged to capture corner cases of the proposed methodology, allowing us not only to validate the performance of the downscaling results but also to assess the performance of the input data. It should be noted, however, that validation against the SWSC should be interpreted with a degree of caution, as the SWSC is also space-based and subject to uncertainties. Both validations arrive at more or less similar conclusions despite the fact that they are based on fundamentally different variables. As expected, the performance of the downscaling products depends on the quality of the input data. The two TWSF input models, PCR-GLOBWB and SURFEX-TRIP, used in realizations 3–4 and 5–6, respectively, generally appear to produce slightly better-downscaled results compared to the widely used WGHM model. These datasets are also used in (Tangdamrongsub et al., 2017) and (Mehrnegar et al., 2020), which also report their good performance in many river basins investigated.

In interpreting the results, it is important to remember that the likelihood functions are obtained by conditioning on the joint probability distribution functions, as defined by the copula of the spherical harmonic coefficients of the GRACE TWSF and the fine-scale data generated from field data. To derive copulas that best represent the dependencies between the datasets and are not affected by mismodeling or noise in the data, copulas are generated using lower-degree spherical harmonic coefficients with $l < 30$. This, in general, makes less noisy and less scattered copula densities, as can be seen in Figure 4.6 compared to Figure 4.3. Since the likelihood functions are obtained directly from the copula densities by sampling certain quantiles (reading a certain row from the copula density), a less scattered and less noisy copula would automatically lead to more informed likelihood functions with less dispersion. Such a truncation is acceptable only if it can be assumed that the dependencies captured in the lower spherical harmonic degrees would also hold for the higher degrees. Although it is not easy to prove such an assumption, since coefficients of higher degree are less representative of reality, results (figures 4.12,4.14, 4.15 and 4.16) and validations indicate that the river system is correctly captured. In the spatial domain, this approach involves reconstructing short wavelengths (higher degrees of spherical harmonic coefficients). This allows the argument that dependencies extracted from long wavelengths can generally be transferred to shorter wavelengths. However, it is acknowledged that if the dependence between short and long wavelengths differs significantly, this assumption might lead to inaccurate downscaled values and/or overly optimistic uncertainty estimates.

Finally, it should be emphasized that, given the nature of the downscaling problem, the downscaled results are not necessarily the best possible representation of the ground truth. Despite a careful analysis of the available fine-scale data and efforts to use the most suitable models, it is acknowledged that the results would improve with better models and could be less accurate with inferior ones. For example, in regions with very local human interventions that are not properly captured by GARCE, and where hydrologic models often fail to model storage properly, the chance of obtaining accurate downscaled estimates is indeed low. The proposed methodology is also applicable for downscaling other datasets with stochastic properties, as demonstrated in Section 4.2.4 for TWSA. The proposed method is also applicable to other regions. Note, however, that in regions where the GRACE data have lower signal-to-noise ratios and less obvious seasonal characteristics, e.g., arid and semiarid regions, the obtained prior from GRACE will be either diffuse or weakly informative with very large uncertainty, so the downscaled values will automatically rely more heavily on the likelihood functions.

5 Using a graphical model to improve inland water altimetry

Over the past 30 years, satellite altimetry has become a crucial tool for studying the Earth system. Initially developed for applications in oceanography and geodesy, it has demonstrated significant value in monitoring water level variations in lakes and rivers (Berry et al., 2005). Most applications of inland water altimetry demand accuracies on the order of a few centimeters. For lakes and reservoirs, achieving water level measurement accuracy below a decimeter is critical for precise estimation of changes in water volume. Similarly, sub-decimeter accuracy over rivers enables a better understanding of river dynamics and obtaining accurate estimates of river discharge (Tourian et al., 2013).

For inland water altimetry, the primary source of uncertainty typically lies in the range estimation between the altimeter and the water surface (Calmant et al., 2016). As discussed in Section 1.2.2, addressing this uncertainty has led to the development of various algorithms over the past two decades. These algorithms aim to improve the accuracy of range estimates by post-processing the corresponding waveforms to identify the water height representative point of the leading edge, determine its deviation from the predefined tracking point, and apply corrections to the resulting water level estimates. This process is known as the *retracking* procedure (Calmant and Seyler, 2006). The fundamental concept underlying various retracking algorithms, some of which are listed in Table 5.1, is to refine the range measurement either by fitting a physical or non-physical model to the waveform to extract the range or by identifying a point in the waveform that is considered representative of the height measurement. The latter involves either analyzing the entire waveform or isolating the region in the waveforms that most accurately represents the water surface.

Tab. 5.1: Overview of some of the most relevant retracking algorithms for inland altimetry.

Retracker	Description	Reference
Ocean	Developed for ocean surface measurements but can also be used for inland waters	Brown (1977)
5β parameter	Uses a five-parameter model for retracking.	Martin et al. (1983)
Ice-1	Defines the waveform peak and sets a threshold.	Wingham et al. (1986)
Ice-2	Fits an error function only the first part of the waveform	Legresy et al. (2005)
OCOG	Determines the Offset Center Of Gravity of a waveform.	Wingham et al. (1986)
MLE3	Uses the maximum likelihood to estimate the range, backscatter coefficient, and significant wave height	Thibaut et al. (2010)
MLE4	Estimates the range, significant wave height, backscatter coefficient, and square of the mispointing angle.	Thibaut et al. (2010)
Subwaveform	Identifies sub-waveform segments for retracking.	Idris and Deng (2012)
TFMRA	Sets a threshold on the first maxima of the waveform to define the retracking point.	Ricker et al. (2014)
SAMOSA	Based on theoretical modeling of radar altimeter waveforms over open water.	Ray et al. (2014)
Improved threshold	threshold retracker that benefits from adjacent waveforms.	Villadsen et al. (2016)
STAR	Uses information from neighboring waveforms within a Conditional Random Field (CRF).	Roscher et al. (2017)
IP method	Identifies the Inflection Point (IP) in a waveform.	Arabsahebi et al. (2018b)
ALES	Uses Adaptive Leading Edge Subwaveform retracking.	Passaro et al. (2014)
ALES+	Adapts the signal fitting based on sea state and trailing edge slope.	Passaro et al. (2018)
SAMOSA+	Modified SAMOSA algorithm for coastal zones (also relevant for inland waters).	Dinardo (2020)
SAMOSA++	Utilizes Range Integrated Power (RIP).	Dinardo et al. (2021)
INPPTR method	Uses the Improved Narrow Primary Peak Threshold Retracking algorithm.	Chen et al. (2022)
ALES+ SAR	Applies an empirical retracking strategy with dedicated sea state bias correction.	Passaro et al. (2022)
Multipeak	Designed for complex ice surfaces, addressing areas with significant ice mass imbalance.	Huang et al. (2024)

Among the methods listed in Table 5.1, those that focus solely on a waveform i.e., the evolution of reflected power along the bin coordinate—referred to here as 1-D waveform retracking methods—are affected by noise in the waveform and may face the following limitations:

1. Sensitivity to waveform variations: The performance of all 1-D waveform retracking methods can be significantly affected by variations in the waveform. These methods can be misled by peaks that do not correspond to the water surface.

2. Dependency on specific waveform types: The efficacy of these methods is assured only for specific waveform types. Such dependency often necessitates dedicated pre-processing steps, such as waveform classification, to ensure reliable results (Tourian, 2012).

3. Neglecting spatiotemporal information: A significant limitation arises from neglecting spatiotemporal information. Conventional 1-D retracking methods independently estimate retracking offsets for each waveform within the Virtual Station (VS), leading to a lack of continuity.

    - Spatial information: Since each waveform is retracked individually, the along-track evolution of the waveform is ignored. In many cases, the evolution of the waveform shape contains useful information that can help to avoid peaks in the waveform that do not represent the water surface.
    - Temporal information: Altimetry satellites typically follow a repeat orbit, with a revisit period of 10 days for the Jason-series and 27 days for Sentinel-3A and -3B. The water level change within these 10 or 27 days often reflects the water level dynamics, with a strong correlation over time. However, 1-D retracking algorithms disregard this temporal information.

5.1 Incorporation of spatiotemporal information

To address the limitations mentioned above, utilizing the spatial correlation among successive along-track waveforms offers a promising approach for accommodating the evolving characteristics of waveforms along the track. This, in principle, involves instead of retracking a waveform applying the retracking algorithm on all consecutive waveforms within a VS, referred to as a *radargram* (see Figure 5.1). Since the waveform is represented in bins, a radargram can be considered an image defined in the bin-space domain (Figure 5.1), where *space* here refers to the along-track dimension. In a radargram, the bin-axis represents the variation of each waveform, while the space-axis is defined by the succession of along-track measurements. The horizontal width of each pixel (width in the bin-axis) corresponds to one bin, while the vertical axes (width in the space-axis) represent two successive measurements along the track. This means in the case of a 20 Hz sampling rate (when all measurements are available), the size of a pixel in the vertical direction (space-axis) corresponds to about 300 m. A radargram typically depicts an image with high intensity in its central region and carries useful information about water level variation, the neighboring area, and the along-track evolution of reflected power.

The key idea of incorporating spatial correlation is to utilize spatial information under the assumption that the water level within a VS remains constant. This approach allows for the effective handling of noise and the mitigation of unwanted patterns. Roscher et al. (2017); Boy et al. (2021); Villadsen et al. (2016) has followed such a philosophy and indeed achieved results that are less sensitive to outliers compared to other retracking methods. However, none of these methods benefited from temporal information acquired in different cycles.

In addition to spatial dependencies, temporal variations in radargrams over different cycles, where *cycles* refer to repeated groundtracks, also provide valuable information on water level changes, which can be useful for retracking. While spatial information refers to data in both the bin-domain and the space-domain, temporal information pertains to data acquired across different cycles, as illustrated in Figure 5.1. It should be noted that essentially, the quantity of all these axes is time, but with different sampling intervals: a bin corresponds to an interval of typically 3.125 ns, the space domain has an interval of 50 ms in the case of 20 Hz data, and the time domain has an interval of 10 days (in the case of Jason-series) or 27 days (in

the case of Sentinel-3 missions). However, for clarity's sake, these terms are maintained throughout this chapter.

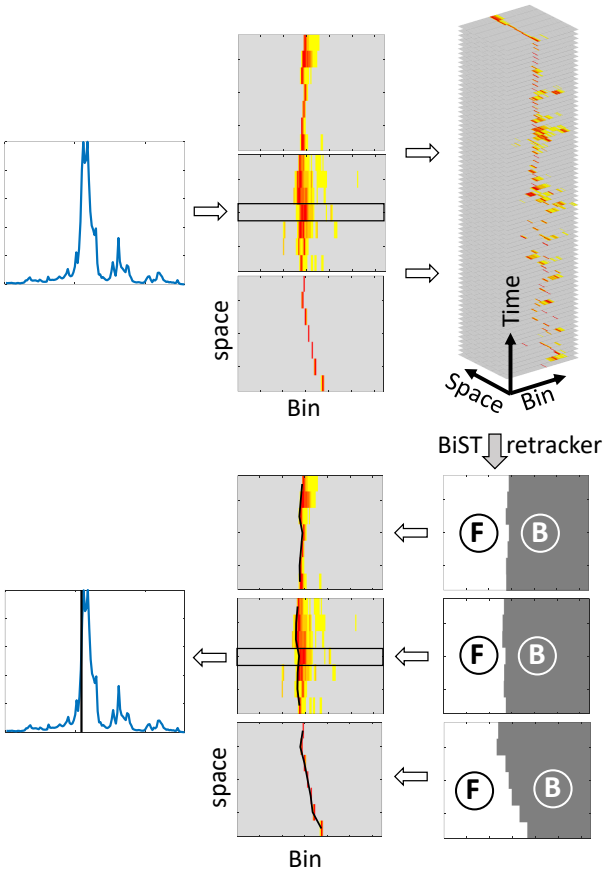

Fig. 5.1: From a waveform stack to a radargram and a radargram stack defined in the bin-space-time domain. The *bin* refers to the range bin of a waveform, *space* refers to the along-track dimension, and *time* refers to cycles, in the sense of repeated groundtracks. Consecutive retracking points of successive waveforms generate a retracking line in the radargram, segmenting it into two regions: *Front* indicated by F and *Back* indicated by B.

To optimally incorporate spatiotemporal information within the radargram, all waveforms within a stack of radargrams must share a consistent origin in bin-dimension over time. To achieve this, a process of shifting the waveforms in the bin domain is needed. To this end, over all cycles, the epoch t_m that yields the median value of satellite altitude is first selected. Subsequently, an arbitrary fixed raw water level h^0 is obtained by:

$$h^0 = H(t_m) - \rho(t_m) \tag{5.1}$$

where $H(t_m)$ denotes the satellite altitude on the selected epoch, and $\rho(t_m)$ represents the tracker range on that specific epoch. Following this, for each measurement, a bin shift value Δb_i^0 is calculated by:

$$\Delta b_i^0 = \frac{2(H_i - \rho_i - h^0)}{\tau \times c} \tag{5.2}$$

where H_i and ρ_i refer to all individual satellite altitudes and the tracker range of measurements of each cycle, respectively. So the index i refers to the number of waveforms in the VS in one cycle. τ is the bin width or sampling interval of a waveform in the bin domain (3.125 ns) and c is the light speed.

The calculated Δb_i^0 is then applied to all waveforms within the VS, ensuring the alignment of radargrams to a fixed location (Figure 5.2). Through this process, all radargrams become anchored to a consistent benchmark, enabling the extraction of information in both spatial and temporal dimensions.

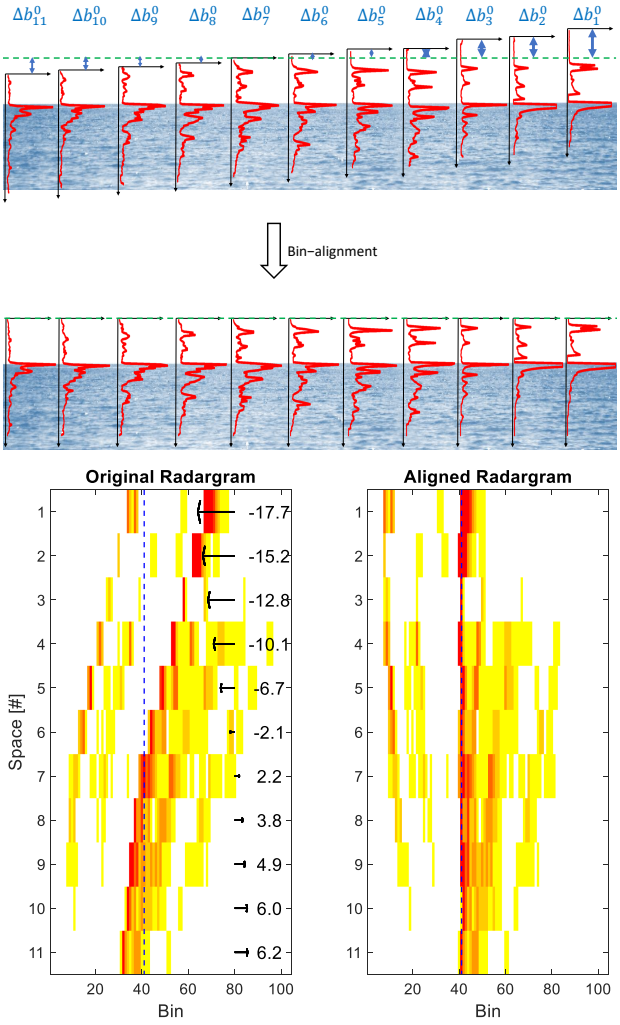

Fig. 5.2: Schematic representation of the bin-alignment procedure with its corresponding radargram before and after the bin-alignment procedure

5.2 Using a graphical model to incorporate spatiotemporal information for retracking altimetry waveforms

If the retracking procedure is targeted at an image (radargram), the search for a retracking line corresponds to a division of the image into two segments: *Front* and *Back* of the retracking line. This means that after retracking, each pixel in a radargram receives a label of either *Front* (F) or *Back* (B) (Figure 5.1). To achieve this, a Bayesian approach is proposed to formulate a probabilistic graphical model known as a Markov Random Field (MRF). As discussed in Chapter 2, the MRF provides a suitable framework for modeling spatial and contextual interrelations between pixels, and has been widely employed for various types of image problems, e.g. image segmentation (Boykov and Veksler, 2006; Kolmogorov and Zabin, 2004), multi-camera scene reconstruction (Kolmogorov and Zabih, 2002), denoising (Raj and Zabih, 2005), surface water extraction from satellite images (Elmi et al., 2016; Elmi, 2019) and also recently in retrieving time series of river water extent from global inland water data sets (Elmi and Tourian, 2023).

Here, the MRF is setup based on the fact that in a radargram with m pixels, outcome labels for all pixels $\boldsymbol{L} = \{L_1, L_2, ..., L_m\}$ will be either F or B and are to be identified from the observed pixel intensities $\boldsymbol{I} = \{I_1, I_2, ..., I_m\}$. To this end, a radargram can be represented as a graph shown in Figure 5.3 with nodes representing the labels of each pixel and links connecting a pair of nodes. Within such a probabilistic

graphical model with a graph shown in Figure 5.3, the goal of the segmentation will be maximizing the conditional probability $\mathrm{P}(\boldsymbol{L}|\boldsymbol{I})$.

$$\mathrm{P}(\boldsymbol{L}|\boldsymbol{I}) \rightarrow \text{maximum} \tag{5.3}$$

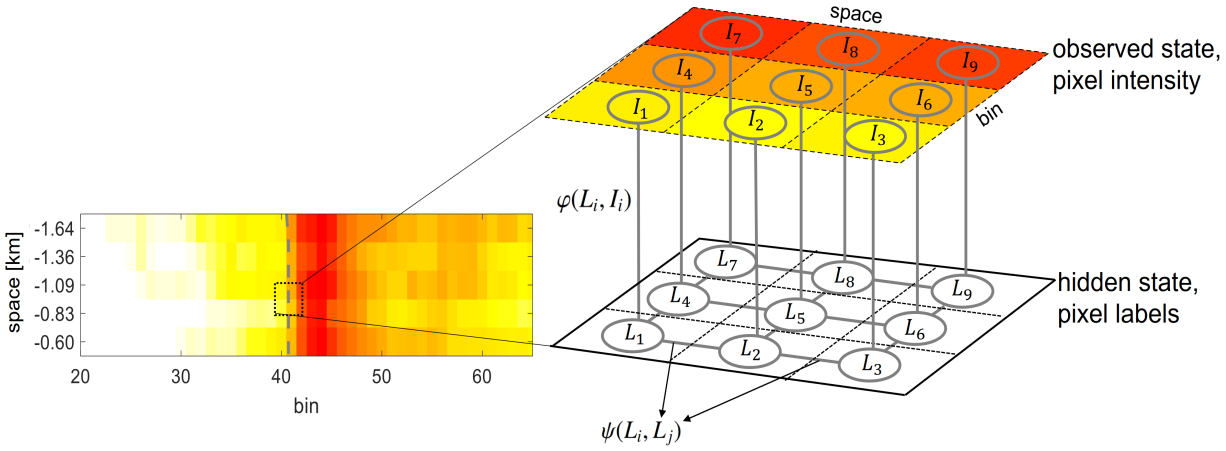

Fig. 5.3: Representation of the radargram as a graph with nodes representing the labels of each pixel L_i and links connecting a pair of nodes. Here, the pixel intensity I_i is considered as an observation for the sought labels. $\varphi(L_i, I_i)$ is a single-node (unary) potential capturing the likelihood of L_i given I_i, and $\psi(L_i, L_j)$ represents joint potentials characterizing the relationships between labels in the bin-space domain.

In other words, the aim is to find a set of labels $\boldsymbol{L}$ which features the maximum likelihood, given the observed pixel intensities $\boldsymbol{I}$. Following the Bayesian rule, we may represent $\mathrm{P}(\boldsymbol{L}|\boldsymbol{I})$ as a posterior probability by means of the likelihood function $\mathrm{P}(\boldsymbol{I}|\boldsymbol{L})$ and the prior $\mathrm{P}(\boldsymbol{L})$:

$$\mathrm{P}(\boldsymbol{L}|\boldsymbol{I}) = \frac{\mathrm{P}(\boldsymbol{I}|\boldsymbol{L})\mathrm{P}(\boldsymbol{L})}{\mathrm{P}(\boldsymbol{I})} \tag{5.4}$$

Since $\mathrm{P}(\boldsymbol{I})$ acts as a normalization factor only, it can be omitted in the maximization process of the posterior distribution

$$\mathrm{P}(\boldsymbol{L}|\boldsymbol{I}) \propto \mathrm{P}(\boldsymbol{I}|\boldsymbol{L})\mathrm{P}(\boldsymbol{L}) \rightarrow \text{maximum} \tag{5.5}$$

So in principle, if we select from all possible binary images $\boldsymbol{L}$ the one that maximizes the posterior, we achieve the desired segmentation and consequently the retracking line. The question remains how to obtain the likelihood and the prior, so as to achieve the posterior. A suitable model for the posterior is the so-called Gibbs-Boltzmann distribution; here the probability that a thermodynamic system assumes a certain state is a function of the energy of that state (Li, 2009) :

$$\mathrm{P}(\boldsymbol{L}|\boldsymbol{I}) = \frac{1}{Z}\prod_{i\in K}\varphi(L_i, I_i)\prod_{i,j\in C}\psi(L_i, L_j) = \frac{1}{Z}e^{-E_\mathrm{t}}e^{-E_\mathrm{bs}} \tag{5.6}$$

In this context, with Z as a constant term, the posterior probability is formulated as a composite of single-node (unary) potentials $\varphi(L_i, I_i)$ and joint potentials $\psi(L_i, L_j)$ (See Figure 5.3). The product $\varphi(L_i, I_i)$ extends over all pixels in the set K; it can be likewise represented by the exponential of the negative energy term E_t. Each factor in this product captures the likelihood of I_i for a given label L_i in pixel i. Conversely, the product $\psi(L_i, L_j)$ extends over all pairs of neighbouring pixels (i, j) which feature different labels (set C); it is likewise represented by the exponential of the negative energy term E_bs. Each factor $\psi(L_i, L_j)$ in this latter product characterizes the prior probability that the pixel pair (i, j) is separated by the retracking line.

Comparing (5.5) with (5.6), it becomes evident that the term $\exp(-E_{\mathrm{t}})$ corresponds to the likelihood function $\mathrm{P}(\boldsymbol{I}|\boldsymbol{L})$ as it captures the agreement between the observed pixel intensities $\boldsymbol{I}$ and the hypothesized label configuration $\boldsymbol{L}$. Essentially, it quantifies how well the observed data fits the proposed labels. On the other hand, $\exp(-E_{\mathrm{bs}})$ represents the prior $\mathrm{P}(\boldsymbol{L})$ as it encapsulates our prior knowledge or assumptions about the distribution of labels $\boldsymbol{L}$. It represents the inherent constraints or preferences regarding label configurations, such as smoothness or consistency assumptions.

With the above formulation, by obtaining the negative logarithm of Equation (5.6), the maximization of $\mathrm{P}(\boldsymbol{L}|\boldsymbol{I})$ can also be regarded as the minimization of $E_{\mathrm{bs}} + E_{\mathrm{t}}$ (Geman and Geman, 1984; Szeliski et al., 2008). By adding a hyperparameter λ between these two energy terms, obtaining the retracking line corresponds to minimizing the energy function (E):

$$E = E_{\mathrm{bs}} + \lambda E_{\mathrm{t}} \,, \tag{5.7}$$

Here, E_{bs} is the bin-space energy term, E_{t} is the temporal energy function, and the hyperparameter λ acts as a weight that controls the relative impact of the two energy terms. With this setup, one can incorporate spatial information by defining the cost function E_{bs} and temporal information by defining the cost function E_{t}. In principle, defining the retracking line in a radargram involves determining a retracker line that minimizes the total cost/energy E. The term E_{bs} should ensure the identification of a retracking line that accounts for the behavior of all consecutive waveforms, thereby avoiding the selection of a non-representative peak in a waveform as the retracking point by assigning a high penalty in such cases. Moreover, E_{t} should impose a high penalty on peaks in the waveform that would lead to non-feasible results in terms of water level variation in time.

From the set of all possible labeling vectors L for a certain radargram, the search is conducted for the one that yields the minimal total energy E; this vector corresponds to the desired segmentation and consequently to the retracking line. This is a classical optimization problem. A possible solver, which has been demonstrated to be effective in dealing with similar problems, is the graph-cuts technique (Greig et al., 1989). This technique, as a powerful optimization algorithm, has been proven to be highly effective in addressing various vision problems, encompassing areas such as stereo vision, motion analysis, image restoration, and segmentation (Boykov and Jolly, 2001; Boykov et al., 2001; Ishikawa, 2003; Kolmogorov and Zabin, 2004). The essence of the graph-cuts technique is to represent the radargram as an undirected graph $\mathcal{G} = \langle \Omega, \mathcal{E} \rangle$ that consists of a set of nodes (Ω) (shown in Figure 5.3) and a set of weighted edges $\mathcal{E}$ connecting the graph nodes (n-links). Besides the pixels, the graph receives two additional nodes, the so-called terminals, corresponding to possible labels (responding to possible labels (*Front* and *Back*) that are to be assigned to each pixel of a radargram (Figure 5.4). Initially, all nodes are connected to both terminals by edges, the so-called t-links (Figure 5.4). The weight of each n-link is identical with a constituent of the energy function E_{bs}; the weight of each t-link is identical with a constituent of the energy function E_{t}.

Segmenting the radargram corresponds to cutting the graph. A *cut* (C) in a graph is a subset of graph edges ($C \subset \mathcal{E}$) such that the terminals would be disconnected if they were removed from the graph ($\mathcal{G}' = \langle \Omega, \mathcal{E} - C \rangle$) (Veksler, 1999). In $\mathcal{G}'$, each pixel node is connected to exactly one terminal directly by a t-link and, possibly, in addition, indirectly through other nodes via n-links. The cost of a cut equals the sum of its edge weights. The aim of the minimum cut algorithm in a graph is to find a cut that has the minimum cost among all possible cuts, which implicitly means to minimize $E = E_{\mathrm{bs}} + \lambda E_{\mathrm{t}}$.

Here, the minimum cut is determined using the maxflow algorithm introduced by Boykov and Kolmogorov (2004), implemented via the Matlab function *maxflow* (Rubinstein, 2020). This algorithm efficiently identifies a set of labels that minimizes total energy, thereby segmenting the radargram. In the subsequent sections, the approach for modeling the energy terms of E_{bs} and E_{t} is elaborated.

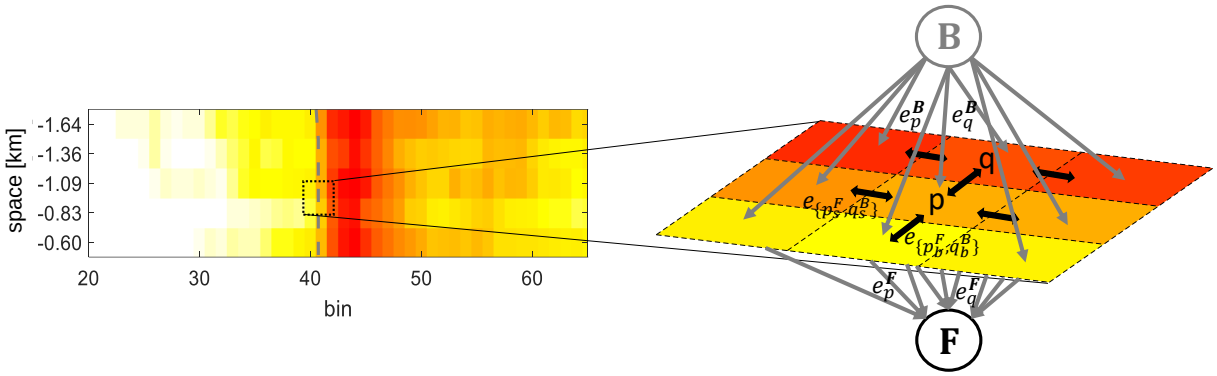

Fig. 5.4: A schematic representation of a 4-neighbour graph with n-link weights determined by energy functions in the bin-space domain and two terminals linked to all nodes via t-links, with weights derived from the temporal energy terms (equations (5.18) to (5.21)).

5.2.1 Prior: the energy term in the bin-space domain

Following Equation (5.6), the prior should represent all possible joint potentials that characterize the relationships between labels in the bin-space domain. To obtain the prior, the Markovian properties are relied upon, which assert that the label assigned to any pixel correlates solely with the labels of its neighbors. In other words, the label field is assumed to be independent overall, with interdependence confined to neighboring regions. For the sake of simplicity, a four-neighbor system is assumed, implying that each pixel's label correlates with the labels of pixels on the 1) left, 2) right, 3) top, and 4) bottom. In such a configuration, diagonal neighbors among the eight possible neighboring pixels are not taken into consideration. The right and left neighbors are in the bin domain, and the top and bottom neighbors are in the space domain. The bin-space energy term is defined for all pairs of neighboring pixels located on different sides of the border between *Front* and *Back* regions (subset $\mathcal{N}$ or the *cut*), i.e., for all pixel pairs across the retracking line (Figure 5.5):

$$\begin{aligned} E_{\mathrm{bs}} =& E_{\mathrm{b}} + E_{\mathrm{s}} \\ =& \sum_{\{p_b^{\mathrm{F}}, q_b^{\mathrm{B}} \in \mathcal{N}\}} e_b(I_{p_b^{\mathrm{F}}}, I_{q_b^{\mathrm{B}}}) + \sum_{\{p_s^{\mathrm{F}}, q_s^{\mathrm{B}} \in \mathcal{N}\}} e_s(I_{p_s^{\mathrm{F}}}, I_{q_s^{\mathrm{B}}}) \,. \end{aligned} \tag{5.8}$$

E_{bs} is the sum of the energy between all pairs of pixels around the *cut* separated by the border, i.e, retracking line (subset $\mathcal{N}$) (Figure 5.5). So the penalty for a change of the label from *Front* to *Back* or vice versa between a pixel p_b or p_s and its neighboring pixels in bin q_b and space q_s is comprised in the term E_{bs}. E_{bs} is represented by two sums, because the penalty for a pair of pixels neighbouring in bin direction may differ from the penalty of a pair in neighbouring in space direction. For instance, the illustrated $\mathcal{N}$ in Figure 5.5 includes 20 pairs of neighboring pixels in the bin direction, where E_{b} is defined, and 7 pairs of neighboring pixels in the space direction, where E_{s} is defined.

Let us first define d as the intensity difference between two adjacent pixels, regardless of whether the pixels are adjacent in bin or space direction:

$$d = I_{p^{\mathrm{F}}} - I_{q^{\mathrm{B}}} = \begin{bmatrix} 1 & -1 \end{bmatrix} \begin{bmatrix} I_{p^{\mathrm{F}}} \\ I_{q^{\mathrm{B}}} \end{bmatrix} \tag{5.9}$$

The variance of d is therefore

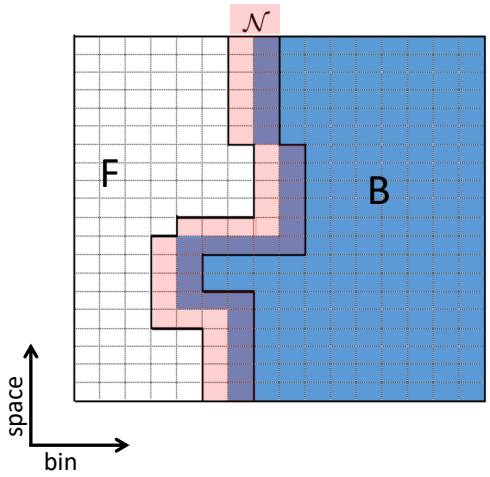

Fig. 5.5: A schematic representation of a radargram with pixels labeled as *Front* indicated by F and *Back* indicated by B. $\mathcal{N}$ is a set of all pairs of pixels around the border i.e. retracking line, for which E_{bs} is defined. Note that the illustrated $\mathcal{N}$ includes 20 pairs of neighboring pixels in the bin direction, where E_{b} is defined, and 7 pairs of neighboring pixels in the space direction, where E_{s} is defined.

$$\sigma_d^2 = \begin{bmatrix} 1 & -1 \end{bmatrix} \begin{bmatrix} \sigma^2_{I_{p^{\mathrm{F}}}} & \sigma_{I_{p^{\mathrm{F}}} I_{q^{\mathrm{B}}}} \\ \sigma_{I_{p^{\mathrm{F}}} I_{q^{\mathrm{B}}}} & \sigma^2_{I_{q^{\mathrm{B}}}} \end{bmatrix} \begin{bmatrix} 1 \\ -1 \end{bmatrix} \tag{5.10}$$

Under the Markovian assumption stated above, which permits a dependency of pixel intensities on their neighbours, the covariance $\sigma_{I_{p^{\mathrm{F}}} I_{q^{\mathrm{B}}}}$ may be non-zero. If we presume equal variances for pixel intensities labeled as *Back* and *Front*, denoted by σ_I^2, the covariance simplifies to

$$\sigma_{\mathrm{d}}^2 = 2\big(\sigma_I^2 - \sigma_{I_{p^{\mathrm{F}}} I_{q^{\mathrm{B}}}}\big); \tag{5.11}$$

The term $\sigma_{I_{p^{\mathrm{F}}} I_{q^{\mathrm{B}}}}$ always refers to the covariance of two neighboring pixel intensities, which in the bin domain would always be one bin apart from each other. In the space domain, however, the rows in a radargram depict successive altimeter measurements during an overflight above a water body. Under typical circumstances, with an output sampling rate of 20 Hz, the inter-measurement distance is approximately 300 m. However, in scenarios common to inland altimetry and coastal zones, certain measurements may be flagged as erroneous, necessitating their exclusion from the database. Consequently, in such cases, the inter-measurement intervals are not uniformly equal. So in the space domain

$$\sigma_d^s = \sqrt{2(C^s(0) - C^s(\delta s))} \tag{5.12}$$

where $C^s(0)$ represents the variance of pixel intensities and $C^s(\delta s)$ represents the covariance of intensities for pixels neighbouring in space direction with time difference δs. On the other hand, in the bin axes, δb is always equal 1, since the bin interval is always equally spaced:

$$\sigma_d^b = \sqrt{2(C^b(0) - C^b(\delta b))} = \sqrt{2(C^b(0) - C^b(1))} \tag{5.13}$$

In essence, the bin-space energy is designed to penalize similarity between adjacent pixels. This implies that both E_{b} and E_{s} attribute high energy values to pairs of pixels featuring similar intensity levels while assigning lower energy values to those exhibiting strongly different power characteristics within a radargram. To this end, a function of the argument d/σ_d is selected as the penalty function. This ratio represents the

normalized difference d, normalized with respect to the overall variation of the radargram. Therefore, in instances where a radargram exhibits substantial variation, a small or large d will be effectively normalized by this ratio. Consequently, when the ratio is small, we prescribe high energy, and conversely, when the ratio is large, low energy is stipulated. Various functions may represent such relationships; a simple approach consists of the use of the exponential function. So the spatial energy between two neighbors p_s and q_s in the space direction (vertical direction in a radargram) with a distance of δs is:

$$\begin{aligned} e_s(I_{p_s^{\mathrm{F}}}, I_{q_s^{\mathrm{B}}}) &= \exp\left(-\left|\frac{d^s}{\sigma_d^s}\right|\right) = \exp\left(-\frac{\left|I_{p_s^{\mathrm{F}}} - I_{q_s^{\mathrm{B}}}\right|}{\sigma_d^s}\right) \\ &= \exp\left(-\frac{\left|I_{p_s^{\mathrm{F}}} - I_{q_s^{\mathrm{B}}}\right|}{\sqrt{2(C^s(0) - C^s(\delta s))}}\right), \end{aligned} \tag{5.14}$$

The modulus operator ensures that when two neighbors have the highest similarity, the energy is maximal.

For the energy function in the bin direction, the ratio d^b/σ_d^b can be used, but a special modification needs to be implemented. Here, it is necessary not only to penalize similarity but also to penalize the possible placement of the retracking line in the trailing edge regions of radargrams. This region is typically characterized by decreasing pixel intensities from left to right. Therefore, a high penalty is also implemented if the left pixel intensity is higher than the right one. To this end, here the absolute operator is not needed anymore.

$$\begin{aligned} e_b(I_{p_b^{\mathrm{F}}}, I_{q_b^{\mathrm{B}}}) &= \exp\left(-\frac{d^b}{\sigma_d^s}(\mathrm{Bin}_p^{\mathrm{F}} - \mathrm{Bin}_q^{\mathrm{B}})\right) \\ &= \exp\left(-\frac{(I_{p_b^{\mathrm{F}}} - I_{q_b^{\mathrm{B}}})}{\sigma_d^b}(\mathrm{Bin}_p^{\mathrm{F}} - \mathrm{Bin}_q^{\mathrm{B}})\right), \end{aligned} \tag{5.15}$$

In this context, $\mathrm{Bin}_p^{\mathrm{F}}$ and $\mathrm{Bin}_q^{\mathrm{B}}$ represent the bin numbers of two neighboring pixels, with their difference constrained to either 1 or -1. This additional factor, which is given by the difference of the bins, ensures that the same energy is obtained for swapped neighbors. In other words, regardless of how the order of p and q (whether left-right or right-left) is chosen, the result remains consistent.

It should be noted that using d/σ_d as the foundational metric for computing both E_{b} and E_{s} eliminates the need for a separate hyperparameter to balance these two energy terms. Since both E_{b} and E_{s} represent cost functions of comparable scale and weighting, introducing an additional hyperparameter to adjust their relative influence becomes unnecessary, unlike the approach taken in Roscher et al. (2017).

5.2.2 Likelihood: the energy term in the time domain

According to Equation (5.6), the likelihood is represented by all single-node (unary) potentials $\varphi(L_i, I_i)$. To establish this likelihood, temporal information can be incorporated by considering the probability of a pixel receiving either a *Back* or *Front* label over time. That is why this energy term is denoted as E_{t}, with the index t representing the temporal domain. This energy term can represent the penalty of a pixel being segmented as *Front* F or *Back* B based on its pixel intensity alone (denoted as $E_{\mathrm{t}}^{1\mathrm{D}}$), or based on both pixel intensity and bin location (denoted as $E_{\mathrm{t}}^{2\mathrm{D}}$).:

$$E_{\mathrm{t}}^{1\mathrm{D}} = \sum_{p \in F} e_p^{\mathrm{F}}(I_p) + \sum_{p \in B} e_p^{\mathrm{B}}(I_p), \tag{5.16}$$

$$E_{\mathrm{t}}^{\mathrm{2D}} = \sum_{p \in F} e_p^{\mathrm{F}}(I_p, \mathrm{Bin}_p) + \sum_{p \in B} e_p^{\mathrm{B}}(I_p, \mathrm{Bin}_p)\,. \tag{5.17}$$

Higher energy is assigned to pixels when the probability of I_i given L_i is low, and vice versa. To achieve this, the energy and probability measures are swapped, such that the energy for a pixel intensity value to be segmented as *Back* is proportional to the probability of that pixel intensity receiving a *Front* label, and vice versa:

$$e_p^{\mathrm{F}}(I_p) = \mathrm{P}(I_p | p \in B) \tag{5.18}$$
$$e_p^{\mathrm{B}}(I_p) = \mathrm{P}(I_p | p \in F) \tag{5.19}$$

$$e_p^{\mathrm{F}}(I_p, \mathrm{Bin}_p) = \mathrm{P}(I_p, \mathrm{Bin}_p | p \in B) \tag{5.20}$$
$$e_p^{\mathrm{B}}(I_p, \mathrm{Bin}_p) = \mathrm{P}(I_p, \mathrm{Bin}_p | p \in F) \tag{5.21}$$

in which $\mathrm{P}(I_p|p \in F)$ and $\mathrm{P}(I_p|p \in B)$ are the probabilities of a certain pixel intensity I_p given the label *front* or *back*, respectively. Similarly $\mathrm{P}(I_p, \mathrm{Bin}_p|p \in F)$ and $\mathrm{P}(I_p, \mathrm{Bin}_p|p \in B)$ are the probabilities of a certain pixel intensity I_p at Bin_p given the label *front* or *back* and the bin Bin_p.

These probabilities are obtained by relying on the results of a 1D reatracking method and the resulting segmented radargrams. For this purpose, a simple 50% threshold retracker, hereafter referred to as the *initial retracker*, can be used. This involves finding the retracking point in each waveform associated with 50% of its maximum peak, providing a preliminary delineation that helps to define the initial boundary line.

To obtain the probabilities, the labels from the initial retracker are utilized. Intensity histograms for the two labels are computed separately. From these histograms, the probability of a certain intensity, given a certain label, is derived (Figure 5.6). In the case of $E_{\mathrm{t}}^{\mathrm{1D}}$, the penalty assigned to a pixel for being labeled as, for instance, *Back*, is solely determined by its pixel intensity. Naturally, when the pixel intensity is low—indicative of the thermal noise in the waveform, theoretically associated with *Front*—the penalty for being labeled as *Back* is notably high. On the other hand, $E_{\mathrm{t}}^{\mathrm{2D}}$ imposes a high penalty on assigning *Back* to low pixel intensities only if the thermal noise region is present. This characteristic makes $E_{\mathrm{t}}^{\mathrm{2D}}$ more informed by the bin and generally more suitable for radargrams, in contrast to $E_{\mathrm{t}}^{\mathrm{1D}}$, which is solely influenced by pixel intensity.

5.2.3 Water height determination

Once the retracking line is defined in each radargram, a retracker offset δb_i is determined for each waveform in a bin-aligned radargram. Subsequently, to correct the tracker range ρ_i, the bin shift value Δb_i^0, introduced during the bin-alignment procedure, is first subtracted from the estimated δb_i. The range correction $\delta\rho_i$ is then estimated as follows:

$$\delta\rho_i = \frac{(\delta b_i - \Delta b_i^0) \times \tau \times c}{2}\,, \tag{5.22}$$

Depending on the size of the selected VS, a radargram contains several waveforms, each of which has a specified range $\rho_i + \delta\rho_i$. The estimated range $\hat{\rho}_i = \rho_i + \delta\rho_i$ is then further corrected for geophysical effects of solid earth tide $\delta\rho_i^{\mathrm{solid}}$ and pole tide $\delta\rho_i^{\mathrm{pole}}$ and also path delays caused by the atmosphere including wet tropospheric $\delta\rho_i^{\mathrm{wet}}$, dry tropospheric $\delta\rho_i^{\mathrm{dry}}$, and ionospheric corrections $\delta\rho_i^{\mathrm{iono}}$. The corrected range and the

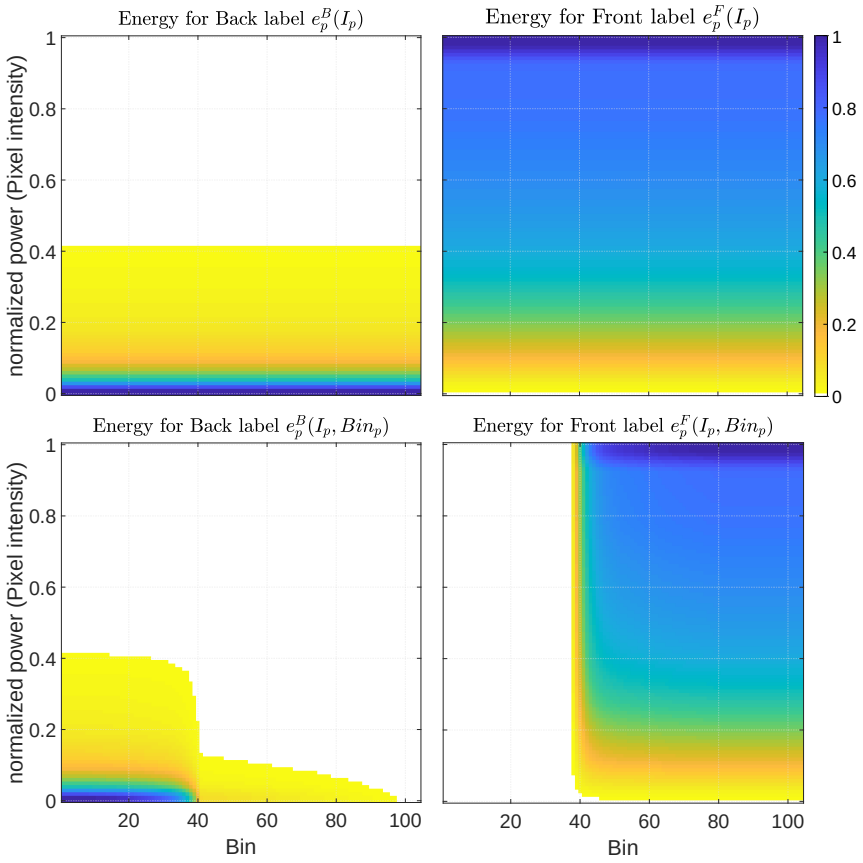

Fig. 5.6: An example of the temporal energy term (likelihood) is given for both cases: $E_{\mathrm{t}}^{1\mathrm{D}}$ with $e^{\mathrm{B}}p(I_p)$ and $e^{\mathrm{F}}p(I_p)$, and $E_{\mathrm{t}}^{2\mathrm{D}}$ with $e_p^{\mathrm{B}}(I_p, \mathrm{Bin}p)$ and $e^{\mathrm{F}}p(I_p, \mathrm{Bin}_p)$. This example belongs to Waubesa Lake for the Jason-2 dataset spanning from 2008 to 2016, where the waveforms were initially retracked by a 50% threshold retracker

geoid height N are then subtracted from satellite altitude h_i to obtain an orthometric surface water height H_i:

$$H_i = h_i - (\hat{\rho}_i + \delta\rho_i^{\mathrm{dry}} + \delta\rho_i^{\mathrm{wet}} + \delta\rho_i^{\mathrm{iono}} + \delta\rho_i^{\mathrm{solid}} + \delta\rho_i^{\mathrm{pole}}) - N \tag{5.23}$$

To obtain the geoid height N, the static gravity field model XGM2019e (Pail et al., 2018) is utilized.

In principle, for every M measurement within a VS, there is a height estimate H_i, which can be considered the final height value. To obtain a representative water height estimate for comparison with the in situ data, the median of all M estimated height values H_i within the VS is taken as the representative surface water height for each VS, as follows:

$$\hat{H} = \underset{i \in 1,..M}{\mathrm{median}}(H_i)\ , \tag{5.24}$$

with the uncertainty estimate obtained by calculating Median Absolute Deviation (MAD):

$$\sigma_{\hat{H}} = \mathrm{median}(|H_i - \hat{H}|) \tag{5.25}$$

In an ideal situation, all estimated water height values H_i within the VS should be the same, and consequently, $\sigma_{\hat{H}}$ should be close to zero. However, this is not the case due to the inherent noise of altimetry, imperfect retracking, or inaccurate modeling of geophysical corrections.

5.2.4 Defining an optimal hyperparameter parameter λ

To find the Maximum A-Posteriori solution, the hyperparameter λ, a parameter crucial in determining the retracking, should be set in advance (see the flowchart in Figure 5.8). This means the proposed methodology described in Sections 5.2 works with any λ values, and similar to other hyperparameter scenarios, the resulting retracking line may vary based on the defined λ. Therefore, it is important to define the optimal λ, with which the best water height is estimated. This can be done within the validation step, where all the results are compared to the in situ data. However, since generally in situ data are very limited, it is important to find the optimal λ without relying on the in situ data.

To find the optimal λ, the selection can be based on an analysis of the available energy estimates E_{bs} and E_{t}, as well as an analysis of the estimated water height, specifically the variation of estimated water height within a radargram. It is important to recall that E_{bs} and E_{t} are not normalized functions. Therefore, a value of λ larger or smaller than 1 does not necessarily indicate whether E_{bs} or E_{t} is dominant. However, by increasing λ, the influence of neighboring information, i.e., the prior, decreases, leading to larger E_{bs}. Conversely, as λ increases, the temporal information, i.e., the likelihood function, gains more weight, which automatically implies a reduction of E_{t} in the total energy. This relationship is illustrated in Figure 5.7, where increasing λ leads to smaller $E_{\mathrm{t}}^{\mathrm{2D}}$ and larger E_{bs}. In the combined energy $E_{\mathrm{t}}^{\mathrm{2D}} + E_{\mathrm{bs}}$ shown in Figure 5.7 (and also in E_{bs}), a sudden increase is observed (for instance, in the example above, from $\lambda = 9$ to $\lambda = 10$, and in the example below, from $\lambda = 10$ to $\lambda = 11$). Such changes in energy levels suggest that with the alteration of the target function, the retracking line shifts to a region associated with higher E_{bs}.

In the example shown below in Figure 5.7, the elevated energy level appears consistent even for very small $\lambda = 0.01$, as indicated by the cyan retracking line in Figure 5.7(right). Interestingly, in the example of 10.11.2011 (bottom example in Figure 5.7) for $\lambda > 11$, the maxflow algorithm seems to define the retracking line in a region similar to that of $\lambda = 0.01$, as depicted by the blue retracking line. This heightened energy level, primarily stemming from E_{bs}, indicates that the defined retracking line does not pass directly through the leading edge but instead encounters a minor peak before the main leading edge. Such a pattern exists in BiST results for almost all radargrams. Therefore, to determine the optimal λ,

- Firstly, drops and jumps in $E_{\mathrm{t}}^{\mathrm{2D/1D}} + E_{\mathrm{bs}}$ are identified, and the focus is placed on λ values where the energy $E_{\mathrm{t}}^{\mathrm{2D/1D}} + E_{\mathrm{bs}}$ is relatively low, specifically those lying between significant drops and jumps.
- Among the λ values exhibiting low total energy $E_{\mathrm{t}}^{\mathrm{2D/1D}} + E_{\mathrm{bs}}$, the one that results in the smallest $\sigma_{\hat{h}}$, as calculated in Equation (5.25), is selected.

Given the setup above, for each epoch in the automated procedure detailed in Figure 5.9, the selected λ and its corresponding retracking line yield low energy based on the specified energy functions, while also providing a water level estimate with reduced uncertainty. Furthermore, this configuration indirectly ensures a balance between E_{bs} and E_{t}, preventing either term from being significantly larger than the other (as indicated by the optimal λ marked with $*$ in the bottom-left panel of each example in Figure 5.7).

Figure 5.8 shows the flowchart of the proposed methodology.

5.3 Results and validation

The proposed methodology is implemented on both pulse-limited and Synthetic Aperture Radar (SAR) altimetry datasets across nine lakes and reservoirs in the United States (Table 5.2): Boca Reservoir, Lake Mohave, Abiquiu Reservoir, Lake Mendota, Lake Waubesa, Lake Kegonsa, Lake Michigan, Rathbun Lake, and Lake Maumelle. They vary in size and exhibit distinct altimetry characteristics (Figure 5.10).

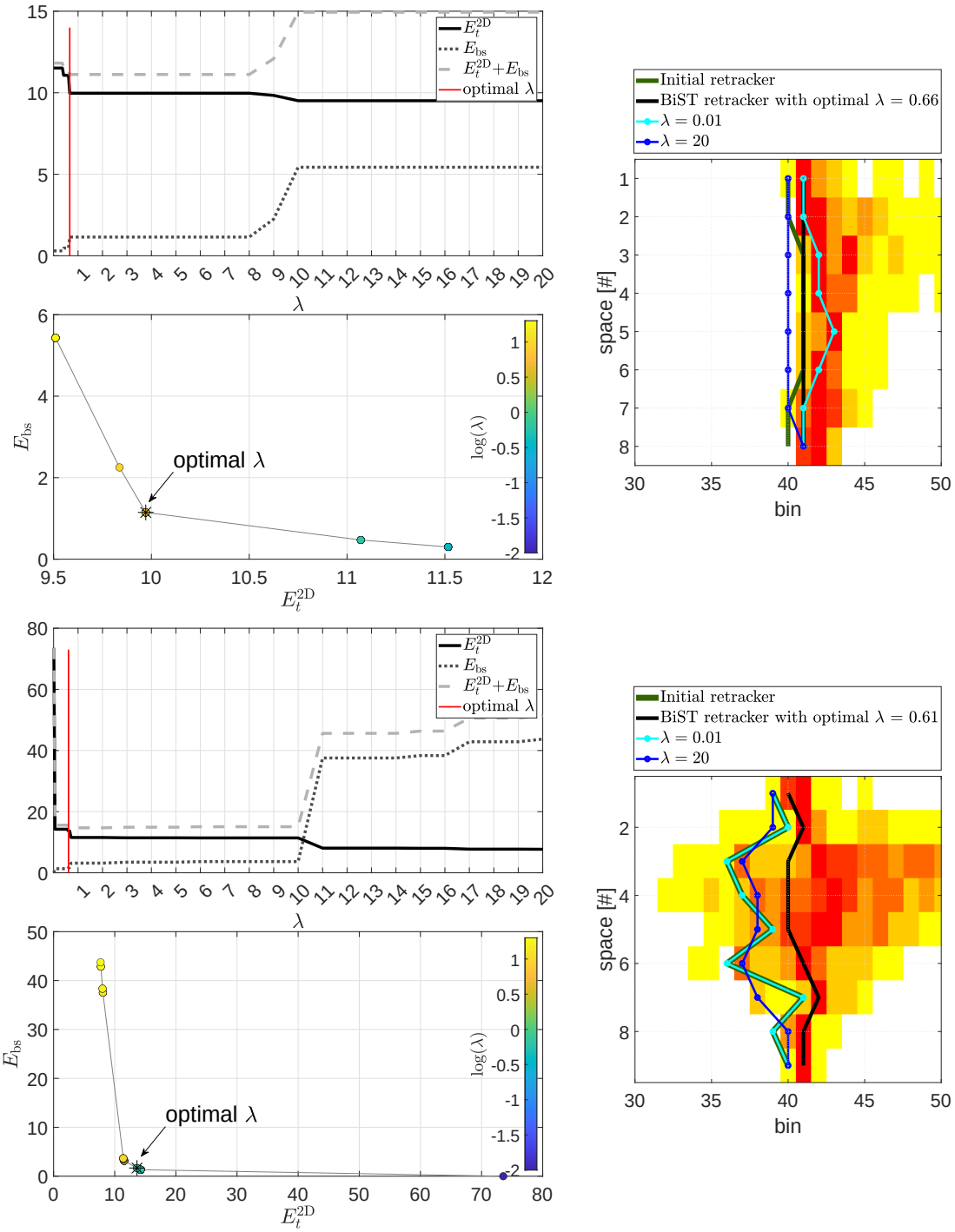

Fig. 5.7: Two examples over the Lake Waubesa for 13.10.2010 (top) and 10.11.2011 (bottom). Left-top of each example: A-posteriori values for the temporal energy E_t^{2D}, the bin-space energy function E_{bs}, and the total energy without the hyperparameter $E_t^{2D} + E_{bs}$ obtained for different λ. Left-bottom of each example: E_{bs} vs. E_t^{2D} color-coded with the $\log 10(\lambda)$. Right of each example) Corresponding radargram with the obtained retracking line using the initial retracker (green), optimal λ (black) and those for $\lambda = 0.01$ (cyan) and $\lambda = 0.20$ (blue)

For each case study, first, a VS is defined by setting a center point and a search radius, within which altimetry measurements are collected. The center point is located at the midpoint of the satellite track over the lake, as specified in Table 5.2, while the search radius is adjusted according to the size of the lake, also detailed in Table 5.2. The Global Surface Water (GSW) dataset (Pekel et al., 2016) occurrence map is then applied to filter out measurements with water occurrence values below 75%, ensuring that only

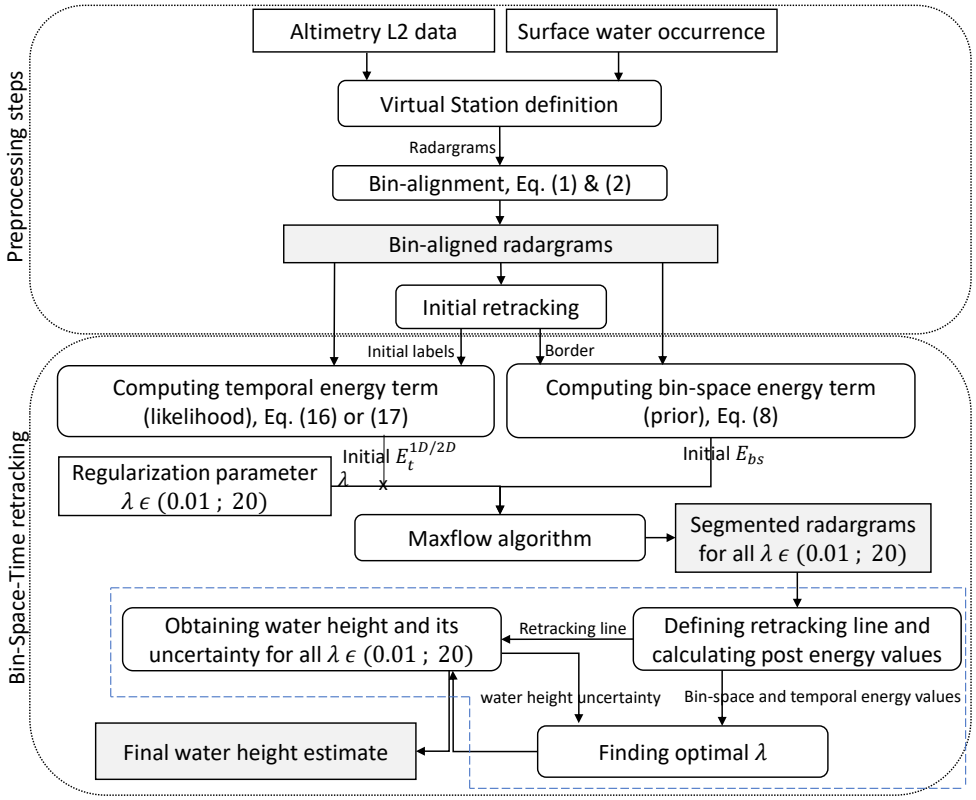

Fig. 5.8: Flowchart of the proposed methodology including the preprocessing step and the Bin-Space-Time retracking step. White rectangles represent inputs, rounded rectangles represent processes, and gray rectangles show the outputs. The blue dashed region is further detailed in Figure 5.9.

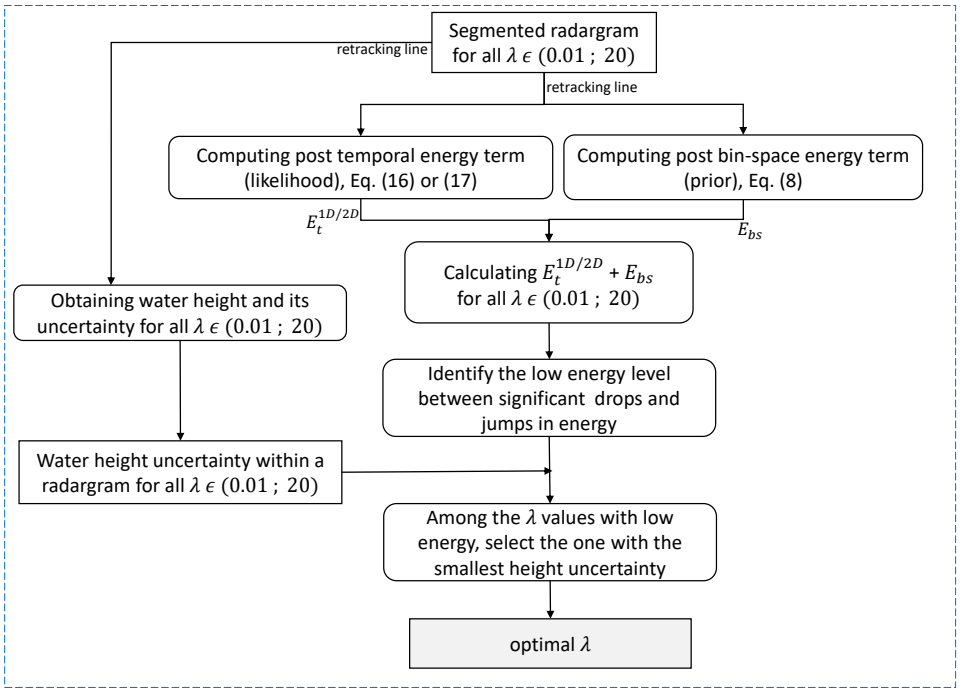

Fig. 5.9: Flowchart of finding optimal hyperparameter λ. White rectangles represent inputs, rounded rectangles represent processes, and gray rectangles show the outputs.

data corresponding to water bodies within the VS are considered, while excluding measurements from surrounding areas and non-water surfaces. This approach allows for effective data collection even over

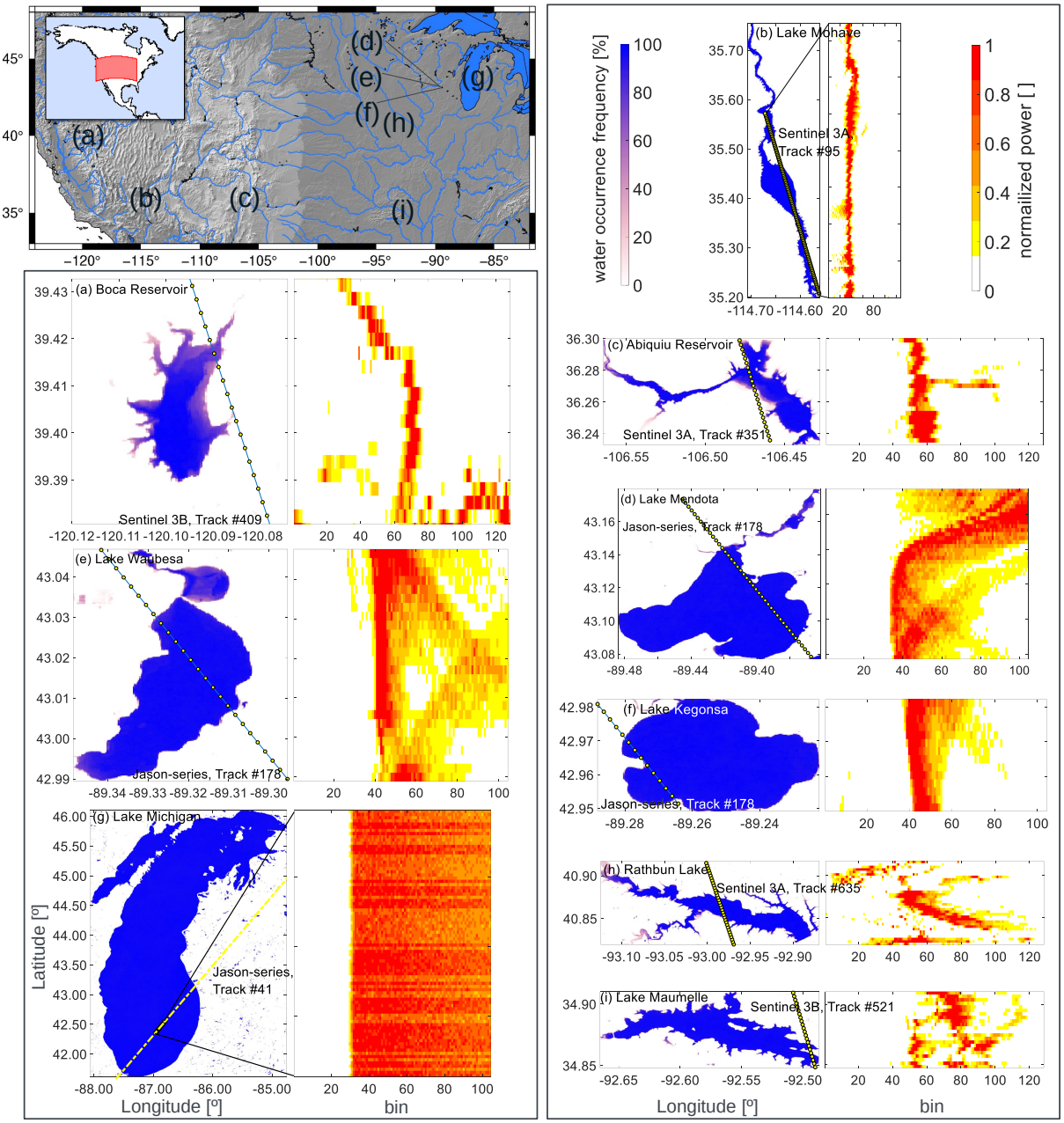

Fig. 5.10: Selected case studies including nine lakes and reservoirs in the United States: (a) Boca Reservoir, (b) Lake Mohave, (c) Abiquiu Reservoir, (d) Lake Mendota, (e) Lake Waubesa, (f) Lake Kegonsa, (g) Lake Michigan, (h) Rathbun Lake, and (I) Lake Maumelle. For each case study a sample radargram is shown.

small lakes and reservoirs, such as Boca Reservoir, and lakes where altimetry overpasses are near offshore regions, such as Lake Maumelle (see Figure 5.10). Within the defined VS, radargrams are generated using consecutive waveforms, and a *radargram stack* is constructed by aggregating radargrams from successive overpasses.

Afterward, an initial retracking line is defined, based on which the a priori energy estimates are obtained. The Bayesian approach aims to find a retracking line that minimizes the total energy based on the defined energies in both the bin, space ,and time domains, which implicitly means finding a posterior based on the defined prior and likelihood. To achieve this, the maxflow algorithm is employed with a set of predefined hyperparameters λ. The maxflow algorithm separates the radargram into two segments by cutting through edges, minimizing the total cost. The outcome is a binary segmented radargram, with a retracking line at

Tab. 5.2: Selected case studies including nine lakes and reservoirs in the United States, including information on topography and data from the United States Geological Survey (USGS) for each lake and reservoir. The table includes details on surrounding terrain type and average elevation, as well as satellite missions and in situ measurement stations.

		Topography			Virtual Station				In Situ Station		
Case study	Size [km^2]	Surrounding terrain	Avg. elev. [m]	Mission(s)	Track #	Lat [°]	Lon [°]	Radius [km]	Station	Lat. [°]	Lon. [°]
Boca Reservoir	4	Mountainous	2 100	Sentinel 3B	409	39.41	−120.09	2	near Truckee	39.38	−120.09
Lake Mohave	114	Desert basin	200	Sentinel 3A	95	35.42	−114.63	6	Davis Dam	35.19	−114.57
Abiquiu Reservoir	21	Hilly plateau	1,880	Sentinel 3A	351	36.27	−106.47	4	near Abiquiu	36.24	−106.43
Lake Mendota	39	Flat to gently rolling	259	Jason-2, -3	178	43.09	−89.38	2	Madison	43.09	−89.37
Lake Waubesa	8	Flat to gently rolling	260	Jason-2, -3	178	43.01	−89.32	4	McFarland	43.01	−89.31
Lake Kegonsa	13	Flat	259	Jason-2, -3	178	42.95	−89.27	4	Barber Drive	42.95	−89.28
Lake Michigan	58030	Flat to rolling coastal	176	Jason-2, -3, -6MF	41	42.45	−86.88	10	Chicago Lock at Chicago	41.89	−87.61
Rathbun Lake	45	Gently rolling	296	Sentinel 3A	635	40.86	−92.98	2	near Rathbun, IA	40.82	−92.89
Lake Maumelle	36	Rolling hills	99	Sentinel 3B	521	34.86	−92.49	2	Mouth of Pigeon Roost	34.87	−92.63

the boundary between the *Back* and *Front* regions. As described in Section 5.2.4, λ is varied in each epoch from 0.01 to 20, resulting in different retracking lines. The optimal λ is then obtained using the proposed method in Section 5.2.4. Figures 5.11 and 5.12(second rows) show the obtained optimal hyperparameter, λ, for each epoch over Lake Waubesa, Jason-2 mission, and Rathbun Lake, Sentinel-3A. The optimal λ varies unsystematically between 0.06 and 11 for Lake Waubesa and between 0.06 and 15 for Rathbun Lake. Such unsystematic variation is expected, as the radargrams of different cycles vary in shape, causing the algorithm to place more or less weight on the temporal energy terms. For instance, when the radargram shows a complex pattern, such as the one on 2016-06-24, more weight should be placed on E_{bs} and less on $E_{\mathrm{t}}^{\mathrm{2D/1D}}$, leading to a smaller λ.

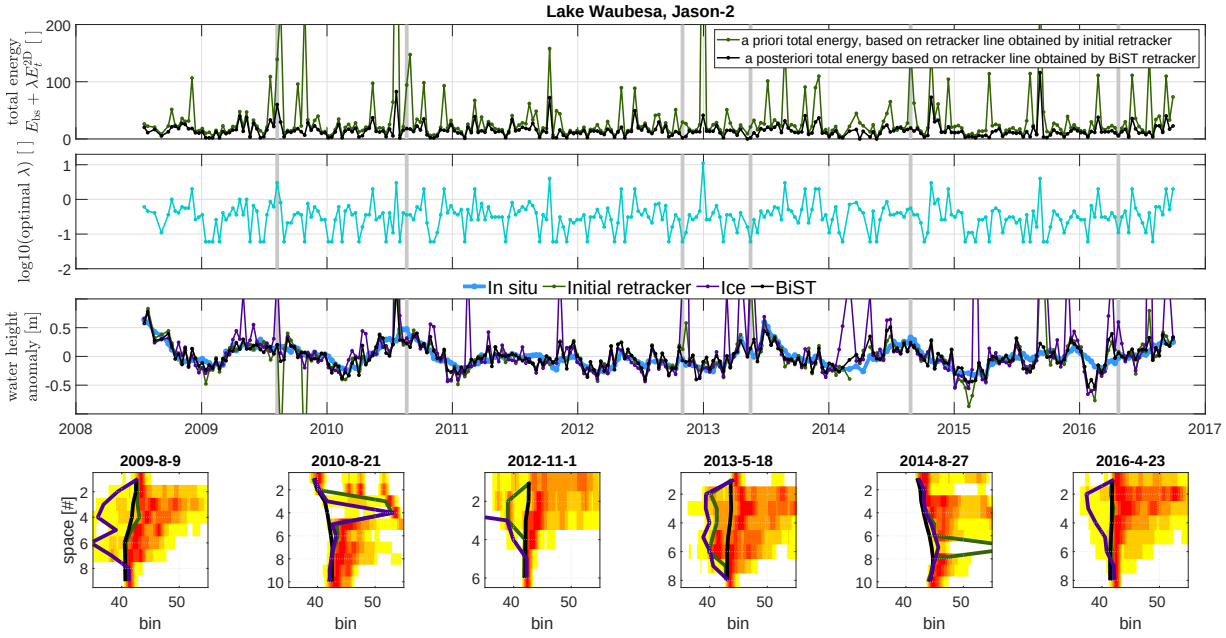

Fig. 5.11: Results over Lake Waubesa, depicted in four rows for each case: 1) The first row shows a priori and a posteriori energies. 2) The second row displays the optimal λ obtained in each epoch. 3) The third row exhibits water height anomaly time series from in situ measurements alongside those obtained by the BiST retracker and those from the initial retracker and one of the available retrackers in the geophysical data records. 4) The fourth row shows six selected radargrams for the epochs highlighted in the first three rows with gray lines, depicting retracking lines from BiST (black), initial retracker (dark green), and Ice retracker (magenta).

The minimized total energy E corresponding to the selected optimal λ is depicted in Figure 5.11 (first row), along with the a priori total energy derived from the initial retracking. As expected, this comparison illustrates the energy reduction, indicating that the BiST retracking line is located within the radargram

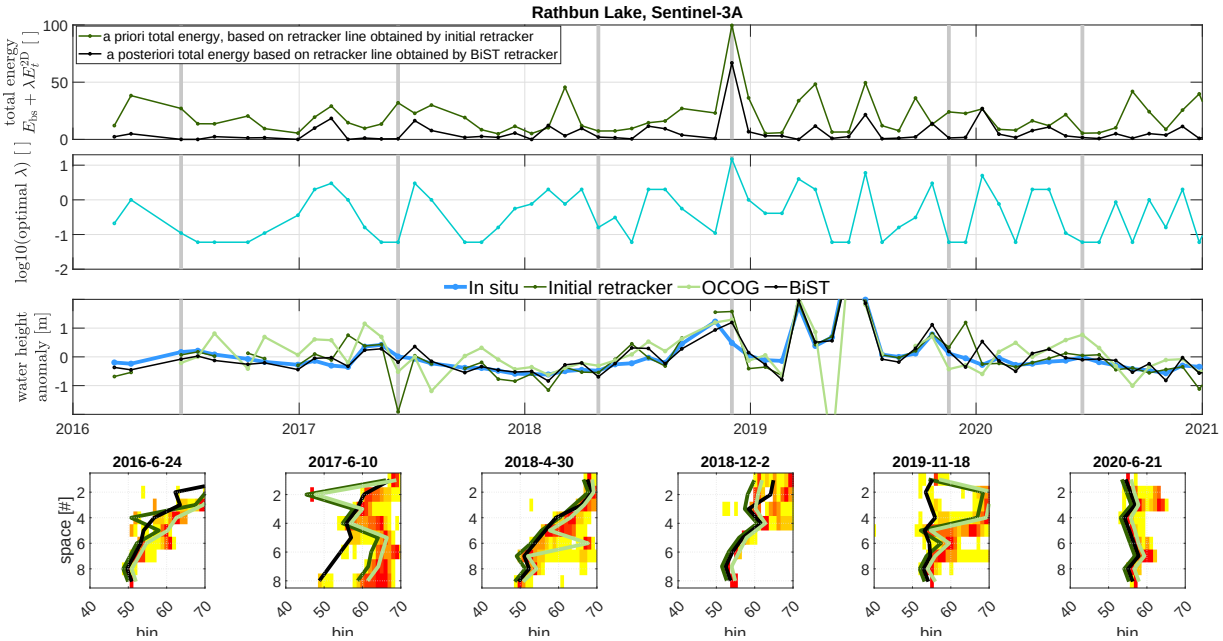

Fig. 5.12: Results over Rathbun Lake, depicted in four rows for each case: 1) The first row shows a priori and a posteriori energies. 2) The second row displays the optimal λ obtained in each epoch. 3) The third row exhibits water height anomaly time series from in situ measurements alongside those obtained by the BiST retracker and those from the initial retracker and one of the available retrackers in the geophysical data records. 4) The fourth row shows six selected radargrams for the epochs highlighted in the first three rows with gray lines, depicting retracking lines from BiST (black), initial retracker (dark green), and OCOG (light green).

where less energy is produced. For example, in Rathbun Lake on 2017-06-10 (second radargram in bottom row), for the second waveform, the initial retracker selects the leading edge of the peak around bin 47, whereas the BiST retracker follows the second peak, consistent with the peak of the first and third waveforms of that radargram. In this particular case, the retracking line by the initial retracker results in an elevated E_{bs}, as it passes through a region in the radargram with numerous pixel pairs on the right and left of the line with similar intensity. In other words, in this case, $\mathcal{N}$ (introduced in Section 5.2.1) contains many pairs of pixels with very similar intensity, which, according to the definition of E_{bs}, results in a high energy due to the calculation of the exponential of the negative intensity difference.

Based on the retracked radargrams, the water height $\hat{h}$ for each epoch is estimated. It is important to note that to ensure consistency among all water height time series, similar correction values for all retrackers are employed. Consequently, differences observed when comparing water height time series from different retrackers are primarily due to the retracking process's performance. This is evident in the water height time series in Figure 5.11, particularly in the first highlighted epoch (2009-08-09) of Lake Waubesa. There, the outlier in the Ice retracker's water height anomaly results from selecting the first (insignificant) peaks of each waveform as the retracking point. In contrast, the BiST retracker avoids selecting the first peak, as it would have led to high energy values for both $E_{\mathrm{t}}^{2\mathrm{D}}$ and E_{bs}. $E_{\mathrm{t}}^{2\mathrm{D}}$ becomes high if the first peak is chosen, given the relatively low intensity around bin 35, which reduces the probability of having a leading edge there. Additionally, in the case of $E_{\mathrm{t}}^{2\mathrm{D}}$ compared to $E_{\mathrm{t}}^{1\mathrm{D}}$, the bin location also plays a role, which further reduces the probability. On the other hand, E_{bs} will increase around the first peak in comparison with the BiST result due to the high energy required to define a retracking line in a region where pixel intensity differences are minimal. Therefore, the BiST retracker, with an optimal $\lambda = 3$, selects the black line as the retracking line, reducing the total energy from an initial value of about 140 to around 60. Such a consistently stable retracking line, one that remains unchanged across different waveforms within a radargram, is evident in all highlighted epochs, including the second one (2010-08-21) and the fifth one (2014-08-27) over Lake Waubesa and the fifth one over Rathbun Lake (2019-11-18). In these epochs, some

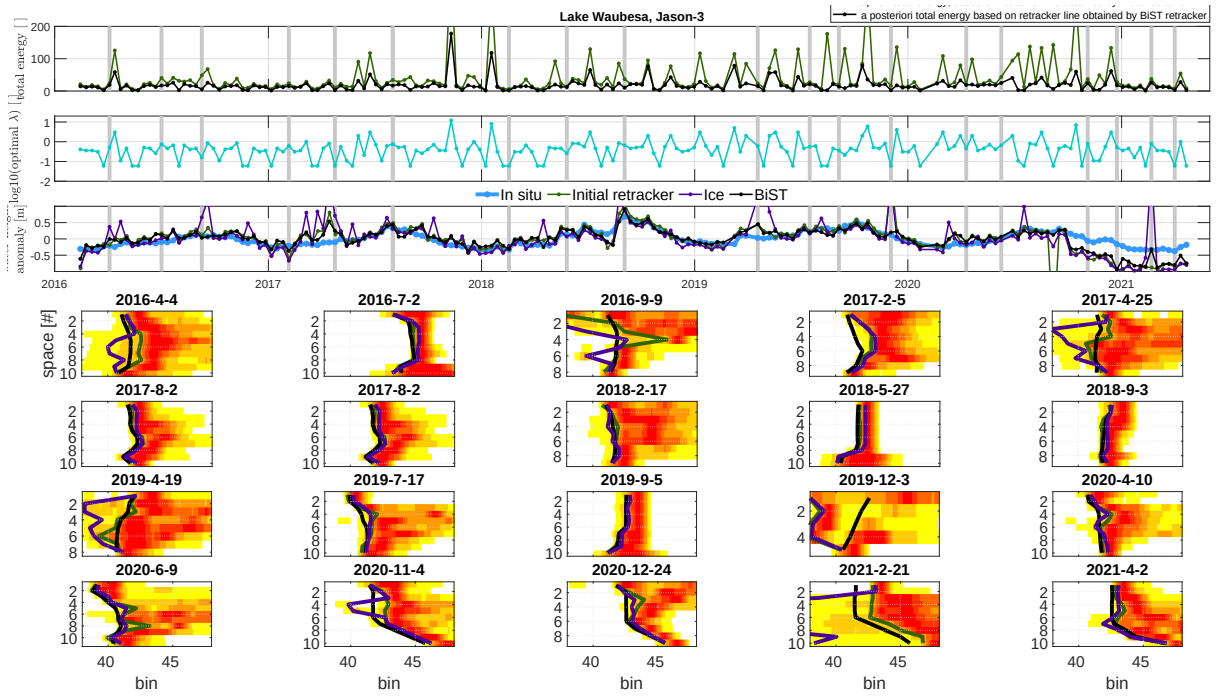

Fig. 5.13: Results over Lake Waubesa, Jason-3 1) The first row shows a priori and a posteriori energies. 2) The second row displays the optimal λ obtained in each epoch. 3) The third row exhibits water height anomaly time series from in situ measurements alongside those obtained by the BiST retracker and those from the initial retracker and one of the available retrackers in the geophysical data records. 4) The fourth-seven rows show 20 selected radargrams for the epochs highlighted in the first three rows with gray lines, depicting retracking lines from BiST, the initial retracker, and the selected conventional retracker.

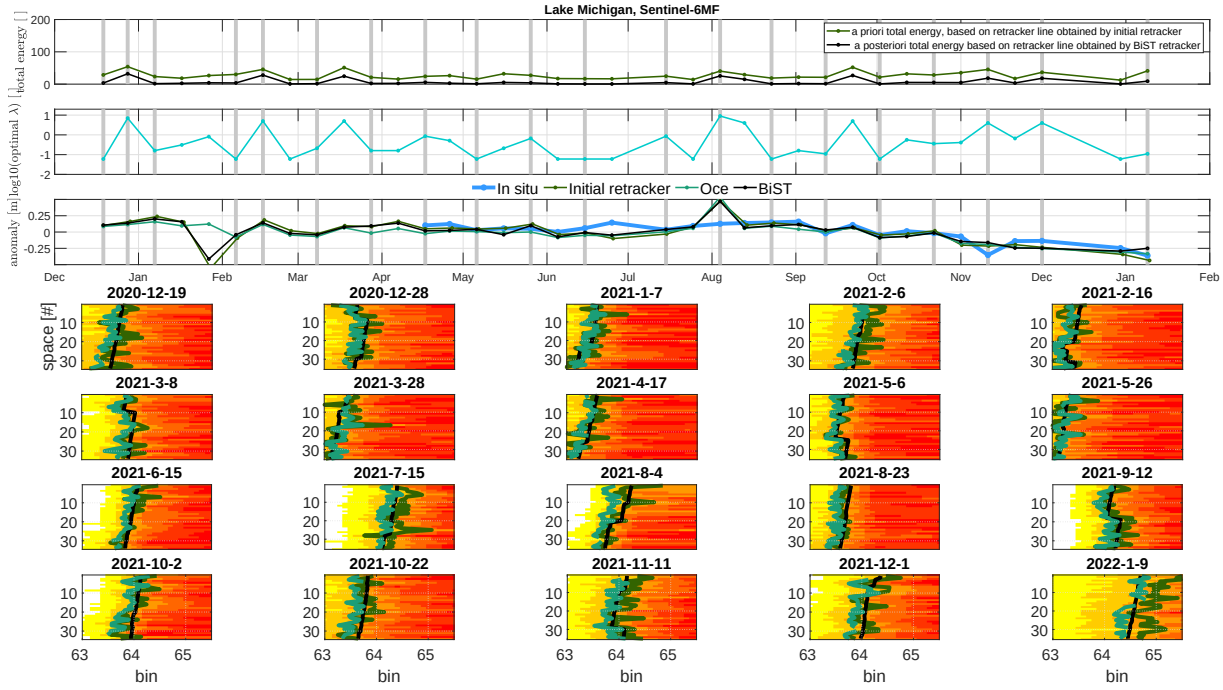

Fig. 5.14: Results over Lake Michigan, Sentinel-6MF 1) The first row shows a priori and a posteriori energies. 2) The second row displays the optimal λ obtained in each epoch. 3) The third row exhibits water height anomaly time series from in situ measurements alongside those obtained by the BiST retracker and those from the initial retracker and one of the available retrackers in the geophysical data records. 4) The fourth-seven rows show 20 selected radargrams for the epochs highlighted in the first three rows with gray lines, depicting retracking lines from BiST, the initial retracker, and the selected conventional retracker.

waveforms exhibit a sharp peak in the trailing edge region. The Ice retracker in Waubesa and the OCOG retracker in Rathbun, which analyze waveforms individually, appear insensitive to waveforms before and after selecting a peak in the trailing edge region. Similarly, the initial retracker selects those peaks, resulting in a high a priori total energy value.

In general, the findings indicate that considering both temporal and spatial information for retracking reduces sensitivity to irregular behavior in individual waveforms. This leads to improved water height time series and closer alignment with in situ data. As depicted in Figure 5.11 and 5.12, this improvement is evident in both Lake Waubesa and Rathbun Lake, one with pulse-limited altimetry and one with SAR altimetry. In the case of Lake Waubesa, the water height data from the Ice retracker displays numerous outliers that are not present in the BiST results. Similarly, for Rathbun Lake, aside from the absence of a blunder in mid-2019 in the BiST retracker, it generally demonstrates better alignment with in situ data compared to other retracking methods. Similar findings can be drawn from the results of the Jason-3 mission over Lake Waubesa (Figure 5.13), and Sentinel-6MF over Lake Michigan (Figure 5.14).

While figures 5.11– 5.14 provide a focused examination of specific instances with a single selected retracker, Figure 5.15 presents the water height anomaly obtained from the BiST retracker alongside results from all other available retracking methods in their geophysical data records. In this case, BiST results refer to those for which the 2D temporal energy function $E_{\mathrm{t}}^{2\mathrm{D}}$ is used. Notably, Figure 5.15 shows that over small challenging lakes of Mendota, Waubesa, and Kegonsa, MLE3 and Ice retrackers produce highly noisy time series. In contrast, the BiST retracker demonstrates a closer alignment with the in situ data. What can be visually captured in figures like 5.11 and 5.15 is numerically abstracted in two metrics: the Correlation Coefficient (CC) and root mean square error (RMSE), which are listed in Table 5.3 and shown in Figure 5.16. There, CC and RMSE values for all available retrackers, including the BiST retracker, are shown. Over Mendota, Waubesa, and Kegonsa for both Jason-2 and Jason-3, the available conventional retrackers struggle with low CC and high RMSE. The BiST retracker outperforms all other retrackers in these challenging cases, with results obtained using the 2D temporal energy function $E_{\mathrm{t}}^{2\mathrm{D}}$ delivering even better outcomes. This underscores the robustness and accuracy of the BiST retracker, particularly in complex lake environments.

Over Boca Reservoir, Sentinel-3B passes a part where the reservoir often lacks water for the majority of the year, with water occurrence frequencies fluctuating between 40 and 90 percent (See Figure 5.10). The acquired water level time series fails to accurately depict the in situ water level dynamics, exhibiting an RMSE exceeding 2 m (see Figure 5.16). This observation indicates that in challenging conditions, BiST cannot produce miraculous results and delivers comparably bad results like other methods, highlighting the inherent limitations in such scenarios.

Over Lake Mohave, Abiquiu Reservoir, Rathbun Lake, and Lake Maumelle, with SAR altimetry conventional retrackers generally exhibit better performance compared to those over Lake Mendota, Waubesa, and Kegonsa. However, even in these cases, BiST results surpass them both in terms of CC and RMSE. Over Lake Mohave, where Sentinel-3A passes along the lake's extent (Figure 5.10), presenting a potentially challenging scenario for SAR altimetry due to a near-zero crossing angle leading to neighboring contamination in the cross-track direction, the Ocean retracker appears to encounter challenges and generates some outliers. There, the BiST retracker closely aligns with the in situ data, yielding similar results to OCOG and Ice retrackers, achieving a CC of 0.99 and RMSE of 10 cm. Over Rathbun Lake, the BiST retracker closely mirrors the behavior observed in the in situ data, achieving CC of 0.92 and RMSE of 0.25 cm. In contrast, the other retrackers, including Ocean, Ice, Ice Sheet, and Sea-ice, show notable discrepancies and outliers in their estimations, failing to achieve a CC better than 0.79 and with an RMSE of 0.52 cm.

Figure 5.17 compares BiST validation results using $E_{\mathrm{t}}^{2\mathrm{D}}$ against other retrackers across all lakes for both CC and RMSE. The improvement is evident, as most points lie above the diagonal in the CC plots, indicating higher correlation, and below the diagonal in the RMSE plots, indicating reduced error.

The only water body in the case studies where BiST results do not notably outperform other retracking methods and demonstrate comparable performance to one of the retracker is Lake Michigan. Due to its large size, its waveforms exhibit lower levels of noise, as illustrated in Figure 5.10 and Figure 5.14, thereby presenting less challenge for the conventional retracker. Specifically, in the case of Jason-3 MLE3, it even surpasses the performance of the BiST results. For Jason-2 and Sentinel-6MF (see Figure 5.14), BiST results align closely with those from Ice and MLE3, respectively. This suggests that for larger water bodies with less noisy waveforms, the use of a conventional retracker is sufficient. Unlike other cases, over Lake Michigan and Lake Mohave, the BiST results with E_t^{1D} outperform E_t^{2D}. This can again be attributed to the less noisy nature of the radargrams, where it is sufficient to define the temporal energy function based solely on pixel intensity, without considering bin location.

Tab. 5.3: Validation results of the obtained water height time series from the BiST retracker and other available retrackers, presented in terms of Correlation Coefficient (CC) and Root Mean Squared Error (RMSE) in meter, across all case studies listed in Table 5.2. The numbers are reported in the format CC/RMSE. In case of BiST retracker results are shown for both cases of using 1D temporal energy function E_t^{1D} or 2D temporal energy function E_t^{2D}. Those results represented by NaN indicates that the corresponding retracker failed to deliver a time series. Bolded numbers in each category of "existing retrackers" or "BiST" represent the best of that category.

		existing retrackers							BiST	
Lake	Mission	Ocean	OCOG	MLE3	MLE4	Ice	Ice sheet	Sea-ice	w. E_t^{1D}	w. E_t^{2D}
Boca Reservoir	Sentinel-3B	NaN	0.48/2.64	–	–	−0.36/2.51	0.10/2.87	**0.52/4.47**	0.57/4.32	**0.54/3.51**
Lake Mohave	Sentinel-3A	−0.11/3.56	**0.99/0.05**	–	–	0.97/0.21	0.46/1.31	−0.30/13.16	**0.99/0.10**	0.98/0.13
Abiquiu Reservoir	Sentinel-3A	NaN	**0.99/0.10**	–	–	0.99/0.14	0.99/0.38	0.99/0.15	0.99/0.21	**0.99/0.08**
Lake Mendota	Jason-2	–	–	0.05/1.85	−0.01/0.77	**0.18/1.86**	–	–	0.22/1.10	**0.33/0.39**
	Jason-3	–	–	0.06/1.54	−0.83/6.15	**0.12/1.80**	–	–	0.16/1.04	**0.36/0.50**
Lake Waubesa	Jason-2	–	–	0.13/2.38	0.07/1.51	**0.24/0.69**	–	–	0.55/0.24	**0.71/0.15**
	Jason-3	–	–	0.20/2.58	0.27/1.22	**0.47/0.43**	–	–	0.70/0.27	**0.73/0.20**
Lake Kegonsa	Jason-2	–	–	−0.38/3.70	0.08/3.59	**0.11/3.02**	–	–	0.13/2.11	**0.34/0.28**
	Jason-3	–	–	**0.47/1.25**	−0.08/3.91	0.05/3.22	–	–	0.14/0.78	**0.34/0.42**
Lake Michigan	Jason-2	–	–	0.77/0.27	0.79/0.23	**0.94/0.10**	–	–	**0.93/0.12**	0.90/0.15
	Jason-3	–	–	0.82/0.19	**0.92/0.11**	0.81/0.19	–	–	**0.80/0.21**	0.73/0.22
	Sentinel-6MF	0.74/0.11	0.41/0.16	**0.86/0.07**	–	–	–	–	0.82/0.08	**0.84/0.07**
Rathbun Lake	Sentinel-3A	−0.07/5.02	**0.79/0.52**	–	–	0.64/0.65	0.57/0.90	0.77/0.55	0.89/0.31	**0.92/0.25**
Lake Maumelle	Sentinel-3B	−0.41/1.54	0.95/0.09	–	–	0.78/0.25	0.26/0.62	**0.93/0.12**	0.97/0.08	**0.97/0.07**

Overall, the validation results (Table 5.3 and Figure 5.16) show that the BiST retracker is a robust and effective retracking method for both pulse-limited and SAR altimetry applications and show that BiST consistently outperforms conventional retracking methods, such as Ocean, OCOG, MLE3, and Ice, particularly in challenging environments like small lakes with noisy waveforms, which is confirmed by its closer alignment with in situ data, as indicated by higher CC and lower RMSE. On average, the BiST retracker improves the RMSE by approximately 0.25 m with the 1D temporal energy function and 0.51 m with the 2D temporal energy function compared to the best existing retracker (Figure 5.17). Perhaps, the main benefit of the BiST retracker is its robustness against unexpected waveform variations, which cannot be easily abstracted with a statistical metric.

5.4 Outlook

Here, the effectiveness of incorporating both spatial and temporal information in the retracking process is highlighted. However, despite the promising performance of the BiST retracker, there are certain limitations to consider. One limitation is the computational complexity associated with the Bayesian approach and the optimization procedure, particularly when processing large datasets. Although the graph cut optimization algorithm in this study finds the MAP solution more efficient than similar algorithms according to the comparison study by Szeliski et al. (2008), it is quite time-consuming compared to the conventional retrackers. Currently, with a standard desktop with Core(TM) i5-8500 (CPU @3.00 GHz) utilizing the

maxflow configuration without any additional optimization strategies, the process of retracking the entire data of for instance Waubesa Lake, Jason-2 with 299 radargrams (299 epochs) takes 44 seconds, which means about 0.14 seconds for each radargram. While this is not excessively demanding computationally, it is still more resource-intensive compared to a 1D retracking approach. Addressing this limitation may require optimization strategies or parallel computing techniques to expedite the retracking process.

Furthermore, since temporal information is incorporated in constructing the temporal energy function, it is important to evaluate the performance of the proposed method for real-time or near-real-time applications. Practically, this means developing an empirical temporal energy function derived from past data and using it in near-real-time scenarios. While minimal influence on performance is expected based on experience, it remains crucial to analyze the applicability of the BiST retracker for real-time or near-real-time applications.

Another issue that needs careful consideration for the BiST retracker is its application over rivers. There, it is important to recognize that consecutive waveforms from a river surface, depending on the crossing angle, may correspond to different parts of the river with varying heights and varying geometry. Therefore, even after performing the absolute bin-aligning step, the assumption that all waveforms represent similar heights may not hold. Consequently, before applying the BiST retracker, at least an additional step of slope correction is necessary (Da Silva et al., 2023). However, it is expected that after the slope correction step, the results should be superior to the conventional retracking method. This expectation arises mainly because a river typically generates a specific pattern in a radargram, for which the proposed method is fully prepared.

By simultaneously considering both spatial and temporal information, the method achieves a more nuanced and comprehensive understanding of the underlying characteristics within the data, capturing patterns that may be overlooked when analyzed in isolation. This approach leverages the interconnected nature of spatial and temporal data, allowing for more accurate interpretations and potentially revealing relationships that would otherwise remain hidden. The versatility of this method allows it to be applied across various datasets beyond the scope presented in this chapter. For example, in the case of SWOT pixel cloud products, data points are generally categorized into classes such as open water, land, and dark water based on InSAR measurement characteristics. However, these classifications can be ambiguous, especially in areas with mixed or transitional surfaces, such as wetlands or seasonal water bodies. By incorporating spatiotemporal information, the proposed method enhances classification accuracy, enabling a clearer distinction between water and land. This improvement could lead to more precise environmental monitoring, as the method better captures temporal changes and spatial dynamics in the pixel cloud data.

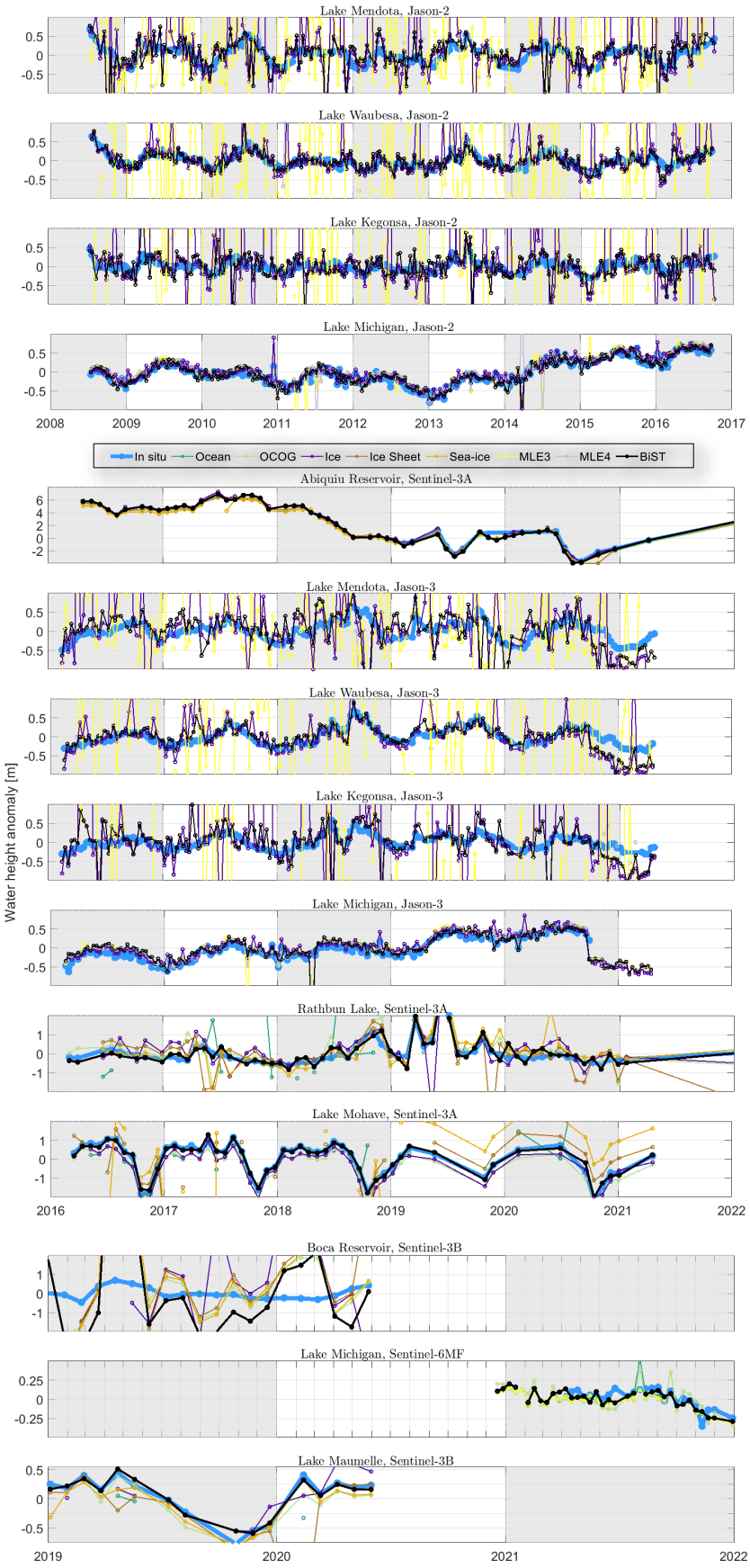

Fig. 5.15: Water height anomaly obtained from the BiST retracker together with in situ data and results from all other available retracking methods in geophysical data records over all case studies listed in Table 5.2.

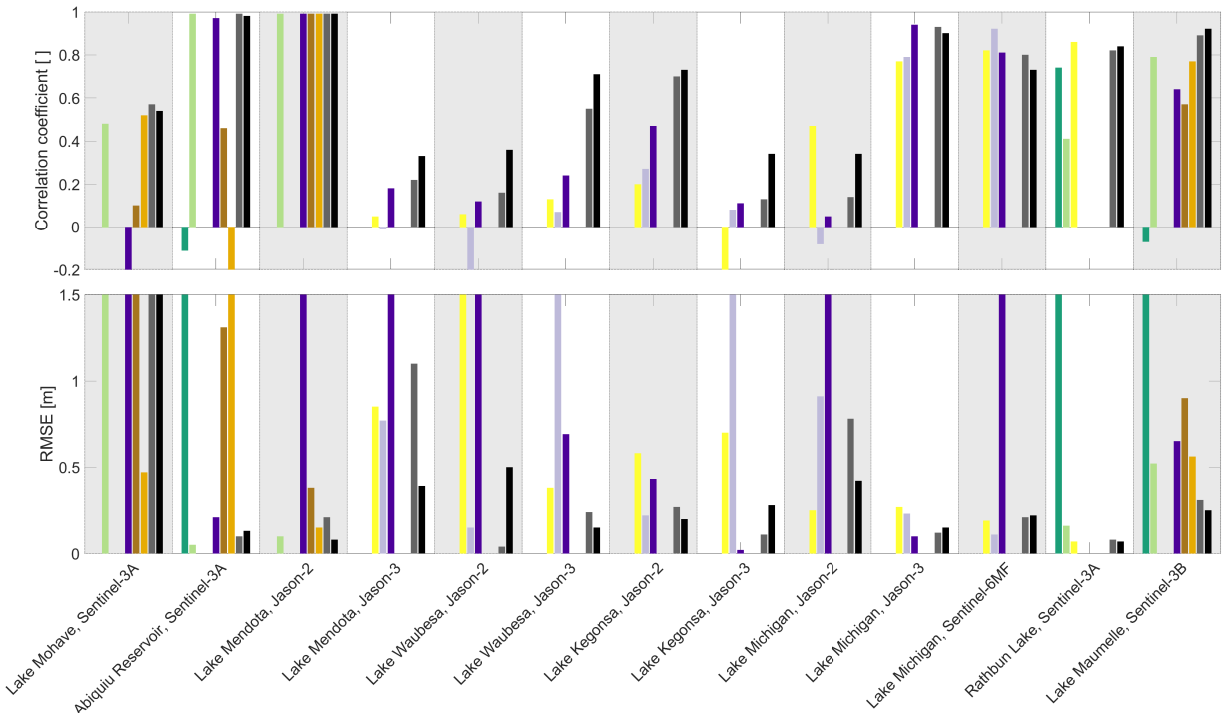

Fig. 5.16: Validation results of the obtained water height time series from the BiST retracker and other available retrackers, presented in terms of correlation coefficient and Root Mean Squared Error (RMSE), across all case studies listed in Table 5.2. In case of the BiST retracker results are shown for both cases with 1D temporal energy function E_t^{1D} and 2D temporal energy function E_t^{2D}.

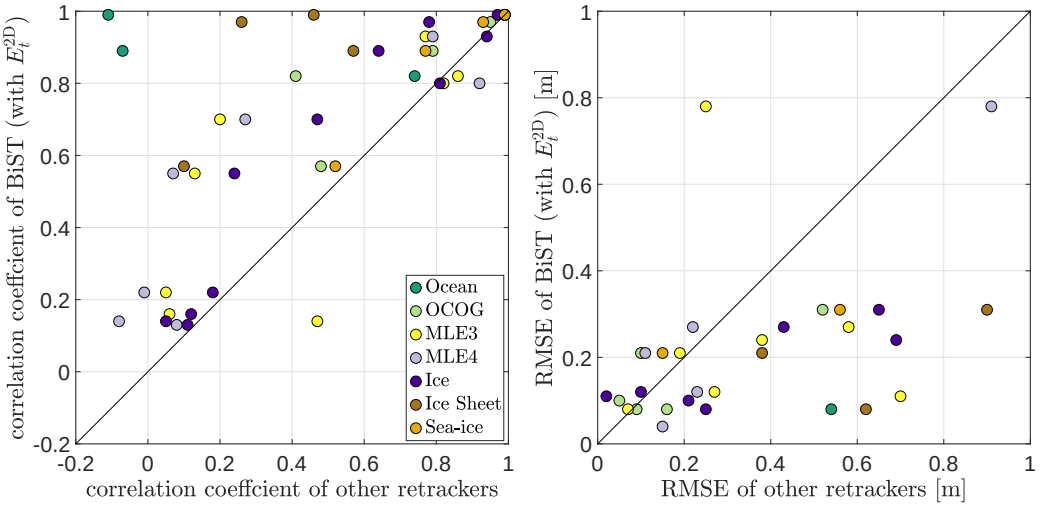

Fig. 5.17: Comparison of BiST validation results with E_t^{2D} against other retrackers for all lakes: (left) correlation coefficient, (right) RMSE.

6 Summary and conclusion

Hydrology, traditionally concerned with the natural occurrence, distribution, and circulation of water, has evolved from local studies to a global perspective, recognizing water as a finite resource. To this end, the global water cycle framework has become essential for understanding water dynamics across different regions and scales. Despite its conceptual clarity, the global water cycle's quantification requires sophisticated measurements across various spatiotemporal scales. Achieving this remains challenging due to the complexity of capturing localized and large-scale patterns, variations in topography, climate, and land use, as well as temporal variability. Additionally, issues such as data accuracy, logistical constraints, and the need for interdisciplinary collaboration further complicate comprehensive measurement efforts, leaving significant knowledge gaps in understanding various components of the water cycle, including river discharge, surface water storage, soil moisture dynamics, and subsurface water storage and flow.

Inspired by the existing knowledge gap, an emerging field referred to as ***Hydrogeodesy*** has recently come to the forefront. Hydrogeodesy is the discipline that uses terrestrial and foremost spaceborne geodetic data, both geometric and gravimetric, in support of global water cycle quantification. The key technologies in hydrogeodesy are satellite altimetry, satellite gravimetry, satellite imaging, Interferometric Synthetic Aperture Radar (InSAR), Global Navigation Satellite System (GNSS), and GNSS-Reflectometry (GNSS-R). These technologies provide either direct or indirect measurements of many water cycle components, including surface water storage, snow water storage, glacial water storage, soil moisture, total water storage, and river discharge. Moreover, geodetic methods reveal how hydrological processes affect Earth's physical structure, particularly through crustal deformation caused by hydrological mass redistribution. This deformation, driven by temporal changes in hydrological loads, results in both vertical and horizontal displacements that are monitored using geodetic techniques.

Despite advancements in spaceborne geodetic sensors, which provide direct or indirect measurements of many water cycle components, hydrogeodesy faces significant challenges. Key issues include limitations in spatiotemporal resolution, measurement uncertainties, unobserved variables, inconsistencies in background models, and the difficulty of separating aggregated measurements. Possible solutions to these challenges involve combining different data types, including satellite, ground-based observations, and model outputs, to benefit from their complementary strengths. However, this presents its own challenges, as it requires reconciling datasets with varying resolutions, accuracies, and temporal scales.

While AI techniques have gained attention for addressing some of the challenges listed above, Bayesian approaches offer a complementary advantage by providing probabilistic interpretations and uncertainty quantification. Rooted in the Bayes theorem, Bayesian approaches provide a robust framework for updating initial knowledge about parameters with new data, resulting in a posterior distribution. The initial knowledge is represented as a prior distribution, which is then combined with the observed data using a likelihood function, resulting in the determination of the posterior distribution. Bayesian methods offer a clear advantage by providing a probabilistic interpretation of results, allowing for explicit parameter uncertainty estimates. This is particularly important in hydrogeodesy, where hydrological cycle parameters, such as river discharge, soil moisture, and groundwater storage, are often indirectly estimated and subject to significant uncertainties.

This habilitation thesis explores the potential of Bayesian methods to advance hydrogeodesy by dealing with the outlined challenges and improving estimates of water cycle parameters. To this end, first, a

foundational overview of Bayesian statistics and modeling is provided, linking these approaches to classical frequentist methods commonly used in geodesy. Three distinct variants of Bayesian statistics and modeling are then presented to demonstrate Bayesian applications in hydrogeodesy. These variants target some of the challenges in hydrogeodesy, including estimating daily river discharge from space, downscaling GRACE data, and retracking altimetry radargrams, as summarized in terms of their Bayesian components in Table 6.1.

Tab. 6.1: Summary of different Bayesian studies discussed in this thesis.

Goal	Prior	Likelihood	MAP solution	How the posterior is obtained?
estimating daily river discharge from space	cyclostationary behavior of discharge represented by covariance and cross-covariance of discharge across gauges	Observed altimetric discharge	unbiased daily river discharge and its uncertainty	through Kalman filter and smoother
downscaling GRACE data	distribution of GRACE data over grid cells	conditional probability obtained from joint copula derived joint distribution of GRACE and fine-scale data	downscaled GRACE data and its uncertainty	by direct multiplication of prior and likelihood
retracking altimetry radargrams	derived from the spatial dependency in a radargram	temporal evolution of initial segmentations labels (*Front* and *Back*) for each pixel in radargram	a segmented radargram with the border being the retracking line	optimization, via maxflow algorithm

The first study uses a Bayesian approach in dynamic systems, particularly the Kalman filter, to estimate daily river discharge using measurements from spaceborne geodetic sensors. In hydrogeodetic studies, the Kalman filter and dynamic systems are especially valuable, as they enable the integration of multiple data sources and continuously update estimates with incoming measurements. This is particularly beneficial for river systems, which inherently function as dynamic systems. By combining altimetric water height and imaging-based river width with hydrological models or empirical state-space representation of the river system, the Kalman filter allows for real-time model updates and corrections based on new observations, leading to more reliable predictions of river discharge and other hydrological parameters. To explore this potential, a method is proposed to use the cyclostationary behavior of discharge—represented by covariance and cross-covariance relationships across river gauges—as prior information. The observed altimetric discharge data provide the likelihood and yield an unbiased daily discharge estimate when combined with the prior. The posterior distribution is obtained through the Kalman filter formulation, which is essentially derived by multiplying the conjugate normally distributed prior and likelihood function.

The method is employed over the Niger River basin, including its two main tributaries. The unbiased solutions derived from the Kalman filter and smoother for the six variants of the observation equation are validated against *in situ* data at 18 gauges along the Niger River. Validation reveals an average Correlation Coefficient (CC) of 0.9, an average relative Root Mean Squared Error (RMSE) and relative bias of 15%, a Nash–Sutcliffe Efficiency (NSE) coefficient with respect to the long-term mean ($\mathrm{NSE}_{\mathrm{mean}}$) greater than 0.5 for 15 gauges, and an NSE coefficient concerning the monthly mean ($\mathrm{NSE}_{\mathrm{cycle}}$) above 0 for all gauges. These results demonstrate that the method effectively estimates daily river discharge across the entire river basin. Results for a previously gauged basin like Niger are especially promising, as numerous river basins globally experience similarly limited discharge availability. This suggests that, with satellite altimetry at multiple virtual stations along a river and the availability of historical discharge data, daily river discharge estimates can be achieved with an expected error below 20% for many basins worldwide. This method, which enhances discharge estimation accuracy compared to legacy mean daily discharge, offers substantial value for hydrological studies and hydraulic model calibration. This potential is further underscored by the increasing availability of spaceborne geodetic data, including SWOT, which provides simultaneous measurements of height, width, and discharge for nearly all rivers worldwide with a temporal resolution of no more than 21 days, following its placement into its science orbit in July 2023.

While in the Kalman filter, both the prior and likelihood are considered to be normally distributed, allowing the normally distributed posterior to be obtained analytically, in most real-world applications—including

those in hydrogeodesy—the Gaussianity assumption does not hold for many parameters, limiting the use of the Kalman filter. Inspired by this challenge and motivated by the need to overcome the limitations of the poor spatial resolution of the GRACE and GRACE-FO missions, the second study discussed in Chapter 4 presents a method to infer the posterior directly, without any assumptions about the distribution of the likelihood and the posterior. So, a kind of empirically driven solution within the Bayesian framework. There, nonparametric likelihood functions are obtained from the data itself, from which the entire posterior is directly derived through the multiplication of the prior and likelihood. For the prior, the GRACE values realized on a 0.5° by 0.5° grid cell are taken into account since they truly provide a prior estimate for the downscaled data. To obtain the prior distribution, the standard deviation and kurtosis of GRACE estimates in each grid cell are used for each specific month, resulting in 12 priors for each grid cell from January to December. For the likelihood functions, the copula is used to describe the dependence of multivariate distributions on any kind of marginal distribution. Copulas are built based on the dependency between GRACE and fine-scale data. The likelihood functions are obtained by constructing empirical copulas on data for each month and fitting an appropriate analytical copula, conditioning on the respective quantile value. Since GRACE data is coarse and its statistical dependency on fine-scale data can be deteriorated by its imperfect estimates of GRACE data, the grid-based data is transformed into spherical harmonic coefficients, the data is truncated, and the desired copulas are built based on the low-degree (long wavelength) spherical harmonic coefficients. Here, it is assumed that the dependencies between long wavelengths would represent the dependencies at short wavelengths as well. The truncation helps avoid the deterioration of the dependencies among the datasets in copulas. A copula model built from spherical harmonic coefficients can also be used for grid-based data since copulas are invariant to monotonic transformations of the marginal variables. This is a significant advantage compared to approaches using covariances, as covariances depend strongly on the marginal distributions.

The proposed downscaling approach is applied to the Amazon Basin, utilizing four different fine-scale datasets: WGHM, PCR-GLOBWB, SURFEX-TRIP, and the ensemble of flux data and soil moisture data from GLEAM and ASCAT. All permutations of the selected data are considered, obtaining eight realizations for downscaling Terrestrial Water Storage Anomaly (TWSA) and its time derivative Terrestrial Water Storage Flux (TWSF). In each realization, for each grid cell and each monthly value, the corresponding prior and likelihood functions are taken to calculate a posterior distribution based on the month of data. From the obtained posterior distribution, the downscaled result is then obtained by finding the Maximum A Posteriori (MAP) solution. Additionally, over larger basins, a mass-conserved downscaled product is introduced by matching the CDF of TWSF or TWSA with that of GRACE. This ensures that the downscaled results conserve the mass over a large basin, as GRACE should provide the best representation of the total mass of a large basin.

The downscaling results are validated against two independent datasets: 1) space-based Surface Water Storage Change (SWSC) in the river system of the Amazon and 2) Vertical Crustal Displacements Change (VCDR) observed by the Global Positioning System (GPS). In the first validation, SWSC profiles of nine river branches in the Amazon Basin from 2003 to 2010 are compared with TWSF profiles from GRACE, the fine-scale model, and the downscaled products. The validation shows that the downscaled results capture the spatial details of the variations in water storage in the rivers, resulting in high CC. Furthermore, this validation shows that a downscaled product with a relative RMSE of 26% with SWSC is obtained while the input fine-scale TWSF showed a relative RMSE of 70%. In the second validation, the results are validated against the VCDR time series in two ways: 1) by comparison with the TWSF-based VCDR obtained by convolving the TWSF load with the Green's function, and 2) by direct comparison with the TWSF of the grid cell where the GPS station is located. In the first analysis, RMSE values between GPS-VCDR and TWSF-based VCDR series are calculated. The downscaled products result in RMSE values between 2.27 and 5.65 mm/month, a significant improvement compared to the input fine-scale TWSF with RMSE values of up to 14 mm/month. In the second analysis, CC between the GPS-VCDR and the respective TWSF products

over the 10 GPS locations throughout the different realizations is calculated. On average, the downscaling products are well anti-correlated, exhibiting a CC of -0.81, while the input fine-scale TWSF yields a CC of -0.73.

The downscaling results highlight that the proposed Bayesian framework can successfully downscale GRACE data. However, the performance of the results seems to depend strongly on the quality of the input data. Even when the input data comes with high inconsistencies, the main benefit of the proposed copula-supported Bayesian approach is presenting the uncertainties associated with data and models. The present study supports understanding the variation in water storage fluxes in many small catchments, thus instrumental for local hydrological studies. The method can be implemented to downscale other water cycle parameters different from TWSF and TWSA and, as such, is an alternative to traditional methods such as those based on machine learning.

In the downscaling study presented in Chapter 4, the proposed method allows for obtaining the posterior directly without any assumptions about the distribution of the data. However, although in many cases an assumption about the distribution can be made, obtaining an analytical posterior distribution is not feasible, especially in high-dimensional parameter spaces, making Bayesian inference computationally challenging. In such cases, sampling techniques such as Markov Chain Monte Carlo (MCMC) are required to approximate posterior distributions. Despite the general effectiveness of sampling techniques, as the complexity of probabilistic models increases—particularly in high-dimensional data contexts—these methods can become computationally demanding and difficult to implement. A primary challenge lies in efficiently capturing and representing the intricate dependencies among a large number of random variables within these complex models. *Graphical models* address this challenge by visually and mathematically representing dependencies among random variables, simplifying probabilistic structures, and enabling more efficient computation of posterior distributions, making Bayesian inference more feasible in high-dimensional spaces. Furthermore, in the downscaling study, although a direct posterior was obtained for each grid cell, spatial dependencies among neighboring grid cells are not considered. Also in such contexts, graphical models are well-suited to capture spatial dependencies or covariances within the Bayesian framework. To explore this potential, and inspired by the challenge of noisy water level estimates from satellite altimetry over inland water bodies, Chapter 5 presents a Bayesian approach to retrack altimetry waveforms by formulating a probabilistic graphical model known as a Markov Random Field (MRF), where a Maximum A Posteriori estimation of the MRF (MRF-MAP) is sought. The Bayesian aspect of the MAP-MRF framework involves incorporating prior knowledge and using the Bayes theorem to update beliefs about hidden variables based on observed data. In such a formulation, inference involves finding the configuration that maximizes the posterior probability, effectively minimizing an energy function defined by the sum of potential functions.

Unlike conventional retracking methods that focus solely on identifying a single point in a waveform, the method presented in Chapter 5 adopts a holistic approach by seeking retracking lines within 2D radargrams. Treating a satellite altimetry radargram as an image, a retracking line divides the radargram into two segments: the left (*Front*) and the right (*Back*) side of the retracking line. This segmentation approach can be interpreted as a binary image segmentation problem. In the proposed MRF-MAP framework, spatial dependencies within radargrams are used as prior information. For the likelihood function, the temporal evolution of each pixel's label (*Front* and *Back*) across different groundtrack cycles is used. Two types of temporal energy functions are suggested: one that depends solely on pixel intensity (1D temporal energy) and another that relies on both pixel intensity and bin values (2D temporal energy). The MAP solution is then a segmented radargram that minimizes labeling costs, achieved by maximizing the posterior probability using the maxflow algorithm. By incorporating spatiotemporal information—specifically in the bin, time, and space domains—this algorithm identifies a labeling set that maximizes the posterior function or minimizes the posterior energy/cost function. The retracking line is then defined as the boundary between the two segments from the segmented radargram.

The methodology, abbreviated as the BiST (Bin-Space-Time) retracker is applied to both pulse-limited and SAR altimetry datasets across nine lakes and reservoirs in the United States, encompassing diverse altimetry characteristics: Boca Reservoir, Lake Mohave, Abiquiu Reservoir, Lake Mendota, Lake Waubesa, Lake Kegonsa, Lake Michigan, Rathbun Lake, and Lake Maumelle. The resulting water level time series are then validated against in situ data. Overall validation results show that the BiST retracker is a robust and effective method for both pulse-limited and SAR altimetry applications and show that BiST consistently outperforms conventional retracking methods, such as Ocean, OCOG, MLE3, and Ice, particularly in challenging environments like small lakes with noisy waveforms. On average, the BiST retracker improves the RMSE by approximately 0.25 m with the 1D temporal energy function and 0.51 m with the 2D temporal energy function compared to the best existing retracker.

The main benefit of the BiST retracker is its robustness against unexpected waveform variations, which cannot be easily abstracted with a statistical metric. However, the results show that for larger water bodies with less noisy waveforms (e.g., Lake Michigan), using a conventional retracker may suffice. It is also observed that generally, BiST results with the 2D temporal energy likelihood functions outperform those with the 1D temporal energy, except for case studies with less noisy waveforms. This difference is attributed to the less noisy nature of the radargrams, where it is adequate to define the temporal energy function based solely on pixel intensity, without considering bin location. Overall, by simultaneously considering both spatial and temporal information, the method achieves a more comprehensive understanding of the underlying characteristics within the data. The proposed method can be applied to many other datasets. For instance, SWOT pixel cloud products are typically classified into different categories—such as open water, land, and dark water—based on the characteristics of InSAR measurements. The proposed method can improve the classification of SWOT pixel cloud points by incorporating spatiotemporal information.

As a final word, this thesis not only highlights the challenges in hydrogeodesy and provides a foundational discussion on Bayesian modeling and statistics but also demonstrates the versatility and power of Bayesian methods in enhancing our understanding of water cycle components. It shows specifically how Bayesian methods can effectively improve spatiotemporal resolution, quantify uncertainties, enhance data fusion, and address the complexities inherent in hydrological systems. Each chapter exemplifies the transformative potential of Bayesian approaches in tackling specific hydrological challenges. The proposed methodologies, with their applicability to other parameters and challenges, collectively advance the precision and reliability of hydrological parameters observed by spaceborne geodetic sensors. Moreover, by highlighting the challenges in hydrogeodesy, this thesis provides a clear direction for future research and development in the field. It emphasizes critical areas that require further attention, such as improving the spatial and temporal resolution of hydrological estimates, addressing uncertainties inherent in geodetic observations, and developing more effective methods for assimilating diverse data sources. The thesis encourages the refinement of geodetic data processing techniques and the broader adoption of probabilistic frameworks, such as Bayesian modeling, in future work. Building upon the insights presented here, future studies have the potential to achieve more accurate and reliable understandings of Earth's systems.

Bibliography

Abdalati, W., Zwally, H.J., Bindschadler, R., Csatho, B., Farrell, S.L., Fricker, H.A., Harding, D., Kwok, R., Lefsky, M., Markus, T., et al., 2010. The ICESat-2 laser altimetry mission. Proceedings of the IEEE 98, 735–751. doi:10.1109/JPROC.2009.2034765.

Adler, R.F., Huffman, G.J., Chang, A., Ferraro, R., Xie, P.P., Janowiak, J., Rudolf, B., Schneider, U., Curtis, S., Bolvin, D., et al., 2003. The version-2 global precipitation climatology project (GPCP) monthly precipitation analysis (1979–present). Journal of hydrometeorology 4, 1147–1167. doi:10.1175/1525-7541(2003)004<1147:tvgpcp>2.0.co;2.

Aldrich, J., 2008. R. A. Fisher on Bayes and Bayes' theorem. Bayesian Analysis 3, 161–170. doi:10.1214/08-BA306.

Alizadeh, M., Schuh, H., Todorova, S., Schmidt, M., 2011. Global ionosphere maps of VTEC from GNSS, satellite altimetry, and Formosat-3/COSMIC data. Journal of Geodesy 85, 975–987. doi:10.1007/s00190-011-0449-z.

Allan, R.P., Barlow, M., Byrne, M.P., Cherchi, A., Douville, H., Fowler, H.J., Gan, T.Y., Pendergrass, A.G., Rosenfeld, D., Swann, A.L., et al., 2020. Advances in understanding large-scale responses of the water cycle to climate change. Annals of the New York Academy of Sciences 1472, 49–75. doi:10.1111/nyas.14337.

Allen, G.H., Pavelsky, T.M., 2018. Global extent of rivers and streams. Science 361, 585–588. doi:10.1126/science.aat0636.

Alley, W.M., Healy, R.W., LaBaugh, J.W., Reilly, T.E., 2002. Flow and storage in groundwater systems. Science 296, 1985–1990. doi:10.1126/science.1067123.

Alsdorf, D.E., Lettenmaier, D.P., 2003. Tracking fresh water from space. Science 301, 1491–1494. doi:10.1126/science.1089802.

Alsdorf, D.E., Rodríguez, E., Lettenmaier, D.P., 2007. Measuring surface water from space. Reviews of Geophysics 45. doi:8755-1209/07/2006RG000197.

Altuntas, C., Iban, M.C., Şentürk, E., Durdag, U.M., Tunalioglu, N., 2022. Machine learning-based snow depth retrieval using GNSS signal-to-noise ratio data. GPS Solutions 26, 117. doi:10.1007/s10291-022-01307-2.

Aminjafari, S., Brown, I., Mayamey, F., Jaramillo, F., 2024. Tracking centimeter-scale water level changes in Swedish lakes using D-InSAR. Water Resources Research 60, e2022WR034290. doi:10.1029/2022WR034290.

Andreadis, K.M., Clark, E.A., Lettenmaier, D.P., Alsdorf, D.E., 2007. Prospects for River Discharge and Depth Estimation Through Assimilation of Swath-Altimetry into a Raster-Based Hydrodynamics Model. Geophysical Research Letters 34. doi:10.1029/2007GL029721.

Andreadis, K.M., Coss, S.P., Durand, M., Gleason, C.J., Simmons, T.T., Tebaldi, N., Bjerklie, D.M., Brinkerhoff, C., Dudley, R.W., Gejadze, I., et al., 2025. A first look at river discharge estimation from SWOT satellite observations. Geophysical Research Letters 52, e2024GL114185. doi:10.1029/2024GL114185.

Arabsahebi, R., Voosoghi, B., Tourian, M.J., 2018a. An estimation of tropospheric corrections using GPS and synoptic data: improving Urmia Lake water level time series from Jason-2 and SARAL/AltiKa satellite altimetry. Advances in Space Research 61, 2406–2417. doi:10.1016/j.asr.2018.02.013.

Arabsahebi, R., Voosoghi, B., Tourian, M.J., 2018b. The inflection-point retracking algorithm: improved Jason-2 sea surface heights in the Strait of Hormuz. Marine Geodesy 41, 331–352. doi:10.1080/01490419.2018.1448029.

Arasaratnam, I., Haykin, S., 2009. Cubature kalman filters. IEEE Transactions on automatic control 54, 1254–1269. doi:10.1109/TAC.2009.2019800.

Argus, D.F., Fu, Y., Landerer, F.W., 2014. Seasonal variation in total water storage in California inferred from GPS observations of vertical land motion. Geophysical Research Letters 41, 1971–1980. doi:10.1002/2014GL059570.

Argus, D.F., Landerer, F.W., Wiese, D.N., Martens, H.R., Fu, Y., Famiglietti, J.S., Thomas, B.F., Farr, T.G., Moore, A.W., Watkins, M.M., 2017. Sustained water loss in California's mountain ranges during severe drought from 2012 to 2015 inferred from GPS. Journal of Geophysical Research: Solid Earth 122, 10–559. doi:10.1002/2017JB014424.

Ashouri, H., Hsu, K.L., Sorooshian, S., Braithwaite, D.K., Knapp, K.R., Cecil, L.D., Nelson, B.R., Prat, O.P., 2015. PERSIANN-CDR: Daily precipitation climate data record from multisatellite observations for hydrological and climate studies. Bulletin of the American Meteorological Society 96, 69–83. doi:10.1175/BAMS-D-13-00068.1.

Auriac, A., Sigmundsson, F., Hooper, A., Spaans, K., Björnsson, H., Pálsson, F., Pinel, V., Feigl, K., 2014. InSAR observations and models of crustal deformation due to a glacial surge in Iceland. Geophysical Journal International 198, 1329–1341. doi:10.1093/gji/ggu205.

Balsamo, G., Albergel, C., Beljaars, A., Boussetta, S., Brun, E., Cloke, H., Dee, D., Dutra, E., Muñoz-Sabater, J., Pappenberger, F., et al., 2015. ERA-Interim/Land: a global land surface reanalysis data set. Hydrology and Earth System Sciences 19, 389–407. doi:10.5194/hess-19-389-2015.

Baur, O., Kuhn, M., Featherstone, W., 2009. GRACE-derived ice-mass variations over Greenland by accounting for leakage effects. Journal of Geophysical Research: Solid Earth 114. doi:10.1029/2008JB006239.

Beaumont, M., 2010. Approximate Bayesian computation in evolution and ecology. Annual Review of Ecology, Evolution, and Systematics 41, 379–406. doi:10.1146/annurev-ecolsys-102209-144621.

Beck, H.E., Pan, M., Miralles, D.G., Reichle, R.H., Dorigo, W.A., Hahn, S., Sheffield, J., Karthikeyan, L., Balsamo, G., Parinussa, R.M., et al., 2021. Evaluation of 18 satellite-and model-based soil moisture products using in situ measurements from 826 sensors. Hydrology and Earth System Sciences 25, 17–40. doi:10.5194/hess-25-17-2021.

Beck, H.E., Wood, E.F., Pan, M., Fisher, C.K., Miralles, D.G., van Dijk, A.I., McVicar, T.R., Adler, R.F., 2019. MSWEP V2 global 3-hourly 0.1 precipitation: methodology and quantitative assessment. Bulletin of the American Meteorological Society 100, 473–500. doi:10.1175/bams-d-17-0138.1.

Begoli, E., Bhattacharya, T., Kusnezov, D., 2019. The need for uncertainty quantification in machine-assisted medical decision making. Nature Machine Intelligence 1, 20–23. doi:10.1038/s42256-018-0004-1.

Berardino, P., Fornaro, G., Lanari, R., Sansosti, E., 2002. A new algorithm for surface deformation monitoring based on small baseline differential SAR interferograms. IEEE Transactions on Geoscience and Remote Sensing 40, 2375–2383. doi:10.1109/TGRS.2002.803792.

Berry, P.A.M., Garlick, J.D., Freeman, J.A., , Mathers, E.L., 2005. Global inland water monitoring from multi-mission altimetery. Geophysical Research Letter 32, L16401. doi:10.1029/2005GL022814.

Besag, J., 1974. Spatial interaction and the statistical analysis of lattice systems. Journal of the Royal Statistical Society: Series B (Methodological) 36, 192–236. doi:10.1111/j.2517-6161.1974.tb00999.x.

Beven, K., 2009. Rainfall-Runoff Modelling: The Primer. Wiley-Blackwell. doi:10.1002/9781119951001.

Bevis, M., Brown, A., 2014. Trajectory models and reference frames for crustal motion geodesy. Journal of Geodesy 88, 283–311. doi:10.1007/s00190-013-0685-5.

Biancamaria, S., Lettenmaier, D.P., Pavelsky, T.M., 2016. The SWOT mission and its capabilities for land hydrology. Surveys in Geophysics 37, 307–337.

Birhanu, Y., Bendick, R., 2015. Monsoonal loading in ethiopia and eritrea from vertical gps displacement time series. Journal of Geophysical Research: Solid Earth 120, 7231–7238. doi:10.1002/2015JB012072.

Birkett, C.M., 1995. The global remote sensing of lakes, wetlands and rivers for hydrological and climate research, in: Geoscience and Remote Sensing Symposium, 1995. IGARSS '95. 'Quantitative Remote Sensing for Science and Applications', International, pp. 1979 –1981 vol.3. doi:10.1109/IGARSS.1995.524084.

Bishop, C.M., 2006. Pattern recognition and machine learning. Springer. doi:10.1117/1.2819119.

Blewitt, G., Hammond, W., Kreemer, C., 2018. Harnessing the gps data explosion for interdisciplinary science. Eos 99. doi:10.1029/2018EO104623.

Boergens, E., Dettmering, D., Seitz, F., 2019. Observing water level extremes in the Mekong River Basin: The benefit of long-repeat orbit missions in a multi-mission satellite altimetry approach. Journal of Hydrology 570, 463–472. doi:10.1016/j.jhydrol.2018.12.041.

Bonnefond, P., Exertier, P., Laurain, O., Guinle, T., Féménias, P., 2021. Corsica: A 20-Yr multi-mission absolute altimeter calibration site. Advances in Space Research 68, 1171–1186. doi:10.1016/j.asr.2019.09.049.

Borsa, A.A., Agnew, D.C., Cayan, D.R., 2014. Ongoing drought-induced uplift in the western United States. Science 345, 1587–1590. doi:10.1126/science.126027.

Boy, F., Crétaux, J.F., Boussaroque, M., Tison, C., 2021. Improving sentinel-3 sar mode processing over lake using numerical simulations. IEEE Transactions on Geoscience and Remote Sensing 60, 1–18. doi:10.1109/TGRS.2021.3137034.

Boykov, Y., Kolmogorov, V., 2004. An experimental comparison of min-cut/max-flow algorithms for energy minimization in vision. IEEE Transactions on Pattern Analysis and Machine Intelligence 26, 1124–1137. doi:10.1109/TPAMI.2004.60.

Boykov, Y., Veksler, O., 2006. Graph cuts in vision and graphics: Theories and applications, in: Handbook of mathematical models in computer vision. Springer, pp. 79–96. doi:10.1007/0-387-28831-7.

Boykov, Y., Veksler, O., Zabih, R., 2001. Fast approximate energy minimization via graph cuts. IEEE Transactions on Pattern Analysis and Machine Intelligence 23, 1222–1239. doi:10.1109/34.969114.

Boykov, Y.Y., Jolly, M.P., 2001. Interactive graph cuts for optimal boundary & region segmentation of objects in nd images, in: Eighth IEEE International Conference on Computer Vision, 2001. ICCV 2001. Proceedings., IEEE. pp. 105–112. doi:10.1109/ICCV.2001.937505.

Brinkerhoff, C.B., Gleason, C.J., Feng, D., Lin, P., 2020. Constraining Remote River Discharge Estimation Using Reach-Scale Geomorphology. Water Resources Research 56, e2020WR027949. doi:https://doi.org/10.1029/2020WR027949. e2020WR027949 2020WR027949.

Brocca, L., Melone, F., Moramarco, T., Wagner, W., Naeimi, V., Bartalis, Z., Hasenauer, S., 2010. Improving runoff prediction through the assimilation of the ASCAT soil moisture product. Hydrology and Earth System Sciences 14, 1881–1893. doi:10.5194/hess-14-1881-2010.

Brown, G.., 1977. The average impulse response of a rough surface and its applications. IEEE transactions on antennas and propagation 25, 67–74. doi:10.1109/TAP.1977.1141536.

Brown, R.G., Hwang, P.Y., 1997. Introduction to random signals and applied Kalman filtering: with MATLAB exercises and solutions. Introduction to random signals and applied Kalman filtering: with MATLAB exercises and solutions .

Calmant, S., Crétaux, J.F., Rémy, F., 2016. Principles of radar satellite altimetry for application on inland waters, in: Microwave Remote Sensing of Land Surface. Elsevier, pp. 175–218. doi:10.1016/B978-1-78548-159-8.50004-9.

Calmant, S., Seyler, F., 2006. Continental surface waters from satellite altimetry. Comptes Rendus Geoscience 338, 1113–1122. doi:10.1016/j.crte.2006.05.012.

Calmant, S., da Silva, J.S., Moreira, D.M., Seyler, F., Shum, C., Crétaux, J.F., Gabalda, G., 2012. "Detection of Envisat RA2/ICE-1 retracked radar altimetry bias over the Amazon basin rivers using GPS". Advances in Space Research 51, 1551–1564. doi:10.1016/j.asr.2012.07.033.

Capelli, A., Koch, F., Henkel, P., Lamm, M., Appel, F., Marty, C., Schweizer, J., 2022. GNSS signal-based snow water equivalent determination for different snowpack conditions along a steep elevation gradient. The Cryosphere 16, 505–531. doi:10.5194/tc-16-505-2022.

Carlson, G., Werth, S., Shirzaei, M., 2022. Joint inversion of GNSS and GRACE for terrestrial water storage change in California. Journal of Geophysical Research: Solid Earth 127, e2021JB023135. doi:10.1029/2021JB023135.

Castellazzi, P., Martel, R., Rivera, A., Huang, J., Pavlic, G., Calderhead, A.I., Chaussard, E., Garfias, J., Salas, J., 2016. Groundwater depletion in Central Mexico: Use of GRACE and InSAR to support water resources management. Water resources research 52, 5985–6003. doi:10.1002/2015WR018211.

Cerbelaud, A., David, C.H., Pavelsky, T., Biancamaria, S., Garambois, P.A., Kittel, C., Papa, F., Bates, P., Tourian, M.J., Durand, M., Frasson, R., Oubanas, H., Simard, M., Schumann, G., Allen, G., Tarpanelli, A., Wongchuig, S., Wade, J., Tom, M., Malaterre, P.O., Gleason, C.J., Crétaux, J.F., Nielsen, K., Elmi, O., Schwatke, C., Scherer, D., Gal, L., Paris, A., Dasgupta, A., Munier, S., Feng, D., Bauer-Gottwein, P., Hossain, F., Yamazaki, D., Kitambo, B., Mischel, S., Bonnema, M., Verma, K., Andreadis, K., Picot, N., Benveniste, J., 2025. Satellite requirements to capture water propagation in earth's rivers. Reviews of Geophysics 63, e2024RG000871. doi:https://doi.org/10.1029/2024RG000871. e2024RG000871 2024RG000871.

Chelton, D.B., Walsh, E.J., MacArthur, J.L., 1989. Pulse compression and sea level tracking in satellite altimetry. Journal of atmospheric and oceanic technology 6, 407–438. doi:10.1175/1520-0426(1989)006.

Chen, J.L., Wilson, C.R., Blankenship, D.D., Tapley, B.D., 2009. Accelerated Antarctic ice loss from satellite gravity measurements. Nature Geoscience 2, 859–862. doi:10.1038/ngeo694.

Chen, J.L., Wilson, C.R., Tapley, B.D., Blankenship, D.D., Ivins, E.R., 2013. Contribution of ice sheet and mountain glacier melt to recent sea level rise. Nature Geoscience 6, 549–552. doi:10.1038/ngeo1829.

Chen, J.M., Liu, J., 2020. Evolution of evapotranspiration models using thermal and shortwave remote sensing data. Remote Sensing of Environment 237, 111594. doi:10.1016/j.rse.2019.111594.

Chen, M., Xie, P., Janowiak, J.E., Arkin, P.A., 2002. Global land precipitation: A 50-yr monthly analysis based on gauge observations. Journal of Hydrometeorology 3, 249–266. doi:10.1175/1525-7541(2002)003<0249:glpaym>2.0.co;2.

Chen, P., An, Z., Xue, H., Yao, Y., Yang, X., Wang, R., Wang, Z., 2022. INPPTR: An improved retracking algorithm for inland water levels estimation using Cryosat-2 SARin data. Journal of Hydrology 613, 128439. doi:10.1016/j.jhydrol.2022.128439.

Chew, C.C., Small, E.E., 2014. Terrestrial water storage response to the 2012 drought estimated from gps vertical position anomalies. Geophysical Research Letters 41, 6145–6151. doi:10.1002/2014GL061206.

Chiang, F., Mazdiyasni, O., AghaKouchak, A., 2021. Evidence of anthropogenic impacts on global drought frequency, duration, and intensity. Nature communications 12, 2754. doi:10.1038/s41467-021-22314-w.

CNES, 2011. OSTM/Jason-2 Products Handbook (Issue: 1 rev 8), SALP-MU-M-OP-15815-CN. Technical Report. CNES.

CNES, 2013. SARAL/AltiKa Products Handbook (Issue: 2 rev 4), SALP-MU-M-OP-15984-CN. Technical Report. CNES.

Crétaux, J.F., Berge-Nguyen, M., Calmant, S., Romanovski, V., Meyssignac, B., Perosanz, F., Tashbaeva, S., Arsen, A., Fund, F., Martignago, N., et al., 2013. Calibration of Envisat radar altimeter over Lake Issykkul. Advances in Space Research 51, 1523–1541. doi:10.1016/j.asr.2012.06.039.

Crétaux, J.F., Birkett, C., 2006. Lake studies from satellite radar altimetry. Comptes Rendus Geoscience 338, 1098–1112. doi:10.1016/j.crte.2006.08.002.

Cretaux, J.F., Calmant, S., Papa, F., Frappart, F., Paris, A., Berge-Nguyen, M., 2023. Inland surface waters quantity monitored from remote sensing. Surveys in Geophysics 44, 1519–1552. doi:10.1007/s10712-023-09803-x.

Crétaux, J.F., Jelinski, W., Calmant, S., Kouraev, A., Vuglinski, V., Bergé-Nguyen, M., Gennero, M.C., Nino, F., Rio, R.A.D., Cazenave, A., Maisongrande, P., 2011. SOLS: A lake database to monitor in the Near Real Time water level and storage variations from remote sensing data. Advances in Space Research 47, 1497–1507. doi:10.1016/j.asr.2011.01.004.

Czado, C., 2019. Analyzing Dependent Data with Vine Copulas. Lecture Notes in Statistics, Springer doi:10.1007/978-3-030-13785-4.

Da Silva, E., Woolliams, E.R., Picot, N., Poisson, J.C., Skourup, H., Moholdt, G., Fleury, S., Behnia, S., Favier, V., Arnaud, L., Aublanc, J., Fouqueau, V., Taburet, N., Renou, J., Yesou, H., Tarpanelli, A., Camici, S., Fredensborg Hansen, R.M., Nielsen, K., Vivier, F., Boy, F., Fjørtoft, R., Cancet, M., Ferrari, R., Picard, G., Tourian, M.J., Sneeuw, N., Munesa, E., Calzas, M., Paris, A., Le Meur, E., Rabatel, A., Valladeau, G., Bonnefond, P., Labroue, S., Andersen, O., El Hajj, M., Catapano, F., Féménias, P., 2023. Towards Operational Fiducial Reference Measurement (FRM) Data for the Calibration and Validation of the Sentinel-3 Surface Topography Mission over Inland Waters, Sea Ice, and Land Ice. Remote Sensing 15. doi:10.3390/rs15194826.

Da Silva, J.S., Calmant, S., Seyler, F., Rotunno Filho, O.C., Cochonneau, G., Mansur, W.J., 2010. Water levels in the Amazon basin derived from the ERS 2 and ENVISAT radar altimetry missions. Remote sensing of environment 114, 2160–2181. doi:10.1016/j.rse.2010.04.020.

van Dam, T.M., Blewitt, G., Heflin, M.B., 2001. Crustal displacements due to continental water loading. Geophysical Research Letters 28, 651–654. doi:10.1029/2000GL012120.

Darvishi, M., Destouni, G., Aminjafari, S., Jaramillo, F., 2021. Multi-sensor InSAR assessment of ground deformations around Lake Mead and its relation to water level changes. Remote Sensing 13, 406. doi:10.3390/rs13030406.

David, C.H., Maidment, D.R., Niu, G.Y., Yang, Z.L., Habets, F., Eijkhout, V., 2011. River Network Routing on the NHDPlus Dataset. Journal of Hydrometeorology 12, 913–934. doi:10.1175/2011JHM1345.1.

De Zan, F., Monti Guarnieri, A., 2006. TOPSAR: Terrain observation by progressive scans. IEEE Transactions on Geoscience and Remote Sensing 44, 2352–2360. doi:10.1109/TGRS.2006.873853.

Decharme, B., Martin, E., Faroux, S., 2013. Reconciling soil thermal and hydrological lower boundary conditions in land surface models. Journal of Geophysical Research: Atmospheres 118, 7819–7834. doi:10.1002/jgrd.50631.

Devaraju, B., 2016. Understanding filtering on the sphere: Experiences from filtering GRACE data. Ph.D. thesis. Universität Stuttgart. Holzgartenstr. 16, 70174 Stuttgart. URL: http://elib.uni-stuttgart.de/opus/volltexte/2014/8796.

Dielacher, A., Fragner, H., Koudelka, O., Beck, P., Wickert, J., Cardellach, E., Høeg, P., 2019. The ESA passive reflectometry and dosimetry (PRETTY) mission, in: IGARSS 2019-2019 IEEE International Geoscience and Remote Sensing Symposium, IEEE. pp. 5173–5176. doi:10.1109/IGARSS.2019.8898720.

van Dijk, A.I.J.M., Renzullo, L.J., Wada, Y., Tregoning, P., 2014. A global water cycle reanalysis (2003–2012) merging satellite gravimetry and altimetry observations with a hydrological multi-model ensemble. Hydrology and Earth System Sciences 18, 2955–2973. doi:10.5194/hess-18-2955-2014.

Dill, R., Dobslaw, H., 2013. Numerical simulations of global-scale high-resolution hydrological crustal deformations. Journal of Geophysical Research: Solid Earth 118, 5008–5017. doi:10.1002/jgrb.50353.

Dinardo, S., 2020. Techniques and Applications for Satellite SAR Altimetry over water, land and ice. volume 56. Technische Universität Darmstadt. doi:10.25534/tuprints-00011343.

Dinardo, S., Fenoglio-Marc, L., Becker, M., Scharroo, R., Fernandes, M.J., Staneva, J., Grayek, S., Benveniste, J., 2021. A RIP-based SAR retracker and its application in North East Atlantic with Sentinel-3. Advances in Space Research 68, 892–929. doi:10.1016/j.asr.2020.06.004.

Dinardo, S., Maraldi, C., Cadier, E., Rieu, P., Aublanc, J., Guerou, A., Boy, F., Moreau, T., Picot, N., Scharroo, R., 2024. Sentinel-6 MF Poseidon-4 radar altimeter: Main scientific results from S6PP LRM and UF-SAR chains in the first year of the mission. Advances in Space Research 73, 337–375. doi:10.1016/j.asr.2023.07.030.

Dingman, S.L., Bjerklie, D.M., 2006. Estimation of River Discharge. John Wiley & Sons, Ltd. volume 5. chapter 61. doi:10.1002/0470848944.hsa069.

Dobslaw, H., Bergmann-Wolf, I., Dill, R., Poropat, L., Thomas, M., Dahle, C., Esselborn, S., König, R., Flechtner, F., 2017. A new high-resolution model of non-tidal atmosphere and ocean mass variability for de-aliasing of satellite gravity observations: AOD1B RL06. Geophysical Journal International 211, 263–269. doi:10.1093/gji/ggx302.

Döll, P., Fiedler, K., 2008. Global-scale modeling of groundwater recharge. Hydrology and Earth System Sciences 12, 863–885. doi:10.5194/hess-12-863-2008.

Domeneghetti, A., Molari, G., Tourian, M.J., Tarpanelli, A., Behnia, S., Moramarco, T., Sneeuw, N., Brath, A., 2021. Testing the Use of Single- and Multi-Mission Satellite Altimetry for the Calibration of Hydraulic Models. Advances in Water Resources 151, 103887. doi:10.1016/j.advwatres.2021.103887.

Doucet, A., Godsill, S., Andrieu, C., 2000. On sequential Monte Carlo sampling methods for Bayesian filtering. Statistics and Computing 10, 197–208. doi:10.1007/978-1-4757-3437-9_1.

Dubois, P.C., Van Zyl, J., Engman, T., 1995. Measuring soil moisture with imaging radars. IEEE transactions on geoscience and remote sensing 33, 915–926. doi:10.1109/36.406677.

Durand, M., Gleason, C., Garambois, P.A., Bjerklie, D., Smith, L., Roux, H., Rodriguez, E., Bates, P.D., Pavelsky, T.M., Monnier, J., et al., 2016. An intercomparison of remote sensing river discharge estimation algorithms from measurements of river height, width, and slope. Water Resources Research 52, 4527–4549. doi:10.1002/2015WR018434.

Durand, M., Gleason, C.J., Pavelsky, T.M., Prata de Moraes Frasson, R., Turmon, M., David, C.H., Altenau, E.H., Tebaldi, N., Larnier, K., Monnier, J., et al., 2023. A framework for estimating global river discharge from the Surface Water and Ocean Topography satellite mission. Water Resources Research 59, e2021WR031614. doi:10.1029/2021WR031614.

Durand, M., Neal, J., Rodríguez, E., Andreadis, K.M., Smith, L.C., Yoon, Y., 2014. Estimating reach-averaged discharge for the River Severn from measurements of river water surface elevation and slope. Journal of Hydrology 511, 92–104. doi:10.1016/j.jhydrol.2013.12.050.

Durand, M., Rodriguez, E., Alsdorf, D.E., Trigg, M., 2009. Estimating river depth from remote sensing swath interferometry measurements of river height, slope, and width. IEEE Journal of Selected Topics in Applied Earth Observations and Remote Sensing 3, 20–31. doi:10.1109/JSTARS.2009.2033453.

Egido, A., Smith, W.H., 2017. Fully focused SAR altimetry: Theory and applications. IEEE Transactions on Geoscience and Remote Sensing 55, 392–406. doi:10.1109/TGRS.2016.2607122.

Eicker, A., Schumacher, M., Kusche, J., Döll, P., Schmied, H., 2014. Calibration/Data Assimilation Approach for Integrating GRACE Data into the WaterGAP Global Hydrology Model (WGHM) Using an Ensemble Kalman Filter: First Results. Surveys in Geophysics 35, 1285–1309. URL: http://dx.doi.org/10.1007/s10712-014-9309-8, doi:10.1007/s10712-014-9309-8.

Elmi, O., 2015. The role of multispectral image transformations in change detection. Master's thesis. University of Stuttgart. URL: elib.uni-stuttgart.de/opus/volltexte/2015/10055/.

Elmi, O., 2019. Dynamic water masks from optical satellite imagery. Ph.D. thesis. University of Stuttgart. URL: http://nbn-resolving.de/urn:nbn:de:bsz:93-opus-ds-106145.

Elmi, O., Ahrari, A., 2025. An automatic google earth engine tool for generating lake water area time series from satellite imagery. IEEE geoscience and remote sensing letters doi:10.1109/LGRS.2025.3528323.

Elmi, O., Tourian, M., Sneeuw, N., 2016. Dynamic river masks from multi-temporal satellite imagery: An automatic algorithm using graph cuts optimization. Remote Sensing 8, 1005. doi:10.3390/rs8121005.

Elmi, O., Tourian, M.J., 2023. Retrieving time series of river water extent from global inland water data sets. Journal of Hydrology 617, 128880. doi:10.1016/j.jhydrol.2022.128880.

Elmi, O., Tourian, M.J., Bárdossy, A., Sneeuw, N., 2021. Spaceborne River Discharge from a Nonparametric Stochastic Quantile Mapping Function. Water Resources Research 57, e2021WR030277. doi:10.1029/2021WR030277. e2021WR030277 2021WR030277.

Elmi, O., Tourian, M.J., Saemian, P., Sneeuw, N., 2024. Remote Sensing-Based Extension of GRDC Discharge Time Series - A Monthly Product with Uncertainty Estimates. Scientific data doi:10.1038/s41597-024-03078-6.

Elmi, O., Tourian, M.J., Sneeuw, N., 2015. River discharge estimation using channel width from satellite imagery, in: 2015 IEEE International Geoscience and Remote Sensing Symposium (IGARSS), IEEE. pp. 727–730. doi:978-1-4799-7929-5/15.

Emery, C., David, C., Andreadis, K., Turmon, M., Reager, J., Hobbs, J., Pan, M., Famiglietti, J., Beighley, E., Rodell, M., 2020. Underlying Fundamentals of Kalman Filtering for River Network Modeling. Journal of Hydrometeorology 21, 453–474. doi:10.1175/JHM-D-19-0084.1.

Emery, C.M., Paris, A., Biancamaria, S., Boone, A., Calmant, S., Garambois, P.A., Santos da Silva, J., 2018. Large-Scale Hydrological Model River Storage and Discharge Correction Using a Satellite Altimetry-Based Discharge Product. Hydrology and Earth System Sciences 22, 2135–2162. doi:10.5194/hess-22-2135-2018.

Erban, L.E., Gorelick, S.M., Zebker, H.A., 2014. Groundwater extraction, land subsidence, and sea-level rise in the Mekong Delta, Vietnam. Environmental Research Letters 9, 084010.

ESA, 2007. ENVISAT RA2/MWR Product Handbook (Issue 2.2). Technical Report. ESA.

Escudier, P., Couhert, A., Mercier, F., Mallet, A., Thibaut, P., Tran, N., Amarouche, L., Picard, B., Carrere, L., Dibarboure, G., et al., 2017. Satellite radar altimetry: Principle, accuracy, and precision, in: Satellite altimetry over oceans and land surfaces. CRC Press, pp. 1–70.

Eshqi Molan, Y., Lu, Z., 2020. Can InSAR coherence and closure phase be used to estimate soil moisture changes? Remote Sensing 12, 1511. doi:10.3390/rs12091511.

Evensen, G., 2003. The ensemble kalman filter: Theoretical formulation and practical implementation. Ocean dynamics 53, 343–367. doi:10.1007/s10236-003-0036-9.

Everard, N., Dixon, H., Sarkar, S., Randall, M., Schumann, G., 2023. The FluViSat project: Measuring streamflow from space with very high resolution Planet satellite video, in: EGU General Assembly Conference Abstracts, pp. EGU–1374.

Famiglietti, J., 2012. Rallying Around Our Known Unknowns: What We Don't Know Will Hurt Us. Water 50/50, June 28.

Farazmand, M., Sapsis, T.P., 2019. Extreme events: Mechanisms and prediction. Applied Mechanics Reviews 71, 050801. doi:10.1115/1.4042065.

Fassoni-Andrade, A.C., Fleischmann, A.S., Papa, F., Paiva, R.C.D.d., Wongchuig, S., Melack, J.M., Moreira, A.A., Paris, A., Ruhoff, A., Barbosa, C., et al., 2021. Amazon hydrology from space: scientific advances and future challenges. Reviews of Geophysics 59, e2020RG000728. doi:10.1029/2020RG000728.

Fekete, B., Looser, U., Robarts, R., 2012. Rationale for monitoring discharge on the ground. Journal of Hydrometeorology 13, 1977–1986. doi:10.1175/JHM-D-11-0126.1.

Fekete, B.M., Vörösmarty, C.J., 2007. The current status of global river discharge monitoring and potential new technologies complementing traditional discharge measurements. Predictions in Ungauged Basins: PUB Kick-off (Proceedings of the PUB Kick-off meeting held in Brasilia, 20-22 November 2002) IAHS Publ. 309.

Feng, D., Gleason, C.J., Yang, X., Allen, G.H., Pavelsky, T.M., 2022. How have global river widths changed over time? Water Resources Research 58, e2021WR031712. doi:10.1029/2021WR031712.

Fernandes, M.J., Lázaro, C., Nunes, A.L., Scharroo, R., 2014. Atmospheric Corrections for Altimetry Studies over Inland Water. Remote Sensing 6, 4952–4997. doi:10.3390/rs6064952.

Fernández-Prieto, D., van Oevelen, P., Su, Z., Wagner, W., 2012. Advances in Earth observation for water cycle science. Hydrology and earth system sciences 16, 543–549. doi:10.5194/hess-16-543-2012.

Ferraiuolo, G., Pascazio, V., Schirinzi, G., 2004. Maximum a posteriori estimation of height profiles in InSAR imaging. IEEE Geoscience and Remote Sensing Letters 1, 66–70. doi:10.1109/LGRS.2003.822882.

Ferreira, V., Montecino, H., Ndehedehe, C., Yuan, P., Xu, T., 2021. The versatility of GNSS observations in hydrological studies, in: GPS and GNSS Technology in Geosciences. Elsevier, pp. 281–298. doi:10.1016/B978-0-12-818617-6.00004-4.

Ferreira, V.G., Montecino, H.D., Ndehedehe, C.E., del Rio, R.A., Cuevas, A., de Freitas, S.R.C., 2019. Determining seasonal displacements of earth's crust in south america using observations from space-borne geodetic sensors and surface-loading models. Earth, Planets and Space 71, 84. doi:10.1186/s40623-019-1062-2.

Ferretti, A., Prati, C., Rocca, F., 2001. Permanent scatterers in SAR interferometry. IEEE Transactions on Geoscience and Remote Sensing 39, 8–20. doi:10.1109/36.898661.

Flechtner, F., Schmidt, R., Meyer, U., 2006. De-aliasing of short-term atmospheric and oceanic mass variations for GRACE. Observation of the earth system from space , 83–97doi:10.1007/3-540-29522-4_7.

Forootan, E., Mehrnegar, N., Schumacher, M., Schiettekatte, L.A.R., Jagdhuber, T., Farzaneh, S., van Dijk, A.I., Shamsudduha, M., Shum, C., 2024. Global groundwater droughts are more severe than they appear in hydrological models: An investigation through a bayesian merging of grace and grace-fo data with a water balance model. Science of the Total Environment 912, 169476. doi:10.1016/j.scitotenv.2023.169476.

Foti, G., Gommenginger, C., Jales, P., Unwin, M., Shaw, A., Robertson, C., Rosello, J., 2015. Spaceborne GNSS reflectometry for ocean winds: First results from the UK TechDemoSat-1 mission. Geophysical Research Letters 42, 5435–5441. doi:10.1002/2015GL064204.

Frappart, F., Blumstein, D., Cazenave, A., Ramillien, G., Birol, F., Morrow, R., Rémy, F., 1999. Satellite altimetry: Principles and applications in Earth sciences. Wiley Encyclopedia of Electrical and Electronics Engineering , 1–25doi:10.1002/047134608X.W1125.pub2.

Frappart, F., Papa, F., Güntner, A., Tomasella, J., Pfeffer, J., Ramillien, G., Emilio, T., Schietti, J., Seoane, L., da Silva Carvalho, J., et al., 2019. The spatio-temporal variability of groundwater storage in the Amazon River Basin. Advances in Water Resources 124, 41–52. doi:10.3390/rs10060829.

Frappart, F., Ramillien, G., 2018. Monitoring groundwater storage changes using the Gravity Recovery and Climate Experiment (GRACE) satellite mission: A review. Remote Sensing 10, 829. doi:10.3390/rs10060829.

Fu, L.L., Cazenave, A., 2001. Satellite Altimetry and Earth Sciences: A Handbook of Techniques and Applications. volume 69 of *International Geophysics*. Academic Press.

Fu, L.L., Pavelsky, T., Cretaux, J.F., Morrow, R., Farrar, J.T., Vaze, P., Sengenes, P., Vinogradova-Shiffer, N., Sylvestre-Baron, A., Picot, N., et al., 2024. The Surface Water and Ocean Topography Mission: A breakthrough in radar remote sensing of the ocean and land surface water. Geophysical Research Letters 51, e2023GL107652. doi:10.1029/2023GL107652.

Fu, Y., Zhang, Y., Li, Z., 2022. Integrating GNSS and InSAR measurements for monitoring ground deformation at regional scales. Remote Sensing 14, 689. doi:10.3390/rs17061059.

Funk, C., Peterson, P., Landsfeld, M., Pedreros, D., Verdin, J., Shukla, S., Husak, G., Rowland, J., Harrison, L., Hoell, A., et al., 2015. The climate hazards infrared precipitation with stations—a new environmental record for monitoring extremes. Scientific data 2, 150066. doi:10.1038/sdata.2015.66.

Gejadze, I., Malaterre, P.O., Oubanas, H., Shutyaev, V., 2022. A New Robust Discharge Estimation Method Applied in the Context of SWOT Satellite Data Processing. Journal of Hydrology 610, 127909. doi:10.1016/j.jhydrol.2022.127909.

Gelb, A., 1974. Applied optimal estimation. The M. I. T. Press.

Geman, S., Geman, D., 1984. Stochastic relaxation, Gibbs distributions, and the Bayesian restoration of images. IEEE Transactions on Pattern Analysis and Machine Intelligence 6, 721–741. doi:10.1109/TPAMI.1984.4767596.

Gerten, D., Rost, S., von Bloh, W., Lucht, W., 2008. Causes of change in 20th century global river discharge. Geophysical Research Letters 35. doi:10.1029/2008GL035258.

Getirana, A.C.V., Peters-Lidard, C., 2012. Water discharge estimates from large radar altimetry datasets in the Amazon basin. Hydrology and Earth System Sciences Discussions 9, 7591–7611. doi:10.5194/hessd-9-7591-2012.

Getoor, L., Taskar, B. (Eds.), 2007. Introduction to Statistical Relational Learning. MIT Press. doi:10.7551/mitpress/7432.001.0001.

Ghiggi, G., Humphrey, V., Seneviratne, S., Gudmundsson, L., 2021. G-RUN ENSEMBLE: A Multi-Forcing Observation-Based Global Runoff Reanalysis. Water Resources Research 57, e2020WR028787. doi:10.1029/2020WR028787.

Ghil, M., Malanotte-Rizzoli, P., 1991. Data assimilation in meteorology and oceanography. Advances in Geophysics 33, 141–266. doi:10.1016/S0065-2687(08)60442-2.

Girotto, M., De Lannoy, G.J., Reichle, R.H., Rodell, M., 2016. Assimilation of gridded terrestrial water storage observations from GRACE into a land surface model. Water Resources Research 52, 4164–4183. doi:10.1002/2015WR018417.

Girotto, M., Reichle, R.H., Rodell, M., Liu, Q., Mahanama, S., De Lannoy, G.J.M., 2019. Multi-sensor assimilation of SMOS brightness temperature and GRACE terrestrial water storage observations for soil moisture and shallow groundwater estimation. Remote Sensing of Environment 227, 12–27. doi:10.1016/j.rse.2019.04.001.

Gleason, C., Garambois, P.A., Durand, M., 2017. Tracking river flows from space. EOS Earth & Space Science News doi:10.1029/2017EO078085.

Gleason, C.J., Brown, C.M., 2025. The once and future hydrology is whole earth hydrology. Perspectives of Earth and Space Scientists 6, e2024CN000267. doi:https://doi.org/10.1029/2024CN000267.

Gleason, C.J., Durand, M.T., 2020. Remote sensing of river discharge: A review and a framing for the discipline. Remote Sensing 12, 1107. doi:10.3390/rs12071107.

Gleason, C.J., Smith, L.C., 2014. Toward global mapping of river discharge using satellite images and at-many-stations hydraulic geometry. Proceedings of the National Academy of Sciences 111, 4788–4791. doi:10.1073/pnas.1317606111.

Gleick, P., 2000. The World's Water 2000-2001: The Biennial Report On Freshwater Resources. The World's Water, Island Press. doi:10.5822/978-1-61091-483-3.

Gleick, P.H., 2003. Water use. Annual Review of Environment and Resources 28, 275–314. doi:10.1146/annurev.energy.28.040202.122849.

Goldstein, R.M., Engelhardt, H., Kamb, B., Frolich, R.M., 1993. Satellite radar interferometry for monitoring ice sheet motion: application to an Antarctic ice stream. Science 262, 1525–1530. doi:10.1126/science.262.5139.152.

Gorugantula, S.S., Kambhammettu, B.P., 2022. Sequential downscaling of GRACE products to map groundwater level changes in Krishna river basin. Hydrological Sciences Journal 0, null. doi:10.1080/02626667.2022.2106142.

Gou, J., Soja, B., 2024. Global high-resolution total water storage anomalies from self-supervised data assimilation using deep learning algorithms. Nature Water 2, 139–150. doi:10.1038/s44221-024-00194-w.

Greig, D., Porteous, B., Seheult, A.H., 1989. Exact maximum a posteriori estimation for binary images. Journal of the Royal Statistical Society. Series B (Methodological) , 271–279doi:10.1111/j.2517-6161.1989.tb01764.x.

Gu, S., Zhou, Y., Zhao, L., Ma, M., She, X., Zhang, L., Li, Y., 2024. A Fast Generative Adversarial Network Combined with Transformer for Downscaling GRACE Terrestrial Water Storage Data in Southwestern China. IEEE Transactions on Geoscience and Remote Sensing doi:10.1109/TGRS.2024.3349548.

Hagemann, M., Gleason, C., Durand, M., 2017. BAM: Bayesian AMHG-Manning inference of discharge using remotely sensed stream width, slope, and height. Water Resources Research 53, 9692–9707. doi:10.1002/2017WR021626.

Haghshenas Haghighi, M., Motagh, M., 2024. Uncovering the impacts of depleting aquifers: A remote sensing analysis of land subsidence in Iran. Science Advances 10, eadk3039. doi:10.1126/sciadv.adk3039.

Halimi, A., Buller, G.S., McLaughlin, S., Honeine, P., 2017. Denoising smooth signals using a Bayesian approach: Application to altimetry. IEEE Journal of Selected Topics in Applied Earth Observations and Remote Sensing 10, 1278–1289. doi:10.1109/JSTARS.2016.2629516.

Harris, I., Osborn, T.J., Jones, P., Lister, D., 2020. Version 4 of the CRU TS monthly high-resolution gridded multivariate climate dataset. Scientific data 7, 1–18. doi:10.1038/s41597-020-0453-3.

Henrion, M., 1988. Propagation of uncertainty by logic sampling in Bayes' networks. Uncertainty in Artificial Intelligence 2 , 149–163doi:10.1016/B978-0-444-70396-5.50019-4.

Hersbach, H., Bell, B., Berrisford, P., Hirahara, S., Horányi, A., Muñoz-Sabater, J., Nicolas, J., Peubey, C., Radu, R., Schepers, D., et al., 2020. The ERA5 global reanalysis. Quarterly Journal of the Royal Meteorological Society 146, 1999–2049. doi:10.1002/qj.3803.

Hirt, C., Gruber, T., Featherstone, W., 2011. Evaluation of the first GOCE static gravity field models using terrestrial gravity, vertical deflections and EGM2008 quasigeoid heights. Journal of geodesy 85, 723–740. doi:10.1007/s00190-011-0482-y.

Hoffman, M., Blei, D., Wang, C., Paisley, J., 2013. Stochastic variational inference. Journal of Machine Learning Research 14, 1303–1347.

Hoffman, M., Gelman, A., 2014. The No-U-Turn sampler: Adaptively setting path lengths in Hamiltonian Monte Carlo. Journal of Machine Learning Research 15, 1593–1623.

Hong, S., Liu, M., 2021. Postseismic Deformation and Afterslip Evolution of the 2015 Gorkha Earthquake Constrained by InSAR and GPS Observations. Journal of Geophysical Research: Solid Earth 126, e2020JB020230. doi:https://doi.org/10.1029/2020JB020230.

Horne, A.C., O'Donnell, E.L., Webb, J.A., Stewardson, M.J., Acreman, M., Richter, B., 2017. The environmental water management cycle, in: Water for the Environment. Elsevier, pp. 3–16. doi:10.1016/B978-0-12-803907-6.00001-2.

Hu, J., Ding, X., Li, Z., Zhang, L., Zhu, J., Sun, Q., Gao, G., 2016. Vertical and horizontal displacements of Los Angeles from InSAR and GPS time series analysis: Resolving tectonic and anthropogenic motions. Journal of Geodynamics 99, 27–38. doi:https://doi.org/10.1016/j.jog.2016.05.003.

Huang, Q., Long, D., Du, M., Zeng, C., Qiao, G., Li, X., Hou, A., Hong, Y., 2018. Discharge Estimation in High-Mountain Regions with Improved Methods Using Multisource Remote Sensing: A Case Study of the Upper Brahmaputra River. Remote Sensing of Environment 219, 115–134. doi:https://doi.org/10.1016/j.rse.2018.10.008.

Huang, Q., McMillan, M., Muir, A., Phillips, J., Slater, T., 2024. Multipeak retracking of radar altimetry waveforms over ice sheets. Remote Sensing of Environment 303, 114020. doi:10.1016/j.rse.2024.114020.

Huffman, G., Stocker, E., Bolvin, D., Nelkin, E., Tan, J., 2019. GPM IMERG Final Precipitation L3 1 day 0.1 degree x 0.1 degree V06. doi:10.5067/GPM/IMERGDF/DAY/06.

Huffman, G.J., Adler, R.F., Bolvin, D.T., Gu, G., 2009. Improving the global precipitation record: GPCP version 2.1. Geophysical Research Letters 36. doi:10.1029/2009GL040000.

Huffman, G.J., Adler, R.F., Morrissey, M.M., Bolvin, D.T., Curtis, S., Joyce, R., McGavock, B., Susskind, J., 2001. Global precipitation at one-degree daily resolution from multisatellite observations. Journal of hydrometeorology 2, 36–50. doi:10.1175/1525-7541(2001)002<0036:gpaodd>2.0.co;2.

Huffman, G.J., Bolvin, D.T., Nelkin, E.J., Wolff, D.B., Adler, R.F., Gu, G., Hong, Y., Bowman, K.P., Stocker, E.F., 2007. The TRMM multisatellite precipitation analysis (TMPA): Quasi-global, multiyear, combined-sensor precipitation estimates at fine scales. Journal of hydrometeorology 8, 38–55. doi:10.1175/jhm560.1.

Humphrey, V., Rodell, M., Eicker, A., 2023. Using satellite-based terrestrial water storage data: a review. Surveys in Geophysics 44, 1489–1517. doi:10.1007/s10712-022-09754-9.

Huntington, T.G., 2006. Evidence for intensification of the global water cycle: Review and synthesis. Journal of Hydrology 319, 83–95. doi:10.1016/j.jhydrol.2005.07.003.

Huyakorn, P.S., 2012. Computational methods in subsurface flow. academic press.

Idris, N., Deng, X., 2012. The retracking technique on multi-peak and quasi-specular waveforms for Jason-1 and Jason-2 missions near the coast. Marine Geodesy 35, 217–237. doi:10.1080/01490419.2012.718679.

Ishikawa, H., 2003. Exact optimization for Markov random fields with convex priors. IEEE transactions on pattern analysis and machine intelligence 25, 1333–1336. doi:10.1109/TPAMI.2003.1233908.

Ishitsuka, Y., Gleason, C.J., Hagemann, M.W., Beighley, E., Allen, G.H., Feng, D., Lin, P., Pan, M., Andreadis, K., Pavelsky, T.M., 2021. Combining Optical Remote Sensing, McFLI Discharge Estimation, Global Hydrologic Modeling, and Data Assimilation to Improve Daily Discharge Estimates Across an Entire Large Watershed. Water Resources Research 57, e2020WR027794. doi:https://doi.org/10.1029/2020WR027794.

Jacob, T., Wahr, J., Pfeffer, W.T., Swenson, S., 2012. Recent contributions of glaciers and ice caps to sea level rise. Nature 482, 514–518. doi:10.1038/nature10847.

Jäggi, A., Weigelt, M., Flechtner, F., Güntner, A., Mayer-Gürr, T., Martinis, S., Bruinsma, S., Flury, J., Bourgogne, S., Steffen, H., et al., 2019. European Gravity Service for Improved Emergency Management (EGSIEM)—from concept to implementation. Geophysical journal international 218, 1572–1590. doi:10.1093/gji/ggz238.

Janiesch, C., Zschech, P., Heinrich, K., 2021. Machine learning and deep learning. Electronic Markets 31, 685–695. doi:10.1007/s12525-021-00475-2.

Jaramillo, F., Aminjafari, S., Castellazzi, P., Fleischmann, A., Fluet-Chouinard, E., Hashemi, H., Hubinger, C., Martens, H.R., Papa, F., Schöne, T., Tarpanelli, A., Virkki, V., Wang-Erlandsson, L., Abarca-del Rio, R., Borsa, A., Destouni, G., Di Baldassarre, G., Moore, M.L., Posada-Marín, J.A., Wdowinski, S., Werth, S., Allen, G.H., Argus, D., Elmi, O., Fenoglio, L., Frappart, F., Huggins, X., Kalantari, Z., Munier, S., Palomino-Ángel, S., Robinson, A., Rubiano, K., Siles, G., Simard, M., Song, C., Spence, C., Tourian, M.J., Wada, Y., Wang, C., Wang, J., Yao, F., Berghuijs, W.R., Cretaux, J.F., Famiglietti, J., Fassoni-Andrade, A., Fayne, J.V., Girard, F., Kummu, M., Larson, K.M., Marañon, M., Moreira, D.M., Nielsen, K., Pavelsky, T., Pena, F., Reager, J.T., Rulli, M.C., Salazar, J.F., 2024. The potential of hydrogeodesy to address water-related and sustainability challenges. Water Resources Research 60, e2023WR037020. doi:https://doi.org/10.1029/2023WR037020. e2023WR037020 2023WR037020.

Jeffreys, H., 1961. Theory of Probability. 3rd ed., Oxford University Press.

Jekeli, C., 1981. Alternative methods to smooth the Earth's gravity field. Technical Report.

Jin, S., Komjathy, A., 2010. GNSS reflectometry and remote sensing: New objectives and results. Advances in Space Research 46, 111–117. doi:10.1016/j.asr.2010.01.014.

Johnson, N.L., Kotz, S., Balakrishnan, N., 1995. Continuous univariate distributions, volume 2. volume 289. John wiley & sons.

Jones, P.B., Walker, G.D., Harden, R.W., McDaniels, L.L., 1963. The development of science of hydrology. Texas Water Comission. URL: https://www.twdb.texas.gov/publications/reports/other_reports/doc/Circ63-03.pdf.

Joodaki, G., Wahr, J., Swenson, S., 2014. Estimating the human contribution to groundwater depletion in the Middle East, from GRACE data, land surface models, and well observations. Water Resources Research 50, 2679–2692. doi:10.1002/2013WR014633.

Jordan, M., Ghahramani, Z., Jaakkola, T., Saul, L., 1999. An introduction to variational methods for graphical models. Machine Learning 37, 183–233. doi:10.1007/978-94-011-5014-9_5.

Jung, M., Koirala, S., Weber, U., Ichii, K., Gans, F., Camps-Valls, G., Papale, D., Schwalm, C., Tramontana, G., Reichstein, M., 2019. The FLUXCOM ensemble of global land-atmosphere energy fluxes. Scientific data 6, 1–14. doi:10.1038/s41597-019-0076-8.

Jyolsna, P.J., Kambhammettu, B.V.N.P., Gorugantula, S., 2021. Application of random forest and multi-linear regression methods in downscaling grace derived groundwater storage changes. Hydrological Sciences Journal 66, 874–887. doi:10.1080/02626667.2021.1896719.

Kalman, R., 1960. A new approach to linear filtering and prediction problems. Journal of Basic Engineering 82, 35–45. doi:10.1115/1.3662552.

Karamvasis, K., Karathanassi, V., 2023. Soil moisture estimation from sentinel-1 interferometric observations over arid regions. Computers & Geosciences 178, 105410. doi:10.1016/j.cageo.2023.105410.

Karegar, M.A., Kusche, J., Geremia-Nievinski, F., Larson, K.M., 2022. Raspberry Pi Reflector (RPR): A Low-Cost Water-Level Monitoring System Based on GNSS Interferometric Reflectometry. Water Resources Research 58, e2021WR031713.

Karegar, M.A., Larson, K.M., Kusche, J., Dixon, T.H., 2020. Novel quantification of shallow sediment compaction by GPS interferometric reflectometry and implications for flood susceptibility. Geophysical Research Letters 47, e2020GL087807. doi:10.1029/2020GL087807.

Karimzadeh, S., Mastuoka, M., 2017. Building damage assessment using multisensor dual-polarized synthetic aperture radar data for the 2016 M 6.2 Amatrice Earthquake, Italy. Remote Sensing 9, 330. doi:10.3390/rs9040330.

Karpatne, A., Atluri, G., Faghmous, J.H., Steinbach, M., Banerjee, A., Ganguly, A., Shekhar, S., Samatova, N.F., Kumar, V., 2017. Machine learning for the geosciences: Challenges and opportunities. IEEE Transactions on Knowledge and Data Engineering 29, 2294–2313.

Khaki, M., Hendricks Franssen, H.J., Han, S.C., 2020. Multi-mission satellite remote sensing data for improving land hydrological models via data assimilation. Scientific Reports 10, 18791. doi:10.1038/s41598-020-75710-5.

Kindermann, R., Snell, J.L., 1980. Markov Random Fields and Their Applications. American Mathematical Society. doi:10.1090/conm/001.

Klein, I., Gessner, U., Dietz, A.J., Kuenzer, C., 2017. Global WaterPack–A 250 m resolution dataset revealing the daily dynamics of global inland water bodies. Remote sensing of environment 198, 345–362. doi:10.1016/j.rse.2017.06.045.

Koch, K.R., 2007. Introduction to Bayesian statistics. Springer Science & Business Media.

Kolmogorov, V., Zabih, R., 2002. Multi-camera scene reconstruction via graph cuts, in: European conference on computer vision, Springer. pp. 82–96. doi:10.1007/3-540-47977-5_6.

Kolmogorov, V., Zabin, R., 2004. What energy functions can be minimized via graph cuts? IEEE Transactions on Pattern Analysis and Machine Intelligence 26, 147–159. doi:10.1109/TPAMI.2004.1262177.

Koster, R.D., Mahanama, S.P., 2012. Land surface controls on hydroclimatic means and variability. Journal of Hydrometeorology 13, 1604–1620. doi:10.1175/JHM-D-12-050.1.

Kschischang, F.R., Frey, B.J., Loeliger, H.A., 2001. Factor Graphs and the Sum-Product Algorithm. IEEE Transactions on Information Theory doi:10.1109/18.910572.

Kundzewicz, Z.W., Mata, L.J., Arnell, N.W., Döll, P., Kabat, P., Jiménez, B., Miller, K.A., Oki, T., Sen, Z., Shiklomanov, I.A., 2007. Freshwater resources and their management. Climate Change 2007: Impacts, Adaptation and Vulnerability , 173–210.

Kurtenbach, E., 2011. Entwicklung eines Kalman-Filters zur Bestimmung kurzzeitiger Variationen des Erdschwerefeldes aus Daten der Satellitenmission GRACE. Ph.D. thesis. University of Bonn.

Kurtenbach, E., Mayer-Gürr, T., Eicker, A., 2009. Deriving daily snapshots of the Earth's gravity field from GRACE L1B data using Kalman filtering. Geophysical Research Letters 36, n/a–n/a. doi:10.1029/2009GL039564.

Kusche, J., 2003. A monte-carlo technique for weight estimation in satellite geodesy. Journal of Geodesy 76, 641–652. doi:10.1007/s00190-002-0302-5.

Kusche, J., 2007. Approximate decorrelation and non-isotropic smoothing of time-variable GRACE-type gravity field models. Journal of Geodesy 81, 733–749. doi:10.1007/s00190-007-0143-3.

Kusche, J., Schmidt, R., Petrovic, S., Rietbroek, R., 2009. Decorrelated GRACE time-variable gravity solutions by GFZ, and their validation using a hydrological model. Journal of Geodesy 83, 903–913. doi:10.1007/s00190-009-0308-3.

Lafferty, J.D., McCallum, A., Pereira, F.C.N., 2001. Conditional Random Fields: Probabilistic Models for Segmenting and Labeling Sequence Data, in: Proceedings of the Eighteenth International Conference on Machine Learning (ICML). URL: https://repository.upenn.edu/handle/20.500.14332/6188.

Larnier, K., Monnier, J., Garambois, P.A., Verley, J., 2021. River discharge and bathymetry estimation from SWOT altimetry measurements. Inverse problems in science and engineering 29, 759–789. doi:10.1080/17415977.2020.1803858.

Larson, K.M., 2016. GPS interferometric reflectometry: applications to surface soil moisture, snow depth, and vegetation water content in the western United States. Wiley Interdisciplinary Reviews: Water 3, 775–787. doi:10.1002/wat2.1167.

Larson, K.M., Gutmann, E.D., Zavorotny, V.U., Braun, J.J., Williams, M.W., Nievinski, F.G., 2008. Can we measure snow depth with GPS receivers? Geophysical Research Letters 36. doi:10.1029/2009GL039430.

Lauritzen, S.L., 1996. Graphical Models. Oxford University Press.

Lawrence, D.M., Fisher, R.A., Koven, C.D., Oleson, K.W., Swenson, S.C., Bonan, G., Collier, N., Ghimire, B., van Kampenhout, L., Kennedy, D., et al., 2019. The Community Land Model version 5: Description of new features, benchmarking, and impact of forcing uncertainty. Journal of Advances in Modeling Earth Systems 11, 4245–4287. doi:10.1029/2018MS001583.

Le Gac, S., Boy, F., Blumstein, D., Lasson, L., Picot, N., 2021. Benefits of the Open-Loop Tracking Command (OLTC): Extending conventional nadir altimetry to inland waters monitoring. Advances in Space Research 68, 843–852. doi:10.1016/j.asr.2019.10.031.

Lee, H., Durand, M., Jung, H.C., Alsdorf, D., Shum, C., Sheng, Y., 2010. Characterization of surface water storage changes in Arctic lakes using simulated SWOT measurements. International Journal of Remote Sensing 31, 3931–3953. doi:10.1080/01431161.2010.483494.

Legresy, B., Papa, F., Remy, F., Vinay, G., Van den Bosch, M., Zanife, O.Z., 2005. ENVISAT radar altimeter measurements over continental surfaces and ice caps using the ICE-2 retracking algorithm. Remote Sensing of Environment 95, 150–163. doi:10.1016/j.rse.2004.11.018.

Lettenmaier, D.P., 2006. Observations of the global water cycle–global monitoring networks. Encyclopedia of hydrological sciences doi:10.1002/0470848944.hsa181.

Lettenmaier, D.P., Famiglietti, J.S., 2006. Water from on high. Nature 444, 562–563. doi:10.1038/444562a.

Li, B., Rodell, M., Kumar, S., Beaudoing, H.K., Getirana, A., Zaitchik, B.F., de Goncalves, L.G., Cossetin, C., Bhanja, S., Mukherjee, A., et al., 2019. Global GRACE data assimilation for groundwater and drought monitoring: Advances and challenges. Water Resources Research 55, 7564–7586. doi:10.1029/2018WR024618.

Li, S.Z., 2009. Markov random field modeling in image analysis. Springer Science & Business Media.

Li, X., Liu, F., 2025. A mathematical comparison of data assimilation and machine learning in earth system state estimation from a bayesian inference viewpoint. Information Geography 1, 100001. doi:https://doi.org/10.1016/j.infgeo.2025.100001.

Lindström, G., Johansson, B., Persson, M., Gardelin, M., Bergström, S., 1997. Development and test of the distributed HBV-96 hydrological model. Journal of hydrology 201, 272–288. doi:10.1016/S0022-1694(97)00041-3.

Lobry, S., Denis, L., Williams, B., Fjørtoft, R., Tupin, F., 2019. Water detection in SWOT HR images based on multiple Markov random fields. IEEE Journal of Selected Topics in Applied Earth Observations and Remote Sensing 12, 4315–4326. doi:10.1109/JSTARS.2019.2948788.

Long, D., Longuevergne, L., Scanlon, B.R., 2015. Global analysis of approaches for deriving total water storage changes from grace satellites. Water Resources Research 51, 2574–2594. doi:10.1002/2014WR016853.

Long, D., Pan, Y., Zhou, J., Chen, Y., Hou, X., Hong, Y., Scanlon, B.R., Longuevergne, L., 2017. Global analysis of spatiotemporal variability in merged total water storage changes using multiple grace products and global hydrological models. Remote Sensing of Environment 192, 198–216. doi:https://doi.org/10.1016/j.rse.2017.02.011.

Long, D., Scanlon, B.R., Longuevergne, L., Sun, A.Y., Fernando, D.N., Save, H., 2013. GRACE satellite monitoring of large depletion in water storage in response to the 2011 drought in Texas. Geophysical Research Letters 40, 3395–3401. doi:https://doi.org/10.1002/grl.50655.

Lorenz, C., Devaraju, B., Tourian, M.J., Riegger, J., Kunstmann, H., Sneeuw, N., 2014. Large-scale runoff from landmasses: a global assessment of the closure of the hydrological and atmospheric water balances. Journal of Hydrometeorology 15, 2111–2139. doi:10.1175/JHM-D-13-0157.1.

Lorenz, C., Kunstmann, H., 2012. The hydrological cycle in three state-of-the-art reanalyses: Intercomparison and performance analysis. Journal of Hydrometeorology 13, 1397–1420. doi:10.1175/JHM-D-11-088.1.

Lorenz, C., Tourian, M.J., Devaraju, B., Sneeuw, N., Kunstmann, H., 2015. Basin-scale runoff prediction: An Ensemble Kalman Filter framework based on global hydrometeorological data sets. Water Resources Research 51. doi:10.1002/2014WR016794.

Lyard, F., Lefevre, F., Letellier, T., Francis, O., 2006. Modelling the global ocean tides: modern insights from FES2004. Ocean Dynamics 56, 394–415. doi:10.1007/s10236-006-0086-x.

Madsen, S.N., Zebker, H.A., 1998. Imaging radar interferometry, in: Principles & Applications of Imaging Radar, Manual of Remote Sensing. Wiley Online Library. volume 3, pp. 359–380. URL: https://cir.nii.ac.jp/crid/1571417125318934656.

Maidment, D.R., 1993. Handbook of hydrology. McGraw-Hill.

Maillard, P., Bercher, N., Calmant, S., 2015. "New processing approaches on the retrieval of water levels in Envisat and SARAL radar altimetry over rivers: A case study of the Sao Francisco River, Brazil ". Remote Sensing of Environment 156, 226 – 241. doi:10.1016/j.rse.2014.09.027.

Mariethoz, G., Renard, P., Caers, J., 2010. Bayesian inverse problem and optimization with iterative spatial resampling. Water Resources Research 46. doi:10.1029/2010WR009274.

Martens, B., Miralles, D.G., Lievens, H., Van Der Schalie, R., De Jeu, R.A., Fernández-Prieto, D., Beck, H.E., Dorigo, W.A., Verhoest, N.E., 2017. GLEAM v3: Satellite-based land evaporation and root-zone soil moisture. Geoscientific Model Development 10, 1903–1925. doi:10.5194/gmd-10-1903-2017.

Martin, T.V., Brenner, A.C., Zwally, H.J., Bindschadler, R.A., 1983. Analysis and retracking of continental ice sheet radar altimeter waveforms. Journal of Geophysical Research 88, 1608–1616. doi:10.1029/JC088iC03p01608.

Martinis, S., Kersten, J., Twele, A., 2015. A fully automated TerraSAR-X based flood service. ISPRS Journal of Photogrammetry and Remote Sensing 104, 203–212. doi:10.1016/j.isprsjprs.2014.07.014.

Massonnet, D., Feigl, K.L., 1998. Radar interferometry and its application to changes in the earth's surface. Reviews of Geophysics 36, 441–500. doi:10.1029/97RG03139.

Massonnet, D., Rossi, M., Carmona, C., Adragna, F., Peltzer, G., Feigl, K., Rabaute, T., 1993. Displacement field of the Landers earthquake mapped by radar interferometry. Nature 364, 138–142. doi:10.1038/364138a0.

McCabe, M.F., Rodell, M., Alsdorf, D.E., Miralles, D.G., Uijlenhoet, R., Wagner, W., Lucieer, A., Houborg, R., Verhoest, N.E.C., Franz, T.E., Shi, J., Gao, H., Wood, E.F., 2017. The Future of Earth Observation in Hydrology. Hydrology and Earth System Sciences 21, 3879–3914. doi:10.5194/hess-21-3879-2017.

McFeeters, S.K., 2013. Using the Normalized Difference Water Index (NDWI) within a Geographic Information System to Detect Swimming Pools for Mosquito Abatement: A Practical Approach. Remote Sensing 5, 3544. doi:10.3390/rs5073544.

McMillan, H., Jackson, B., Clark, M., Kavetski, D., Woods, R., 2011. Rainfall uncertainty in hydrological modelling: An evaluation of multiplicative error models. Journal of Hydrology 400, 83–94. doi:10.1016/j.jhydrol.2011.01.026.

Tromp-van Meerveld, H., McDonnell, J.J., 2006. On the interrelations between topography, soil depth, soil moisture, transpiration rates and species distribution at the hillslope scale. Advances in water resources 29, 293–310. doi:10.1016/.advwatres.2005.02.016.

Mehrnegar, N., Jones, O., Singer, M.B., Schumacher, M., Bates, P., Forootan, E., 2020. Comparing global hydrological models and combining them with grace by dynamic model data averaging (dmda). Advances in Water Resources 138, 103528. doi:10.1016/j.advwatres.2020.103528.

Mehrnegar, N., Jones, O., Singer, M.B., Schumacher, M., Jagdhuber, T., Scanlon, B.R., Rateb, A., Forootan, E., 2021. Exploring groundwater and soil water storage changes across the CONUS at 12.5 km resolution by a Bayesian integration of GRACE data into W3RA. Science of the Total Environment 758, 143579. doi:10.1016/j.scitotenv.2020.143579.

Mehrnegar, N., Schumacher, M., Jagdhuber, T., Forootan, E., 2023. Making the best use of grace, grace-fo and smap data through a constrained bayesian data-model integration. Water Resources Research 59, e2023WR034544. doi:10.1029/2023WR034544.

Merchant, M.A., 2020. Classifying open water features using optical satellite imagery and an object-oriented convolutional neural network. Remote Sensing Letters 11, 1127–1136. doi:10.1080/2150704X.2020.1825869.

Metropolis, N., Rosenbluth, A., Rosenbluth, M., Teller, A., Teller, E., 1953. Equation of state calculations by fast computing machines. The Journal of Chemical Physics 21, 1087–1092. doi:10.1063/1.1699114.

Milillo, P., Rignot, E., Mouginot, J., Scheuchl, B., Morlighem, M., Li, X., Salzer, J.T., 2017. On the short-term grounding zone dynamics of Pine Island Glacier, West Antarctica, observed with COSMO-SkyMed interferometric data. Geophysical Research Letters 44, 10–436. doi:10.1002/2017GL074320.

Miro, M.E., Famiglietti, J.S., 2018. Downscaling GRACE remote sensing datasets to high-resolution groundwater storage change maps of California's Central Valley. Remote Sensing 10, 143. doi:10.3390/rs10010143.

Mo, S., Zhong, Y., Forootan, E., Mehrnegar, N., Yin, X., Wu, J., Feng, W., Shi, X., 2022. Bayesian convolutional neural networks for predicting the terrestrial water storage anomalies during GRACE and GRACE-FO gap. Journal of Hydrology 604, 127244. doi:10.1016/j.jhydrol.2021.127244.

Modaresi, F., Araghi, A., 2023. Projecting future reference evapotranspiration in iran based on cmip6 multi-model ensemble. Theoretical and Applied Climatology 153, 101–112. doi:10.1007/s00704-023-04465-6.

Montenbruck, O., Hackel, S., Wermuth, M., Zangerl, F., 2021. Sentinel-6A precise orbit determination using a combined GPS/Galileo receiver. Journal of Geodesy 95, 109. doi:10.1007/s00190-021-01563-z.

Moreira, D.M., Calmant, S., Perosanz, F., Xavier, L., Rotunno Filho, O.C., Seyler, F., Monteiro, A.C., 2016. Comparisons of observed and modeled elastic responses to hydrological loading in the amazon basin. Geophysical Research Letters 43, 9604–9610. doi:10.1002/2016GL070265.

Moritz, H., 1989. Advanced physical geodesy. 2. ed., repr. from the 1. ed. ed., Wichmann, Karlsruhe.

Müller Schmied, H., Cáceres, D., Eisner, S., Flörke, M., Herbert, C., Niemann, C., Peiris, T.A., Popat, E., Portmann, F.T., Reinecke, R., et al., 2021. The global water resources and use model WaterGAP v2. 2d: Model description and evaluation. Geoscientific Model Development 14, 1037–1079. doi:10.5194/gmd-14-1037-2021.

Murphy, K.P., 2002. Dynamic Bayesian Networks: Representation, Inference and Learning. Ph.D. thesis. University of California, Berkeley.

Neal, J., Schumann, G., Bates, P., Buytaert, W., Matgen, P., Pappenberger, F., 2009. A data assimilation approach to discharge estimation from space. Hydrological Processes: An International Journal 23, 3641–3649. doi:10.1002/hyp.7518.

Neal, R., 2003. Slice sampling. The Annals of Statistics 31, 705–767. doi:10.1214/aos/1056562461.

Neal, R.M., 2011. MCMC using Hamiltonian dynamics, in: Handbook of Markov Chain Monte Carlo. CRC Press, pp. 113–162. doi:10.1201/b10905.

Nelsen, R.B., 2007. An introduction to copulas. Springer Science & Business Media.

Nerem, R.S., Eanes, R.J., Thompson, P.F., Chen, J.L., 2000. Observations of annual variations of the Earth's gravitational field using satellite laser ranging and geophysical models. Geophysical Research Letters 27, 1783–1786. doi:10.1029/1999GL008440.

Nielsen, K., Zakharova, E., Tarpanelli, A., Andersen, O.B., Benveniste, J., 2022. River levels from multi mission altimetry, a statistical approach. Remote Sensing of Environment 270, 112876. doi:10.1016/j.rse.2021.112876.

Niemeier, W., 2008. Ausgleichungsrechnung: Statistische Auswertemethoden. Walter de Gruyter.

Nievinski, F.G., Larson, K.M., 2014. Inverse modeling of GPS multipath for snow depth estimation—Part II: Application and validation. IEEE transactions on geoscience and remote sensing 52, 6564–6573. doi:10.1109/TGRS.2013.2297681.

Normandin, C., Frappart, F., Diepkilé, A.T., Marieu, V., Mougin, E., Blarel, F., Lubac, B., Braquet, N., Ba, A., 2018. Evolution of the performances of radar altimetry missions from ERS-2 to Sentinel-3A over the Inner Niger Delta. Remote Sensing 10, 833. doi:10.3390/rs10060833.

Oki, T., Entekhabi, D., Harrold, T.I., 1999. The global water cycle. Global energy and water cycles 10, 27. doi:10.1029/150GM18.

Oleson, K., Lawrence, D., Lombardozzi, D., Wieder, D., 2019. CLM land-only release. doi:10.5065/d6154fwh. accessed: 2021-05-30.

Orth, R., Seneviratne, S.I., 2013. Predictability of soil moisture and streamflow on subseasonal timescales: A case study. Journal of Geophysical Research: Atmospheres 118, 10–963. doi:10.1002/jgrd.50846,2013.

Pail, R., Bingham, R., Braitenberg, C., Eicker, A., Horwath, M., Ivins, E., Longuevergne, L., Panet, I., Wouters, B., Balsamo, G., et al., 2015. Observing Mass Transport to Understand Global Change and and to benefit Society: Science and User Needs-An international multidisciplinary initiative for IUGG .

Pail, R., Fecher, T., Barnes, D., Factor, J., Holmes, S., Gruber, T., Zingerle, P., 2018. Short note: the experimental geopotential model XGM2016. Journal of geodesy 92, 443–451. doi:10.1007/s00190-017-1070-6.

Paiva, R.C.D., Collischonn, W., Bonnet, M.P., de Gonçalves, L.G.G., Calmant, S., Getirana, A., Santos da Silva, J., 2013. Assimilating In Situ and Radar Altimetry Data into a Large-Scale Hydrologic-Hydrodynamic Model for Streamflow Forecast in the Amazon. Hydrology and Earth System Sciences 17, 2929–2946. doi:10.5194/hess-17-2929-2013.

Palmer, S.J., Shepherd, A., Sundal, A., Rinne, E., Nienow, P., 2010. InSAR observations of ice elevation and velocity fluctuations at the Flade Isblink ice cap, eastern North Greenland. Journal of Geophysical Research: Earth Surface 115. doi:10.1029/2010JF001686.

Papa, F., Durand, F., Rossow, W.B., Rahman, A., Bala, S.K., 2010a. Satellite altimeter-derived monthly discharge of the Ganga-Brahmaputra River and its seasonal to interannual variations from 1993 to 2008. Journal of Geophysical Research: Oceans 115. doi:10.1029/2009JC006075.

Papa, F., Frappart, F., 2021. Surface water storage in rivers and wetlands derived from satellite observations: a review of current advances and future opportunities for hydrological sciences. Remote Sensing 13, 4162. doi:10.3390/rs13204162.

Papa, F., Prigent, C., Aires, F., Jimenez, C., Rossow, W.B., Matthews, E., 2010b. Interannual variability of surface water extent at the global scale, 1993–2004. Journal of Geophysical Research: Atmospheres 115. doi:10.1029/2009JD012674.

Papa, F., Prigent, C., Durand, F., Rossow, W.B., 2006a. Wetland dynamics using a suite of satellite observations: A case study of application and evaluation for the Indian Subcontinent. Geophysical Research Letters 33, L08401. doi:10.1029/2006GL025767.

Papa, F., Prigent, C., Rossow, W., Legresy, B., Remy, F., 2006b. Inundated wetland dynamics over boreal regions from remote sensing: The use of Topex-Poseidon dual-frequency radar altimeter observations. International Journal of Remote Sensing 27, 4847–4866. doi:10.1080/01431160600675887.

Paris, A., Dias de Paiva, R., Santos da Silva, J., Medeiros Moreira, D., Calmant, S., Garambois, P.A., Collischonn, W., Bonnet, M.P., Seyler, F., 2016. Stage-discharge rating curves based on satellite altimetry and modeled discharge in the Amazon basin. Water Resources Research 52, 3787–3814. doi:10.1002/2014WR016618.

Passaro, M., Cipollini, P., Vignudelli, S., Quartly, G.D., Snaith, H.M., 2014. ALES: A multi-mission adaptive subwaveform retracker for coastal and open ocean altimetry. Remote Sensing of Environment 145, 173–189. doi:10.1016/j.rse.2014.02.008.

Passaro, M., Rautiainen, L., Dettmering, D., Restano, M., Hart-Davis, M.G., Schlembach, F., Särkkä, J., Müller, F.L., Schwatke, C., Benveniste, J., 2022. Validation of an empirical subwaveform retracking strategy for sar altimetry. Remote Sensing 14, 4122. doi:10.3390/rs14164122.

Passaro, M., Rose, S.K., Andersen, O.B., Boergens, E., Calafat, F.M., Dettmering, D., Benveniste, J., 2018. ALES+: Adapting a homogenous ocean retracker for satellite altimetry to sea ice leads, coastal and inland waters. Remote Sensing of Environment 211, 456–471. doi:10.1016/j.rse.2018.02.074.

Pavelsky, T.M., 2014. Using width-based rating curves from spatially discontinuous satellite imagery to monitor river discharge. Hydrological Processes 28, 3035–3040. doi:10.1002/hyp.10157.

Pearl, J., 1988. Probabilistic Reasoning in Intelligent Systems: Networks of Plausible Inference. Morgan Kaufmann. doi:10.1016/C2009-0-27609-4.

Pecora, S., Lins, H.F., 2020. E-monitoring the nature of water. Hydrological sciences journal 65, 683–698. doi:10.1080/02626667.2020.1724296.

Pekel, J.F., Cottam, A., Gorelick, N., Belward, A.S., 2016. High-resolution mapping of global surface water and its long-term changes. Nature 540, 418–422. doi:10.1038/nature20584.

Peral, E., Esteban-Fernández, D., Rodríguez, E., McWatters, D., De Bleser, J.W., Ahmed, R., Chen, A., Slimko, E., Somawardhana, R., Knarr, K., et al., 2024. KaRIn, the Ka-Band Radar Interferometer of the SWOT Mission: Design and In-Flight Performance. IEEE Transactions on Geoscience and Remote Sensing doi:10.1109/TGRS.2024.3405343.

Pereira, L.S., Perrier, A., Allen, R.G., Alves, I., 1999. Evapotranspiration: concepts and future trends. Journal of irrigation and drainage engineering 125, 45–51. doi:10.1061/(ASCE)0733-9437(1999)125:2(45).

Pham-Duc, B., Prigent, C., Aires, F., 2017. Surface water monitoring within Cambodia and the Vietnamese Mekong Delta over a year, with Sentinel-1 SAR observations. Water 9, 366. doi:10.3390/w9060366.

Polcher, J., Bertrand, N., Biemans, H., Clark, D.B., Floerke, M., Gedney, N., Gerten, D., Stacke, T., van Vliet, M., Voss, F., 2011. Improvements in hydrological processes in general hydrological models and land surface models within WATCH.

Pomeroy, J., Essery, R., Toth, B., 2004. Implications of spatial distributions of snow mass and melt rate for snow-cover depletion: observations in a subarctic mountain catchment. Annals of Glaciology 38, 195–201. doi:10.3189/172756404781814744.

Prigent, C., Papa, F., Aires, F., Rossow, W.B., Matthews, E., 2007. Global inundation dynamics inferred from multiple satellite observations, 1993–2000. Journal of Geophysical Research: Atmospheres 112. doi:10.1029/2006JD007847.

Radić, V., Hock, R., 2014. Glaciers in the earth's hydrological cycle: assessments of glacier mass and runoff changes on global and regional scales. Surveys in Geophysics 35, 813–837. doi:10.1007/s10712-013-9262-y.

Raj, A., Zabih, R., 2005. A graph cut algorithm for generalized image deconvolution, in: Tenth IEEE International Conference on Computer Vision (ICCV'05) Volume 1, IEEE. pp. 1048–1054. doi:10.1109/ICCV.2005.8.

Raney, R.K., 1998. The delay/Doppler radar altimeter. IEEE Transactions on Geoscience and Remote Sensing 36, 1578–1588. doi:10.1109/36.718861.

Raney, R.K., Phalippou, L., 2011. The future of coastal altimetry. Coastal altimetry , 535–560.

Ranndal, H., Sigaard Christiansen, P., Kliving, P., Baltazar Andersen, O., Nielsen, K., 2021. Evaluation of a Statistical Approach for Extracting Shallow Water Bathymetry Signals from ICESat-2 ATL03 Photon Data. Remote Sensing 13. doi:10.3390/rs13173548.

Rateb, A., Sun, A., Scanlon, B.R., Save, H., Hasan, E., 2022. Reconstruction of grace mass change time series using a bayesian framework. Earth and Space Science 9, e2021EA002162. doi:10.1029/2021EA002162.

Ray, C., Martin-Puig, C., Clarizia, M.P., Ruffini, G., Dinardo, S., Gommenginger, C., Benveniste, J., 2014. SAR altimeter backscattered waveform model. IEEE Transactions on Geoscience and Remote Sensing 53, 911–919. doi:10.1109/TGRS.2014.2330423.

Ray, R.D., Egbert, G.D., Erofeeva, S.Y., 2011. Tide predictions in shelf and coastal waters: status and prospects. Ocean Dynamics 61, 349–379. doi:10.1007/978-3-642-12796-0_8.

Reager, J., Thomas, B., Famiglietti, J., 2014. River basin flood potential inferred using GRACE gravity observations at several months lead time. Nature Geoscience 7, 588–592. doi:10.1038/ngeo2203.

Reager, J.T., Thomas, A.C., Sproles, E.A., Rodell, M., Beaudoing, H.K., Li, B., Famiglietti, J.S., 2015. Assimilation of GRACE Terrestrial Water Storage Observations into a Land Surface Model for the Assessment of Regional Flood Potential. Remote Sensing 7, 14663. doi:10.3390/rs71114663.

Reichstein, M., Camps-Valls, G., Stevens, B., Jung, M., Denzler, J., Carvalhais, N., Prabhat, 2019. Deep learning and process understanding for data-driven Earth system science. Nature 566, 195–204. doi:10.1038/s41586-019-0912-1.

Reigber, C., Lühr, H., Grunwaldt, L., Förste, C., König, R., Massmann, H., Falck, C., 2006. CHAMP mission 5 years in orbit. Observation of the Earth system from space , 3–15doi:10.1007/3-540-29522-4_1.

Ricker, R., Hendricks, S., Helm, V., Skourup, H., Davidson, M., 2014. Sensitivity of CryoSat-2 Arctic sea-ice freeboard and thickness on radar-waveform interpretation. The Cryosphere 8, 1607–1622. doi:10.5194/tc-8-1607-2014.

Riegger, J., Tourian, M., Devaraju, B., Sneeuw, N., 2012. Analysis of grace uncertainties by hydrological and hydro-meteorological observations. Journal of Geodynamics 59, 16–27. doi:10.1016/j.jog.2012.02.001.

Rius, A., Alonso-Arroyo, A., Camps, A., 2017. Soil moisture estimation using GNSS-R techniques: Experimental results over a bare soil field. IEEE Journal of Selected Topics in Applied Earth Observations and Remote Sensing 10, 5033–5044. doi:10.1109/TGRS.2009.2030672.

Roberts, G., Tweedie, R., 1996. Exponential convergence of Langevin distributions and their discrete approximations. Bernoulli 2, 341–363.

Rodell, M., Chen, J., Kato, H., Famiglietti, J., Nigro, J., Wilson, C., 2006. Estimating groundwater storage changes in the Mississippi River basin (USA) using GRACE. Hydrogeology Journal 15, 159–166. doi:10.1007/s10040-006-0103-7.

Rodríguez, E., 1988. Altimetry for non-Gaussian oceans: Height biases and estimation of parameters. Journal of Geophysical Research: Oceans 93, 14107–14120. doi:10.1029/jc093ic11p14107.

Rodriguez, E., Fernandez, D.E., Peral, E., Chen, C.W., De Bleser, J.W., Williams, B., 2017. Wide-swath altimetry: A review. Satellite altimetry over oceans and land surfaces , 71–112doi:10.1201/9781315151779-2.

Rodriguez-Alvarez, N., Bosch-Lluis, X., Camps, A., Vall-llossera, M., Valencia, E., Marchan-Hernandez, J.F., Ramos-Perez, I., 2009. Soil Moisture Retrieval Using GNSS-R Techniques: Experimental Results Over a Bare Soil Field. IEEE Transactions on Geoscience and Remote Sensing 47, 3616–3624. doi:10.1109/TGRS.2009.2030672.

Rodriguez-Alvarez, N., Munoz-Martin, J.F., Morris, M., 2023. Latest advances in the global navigation satellite system—reflectometry (GNSS-R) field. Remote Sensing 15, 2157. doi:10.3390/rs15082157.

Roscher, R., Uebbing, B., Kusche, J., 2017. STAR: Spatio-temporal altimeter waveform retracking using sparse representation and conditional random fields. Remote sensing of Environment 201, 148–164. doi:10.1016/j.rse.2017.07.024.

Ruane, A.C., Goldberg, R., Chryssanthacopoulos, J., 2015. Climate forcing datasets for agricultural modeling: Merged products for gap-filling and historical climate series estimation. Agricultural and Forest Meteorology 200, 233–248. doi:10.1016/j.agrformet.2014.09.016.

Rubin, D., 1981. The Bayesian bootstrap. The Annals of Statistics 9, 130–134. URL: http://www.jstor.org/stable/2240875.

Rubinstein, M., 2020. maxflow matlab package. https://www.mathworks.com/matlabcentral/fileexchange/21310-maxflow), MATLAB Central File Exchange. Accessed: February 20, 2024.

Rubinstein, R., 1981. Simulation and the Monte Carlo Method. John Wiley & Sons.

Rudenko, S., Dettmering, D., Zeitlhöfler, J., Alkahal, R., Upadhyay, D., Bloßfeld, M., 2023. Radial orbit errors of contemporary altimetry satellite orbits. Surveys in Geophysics 44, 705–737. doi:10.1007/s10712-022-09758-5.

Ruf, C.S., et al., 2016. CYGNSS: Enabling the future of hurricane prediction. IEEE Geoscience and Remote Sensing Magazine 4, 27–37. doi:10.1109/MGRS.2013.2260911.

Ruffini, n.G., Soulat, F., Caparrini, M., Germain, O., Martín-Neira, M., 2004. The Eddy Experiment: Accurate GNSS-R ocean altimetry from low altitude aircraft. Geophysical research letters 31. doi:10.1029/2004GL019994.

Rummel, R., 2010. The interdisciplinary role of space geodesy—Revisited. Journal of Geodynamics 49, 112–115. doi:10.1007/BFb0049637.

Saemian, P., Elmi, O., Stroud, M., Riggs, R., Kitambo, B.M., Papa, F., Allen, G.H., Tourian, M.J., 2025. Satellite altimetry-based extension of global-scale in situ river discharge measurements (saem). Earth System Science Data 17, 2063–2085. doi:10.5194/essd-17-2063-2025.

Saemian, P., Elmi, O., Vishwakarma, B., Tourian, M., Sneeuw, N., 2020. Analyzing the Lake Urmia restoration progress using ground-based and spaceborne observations. Science of The Total Environment 739, 139857. doi:10.1016/j.scitotenv.2020.139857.

Saemian, P., Tourian, M.J., AghaKouchak, A., Madani, K., Sneeuw, N., 2022. How much water did Iran lose over the last two decades? Journal of Hydrology: Regional Studies 41, 101095. doi:https://doi.org/10.1016/j.ejrh.2022.101095.

Saemian, P., Tourian, M.J., Elmi, O., Sneeuw, N., AghaKouchak, A., 2024. A probabilistic approach to characterizing drought using satellite gravimetry. Water Resources Research 60, e2023WR036873. doi:10.1029/2023WR036873.

Savage, L.J., 1954. The Foundations of Statistics. Wiley.

Scanlon, B.R., Healy, R.W., Cook, P.G., 2002. Choosing appropriate techniques for quantifying groundwater recharge. Hydrogeology Journal 10, 18–39. doi:10.1007/s10040-001-0176-2.

Scharroo, R., Visser, P., 1998. Precise orbit determination and gravity field improvement for the ERS satellites. Journal of Geophysical Research: Oceans 103, 8113–8127. doi:10.1029/97JC03179.

Scherer, D., Schwatke, C., Dettmering, D., Seitz, F., 2023. ICESat-2 river surface slope (IRIS): A global reach-scale water surface slope dataset. Scientific Data 10, 359. doi:10.1038/s41597-023-02215-x.

Scherer, D., Schwatke, C., Dettmering, D., Seitz, F., 2024. Monitoring river discharge from space: An optimization approach with uncertainty quantification for small ungauged rivers. Remote Sensing of Environment 315, 114434. doi:10.1016/j.rse.2024.114434.

Schmidt, R., Flechtner, F., Meyer, U., Neumayer, K.H., Dahle, C., König, R., Kusche, J., 2008. Hydrological signals observed by the GRACE satellites. Surveys in Geophysics 29, 319–334. doi:10.1007/s10712-008-9033-3.

Schneider, U., Becker, A., Finger, P., Rustemeier, E., Ziese, M., 2020. GPCC full data monthly product version 2020 at 0.25°: monthly land-surface precipitation from rain-gauges built on GTS-based and historical data. Global Precipitation Climatology Centre at Deutscher Wetterdienst: Offenbach, Germany doi:10.5676/DWD_GPCC/FD_M_V2020_025.

van de Schoot, R., Depaoli, S., King, R., Kramer, B., Märtens, K., Tadesse, M.G., Vannucci, M., Gelman, A., Veen, D., Willemsen, J., et al., 2021. Bayesian statistics and modelling. Nature Reviews Methods Primers 1, 1. doi:10.1038/s43586-020-00001-2.

Schulze, K., Kusche, J., Gerdener, H., Döll, P., Müller Schmied, H., 2024. Benefits and pitfalls of grace and streamflow assimilation for improving the streamflow simulations of the watergap global hydrology model. Journal of Advances in Modeling Earth Systems 16, e2023MS004092. doi:10.1029/2023MS004092.

Schumacher, M., Forootan, E., van Dijk, A., Schmied, H.M., Crosbie, R., Kusche, J., Döll, P., 2018. Improving drought simulations within the Murray-Darling Basin by combined calibration/assimilation of GRACE data into the WaterGAP Global Hydrology Model. Remote Sensing of Environment 204, 212–228. doi:10.1016/j.rse.2017.10.029.

Schwatke, C., Halicki, M., Scherer, D., 2024. Generation of high-resolution water surface slopes from multi-mission satellite altimetry. Water Resources Research 60, e2023WR034907. doi:10.1029/2023WR034907.

Seo, K.W., Wilson, C.R., Han, S.C., Waliser, D.E., 2008. Gravity recovery and climate experiment (GRACE) alias error from ocean tides. Journal of Geophysical Research 113, B03405. doi:10.1029/2006JB004747.

Seyoum, W.M., Kwon, D., Milewski, A.M., 2019. Downscaling GRACE TWSA Data into High-Resolution Groundwater Level Anomaly Using Machine Learning-Based Models in a Glacial Aquifer System. Remote Sensing 11. doi:10.3390/rs11070824.

da Silva, J.S., Calmant, S., Seyler, F., Filho, O.C.R., Cochonneau, G., Mansur, W.J., 2010. Water levels in the Amazon basin derived from the ERS 2 and ENVISAT radar altimetry missions. Remote Sensing of Environment 114, 2160–2181. doi:10.1016/j.rse.2010.04.020.

Skilling, J., 2006. Nested sampling for general Bayesian computation. Bayesian Analysis 1, 833–859. doi:10.1214/06-BA127.

Sklar, A., 1973. Random variables, joint distribution functions, and copulas. Kybernetika 9, 449–460.

Smith, A., Gelfand, G., 1992. Bayesian statistics without tears: A sampling-resampling perspective. The American Statistician 46, 84–88. doi:10.2307/2684170.

Smith, J., 2010. Bayesian Reasoning in Data Analysis: A Critical Introduction. Cambridge University Press. doi:10.1142/5262.

Smith, L.C., Pavelsky, T.M., 2008. Estimation of river discharge, propagation speed, and hydraulic geometry from space: Lena River, Siberia. Water Resources Research 44. doi:10.1029/2007WR006133. w03427.

Sneeuw, N., Flury, J., Rummel, R., 2005. Science requirements on future missions and simulated mission scenarios. Future Satellite Gravimetry and Earth Dynamics , 113–142doi:10.1007/0-387-33185-9_10.

Sneeuw, N., Lorenz, C., Devaraju, B., Tourian, M.J., Riegger, J., Kunstmann, H., Bárdossy, A., 2014. Estimating runoff using hydro-geodetic approaches. Surveys in Geophysics 35, 1333–1359. doi:10.1007/s10712-014-9300-4.

Soergel, U., 2010. Review of radar remote sensing on urban areas. Springer. doi:10.1007/978-90-481-3751-0_1.

Solander, K.C., Reager, J.T., Wada, Y., Famiglietti, J.S., Middleton, R.S., 2017. Grace satellite observations reveal the severity of recent water over-consumption in the united states. Scientific reports 7, 8723. doi:10.1038/s41598-017-07450-y.

Springer, A., 2019. A water storage reanalysis over the European continent: assimilation of GRACE data into a high-resolution hydrological model and validation. Ph.D. thesis. Universitäts-und Landesbibliothek Bonn. URL: https://hdl.handle.net/20.500.11811/7987.

Stammer, D., Cazenave, A., 2017. Satellite altimetry over oceans and land surfaces. CRC press. doi:10.1201/9781315151779.

Steiner, L., 2019. Snow Water Equivalent Observations Using Refracted GPS Signals. Ph.D. thesis. ETH Zurich. URL: https://www.research-collection.ethz.ch/handle/20.500.11850/345249.

Steiner, L., Schmithüsen, H., Wickert, J., Eisen, O., 2023. Combined GNSS reflectometry–refractometry for automated and continuous in situ surface mass balance estimation on an Antarctic ice shelf. The Cryosphere 17, 4903–4916. doi:10.5194/tc-17-4903-2023.

Strassberg, G., Scanlon, B., Rodell, M., 2007. Comparison of seasonal terrestrial water storage variations from GRACE with groundwater-level measurements from the High Plains Aquifer (USA). Geophysical Research Letters 34, L14402. doi:10.1029/2007GL030139.

SU, S.L., Singh, D.N., Baghini, M.S., 2014. A critical review of soil moisture measurement. Measurement 54, 92–105. doi:10.1016/j.measurement.2014.04.007.

Sun, A.Y., Green, R., Swenson, S., Rodell, M., 2012. Toward calibration of regional groundwater models using GRACE data . Journal of Hydrology 422–423, 1 – 9. doi:10.1016/j.jhydrol.2011.10.025.

Sun, A.Y., Scanlon, B.R., Save, H., Rateb, A., 2021. Reconstruction of grace total water storage through automated machine learning. Water Resources Research 57, e2020WR028666. doi:https://doi.org/10.1029/2020WR028666.

Sun, Y., Bao, W., Qu, S., Li, Q., Jiang, P., Zhou, Z., Shi, P., 2023. Development of the consider cubature Kalman filter for state estimation of hydrological models with parameter uncertainty. Journal of Hydrology 625, 130080. doi:10.1016/j.jhydrol.2023.130080.

Sutanudjaja, E.H., Van Beek, R., Wanders, N., Wada, Y., Bosmans, J.H., Drost, N., Van Der Ent, R.J., De Graaf, I.E., Hoch, J.M., De Jong, K., et al., 2018. PCR-GLOBWB 2: a 5 arcmin global hydrological and water resources model. Geoscientific Model Development 11, 2429–2453. doi:10.5194/gmd-11-2429-2018.

Swenson, S., Wahr, J., 2006. Post-processing removal of correlated errors in GRACE data. Geophysical Research Letters 33, L08402. doi:10.1029/2005GL025285.

Swenson, S., Wahr, J., Milly, P., 2006. Estimated accuracies of regional water storage variations inferred from the Gravity Recovery and Climate Experiment (GRACE). Water Resources Research 42. doi:10.1029/2002WR001808.

Szeliski, R., Zabih, R., Scharstein, D., Veksler, O., Kolmogorov, V., Agarwala, A., Tappen, M., Rother, C., 2008. A comparative study of energy minimization methods for markov random fields with smoothness-based priors. IEEE transactions on pattern analysis and machine intelligence 30, 1068–1080. doi:10.1109/TPAMI.2007.70844.

Tang, Q., Durand, M., Lettenmaier, D.P., Hong, Y., 2010. Satellite-based observations of hydrological processes. doi:10.1080/01431161.2010.483496.

Tangdamrongsub, N., Han, S.C., Yeo, I.Y., Dong, J., Steele-Dunne, S.C., Willgoose, G., Walker, J.P., 2020. Multivariate data assimilation of GRACE, SMOS, SMAP measurements for improved regional soil moisture and groundwater storage estimates. Advances in Water Resources 135, 103477. doi:10.1016/j.advwatres.2019.103477.

Tangdamrongsub, N., Steele-Dunne, S.C., Gunter, B.C., Ditmar, P.G., Sutanudjaja, E.H., Sun, Y., Xia, T., Wang, Z., 2017. Improving estimates of water resources in a semi-arid region by assimilating GRACE data into the PCR-GLOBWB hydrological model. Hydrology and Earth System Sciences 21, 2053–2074. doi:10.5194/hess-21-2053-2017.

Tapley, B.D., Bettadpur, S., Ries, J.C., Thompson, P.F., Watkins, M.M., 2004a. GRACE measurements of mass variability in the Earth system. Science 305, 503–505. doi:10.1126/science.1099192.

Tapley, B.D., Bettadpur, S., Watkins, M., Reigber, C., 2004b. The Gravity Recovery and Climate Experiment: Mission overview and early results. Geophysical Research Letters 31. doi:10.1029/2004GL019779.

Tarantola, A., 2005. Inverse Problem Theory and Methods for Model Parameter Estimation. SIAM. doi:10.1137/1.9780898717921.

Tarpanelli, A., Barbetta, S., Brocca, L., Moramarco, T., 2013a. River Discharge Estimation by Using Altimetry Data and Simplified Flood Routing Modeling. Remote Sensing 5, 4145–4162. doi:10.3390/rs5094145.

Tarpanelli, A., Brocca, L., Lacava, T., Melone, F., Moramarco, T., Faruolo, M., Pergola, N., Tramutoli, V., 2013b. Toward the estimation of river discharge variations using MODIS data in ungauged basins. Remote Sensing of Environment 136, 47–55. doi:10.1016/j.rse.2013.04.010.

Tarpanelli, A., Camici, S., Nielsen, K., Brocca, L., Moramarco, T., Benveniste, J., 2021. Potentials and limitations of sentinel-3 for river discharge assessment. Advances in Space Research 68, 593–606. doi:10.1016/j.asr.2019.08.005.

Tarpanelli, A., Santi, E., Tourian, M.J., Filippucci, P., Amarnath, G., Brocca, L., 2018. Daily river discharge estimates by merging satellite optical sensors and radar altimetry through artificial neural network. IEEE Transactions on Geoscience and Remote Sensing 57, 329–341. doi:10.1109/TGRS.2018.2854625.

Thibaut, P., Poisson, J., Bronner, E., Picot, N., 2010. Relative performance of the MLE3 and MLE4 retracking algorithms on Jason-2 altimeter waveforms. Marine Geodesy 33, 317–335. doi:10.1080/01490419.2010.491033.

Tian, S., Tregoning, P., Renzullo, L.J., van Dijk, A.I.J.M., Walker, J.P., Pauwels, V.R.N., Allgeyer, S., 2017. Improved water balance component estimates through joint assimilation of grace water storage and smos soil moisture retrievals. Water Resources Research 53, 1820–1840. doi:https://doi.org/10.1002/2016WR019641.

Tourian, M., Elmi, O., Chen, Q., Devaraju, B., Roohi, S., Sneeuw, N., 2015. A spaceborne multisensor approach to monitor the desiccation of lake urmia in iran. Remote Sensing of Environment 156, 349–360. doi:10.1016/j.rse.2014.10.006.

Tourian, M., Elmi, O., Mohammadnejad, A., Sneeuw, N., 2017a. Estimating river depth from SWOT-type observables obtained by satellite altimetry and imagery. Water 9, 753. doi:10.3390/w9100753.

Tourian, M., Schwatke, C., Sneeuw, N., 2017b. River Discharge Estimation at Daily Resolution from Satellite Altimetry over an Entire River Basin. Journal of Hydrology 546, 230–247. doi:10.1016/j.jhydrol.2017.01.009.

Tourian, M., Sneeuw, N., Bárdossy, A., 2013. A quantile function approach to discharge estimation from satellite altimetry (ENVISAT). Water Resources Research 49, 4174–4186. doi:10.1002/wrcr.20348.

Tourian, M.J., 2012. Controls on satellite altimetry over inland water surfaces for hydrological purposes. Master's thesis. University of Stuttgart. URL: http://elib.uni-stuttgart.de/handle/11682/3896.

Tourian, M.J., 2013. Application of spaceborne geodetic sensors for hydrology. Ph.D. thesis. Universität Stuttgart. Holzgartenstr. 16, 70174 Stuttgart. URL: http://elib.uni-stuttgart.de/opus/volltexte/2014/8796.

Tourian, M.J., Elmi, O., Khalili, S., Engels, J., 2025. Improving Inland Water Altimetry Through Bin-Space-Time (BiST) Retracking: A Bayesian Approach to Incorporate Spatiotemporal Information. IEEE Transactions on Geoscience and Remote Sensing 63, 1–19. doi:10.1109/TGRS.2025.3528856.

Tourian, M.J., Elmi, O., Shafaghi, Y., Behnia, S., Saemian, P., Schlesinger, R., Sneeuw, N., 2022. HydroSat: geometric quantities of the global water cycle from geodetic satellites. Earth System Science Data 14, 2463–2486. doi:10.5194/essd-14-2463-2022.

Tourian, M.J., Papa, F., Elmi, O., Sneeuw, N., Kitambo, B., Tshimanga, R.M., Paris, A., Calmant, S., 2023a. Current availability and distribution of Congo Basin's freshwater resources. Communications Earth & Environment 4, 174. doi:10.1038/s43247-023-00836-z.

Tourian, M.J., Reager, J., Sneeuw, N., 2018. The total drainable water storage of the Amazon River Basin: A first estimate using GRACE. Water Resources Research 54, 3290–3312. doi:10.1029/2017WR021674.

Tourian, M.J., Saemian, P., Ferreira, V.G., Sneeuw, N., Frappart, F., Papa, F., 2023b. A copula-supported Bayesian framework for spatial downscaling of GRACE-derived terrestrial water storage flux. Remote Sensing of Environment 295, 113685. doi:10.1016/j.rse.2023.113685.

Tourian, M.J., Sneeuw, N., Bárdossy, A., 2013. A Quantile Function Approach to Discharge Estimation from Satellite Altimetry (ENVISAT). Water Resources Research 49, 1–13. doi:10.1002/wrcr.20348.

Tourian, M.J., Tarpanelli, A., Elmi, O., Qin, T., Brocca, L., Moramarco, T., Sneeuw, N., 2016. Spatiotemporal densification of river water level time series by multimission satellite altimetry. Water Resources Research doi:10.1002/2015WR017654.

Trenberth, K., Asrar, G., 2014. Challenges and Opportunities in Water Cycle Research: WCRP Contributions. Surveys in Geophysics 35, 515–532. doi:10.1007/s10712-012-9214-y.

Twele, A., Cao, W., Plank, S., Martinis, S., 2016. Sentinel-1-based flood mapping: a fully automated processing chain. International Journal of Remote Sensing 37, 2990–3004. doi:10.1080/01431161.2016.1192304.

Uebbing, B., Forootan, E., Braakmann-Folgmann, A., Kusche, J., 2017. Inverting surface soil moisture information from satellite altimetry over arid and semi-arid regions. Remote sensing of environment 196, 205–223. doi:10.1016/j.rse.2017.05.004.

Unwin, M.J., Pierdicca, N., Cardellach, E., Rautiainen, K., Foti, G., Blunt, P., Guerriero, L., Santi, E., Tossaint, M., 2021. An introduction to the HydroGNSS GNSS reflectometry remote sensing mission. IEEE Journal of Selected Topics in Applied Earth Observations and Remote Sensing 14, 6987–6999. doi:10.1109/JSTARS.2021.3089550.

Van Der Knijff, J., Younis, J., De Roo, A., 2010. LISFLOOD: a GIS-based distributed model for river basin scale water balance and flood simulation. International Journal of Geographical Information Science 24, 189–212. doi:10.1080/13658810802549154.

Van Dijk, A., 2010. The australian water resources assessment system technical report 3. landscape model (version 0.5) technical description.

Vanthof, V., Kelly, R., 2019. Water storage estimation in ungauged small reservoirs with the TanDEM-X DEM and multi-source satellite observations. Remote Sensing of Environment 235, 111437. doi:10.1016/j.rse.2019.111437.

Vargas Godoy, M.R., Markonis, Y., Hanel, M., Kyselỳ, J., Papalexiou, S.M., 2021. The global water cycle budget: A chronological review. Surveys in Geophysics 42, 1075–1107. doi:10.1007/s10712-021-09652-6.

Veksler, O., 1999. Efficient graph-based energy minimization methods in computer vision. Ph.D. thesis. Cornell University.

Verhoest, N.E., Van Den Berg, M.J., Martens, B., Lievens, H., Wood, E.F., Pan, M., Kerr, Y.H., Al Bitar, A., Tomer, S.K., Drusch, M., et al., 2015. Copula-based downscaling of coarse-scale soil moisture observations with implicit bias correction. IEEE Transactions on geoscience and remote sensing 53, 3507–3521. doi:10.1109/TGRS.2014.2378913.

Villadsen, H., Deng, X., Andersen, O.B., Stenseng, L., Nielsen, K., Knudsen, P., 2016. Improved inland water levels from sar altimetry using novel empirical and physical retrackers. Journal of hydrology 537, 234–247. doi:10.1016/j.jhydrol.2016.03.051.

Vishwakarma, B.D., Devaraju, B., Sneeuw, N., 2018. What is the spatial resolution of GRACE satellite products for hydrology? Remote Sensing 10, 852. doi:10.3390/rs10060852.

Vishwakarma, B.D., Horwath, M., Devaraju, B., Groh, A., Sneeuw, N., 2017. A Data-Driven Approach for Repairing the Hydrological Catchment Signal Damage Due to Filtering of GRACE Products. Water Resources Research 53, 9824–9844. doi:10.1002/2017WR021150.

Vishwakarma, B.D., Zhang, J., Sneeuw, N., 2021. Downscaling GRACE total water storage change using partial least squares regression. Scientific data 8, 1–13. doi:10.1038/s41597-021-00862-6.

Vörösmarty, C., Fekete, B.M., Meybeck, M., Lammers, R.B., 2000. Global system of rivers: Its role in organizing continental land mass and defining land-to-ocean linkages. Global Biogeochemical Cycles 14, 599–621. doi:10.1029/1999GB900092.

Vörösmarty, C.J., Sahagian, D., 2000. Anthropogenic disturbance of the terrestrial water cycle. Bioscience 50, 753–765. doi:10.1641/0006-3568(2000)050[0753:ADOTTW]2.0.CO;2.

Voss, K.A., Famiglietti, J.S., Lo, M., De Linage, C., Rodell, M., Swenson, S.C., 2013. Groundwater depletion in the Middle East from GRACE with implications for transboundary water management in the Tigris-Euphrates-Western Iran region. Water resources research 49, 904–914. doi:10.1002/wrcr.20078.

Vrugt, J.A., Gupta, H.V., Bouten, W., Sorooshian, S., 2008. A Bayesian approach to multiobjective parameter estimation using Markov chain Monte Carlo simulation. Water Resources Research 39, 1345. doi:10.1029/2002WR001746.

Wada, Y., Wisser, D., Bierkens, M.F., 2014. Global modeling of withdrawal, allocation and consumptive use of surface water and groundwater resources. Earth System Dynamics 5, 15–40. doi:10.5194/esd-5-15-2014.

Wagner, W., Hahn, S., Kidd, R., Melzer, T., Bartalis, Z., Hasenauer, S., Figa-Saldaña, J., De Rosnay, P., Jann, A., Schneider, S., et al., 2013. The ASCAT soil moisture product: A review of its specifications, validation results, and emerging applications. Meteorologische Zeitschrift 22, 5–33. doi:10.1127/0941-2948/2013/0399.

Wahr, J., Molenaar, M., Bryan, F., 1998. The time-varibility of the earth's gravity field: Hydrological and oceanic effects and their possible detection using GRACE. Journal of Geophysical Research 103, 30205–30230. doi:10.1029/98JB02844.

Wan, E.A., Van Der Merwe, R., 2000. The unscented Kalman filter for nonlinear estimation, in: Proceedings of the IEEE 2000 adaptive systems for signal processing, communications, and control symposium (Cat. No. 00EX373), Ieee. pp. 153–158. doi:10.1109/ASSPCC.2000.882463.

Wang, B., 2024. Assessment of ICESat-2 laser altimetry in hydrological applications. Ph.D. thesis. Dissertation, Stuttgart, Universität Stuttgart, 2024. URL: http://elib.uni-stuttgart.de/handle/11682/14165.

Wang, H., Yeung, D.Y., 2016. Towards Bayesian deep learning: A framework and some existing methods. IEEE Transactions on Knowledge and Data Engineering 28, 3395–3408. doi:10.1109/TKDE.2016.2606428.

Wang, X., He, X., Xiao, R., Song, M., Jia, D., 2021. Millimeter to centimeter scale precision water-level monitoring using GNSS reflectometry: Application to the South-to-North Water Diversion Project, China. Remote Sensing of Environment 265, 112645. doi:https://doi.org/10.1016/j.rse.2021.112645.

Weigelt, M., van Dam, T., Jäggi, A., Prange, L., Tourian, M.J., Keller, W., Sneeuw, N., 2013. Time-variable gravity signal in Greenland revealed by high-low satellite-to-satellite tracking. Journal of Geophysical Research: Solid Earth 118, 3848–3859. doi:10.1002/jgrb.50283.

Weise, K., Woger, W., 1993. A Bayesian theory of measurement uncertainty. Measurement Science and Technology 4, 1. doi:10.1088/0957-0233/4/1/001.

Welch, G., Bishop, G., 1995. An introduction to the Kalman Filter. University of North Carolina at Chapel Hill.

Willmott, C.J., Matsuura, K., 1995. Smart interpolation of annually averaged air temperature in the United States. Journal of Applied Meteorology 34, 2577–2586. doi:10.1175/1520-0450(1995)034<2577:sioaaa>2.0.co;2.

Wilson, D.J., Western, A.W., Grayson, R.B., 2004. Identifying and quantifying sources of variability in temporal and spatial soil moisture observations. Water Resources Research 40. doi:10.1029/2003WR002306.

Wingham, D.J., Rapley, C.G., Griffiths, H., 1986. "New techniques in satellite altimeter tracking systems", in: In ESA Proceedings of the 1986 International Geoscience and Remote Sensing Symposium (IGARSS '86) on Remote Sensing: Today's Solutions for Tomorrow's Information Needs, NASA Foreign Exchange Program. pp. 1339–1344.

Wu, W.Y., Yang, Z.L., Zhao, L., Lin, P., 2022. The impact of multi-sensor land data assimilation on river discharge estimation. Remote Sensing of Environment 279, 113138. doi:10.1016/j.rse.2022.113138.

Wu, X., Ma, W., Xia, J., Bai, W., Jin, S., Calabia, A., 2021. Spaceborne GNSS-R Soil Moisture Retrieval: Status, Development Opportunities, and Challenges. Remote Sensing 13. doi:10.3390/rs13010045.

Wulder, M.A., et al., 2012. Opening the archive: How free data has enabled the science and monitoring promise of Landsat. Remote Sensing of Environment 122, 2–10. doi:10.1016/j.rse.2012.01.010.

Xu, H., Luo, Y., 2015. Climate change and its impacts on river discharge in two climate regions in China. Hydrology and Earth System Sciences 19, 4609–4618. doi:10.5194/hess-19-4609-2015.

Xue, L., Fu, Y., Martens, H.R., 2021. Seasonal hydrological loading in the Great Lakes region detected by GNSS: A comparison with hydrological models. Geophysical Journal International 226, 1174–1186. doi:10.1093/gji/ggab158.

Yang, D., Yang, Y., Xia, J., 2021. Hydrological cycle and water resources in a changing world: A review. Geography and Sustainability 2, 115–122. doi:10.1016/j.geosus.2021.05.003.

Yao, F., Livneh, B., Rajagopalan, B., Wang, J., Crétaux, J.F., Wada, Y., Berge-Nguyen, M., 2023. Satellites reveal widespread decline in global lake water storage. Science 380, 743–749. doi:10.1126/science.abo2812.

Yao, F., Wang, J., Wang, C., Crétaux, J.F., 2019. Constructing long-term high-frequency time series of global lake and reservoir areas using Landsat imagery. Remote Sensing of Environment 232, 111210. doi:10.1016/j.rse.2019.111210.

Yi, S., Song, C., Wang, Q., Wang, L., Heki, K., Sun, W., 2017. The potential of GRACE gravimetry to detect the heavy rainfall-induced impoundment of a small reservoir in the upper Yellow River. Water Resources Research 53, 6562–6578. doi:10.1002/2017WR020793.

Yin, G., Forman, B.A., Loomis, B.D., Luthcke, S.B., 2020. Comparison of vertical surface deformation estimates derived from space-based gravimetry, ground-based GPS, and model-based hydrologic loading over snow-dominated watersheds in the United States. Journal of Geophysical Research: Solid Earth 125, e2020JB019432. doi:10.1029/2020JB019432.

Yin, W., Hu, L., Zhang, M., Wang, J., Han, S.C., 2018. Statistical Downscaling of GRACE-Derived Groundwater Storage Using ET Data in the North China Plain. Journal of Geophysical Research: Atmospheres 123, 5973–5987. doi:10.1029/2017JD027468.

Yoon, Y., Durand, M., Merry, C.J., Clark, E.A., Andreadis, K.M., Alsdorf, D.E., 2012. Estimating river bathymetry from data assimilation of synthetic SWOT measurements. Journal of Hydrology 464, 363–375. doi:10.1016/j.jhydrol.2012.07.028.

Yu, Q., Wang, S., He, H., Yang, K., Ma, L., Li, J., 2021. Reconstructing GRACE-like TWS anomalies for the Canadian landmass using deep learning and land surface model. International Journal of Applied Earth Observation and Geoinformation 102, 102404. doi:10.1016/j.jag.2021.102404.

Zaitchik, B.F., Rodell, M., Olivera, F., 2010. Evaluation of the Global Land Data Assimilation System using global river discharge data and a source-to-sink routing scheme. Water Resources Research 46, W06507. doi:10.1029/2009WR007811.

Zaitchik, B.F., Rodell, M., Reichle, R.H., 2008. Assimilation of GRACE terrestrial water storage data into a land surface model: Results for the Mississippi River Basin. Journal of Hydrometeorology 9, 535–548. doi:10.1175/2007JHM951.1.

Zebker, H.A., Goldstein, R.M., 1986. Topographic mapping from interferometric synthetic aperture radar observations. Journal of Geophysical Research: Solid Earth 91, 4993–4999. doi:10.1029/JB091iB05p04993.

Zenner, L., Gruber, T., Jäggi, A., Beutler, G., 2010. Propagation of atmospheric model errors to gravity potential harmonics—impact on GRACE de-aliasing. Geophysical Journal International 182, 797–807. doi:10.1111/j.1365-246X.2010.04669.x.

Zhang, J., 2010. Multi-source remote sensing data fusion: status and trends. International Journal of Image and Data Fusion 1, 5–24. doi:10.1080/19479830903561035.

Zhang, K., Kimball, J.S., Mu, Q., Jones, L.A., Goetz, S.J., Running, S.W., 2009. Satellite based analysis of northern et trends and associated changes in the regional water balance from 1983 to 2005. Journal of Hydrology 379, 92–110. doi:10.1016/j.jhydrol.2009.09.047.

Zhang, K., Kimball, J.S., Nemani, R.R., Running, S.W., 2010. A continuous satellite-derived global record of land surface evapotranspiration from 1983 to 2006. Water Resources Research 46. doi:10.1029/2009WR008800.

Zhang, S., Wang, T., Wang, L., Zhang, J., Peng, J., Liu, Q., 2021. Evaluation of GNSS-IR for retrieving soil moisture and vegetation growth characteristics in wheat farmland. Journal of surveying engineering 147, 04021009. doi:10.1061/(ASCE)SU.1943-5428.0000355.

Zhang, Y., Kong, D., Gan, R., Chiew, F.H., McVicar, T.R., Zhang, Q., Yang, Y., 2019. Coupled estimation of 500 m and 8-day resolution global evapotranspiration and gross primary production in 2002–2017. Remote Sensing of Environment 222, 165–182. doi:10.1016/j.rse.2018.12.031.

Zhang, Y., Peña-Arancibia, J.L., McVicar, T.R., Chiew, F.H., Vaze, J., Liu, C., Lu, X., Zheng, H., Wang, Y., Liu, Y.Y., et al., 2016. Multi-decadal trends in global terrestrial evapotranspiration and its components. Scientific reports 6, 1–12. doi:10.1038/srep19124.

Zhong, D., Wang, S., Li, J., 2021. Spatiotemporal downscaling of GRACE Total water storage using land surface model outputs. Remote Sensing 13, 900. doi:10.3390/rs13050900.

Zhou, T., Nijssen, B., Gao, H., Lettenmaier, D.P., 2016. The contribution of reservoirs to global land surface water storage variations. Journal of Hydrometeorology 17, 309–325. doi:10.1175/JHM-D-15-0002.1.

Zounemat-Kermani, M., Batelaan, O., Fadaee, M., Hinkelmann, R., 2021. Ensemble machine learning paradigms in hydrology: A review. Journal of Hydrology 598, 126266. doi:10.1016/j.jhydrol.2021.126266.

List of Figures

List of Tables

Abbreviations

AGU American Geophysical Union

ALES Adaptive Leading Edge Sub-waveform

ANN Artificial Neural Network

ASAR Advanced Synthetic Aperture Radar

ASI Italian Space Agency

BMA Bayesian Model Averaging

BRT Boosted Regression Trees

CC Correlation Coefficient

CKF Cubature Kalman Filter

CDF Cumulative Distribution Function

CHAMP CHAllenging Minisatellite Payload

CNES National Centre for Space Studies

CONAE Argentine Space Agency

CRF Conditional Random Fields

CRU Climatic Research Unit

CryoSat-2 ESA's satellite for measuring polar ice

CSA Canadian Space Agency

CSR Center for Space Research

DEM Digital Elevation Model

DLR Deutsche Zentrum für Luft- und Raumfahrt

DORIS Doppler Orbitography and Radiopositioning Integrated by Satellite

DTM Digital Terrain Model

ECMWF European Centre for Medium-Range Weather Forecasts

EKF Extended Kalman Filter

EnKF Ensemble Kalman Filter

ENVISAT ENVIronmental SATellite

EOF Empirical Orthogonal Function

EOT Earth Ocean Tide model

ERS European Remote Sensing satellite

ESA European Space Agency

EUMETSAT European Organisation for the Exploitation of Meteorological Satellites

FES Finite Element Solution

FFT Fast Fourier Transform

FF-SAR Fully Focused Synthetic Aperture Radar

GDR Geophysical Data Record

GFZ GeoForschungsZentrum

GHM Gauss-Helmert Model

GLEAM Global Land-surface Evaporation: the Amsterdam Methodology

GLDAS Global Land Data Assimilation System

GNSS Global Navigation Satellite System

GNSS-IGS International GNSS Service

GNSS-IR GNSS-Interferometric Reflectometry

GNSS-R GNSS-Reflectometry

GRACE Gravity Recovery and Climate Experiment

GRACE-FO Gravity Recovery and Climate Experiment Follow-On

GRDC Global Runoff Data Center

GSW Global Surface Water occurrence map

GFO Geosat Follow-On

HMC Hamiltonian Monte Carlo

ICG International GNSS Service

INPPTR Improved Non-Parametric Peak Threshold Retracker

IP Inflection Point Method

IRNSS Indian Regional Navigation Satellite System

ISRO Indian Space Research Organisation

JAXA Japan Aerospace Exploration Agency

Jason-series Jason satellite missions for ocean topography

LEO Low Earth Orbit

LSTM Long Short-Term Memory

MAP Maximum A Posteriori

MCMC Markov Chain Monte Carlo

McFLI Mass-conserved Flow Law Inversion

ML Maximum Likelihood

MRF Markov Random Field

NASA National Aeronautics and Space Administration

NOAA National Oceanic and Atmospheric Administration

NSE Nash-Sutcliffe Efficiency

NSOAS National Satellite Ocean Application Service

NUTS No-U-Turn Sampler

OCOG Offset Center of Gravity

OLTC Open-Loop Tracking Command

PCR-GLOBWB PCRaster Global Water Balance Model

PDF Probability Density Function

POD Precise Orbit Determination

Rel. RMSE Relative Root Mean Squared Error

RF Random Forest

RMS Root Mean Square

RMSE Root Mean Squared Error

SAR Synthetic Aperture Radar

SARAL/AltiKa Satellite with ARgos and ALtika

SMC Sequential Monte Carlo

SMC Soil Moisture Change

SRAL Synthetic Aperture Radar Altimeter

STAR Spatiotemporal Altimetry Retracking

SURFEX-TRIP Surface Externalisée-Terrain Routing Integrated with Pyrethroids

SWOT Surface Water and Ocean Topography

SWSC Surface Water Storage Change

SWH Significant Wave Height

TWSA Terrestrial Water Storage Anomalies

TWSF Terrestrial Water Storage Flux

TOPEX Ocean Topography Experiment

UKF Unscented Kalman Filter

VCDR Vertical Crustal Displacement Change

VI Variational Inference

VS Virtual Station

WGHM WaterGAP Global Hydrology Model